Studies on Boron-Carbon-Nitrides (B-C-N) Leading to the Discovery of the Novel Boron Oxynitride $B_6N_4O_3$

Shrikant Bhat

Disperse Feststoffe

TECHNISCHE UNIVERSITÄT DARMSTADT

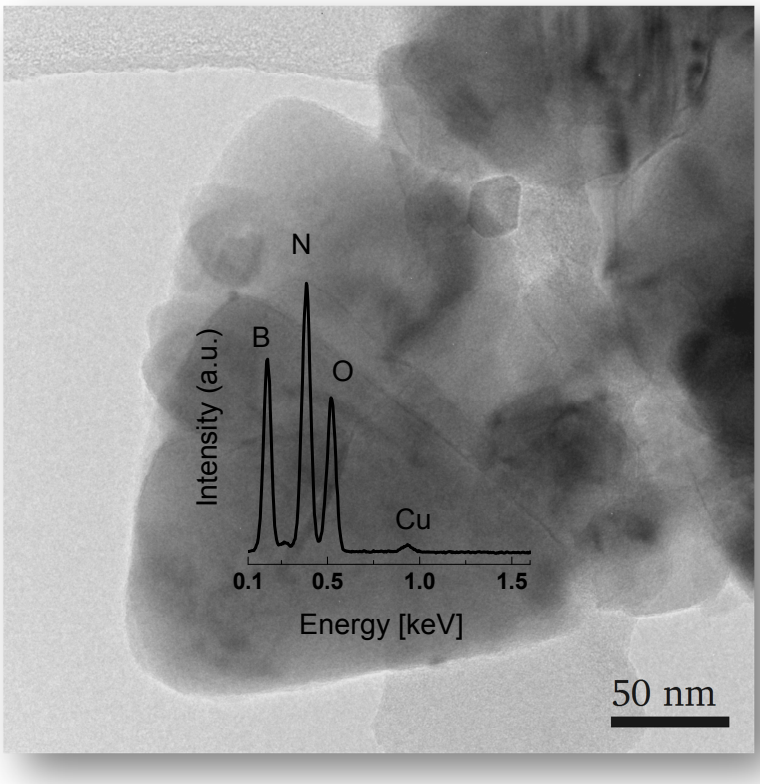

Fachbereich Material- und Geowissenschaften

Technische Universität Darmstadt, Germany

This page is intentionally left blank

A Dissertation Approved by the Department of Materials and Earth Sciences
in fulfillment of the requirements for the degree of Doktor−Ingenieur (Dr.-Ing.)

Studies on Boron-Carbon-Nitrides (B-C-N) Leading to the Discovery of the Novel Boron Oxynitride $B_6N_4O_3$

M. Sc. **Shrikant Bhat**

Born on 22.07.1982, in Itagi-Siddapura, Karnataka, India

TECHNISCHE
UNIVERSITÄT
DARMSTADT

Referee: Prof. Dr. Ralf Riedel

Co-Referee: Prof. Dr. Hans-Joachim Kleebe

Fachbereich Material- und Geowissenschaften
Technische Universität Darmstadt, Germany

Date of Submission: 20th April 2016

Date of Examination: 17th June 2016

Darmstadt, 2016 - D 17

This page is intentionally left blank

Dedicated to my son 'Omkar Bhat'

Contents

Contents ..... **i**

Abstract ..... **v**

Zusammenfassung ..... **vii**

1. Introduction **1**

1.1. Background and Motivation *1*

1.2. Aim and scope of the present work *3*

1.3. State of the Art *4*

1.3.1. Introduction and Motivation for Boron Oxynitrides 4

1.3.2. B-C-N compounds- a review 7

1.3.2.1 Theoretical predictions 7

1.3.2.2 Synthesis of B-C-N compounds 16

1.3.2.3 HP-HT behavior of BCN compounds 22

1.3.2.4 Electrochemical studies of BCN compounds 28

2. Experimental Techniques **29**

2.1. Synthesis of BCN and BON compounds *29*

2.1.1. Synthesis of BC_2N 29

2.1.2. Synthesis of BC_4N 32

2.1.3. Synthesis of B-O-N (BN / B_2O_3 mixtures) 33

2.2. High-Pressure High-Temperature experiments *34*

2.2.1. Introduction to high pressure techniques 34

2.2.2. Toroid Experiments 36

2.2.3. Multi Anvil Experiments 37

2.2.3.1 Single-stage cubic anvil device (MAX80) 37

2.2.3.2 Two-stage multi anvil (6 / 8 Walker type) device 39

2.2.4. Diamond Anvil Cell Experiments 44

2.3. Characterization Methods *49*

2.3.1. Powder X-ray diffraction 49

2.3.2. In-house X-ray diffractometer 50

2.3.3. Synchrotron radiation 50

2.3.4. Transmission electron microscopy (TEM) 51

2.3.4.1 TEM specimen preparation 53

2.3.4.2 High Resolution TEM and Energy-dispersive X-ray spectroscopy 54

2.3.4.3 Scanning transmission electron microscopy (STEM) 55
2.3.4.4 Electron energy-loss spectroscopy (EELS) 55
2.3.4.5 Automated Diffraction Tomography (ADT) 56
2.3.5. Scanning Electron Microscopy (SEM) 57
2.3.6. Raman Spectroscopy 58
2.3.7. Elemental Analysis 58
2.3.8. Electrochemical Characterization 59

3. Results and discussion 63

3.1. Analysis of the synthesized BCN and BON compounds 63
3.1.1. Elemental Analysis of BCN 63
3.1.2. X-ray diffraction analysis of BCN 64
3.1.3. X-ray photoelectron spectroscopy analysis of BCN 65
3.1.4. Raman spectroscopy analysis of BCN 65
3.1.5. Microscopy analysis of BCN 68
3.1.6. X-ray diffraction analysis of BON (BN / B_2O_3 Mixtures) 69

3.2. High pressure high temperature experiments 71
3.2.1. Multi anvil (MAX80) experiments – (5 to 7 GPa) 71
3.2.2. Toroid experiments (12 GPa) 74
3.2.3. Large volume press experiments (15.6 GPa) 75
3.2.3.1 LVP experiments with BC_4N (15.6 GPa) 75
3.2.3.2 LVP experiments with BC_2N (15.6 GPa) 77
3.2.4. Diamond anvil cell experiments (20 -39 GPa) 79
3.2.4.1 DAC experiments with BC_4N 79
3.2.4.2 DAC experiments with BC_2N 80
3.2.4.3 Formation of Boron Oxynitride (BON) Phase 86
3.2.5. Novel Boron Oxynitride (BON) 90
3.2.5.1 Chemical Composition by EELS 90
3.2.5.2 Crystal Structure 91
3.2.5.3 High Resolution Transmission Electron Microscopy 96
3.2.5.4 Density Functional Theory (DFT) Calculations 97

3.3. Electrochemical studies on B-C-N 101

4. Conclusions and Outlook 105

References 111

List of Tables 125

List of Figures **125**

Abrivations **130**

Acknowledgement **131**

Curriculum Vitae **133**

Abstract

The present thesis deals with studies on boron-carbon-nitrides (B-C-N) and with the discovery of a novel boron oxynitride (B-O-N) phase. Polymer-derived amorphous B-C-N compounds are studied under high-pressure and high temperature (HP-HT) conditions in order to investigate the formability of crystalline ternary B-C-N phases. Furthermore, the potential capability of amorphous B-C-N compounds for their electrochemical performance as promising anode materials for Li-ion battery (LIB) is evaluated. Challenges of HP-HT synthesis of ternary B-C-N, hints towards novel BONs and the final discovery of a novel BON phase are discussed in detail.

Diamond-like BCN compounds are of interest due to their extreme hardness and predicted excellent thermal and chemical stability, which are superior to those of diamond and c-BN. In the present work, amorphous BC_2N and BC_4N are studied under HP-HT conditions, as potential precursors (starting materials) for ternary B-C-N compounds. BC_2N and BC_4N precursors were prepared via thermal conversion of piperazine borane and pyridine borane, respectively. X-ray diffraction (XRD) studies showed amorphous nature, and X-ray photoelectron spectroscopy (XPS) confirmed the presence of mixed C-C, C-N, and B-N bonding states. Elemental analysis of the precursors by hot gas extraction methods confirmed the C/N ratios of 2:1 and 4:1 in BC_2N and BC_4N, respectively. These amorphous BCN compounds were subjected to HP-HT conditions using a single-stage multi anvil (MA) press (5-7 GPa, 100- 1700 °C), toroid press (12 GPa, ~ 1000 °C), a double stage large volume press (15.6 GPa, 1900 °C) and also diamond anvil cell (DAC) (20-39 GPa, 1900 - 2000 °C). *In-situ* and *ex-situ* X-ray diffraction revealed the decomposition of BC_4N to graphite and h-BN between 5 to 12 GPa and above 500 °C. In contrast, BC_2N remains amorphous up to 1500 °C between 5 to 12 GPa and starts to decompose into graphite and h-BN above 1600 °C. HP-HT experiments performed in large volume presses and DACs showed that amorphous BC_2N and BC_4N transform into mixtures of c-BN and diamond at pressure above 15 GPa. However in the case of BC_2N, some crystals with triangular morphology were found to contain considerable amount of oxygen along with boron and nitrogen. The outcome gave hints for the existence of boron oxynitrides. Repeated examination of the recovered HP-HT samples using high-resolution transmission electron microscopy (HRTEM), and energy dispersive spectroscopy (EDS), shed light on the tendency of BC_2N to transform into mixtures of triangular shaped crystals of oxygen containing BN (novel boron oxynitrides?) and nano-crystalline diamond.

Metal oxynitrides are known for their excellent optical properties in combination with high mechanical strength, thermal properties and chemical stability. The present thesis deals with the discovery of a novel crystalline boron oxynitride (B-O-N) phase under static pressures exceeding 15 GPa and temperatures above 1900 °C from molar mixtures of B_2O_3 and h-BN. The structure and composition of the synthesized products were studied using high-resolution

transmission electron microscopy, electron diffraction, automated diffraction tomography (ADT), energy dispersive X-ray spectroscopy and electron energy-loss spectroscopy (EELS). The EELS quantification yielded 42 at.% B , 35 at.% N and 23 at.% O (B:N:O ≈ 6:4:3). BON shows a hexagonal cell (*R3m*, Z=3) with lattice parameters a = 2.55(5) Å and c = 6.37(13) Å, and a crystal structure closely related to the cubic sphalerite type. Results of the electronic structure calculations in the framework of Density Functional Theory (DFT) are specified to get indication about the stabilities and properties of selected models with the composition $B_6N_4O_3$. These models contain ordered structural vacancies and are superstructures of the sphalerite structure. The calculated bulk moduli of the structure models with the lowest formation enthalpies are around 300 GPa, higher than that of any other known oxynitride.

Finally, the above synthesized B-C-N materials (a-BC_2N and a-BC_4N) are tested for the electrochemical performance as promising anodes for Li-ion battery. The amorphous BC_2N ceramics found to have initial capacities of 667 mAh g^{-1} and 235 mAh g^{-1} for lithium insertion/extraction, respectively. The amorphous BC_4N ceramics, disclose better reversible lithium storage properties. Initial capacities of 1030 mAh g^{-1} and 737 mAh g^{-1} for lithium insertion and extraction have been recovered for carbon rich BC_4N composition. Extended cycling with high currents up to 2C/2D reveals the cycling stability of BC_4N electrodes. Cycling for more than 75 cycles at constant current rates shows a stable electrochemical behavior of BC_4N anodes with capacities as high as 500 mAh g^{-1}.

This study mainly contains four major sections, 1) Introduction, 2) Experimental, 3) Results and discussions and 4) Conclusions and Outlook. Introduction section includes a background and motivation (chapter 1.1), aim and scope of the present work (chapter 1.2) followed by a state of the art (chapter 1.3). The state of the art chapter covers an introduction towards metal oxynitrides and BONs (chapter 1.3.1) and a review on ternary B-C-N compounds (chapter 1.3.2). Experimental section consists of synthesis route, as well as experimental and characterization methods used in the present effort. Results and discussions section covers all the findings, followed by conclusions and outlook. A more detailed overview of the latter chapters is outlined in the opening of each chapter.

Zusammenfassung

Die vorliegende Arbeit beschäftigt sich mit Untersuchungen zu Bor-Kohlenstoff-Nitriden (B-C-N) und dem Nachweis einer neuen Boroxynitrid Phase (BON). Im Vordergrund des Interesses steht die Bildung kristalliner BCN-Phasen unter Hochdruck- und Hochtemperaturbedingungen (HP-HT). Ferner wird die Performance amorpher B-C-N Verbindungen als Anodenmaterialien in Lithiumionenbatterien (LIB) untersucht. Im Rahmen der HP-HT Synthese ternärer B-C-N Verbindungen, wurde eine neuartige Boroxynitrid-Phase der Zusammensetzung $B_6N_4O_3$ entdeckt und deren Festkörperstruktur detailliert untersucht.

Auf Grund der außergewöhnlichen Härte diamantartiger B-C-N Verbindungen sowie der gegenüber Diamant und c-BN zu erwartenden exzellenten chemischen und thermischen Stabilität stellen sie eine interessante Klasse innerhalb der superharten Werkstoffe dar. In dieser Arbeit werden amorphes BC_2N sowie BC_4N als potentielle Precursoren zur Synthese ternärer B-C-N Verbindungen unter HP-HT Bedingungen untersucht. BC_2N und BC_4N werden über einen Pyrolyseprozess ausgehend von Piperazin-Boran bzw. Pyridin-Boran erhalten. Untersuchungen per Röntgenbeugung (XRD) bestätigen den amorphen Zustand sowohl bei BC_2N als auch bei BC_4N. Röntgenphotoelektronenspektroskopische Untersuchungen (XPS) zeigen die Anwesenheit von C-C, C-N und B-N Bindungen. Elementaranalysen der Precursormaterialien mittels Heißgasextraktion bestätigen die Kohlenstoff:Stickstoff Verhältnisse von 2:1 bei BC_2N und 4:1 bei BC_4N.

Die amorphen B-C-N Verbindungen wurden in den folgenden Setups unter HP-HT Bedingungen untersucht: i) Einstufen-Vielstempel- Hochdruckpresse (single-stage multi anvil (MA) press, 5-7 GPa, 100-1700°C) ii) Toroid Presse (toroid press, 12 GPa, ~1000°C) iii) doppelstufige Großvolumenpresse (double stage large volume press, 15.6 GPa, 1900°C) und iv) Diamantstempelzelle (diamond anvil cell (DAC), 20-39 GPa, 1900-2000°C). Die Zersetzung von BC_4N zu Graphit und h-BN bei 5-12 GPa und oberhalb 500°C geht aus in-situ und ex-situ Röntgenbeugungsdaten hervor. Im Gegensatz dazu behält BC_2N bis 1500°C und 5-12 GPa seinen amorphen Zustand bei und zersetzt sich erst bei über 1600°C zu Graphit und h-BN. HP-HT-Experimente sowohl in großvolumigen Pressen als auch in Diamantstempelzellen zeigen, dass amorphes BC_2N und BC_4N bei Drücken oberhalb 15 GPa zu Mischungen aus Diamant und c-BN transformieren. Allerdings enthalten im Fall von BC_2N einige Kristallite mit triangularer Morphologie neben Bor und Stickstoff auch beträchtliche Sauerstoffanteile, was als Hinweis auf eine bisher unbekannte Boroxynitrid-Phase gewertet wurde. Ausführliche Untersuchungen der HP-HT Proben per hochauflösender Transmissionselektronenmikroskopie (HR-TEM) und energiedispersiver Spektroskopie (EDS) lassen den Schluss zu, dass BC_2N dazu tendiert, ein Gemisch bestehend aus a) sauerstoffhaltigen BN-Kristalliten und b) nanokristallinem Diamant zu bilden.

Metall-Oxynitride sind bekannt für ihre herausragenden optischen Eigenschaften in Kombination mit hoher mechanischer, thermischer und chemischer Belastbarkeit. Die vorliegende Arbeit befasst sich mit der Darstellung einer neuartigen, bisher unbekannten Boroxynitrid-Phase unter statischem Druck oberhalb 15 GPa und bei Temperaturen über 1900°C. Struktur und Zusammensetzung der Phase werden mit hochauflösender Transmissionselektronenmikroskopie, Elektronenbeugung, automatisierter Beugungstomographie, energiedispersiver Röntgenspektroskopie und Elektronenenergie-verlustspektroskopie (EELS) untersucht. Eine quantitative Auswertung der EELS-Spektren ergibt das Vorliegen von 42 at.% B , 35 at.% N und 23 at.% O (B:N:O ≈ 6:4:3). Die B-O-N Phase kristallisiert in einer hexagonalen Einheitszelle (*R3m*, Z=3) mit Gitterkonstanten a = 2.55(5) Å und c = 6.37(13) Å im kubischen Sphalerit-Typ.

Für ausgewählte $B_6N_4O_3$ Modell-Systeme wurden Berechnungen der elektronischen Struktur auf Basis der Dichtfunktionaltheorie (DFT) zur Klärung der Stabilität und Eigenschaften durchgeführt. Die Modelle enthalten geordnete strukturelle Leerstellen und sind Überstrukturen der Sphalerit-Struktur. Die berechneten Kompressionsmoduli der Strukturmodelle mit der geringsten Bildungsenthalpie liegen bei 300 GPa und damit höher als bei allen momentan bekannten Oxynitriden.

Neben Synthese und struktureller Charakterisierung wurden die hergestellten B-C-N-Phasen (a-BC_2N and a-BC_4N) auf ihre Eignung als Anodenmaterial für Lithiumionenbatterien untersucht. Amorphe BC_2N Keramik weist eine Anfangskapazität von 667 mAh g^{-1} und 235 mAh g^{-1} für die Lithiumeinlagerung bzw. Extraktion auf. Die amorphe BC_4N-Keramik zeigt eine weitaus bessere reversible Lithiumionenspeicherung. Für die kohlenstoffreichen BC_4N-Proben wurden Anfangskapazitäten von 1030 mAh g^{-1} und 737 mAh g^{-1} für Lithiumeinlagerung bzw. -extraktion gemessen. Die BC_4N Elektroden bleiben bei weiterer Zyklierung mit hohen Ladeströmen bis zu 2C/2D zyklenstabil. Bei > 75 Ladezyklen bei konstantem Ladestom zeigt sich ein stabiles elektrochemisches Verhalten der BC_4N-Anoden mit Kapazitäten bis zu 500 mAh g^{-1}.

Die vorliegende Arbeit ist in vier Abschitte aufgeteilt: 1) Einleitung, 2) Experimenteller Teil 3) Ergebnisse und deren Diskussion sowie 4) Schlussfolgerungen und Ausblick. Im einleitenden Abschnitt werden der wissenschaftliche Hintergrund und die Motivation (Kapitel 1.1), Ziel und Grund der vorliegenden Arbeit (Kapitel 1.2) sowie eine Übersicht über den aktuellen Wissensstand (Kapitel 1.3) behandelt. Die Einleitung schließt eine Besprechung der Metall-Oxynitride und B-O-N-Verbindungen (Kapitel 1.3.1) sowie der ternären B-C-N-Verbindungen (Kapitel 1.3.2) ein. Im experimentellen Teil (Kapitel 2) werden die Syntheserouten, experimentellen Methoden und Charakterisierungsmethoden beschrieben,

die im Zuge dieser Arbeit zum Einsatz kamen. Das dritte Kapitel enthält alle relevanten Ergebnisse, gefolgt von den sich daraus ergebenden Schlussfolgerungen (Kapitel 4) und einem weiteren Ausblick. Zu Beginn eines jeden Kapitels wird ein detaillierter Überblick über den nachfolgenden Inhalt gegeben.

1. Introduction

1.1. Background and Motivation

Materials are an inseparable part of the human culture ever since the beginning of the history. They rank with energy and information as basic resources of mankind [1]. Search for new materials is an ever-growing demand. Thrust for new materials closely coupled to mankind's requirements for products (for e.g., electronic items), structures (for e.g., buildings), machines, and devices. Technological progress requires sustained development of new tools and maneuvers. This calls for fabricating novel materials and search of innovative properties in existing materials. The exploration of new materials and properties is a never-ending process.

In the family of solids, compounds based on oxides, carbides and nitrides are widely explored and used extensively besides the metals. As oxygen accounts for the nearly half of the mass of the Earth's crust (49.2 wt.%) and third most abundant element [2] in the universe (by mass), there is no surprise that we use considerable amount of oxide materials. Carbon stands fourth in the most abundant element [3] in the universe by mass after hydrogen, helium, and oxygen, it's known for having different allotropes like graphite, diamond, nano-tubes, graphenes, fullerenes etc., and possessing exceptional properties which enables employing it in a variety of applications. In comparison to oxides and carbides, nitrides are less common and pure nitrides are rare in nature. This can be directly correlated to the bond energy for N_2 (945 kJ mol^{-1}) which is twice of that of O_2 (498 kJ mol^{-1}) and the unfavorable electron affinity of nitrogen, which is higher than that of oxygen (1736 kJ mol^{-1} for $N \rightarrow N^{3-}$ vs. 601 kJ mol^{-1} for $O \rightarrow O^{2-}$) [4, 5]. Yet, quite few nitrides have been discovered, synthesized and found application in various fields because they exhibit unique combination of physical, chemical, electrical, optical or mechanical properties [6, 7]. Based on the bond characters, nitride materials can be mainly divided into two groups; transition-metal nitrides and ionic-covalent nitrides [8]. The properties and crystal chemistry of the transition-metal nitrides are close to carbides. And they show very interesting properties like refractory and mechanical (e.g., TiN, ZrN, TaN), catalytic (e.g., Ta_3N_5, TaON, $TiO_{2-x}N_x$), superconducting (e.g., NbN, MoN) and magnetic (e.g., FeN, CoN,) properties [6-10] . The ionic-covalent nitrides are similar to oxides, and their ionic or covalent character depends on the electronegativity of the associated element. For instance, Li_3N is clearly ionic [8], while Si_3N_4 and BN [11]are covalent. The ionic-covalent nitrides also show very exciting properties, like thermo-mechanical (e.g., Si_3N_4, BN), ion conducting (e.g., Li_3N), thermal conducting (e.g., AlN, $MgSiN_2$), optoelectronic (GaN, AlN, BN), and luminescence (α and β- SiAlON, Eu-doped $M_2Si_5N_8$ (M= alkaline rare earth metal), etc.) properties [5-13] .

Development of new synthesis methods substantially helped in the discovery of novel nitride compounds and also in preparation of known compounds with well determined properties in large amounts. High-pressure synthesis is a powerful method for the preparation of novel materials. The era of high-pressure research and technology was started with the work of P. Bridgman, who received the Nobel Prize in Physics in 1946 for his pioneering experimental studies [14]. Upon high pressure treatment of any substance, distances between constituting atoms decrease and its electronic structure deforms, therefore favors the overlap of the orbitals. This leads to increase of the internal energy of the substance, and formation of denser structures could become energetically favorable with further compression. Compared with the lower pressure phases, high pressure phases are characterized by shorter inter-atomic distances and/or higher coordination numbers of the constituent atoms [15, 16]. It is widely believed that *"the application of pressure, in addition to temperature and composition variations, increases the chances of obtaining new materials not attainable at ambient atmosphere"* as pointed out by Zerr et al.,[9] in their review of high-pressure nitrides. High-pressure synthesis is also playing a crucial role in the development of nitride materials. For example, novel nitrides discovered by Riedel and co-workers like the spinel Si_3N_4 (γ-Si_3N_4) [17]or the Th_3P_4-type Zr_3N_4 and Hf_3N_4 [18] are realized under high pressure conditions.

Even though high pressure techniques offer many advantages in finding new materials, it has limitation over sample volume produced in one run (more details in chapter 2.2). These techniques also demand huge infrastructure, therefore the production cost of materials, synthesized using these techniques is considerably higher. However, the hardest known solids, diamond and cubic boron nitride (c-BN) are commercially produced using high-pressure, high temperature technique. Boron nitrides are long known but still interesting materials with exceptional properties. Cubic BN (c-BN), synthesised using HP-HT conditions [19] is the second hardest material after diamond. However it competes with diamond due to its better thermal and oxidation stability [20]. As we know diamond is neither stable in the presence of oxygen even at moderate temperatures (above 600 °C), nor is it a suitable abrasive for machining ferrous alloys. So its actual performance as a super-abrasive is somewhat limited.

Dense B-C-N ternary phase has received lot of attention during last two decades due to its excellent predicted properties, and is considered to be the best alternative for diamond and c-BN. Super-hard BCN phase is believed to be harder than c-BN and to have better thermal and oxidation stability than diamond [21]. The research on super-hard materials has concentrated around diamond theme and the exploration of new materials around B-C-N-O system. Recently, a variety of attracting properties were reported for BCN materials; enhanced lithium storage for battery application [22], compositionally tuneable electronic properties [23], photo-luminescence [24] and hydrogen storage properties [25, 26]. This set the motivation to study B-C-N materials under high pressure and high temperature conditions and

their application as lithium storage devices. A comprehensive review about ternary B-C-N compounds is given in chapter 1.3.2. In the course of efforts to synthesize dense ternary BCN compounds from an amorphous BC_2N precursor under high-pressure, high-temperature (HP-HT) conditions (above 15 GPa and 1800°C), a few crystals having triangular morphology contained a considerable amount of oxygen along with boron and nitrogen [27] were found. The hint towards oxygen containing boron nitride crystals motivated us to search for novel boron oxynitrides. A brief introduction to oxynitrides and the motivation to investigate novel boron oxynitride (B-O-N) materials, are discussed in chapter 1.3.1.

1.2. Aim and scope of the present work

In a broader perspective, the present thesis deals with the B-C-N-O system, namely boron carbon nitrides (B-C-N) and novel boron oxynitrides (B-O-N). With respect to B-C-N compounds primarily two aspects are studied, a) High-pressure (5 - 39 GPa) and high-temperature (up to ~ 2000 °C) behavior of amorphous boron carbon nitride (a-BC_2N and a-BC_4N) prepared via polymer derived ceramic route. HP- HT experiments performed cover different techniques like, single and double stage multi-anvil press, Toroid press and Diamond anvil cell. b) Electro chemical performance of the polymer derived ceramics, namely a-BC_2N and a-BC_4N as promising anode materials for lithium ion battery.

As stated earlier, hints towards oxygen containing boron nitride crystals during HP-HT treatment of amorphous BC_2N precursor, motivated to the search for novel boron oxynitrides. Discovery and synthesis of a novel ternary boron oxynitride (B-O-N) phase under HP- HT conditions (16 GPa, ~ 1900 °C) using large volume press technique will be discussed in detail. The structure and composition of the synthesized products were studied using different techniques like X-ray diffraction, elemental analysis, Raman spectroscopy, scanning electron microscopy (SEM), high-resolution transmission electron microscopy (HRTEM), selected area electron diffraction (SAED), automated diffraction tomography (ADT), energy dispersive X-ray spectroscopy (EDX) and electron energy-loss spectroscopy (EELS). Results of the performed electronic structure calculations are also described to assess the stabilities and properties of the B-O-N phase.

1.3. State of the Art

1.3.1. Introduction and Motivation for Boron Oxynitrides

One of the useful approaches implemented in the synthesis of new materials is to integrate and optimize the properties of end-member components through the formation of compounds containing mixed cation or anion species. This has led to the development of new families of oxynitride materials that can have structures and properties related to those of their parent oxides and nitrides, but can also be quite different [10]. As nitrogen and oxygen have the similar chemical, structural, and electronic characteristics such as polarizability, electronegativity, coordination numbers, and ionic radii, the substitution of nitrogen for oxygen, forming oxynitrides, will significantly extend the nitride family [5, 8]. High-pressure syntheses and studies on oxynitride compounds are now beginning to lead to entirely new classes of materials having interesting physical properties [8-10].

The substantial structural diversity (for example spinels [28], perovskites [29]etc.) enables oxynitrides to have unique and interesting chemical or physical properties, which gives rise to a wide variety of applications across a broad range of fields where advanced mechanical and or functional properties are required [8, 12, 30, 31]. The formation of oxynitrides permits tuning of the bonding and electronic properties. The chemical and physical properties of oxynitrides are significantly coupled with their composition, particularly the O/N ratio. The incorporation of nitrogen into an oxide framework will make changes in the properties, even if this happens at a doping level [5]. The band gap between the anion-based valence band and the cation-based conduction band decreases when nitrogen is introduced into an oxide, because the N 2p orbital has a higher potential energy than that of the O 2p orbital [8]. This nitrogen substitution strategy is often utilized for tuning the absorption edge of oxide photo-catalysts, enhancing their abilities to harvest visible light (e.g., $TiO_2 \rightarrow TiO_{2-x}N_x$)[31]. In addition, nitrogen is less electronegative and more polarizable than oxygen; the nitrogen-metal bonds are thus more covalent than that of the oxygen-metal ones. This increases the nephelauxetic effect (expansion of the electron cloud) in nitrides [5]. Meanwhile, nitrogen has a higher formal charge (3- vs. 2-) than oxygen, and thus the crystal-field strength in nitrides is enhanced [5, 8]. Both of these enhanced effects would reduce the energies of 5d orbitals of rare earth metal ions doped in oxynitrides, and therefore shift the excitation and emission spectra in a broad range (e.g., Sr_2SiO_4:Eu$\rightarrow$ $SrSi_2O_2N_2$:Eu$\rightarrow$ $Sr_2Si_5N_8$:Eu)[5, 8, 12, 13], making them superior photoluminescence materials for light emitting diodes (LEDs).

In the 1970s, oxynitrides were first proposed as a new class of ceramics in the SiO_2–Al_2O_3–Si_3N_4–AlN system, as partial substitution of Si by Al and N by O in Si_3N_4 led to the discovery of so-called SiAlONs [10, 12, 32-34]. They were, in part, designed to improve the

oxidation resistance and high-temperature mechanical properties of Si_3N_4, which is a well-known refractory ceramic used extensively for engine parts and gas turbines, and in cutting and grinding tools [10]. Consequently, different polymorphs/ poly-types (for e.g., β'-sialons, O'-sialons, and X-phase sialons etc.) and metal substituted (for e.g., manganese, copper, zinc and yitrium etc.) SiAlONs were discovered and used in a variety of applications [13, 32, 34]. Recently, rare earth element (e.g., Eu^{2+}) doped silicon based oxynitrides emerged as highly effective optical materials affording phosphor-converted light-emitting diodes (LEDs) [12, 13].

From the group 13 elements, aluminum oxy-nitride (AlON) based on Al_2O_3-AlN binary materials is known over three decades [28], found to have exceptional mechanical and optical properties. AlON is produced commercially [35] and used in applications like military aircraft and missile domes, transparent armor, IR windows, laser windows and military aircraft lenses [30]. Gallium oxy-nitride (GaON) materials are also synthesized over a decade ago, having excellent photoluminescence properties with tunable band gap energies [8]. GaN-ZnO binary materials form $(Ga_{1-x}Zn_x)(N_{1-x}O_x)$ solid solutions , display impressive band gap narrowing and an adsorption edge redshift by 55-150 nm, depending on the Zn and O concentration, making them photocatalyst materials, feasible to be used in solar energy and water splitting applications. [36, 37].

Conversely, no oxynitrides of boron have been reported yet. To the best of our knowledge, ternary boron oxynitride (BON) is still unknown and its properties and potential applications are unexplored. Hubáček et al. [38] was the first one to report the presence of boron oxynitrides as interfacial zone between turbostratic boron nitride and boric oxide. Later Gouin et al. [39] reported the formation of unknown crystals during nitridation of boric acid which they claimed as BON. On the contrary, no evidence provided to support the BON claim except a broad XRD reflection. Recently, a few reports on BON have been presented, for example nano clusters [40], amorphous thin films [41], and as dielectric for high temperature capacitors [42]. Interestingly, a patent on the super hard nature of BON predicted by calculation [43] was published in 2014 and points towards the need for HP-HT conditions to attain the ternary BON phase. Despite the fact that boron nitride materials have been well known over many decades [44] for their excellent properties in a variety of applications, some astonishing properties of these materials and their polymorphs [23, 45, 46] have been studied and revealed quite recently.

Based on the other oxynitrides of group 13 elements, it would be fair to believe that BON provide a new class of materials, having combined properties of the oxynitride family (for e.g., opto-electronic properties) as well as of the boron nitride polymorphs (for e.g., thermo-mechanical properties). In the course of our efforts to synthesize dense ternary BCN compounds from an amorphous BC_2N precursor under high pressure, high temperature (HP-HT) conditions (above 15 GPa and 1800°C), the starting materials were always decomposing into mixtures of c-BN and diamond. However, few crystals having triangular morphology

contained a considerable amount of oxygen (20 at. % confirmed by EELS) along with boron and nitrogen (see section 3.2.4.3) [27]. This hint towards BON crystals was the key motivation to systematically synthesize these materials. During the investigation, the strategies of AlON and GaON synthesis were followed, where the starting materials were molar mixtures of the respective nitrides and oxides. For example, molar mixtures of x AlN and y Al_2O_3 were starting materials for $Al_{(x+y)}O_yN_x$ [28] and molar mixtures of x GaN and y Ga_2O_3 were starting materials for $Ga_{(x+y)}O_yN_x$ [47] compounds.

In the present thesis, the first synthesis of the novel boron oxynitride under HP-HT conditions is reported. Mechanical mixtures of h-BN and B_2O_3 powders were used as starting materials for HP-HT experiments using a large volume press (multi anvil apparatus). The recovered samples were studied using high-resolution transmission electron microscopy (HRTEM), selected area electron diffraction (SAED), automated diffraction tomography (ADT), energy dispersive X-ray spectroscopy (EDX) and electron energy-loss spectroscopy (EELS). Calculations in the framework of the Density Functional Theory have been performed to investigate the structural, electronic, mechanical and thermodynamic properties of proposed structure models, while the composition has unambiguously analyzed by EELS measurements.

1.3.2. B-C-N compounds- a review

Similarity in atom sizes and structures between carbon and boron nitride (i.e. diamond and cubic boron nitride, or graphite and hexagonal graphite-like boron nitride), implicates the possibility to synthesize phases containing all three elements, and has warranted a considerable amount of attention during the last two decades. Indeed, the existence of numerous $B_xC_yN_z$ phases with hexagonal or turbostratic structure has been reported before. These compounds can be synthesized via i) nitridation of solid -phase precursors at high temperatures, ii) using the chemical vapor deposition (CVD) technique, or iii) pyrolysis of inorganic polymers containing boron, carbon, and nitrogen. These compounds are of broad interest because graphitic $B_xC_yN_z$ can be considered for applications such as high temperature semiconductors, especially if doped or structurally altered [48]. The great interest in the super-hard phase of B-C-N has been aroused due to the fact that solid solutions (prepared by Knittle et al.,[49]) of carbon and boron nitride showed a bulk modulus value of 355 GPa, it is expected that the dense forms of ternary B-C-N compounds or diamond-like solid solution with the general formula of $(BN)_xC_y$ can exhibit extreme hardness approaching that of diamond [48-53]. In combination, it also offers excellent thermal and chemical stability (superior to those of diamond)[54], and would therefore be indispensable abrasive materials for high-speed machining of ferrous alloys. Even though interesting properties like photoluminescence[55], hydrogen absorption and storage [25, 26] and exhaust gas absorption[56] have been reported to be exhibited by various B-C-N compounds (e.g. turbostratic-BCN, hexagonal-BCN, cubic-BCN, BCN-nanotubes, etc.) [57-66], the present review will be generally focused on preparation of dense ultra-hard phases of B-C-N. Therefore synthesis routes employing extreme pressures and temperatures are favored in this review, compared to the CVD, thin films and other techniques which do not provide bulk super-hard materials. The synthetic approaches resulting in low-density B-C-N ceramics or films (polymer routes, CVD, sputtering, etc.) will be also briefly considered in the sense of preparing the starting materials (precursors) for subsequent high-pressure high-temperature (HP-HT) treatment, leading to formation of hard phases.

1.3.2.1 Theoretical predictions

Theoreticians have taken the first step in the late 1980s to investigate the electronic structure, bonding, and properties of this interesting class of material preceding to thorough experimental characterization. All the theoretical predictions can be roughly classified under investigation of structural stability and mechanical and electronic properties.

1.3.2.1.a Structural stability

Liu et al.,[67] was one of the first to calculate the electronic structure of monolayer BC_2N compounds using the local density functional formalism. The structural stability of monolayer

BC_2N has also been studied by Nozaki et al.,[68-70] using an empirical molecular mechanics simulation. Both studies had four to eight constituent atoms and different structural models with different atomic arrangements were considered. These initial studies were focused on structural stability using monolayer model and nearest neighbor environments. It has been predicted that BC_2N is formed by maximizing C-C and B-N bonds. It has also been found that a structure with alternate -C-C- and -B-N- chains or rings is the most stable one. While the aforementioned studies predicted that these structures could be assigned to graphitic type BC_2N, some other experiments reported similar structures [71, 72]. Azevedo et al. [73] recently investigated the structural and electronic properties of B-C-N monolayers using pseudopotential method within density functional theory with an emphasis on the effect of composition and atomic arrangement. The calculations confirm that the stable structure of B-C-N monolayers is formed by increasing the number of both C-C and B-N bonds and independent of the size of the unit cell size, in agreement with earlier theoretical studies [67-70] performed using different formalism. Tapas Kar et al., [74] studied the structure, stability, and nature of the bonding of tetra-atomic BC_2N compared with the C_4 and $(BN)_2$ molecules and found that the linear triplet ($^3\Pi$) BCCN is the most stable one.

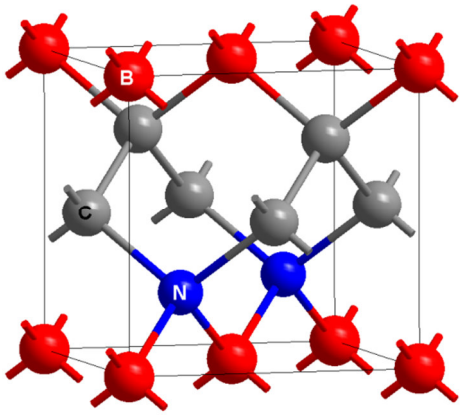

Figure 1-1. A representative atomic arrangement in the unit cell of cubic β-BC_2N structure. Reprinted with permission from [75].

With respect to ternary dense (for e.g., cubic) B-C-N materials, some of early studies on diamond/c-BN superlattices and alloys indicated very limited miscibility with respect to c-BN and diamond in the solid state around the atmospheric pressure [76, 77]. In order to explore possible synthesis routes to single-phase "heterodiamond" BC_2N phase, Tateyama et al., [75] investigated the effect of pressure on (mono) layered structure proposed by Liu et al., [67] and Nozaki et al., [68-70]. Structure optimization was done using monoclinic unit cells with eight atoms. The results showed that a more stable structure corresponds to that with no B-B or N-N bonds and more C-C and B-N bonds, or the so-called β-BC_2N (show in Figure 1-1). It seems that earlier predictions of the structural stability based on the number of B-N and C-C bonds (bond counting rule) in a monolayer structure holds here as well. Among the four possible structure transformations, g-BC_2N to β-BC_2N was energetically most favorable. Other

proposed structures like α, γ and δ - BC_2N are excluded here in discussion as they are energetically less favored. Calculations predicted that β-BC_2N can be synthesized from g-BC_2N at nearly ambient pressure while the super-lattice of BN/C_2 is produced by compression of g-BC_2N to about 16 GPa [75]. The bulk modulus of dense β-BC_2N is calculated to be between 374 and 409 GPa [75, 78-80]. Mattesini et al., [78] predicted the metastable orthorhombic Λ-BC_2N and trigonal Φ-BC_2N, "the most stable forms of the three-dimensional BC_2N system", by replacing the carbon atoms with boron and nitrogen in the crystalline phase of fcc diamond. In the claimed ternary B-C-N phases, the substitution was performed by considering the bond counting rule used by Tateyama et al., [75] furthermore density functional theory (DFT) and local-density approximation (LDA) were used for the calculation. Later Sun J. et al.[81] confirmed that the above described β-BC_2N has the lowest total energy among other possible atomic arrangements, although all the structures seem to be metastable and tend to separate into diamond and c-BN.

Yuge et al., [82] examined the phase stability of c-BCN (diamond-like) with a composition range of $(BN)_{(1-x)}(C_2)_x$ ($0 \leq x \leq 1$) around atmospheric pressure by the combination of cluster expansion technique and Monte Carlo simulation based on first-principles calculations. In their work the authors doubted the results of a few earlier calculations which addressed the phase stability of c-BNC with respect to the c-BN and diamond, showing a significant discrepancy in the predicted phase diagrams due to the differences in the used model: One achieves complete miscibility around T = 3546 K, which is slightly below the melting point of the diamond [83]. Another reaches complete miscibility at T = 8500 K, which is much higher than the melting point of the diamond [77]. In their work Yuge et al. carefully considered the dependence of enthalpy on atomic arrangements, the effect of atomic orderings on configuration entropy, and the effect of lattice vibration [82], which were neglected in earlier theoretical predictions. The final result predicts strong preference of B-N and C-C bonding and disfavors B-C, C-N, B-B, N-N bonds, which suggests phase separation to c-BN and diamond. Complete miscibility is achieved above T = 4500 K, which is higher than the melting points of both diamond and c-BN [82]. Similar trends are found for the miscibility in the wurtzitic w-BCN between hexagonal diamond (londsdaleite) and w-BN, although a significant anisotropy in solubility for the wurtzite-like structure is observed, which leading to a solid solution in dilute composition despite its sp^3 bonding [84]. Furthermore, examination of pressure effects on the phase stability [85] revealed that possibility of decomposition of c-BNC into c-BN and diamond increase with applied pressure. This can also be explained as a result of the decrease in solubility of c-BN and diamond that leads to the decomposition of c-BCN with the applied pressure. The solubility decrease is attributed to the increase of volume with the formation of a c-BNC solid solution. The authors underline that the success in synthesis of c-BNC compounds under high pressure should relate to the kinetic reason, but not to some energy related reason in thermodynamic equilibrium[85].

Structural stability, mechanical and electronic properties of cubic BC_xN ($0.21 < x < 19.28$) crystals within a random solid solution model was investigated by Zhuang et al. from the first principles [86]. The authors have shown that, compared to c-BC_2N, the BC_xN solids with higher carbon content ($x > 2$) exhibit better structural stability and higher elastic moduli. Moreover, significant deviations of the elastic moduli and lattice parameters from the predictions of Vegard's law have indicated that the BC_xN solid solutions are not a simple mixing of diamond and cubic-BN. The computed band gaps are substantially lower than those of diamond and c-BN approaching the lowest value of 2 eV for $x = 4.4$.

Sun H. et al.,[87] studied BC_2N in cubic structure forms using *ab-initio* pseudo-potential LDA calculations. The authors compared their results with the recent experimental claim of cubic-BC_2N of that time [49, 51] with eight atom zinc-blende structured cubic unit cell (the experimental results will be discussed in the next section). Fortunately, out of 420 different configurations only seven are topologically different, due to the high symmetry of the zinc-blende-structured lattice, which makes their study possible. Even-though predicted structures (1) and (2) (Figure 1-2) are more stable due to having the lowest energies, all seven possible structures are metastable and would in turn to separate into diamond and cubic BN. Structure (1) and (2) do not have B-B and N-N bonds, which is also consistent with earlier predictions. However full bond-counting rule is not satisfied in this case because they do have the same number of C-B and C-N bonds as C-C and B-N bonds. Later, the same research group, based on first-principles total-energy and dynamic phonon calculations, investigated the structural transformation to cubic BC_2N and stability of this phases under pressure [88-90]. The authors showed that different forms of starting material (graphitic BC_2N with different atomic arrangement) require distinct synthesis routes and yielding end products with drastically different physical properties. Among all the considered structures, a high density phase with no B-B or N-N bonding (phase (1) or (2) in Figure 1-2) showed the highest structural stability and lowest compressibility at high pressure.

There were many other structures proposed for BC_2N ternary phases, like pseudo-cubic super-lattice BC_2N_{1x1}[91], "low-density" cubic LD-BC_2N[92], tetragonal z-BC_2N, [93] z*-BC_2N and t-BC_2N (Figure 1-3),[94] wurtzite-type w-BC_2N, [95] chalcopyrite-type cp-BC_2N, [79] body-centered bc6-BC_2N [96] etc. (see Table 1-1).

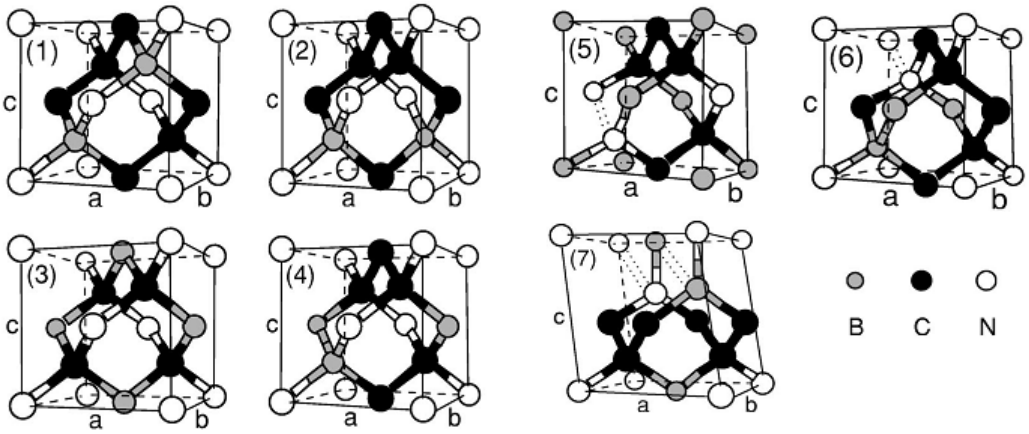

Figure 1-2. All the possible topologically different c-BC2N structures (after structural relaxation) starting from an eight-atom zinc-blende structured unit cell. Reprinted with permission from [87]. The dotted bonds indicate the broken covalent bonds between N atoms.

Zhou et al., [94] have shown that for nano-crystalline powders of z-BC_2N, z*-BC_2N and t-BC_2N reveal no significant difference by comparing the simulated XRD to the results of BC_2N reported by Solozhenko et al.,[51]. However, only tetragonal t-BC_2N[94] seems to address most of the difficulties in explaining Raman splitting of LO and TO modes and higher experimental Vickers hardness values as claimed by Solozhenko et al., [51]. Li et al., [97] employed *ab initio* evolutionary algorithm in order to resolve the crystal structure of the observed super-hard BC_2N. Among twelve considered structures, the author's [97] uncovered two polymorphs with rhombohedral and orthorhombic symmetries, with which the experimental x-ray diffraction pattern is well reproduced. Analysis of the total energy results and the simulated energy-loss near-edge spectroscopy suggested that the rhombohedral structure (*R3m* with two BC_2N units in primitive cell) is the best candidate for the super-hard BC_2N. The electronic structures calculated by DFT show that rh-BC_2N is a wide gap semiconductor with an indirect band gap of 3.8 eV.

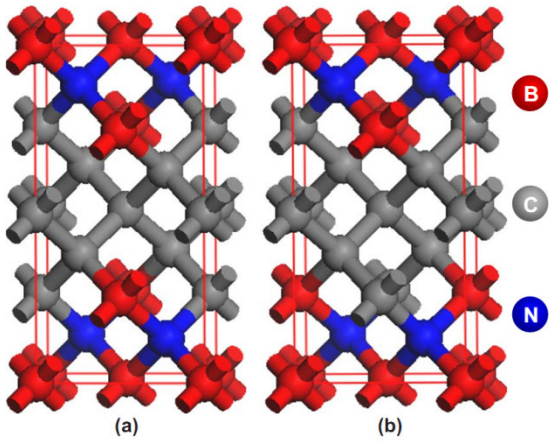

Figure 1-3. Proposed tetragonal crystal structures of diamond-like BC_2N: (a) z*-BC_2N with P-42m symmetry and (b) t-BC_2N with P-421m symmetry. Reprinted with permission from [93, 94]

Luo et al., [98] studied BC_4N different possible crystal structures using DFT coupled with LDA. They tried to correlate the experimentally derived BC_4N structure to the properties reported by Zhao et al., [53] (see Section 1.3.2.3). The authors proposed 3C-BC_4N configurations constructed with Ramsdell notation. Simulated XRD pattern of 3C-BC_4N model conforms well to the experimental XRD pattern of c-BC_4N. Tang et al. investigated five nonequivalent atomic configurations of the suggested 3C-BC_4N structure using first-principle calculations [99]. All the configurations were found to be metastable. The band gaps were calculated to be highly dependent on the atomic arrangement, thus different 3C-BC_4N configuration revealed insulating, semiconductor, semi-metallic or even metallic behavior [99].

Theoreticians also proposed and studied other compositions of B-C-N materials like $B_2C_2N_2$ [100], BC_6N [101] and BC_3N_3 [102] usiing different computationl methods and formalism. As this thesis deals with BC_2N and BC_4N compositions, details about other compositions are excluded here. However, for the sake of comparsion and completeness in Table 1-1, calculated lattie bulk moduli (B), shear moduli (G) and estimated hardness (Hv) (if available) for different B-C-N compositions are listed.

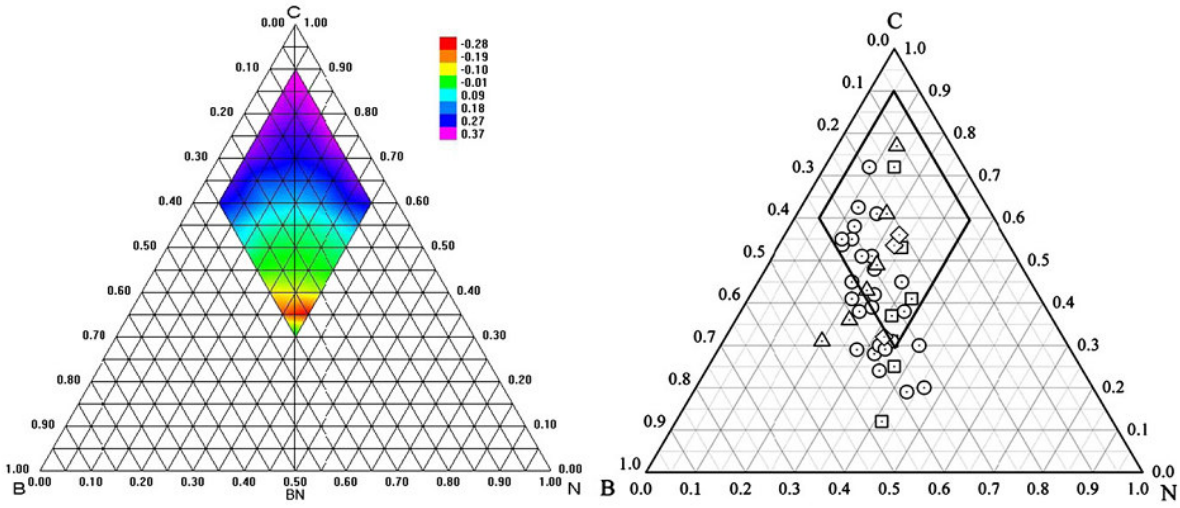

(a) (b)

Figure 1-4. (a) Theoretically predicted distribution of formation energy (eV/atom) on the upper rhombus of ternary B–C–N phase diagram using full spectrum. Less formation energy means that the corresponding composition is easier to form. (b) $B_xC_yN_z$ compositions synthesized in previous experiments. Most compositions locate in the area with negative formation energy, in agreement with the theoretical prediction. Reprinted with permission from [103].

Very recently, formation feasibility of B-C-N ternary phases was studied by Jiang et al., [103] using DFT based on the model employed in the previously synthesized tetrahedral amorphous carbon (ta-C) [104]. The “ta-C” modification was reported to possess not only high mass density (3.2 g/cm^3) and large amount of sp^3-hybridized carbon (84−88%) but also superior hardness (45 GPa) and Young's modulus (340 GPa). Possible B-C-N ternary phases

were studied and plotted in a triangular phase diagram (Figure 1-4) using the DFT and the plane-wave pseudo-potential technique [103]. Formation energies are plotted accordingly and compared with experiential compositions reported till date. It is interesting that the formation energy distributed symmetrically along the C−BN isoelectronic line, in which the compositions in the range of B: 15–35 at.%; C: 30–55 at.%; N: 15–35 at.% are relatively easy to form owing to their negative formation energy. Notably, most of the $B_xC_yN_z$ compositions synthesized in experiments are located in this area.

1.3.2.1.b Mechanical and electronic properties

In this thesis, the considered mechanical properties of the B-C-N ternary phase are mainly restricted to bulk modulus (**B**), shear modulus (**G**) and hardness (Vickers micro-hardness, ***Hv***). Tateyama et al.,[75] was the first to calculate a bulk modulus of 438±14 GPa for his predicted β-BC_2N structure, which is slightly less than that of diamond. Thereafter, many theoretical predictions reported different bulk moduli and hardness depending on the considered structure predicted and the model used for calculations. The available theoretical values of lattice parameters, bulk and shear moduli, and estimated hardness of the predicted super-hard BC_2N structures as well as of dense BCN phases with compositions different from BC_2N are summarized in **Table 1-1.** It can be seen that the predicted bulk moduli for all the different structures generally exceed the experimental ones of c-BN (369-401 GPa) with most of them approaching those of diamond (433-442 GPa) [105, 106].

The claimed successful synthesis of cubic- BC_2N compounds (by Solozhenko et al., [51]) with an experimentally determined extreme Vicker's hardness of 76 GPa (next to diamond) and bulk modulus of 282 GPa (which is lower than c-BN) [51, 53] attracted significant interest to theoretical studies. In particular, Zhang et al. have examined the ideal strength of cubic BC_2N using first-principles calculations [107]. In contrast to the experiment, the authors revealed that, despite the large elastic parameters, compositional anisotropy and strain dependent bonding character impose limitation on their strength. Consequently, the hardness of the optimal BC_2N structure should be even lower than that of c-BN. The measured extreme hardness of BC_2N nano-composites are attibuted to the nano-crystalline size effect and the bonding with the surrounding amorphous carbon matrix. Later Zhuang et al. in their work [108] have shown that the atomic arrangements (B, C, N) within the c-BC_2N crystal lattice, namely the different degrees of mixture (or extent of solubility) of c-BN and diamond, may lead to distinctly different values of Vickers hardness and tensile strength. Similarly, Zhang et al. have investigated elastic constants for several diamond-like BC_2N structures from the first-principles [109]. The authors have shown that, although the deviations of the lattice constants from those of cubic lattices are small (about 1%), the differences among the elastic constant components (C_{12}, C_{23} *and* C_{31}), that in principle should be the same for cubic lattices, can reach up to 75% due to the chemical anisotropy of the BC_2N structures.

Interest in electronic properties of B-C-N ternary phases started as early as their stability and structure prediction begin. Most of the theoretical calculations on structure and mechanical properties also predicted band gap values. However, predicted properties vary from semi-conductor to insulator depending on the structure. For a layered structure, Liu et al., [67] predicted a band gap (E_g) of 1.6 eV, and for tubular and chiral structure Miyamoto et al [110] predicted 1.25-1.75 eV. Experimental results from Watanabe et al., [111] also confirmed semiconductor behavior of layered BC_2N. For BC_2N heterodiamond, Tateyama et al., [75] predicted an indirect band gap of 3.97 eV. For orthorhombic BC_2N [78] band gap of around 1.7-2.01 eV is predicted, whereas for c-BC_2N[87] derived from zinc-blende structure bang gap of ~2.0 eV is calculated. Zhou et al. [93] have shown that despite the only difference between z*-BC_2N and z-BC_2N is that B and N atoms are interchanged with each other, the calculated band structures exhibit a significant change that z*-BC_2N is an indirect semiconductor with a band gap of 3.6 eV, while z-BC_2N is a direct one with a band gap of 2.7 eV. The calculated electronic structures for chalcopyrite-type cp-BC_2N showed that this compound is a wide gap semiconductor with a direct band gap of about 3.3 eV, displaying some potential application in ultraviolet light emitting [79]. Rhombohedral rh-BC_2N[97] and wurtzite-type w-BC_2N [95] are predicted to have indirect wide band gap of 3.6 and 3.99 eV, respectively. Even a wider band gap is calculated for BC_4N, 4.06 eV [98]. In contrast, bc6-BC_2N is an indirect semiconductor with band gap of 0.60 eV.[96] Several reports [75, 78, 87] also pointed out that the employment of LDA in calculation leads to significant underestimation of the band gap (65-75%), thus the values calculated using this model cannot be considered as completely reliable.

Table 1-1. Calculated lattice parameters, bulk moduli (**B**), shear moduli (**G**) and estimated hardness (**Hv**) (if available) of the predicted super-hard B-C-N phases. The experimental values for dense carbon and BN modifications are given for comparison.

Structure	**a (nm)**	**b (nm)**	**c (nm)**	**α (°)**	**β (°)**	**γ (°)**	**B** (GPa)	**G** (GPa)	**Hv** (GPa)	**Ref.**
Diamond[1]	0.3567	0.3567	0.3567	90	90	90	442-433	534-544	60-150	[105, 106]
C-londsdaleite[1]	0.252	0.252	0.412	90	90	120		382	60-70	[105, 106]
c-BN[1]	0.3616	0.3616	0.3616	90	90	90	369-401	409	46-80	[105, 106]
w-BN[1]	0.254	0.254	0.420	90	90	120	390	330	34-60	[105, 106]
c-BC_2N[1]	0.3642	0.3642	0.3642	90	90	90	282	447	76	[51, 112]
	0.3595	0.3595	0.3595	90	90	90			62	[53]
c-BC_4N[1]	0.3586	0.3586	0.3586	90	90	90			68	[53]
β -BC_2N	0.3577	0.3577	0.3577	89.38	90.62	90.62	438±14		-	[75]
	0.3579	0.3579	0.3612	90	90	89.32	383.3		-	[113]
	0.361	0.361	0.361	90	90	90	342.4	453.6	-	[92]
o-BC_2N	0.2528	0.2502	0.3587	90	90	90	408.9		-	[78]
	0.2529	0.2502	0.3591	90	90	90	403.1	446		[80]
Φ -BC_2N	0.2496	0.2496	0.4192	90	90	120	420.1		-	[114]
Λ -BC_2N	0.3554	0.3599	0.3553	90	90	90	459.4	481.96	-	[78, 114]
c-BC_2N-1	0.3570	0.3609	0.3570	89.5	90	90	399.7		-	[87]
BC_2N_{1x1}	0.4355	0.2514	1.2483	90	90	90	419.5		75.8(21)	[91]
	0.3579	0.3579	1.074	90	90	90	420			[115]
z-BC_2N	0.3565	0.3565	0.7168	90	90	90	402.7	447.4	75.9	[93]
	0.3604	0.3604	0.7247	90	90	90	385		65.0	[97]
z*-BC_2N	0.3577	0.3577	0.7122	90	90	90	423.3	471.7	75.6	[94]
t-BC_2N	0.3579	0.3579	0.7116	90	90	90	422.1	466.9	75.3	[94]
r-BC_2N	0.3602	0.3602	0.3602	n.d.	-	-	382			[115]
rh-BC_2N	0.2545	0.2545	2.5068	90	90	120	395		62.1	[97]
w-BC_2N	0.2501	0.2501	0.4205	90	90	120	407.5	466.5	76.8	[95]
cp-BC_2N	0.3613	0.3613	0.7146	90	90	90	367.4	432.0	72	[79]
	0.3653	0.3653	0.7228	90	90	90	349		67.5	[97]
bc6-BC_2N	0.4361	0.4382	0.4405	90	90	90	305		60	[96]
3C-BC_4N	0.2507	0.2507	0.6196	90	90	120	418.8	521.3	84.3	[98]
BC_4N_{2x1}	0.3567	0.3567	n.d.	90	90	90	428			[115]
t-BC_6N	0.3574	0.3574	0.3564	90	90	90	410.4		79.9	[101]
r-BC_6N	0.3565	0.3565	0.3565	90.15	90.15	90.15	399.9		79.1	[101]
rh-BC_3N_3	0.3449	0.3449	0.3449	87.5	-	-	405.3			[102]
$B_2C_2N_2$	0.2521	0.2521	0.6235	90	90	120	398.4		84.3	[100]

[1] experimental value, (Structure name in some predicted structures include prefixes like β,Φ, Λ, etc. and subscripts like 2x1, 1x1 retained as mentioned in their original reference)

1.3.2.2 Synthesis of B-C-N compounds

A few recent first-principles studies on structural transformation and stability of B-C-N phases have indicated that different starting materials may lead to distinct synthesis routes, yielding various dense B-C-N end-products with drastically different physical properties [75, 88, 89]. Therefore different precursor materials used for HP-HT experiments on the synthesis of ultra-hard dense B-C-N compounds are considered in the following.

The oldest, simplest and still widely used method is to synthesize boron carbonitrides from the elements at high temperatures. A typical reaction was used by Kosolapova et al., [116] in which boron and carbon powders were heated at 1800-2000 °C in N_2/NH_3 for prolonged periods promoting the reactions below:

$$B(s)+2C\ (s)+\frac{1}{2}N_2(g) \xrightarrow{1800\text{-}2000\ ^\circ C} BC_2N\ (s)$$

$$B(s)+2C\ (s)+\ NH_3(g) \xrightarrow{\Delta} BC_2N\ (s)\ +\ \frac{3}{2}H_2(g)$$

The formation of BC_2N in such reactions is diffusion-controlled mechanism occurring at the solid interfaces (B/C) by nucleation and growth. At elevated temperatures the reactant atoms have enough energy to diffuse towards the interface forming the product. However the process slows down as the interface thickens and effectively the reactants are no longer in contact [116]. Due to a complex process of diffusion of ions towards the thick interface, there is always some degree of inhomogeneity on the atomic level, which renders this method ineffective for the formation of complete solid solutions. Recently a stoichiometric ternary compound B_4CN_4 was obtained by direct nitridation of commercial boron carbide (B_4C) powder via heating in a stream of nitrogen at temperatures in a range of 1600–1900 °C [117]. The reaction was diffusion-controlled. The resulting powder with elemental composition $B_{3.96\text{-}4.03}C_{1.00}N_{3.96\text{-}4.07}O_{0.01\text{-}0.08}$ ($\sim B_4CN_4$) determined by EPMA had the turbostratic[1] layered structure, where carbon atoms form linear C sp^2–C sp^2 chains bonded to B and N within h-BN layers with molar ratio C/BN = 1/4.

One of the first attempts in synthesizing c-BN and diamond mixed crystals was conducted by Badzian et al.,[48] where they used graphitic BCN (g-BCN) prepared by the CVD route. He used gaseous mixtures of $BCl_3/CCl_4/N_2/H_2$ at 1900°C to deposit polycrystalline BCN on a graphite rod:

$$BCl_3 + CCl_4 + N_2 + H_2 \xrightarrow{1900\ ^\circ C} (BN)_xC_{1-x} + \ldots$$

As the CVD method employed four different gases, controlling the reaction and stoichiometry of end products were very crucial. Later, Bartlett and coworkers [118-120] conducted the

[1] Describing a crystal structure in which basal planes have slipped out of alignment

reaction of boron trichloride with acetylene and ammonia at relatively low temperatures, which resulted in a better ordering and more accurate compositions, e.g. B_2CN_2, $B_{0.485}C_{0.03}N_{0.485}$, $B_{0.35}C_{0.3}N_{0.35}$:

$$BCl_3 + y\,C_2H_2 + z\,NH_3 \xrightarrow{700\text{ -}800\,^{\circ}C} B_xN_yC_z$$

Instead of acetylene other hydrocarbons such as CH_4 and C_3H_8 have been used for the CVD preparation of other ternary B-C-N phases.[121] For example Besmann obtained single-phase $BC_{0.43}N_{0.29}$ with a graphite-like structure from BCl_3-NH_3-CH_4-H_2 mixtures at 1650 K and 3.3 kPa [122]. If boron trichloride and acetonitrile (CH_3CN) are used as the reactants, almost a stoichiometric BC_2N is obtained:[118-120]

$$BCl_3 + CH_3CN \xrightarrow{800\,^{\circ}C} BC_2N + 3\,HCl$$

The films produced through these methods consist of a turbostratic layered structure that contains sp^2-hybridized B, C and N atoms according to XRD and TEM studies. XPS investigations reveal the presence of C-C, B-N, C-N and B-C bonds. The same approach was successfully applied by Watanabe et al. in order to produce amorphous BC_2N films on polycrystalline Ni and quartz substrates [123, 124]. While using the same reactants in a hydrogen and nitrogen atmosphere Kawaguchi et al. deposited new graphite-like films of composition $BC_{0.9\text{-}1.3}N_{0.8\text{-}0.9}H_{0.4\text{-}0.7}$ and $BC_{3.0\text{-}3.2}N_{0.8\text{-}1.0}H_{0.2\text{-}2}$, which can be described as BCN(H) and BC_3N(H) [125]. X-ray and electron diffraction analyses indicate that these materials have hexagonal structures similar to that of graphite.

Hegermann et al., investigated the influence of the carrier gases N_2, Ar, and He and the applied power on the chemical composition of boron carbonitride films deposited by a PA-CVD process [126]. Si(100) wafers were used as substrates and pyridine-borane and triazaborabicyclodecane as B-C-N-forming single-source precursors. Films that were either deposited in He using a low power density or in N_2 using a high power density revealed similar chemical composition of $\sim BC_4N$ as well as comparable properties (in particular outstanding hardness $\sim$ 60 GPa). XRD and TEM analysis of these films showed their amorphous nature. It should be noticed that amorphous B–C–N films have been intensively studied during the last two decades since practically any composition within B-C-N triangle can be synthesized by various conventional chemical and physical deposition methods, such as above mentioned (PA)-CVD [123-129] as well as ion beam assisted deposition (IBAD), [130, 131] pulsed laser deposition (PLD) [132-134] and magnetron sputtering [135-140]. Tuning different deposition parameters and choosing an appropriate atmosphere allows to control not only the composition but also bond contents in the resulting B–C–N films. This can play a key role when choosing precursors for the high-pressure synthesis of ultra-hard

diamond-like B-C-N phases, since the nature of the starting material is found to have a significant influence on the structural features and properties of the end-product.

In contrast to the deposition routes to B-C-N materials resulting in ternary $B_xC_yN_z$ films, large amounts of similar phases can be synthesize via pyrolysis of polymeric B-C-N-based precursors at relatively low temperatures around 1000 °C. In this way, thermal treatment of *B*-triphenylborazine and *N*-triphenylborazine in an autoclave at 1000 °C results in boron carbonitrides with compositions of $BC_{3.9}N$, and $BC_{3.6}N$, respectively,[141]. Ceramic $B_xC_yN_z$ powders with various nonstoichiometric compositions can be also obtained via pyrolysis of decaborane(12)-adducts of diamines $[–B_{10}H_{12}·\text{diamine}–]_n$,[142, 143], pyroazabole polymer[144] or polyethylene-iminoborane $[–CH_2–CH_2–N=BH_2–]_n$ [145].

Riedel and co-workers [71, 146-148] reported the synthesis of turbostratic graphite-like BC_2N and BC_4N from piperazine borane and pyridine borane, respectively (the reactions A and B given below). This method can be ascribed to the so called polymer derived ceramic (PDC) route, where a highly cross linked insoluble, infusible polymeric intermediate is formed followed with pyrolysis under argon atmosphere at 1050 °C. It is important to mention that in the latter reaction, utilization of nitrogen containing atmosphere can lead to completely different results, namely formation of almost pure boron nitride. In a subsequent work of the same research group a crystalline ternary h-BC_2N with graphite-like structure was synthesized from these precursors at elevated pressures and temperatures [149].

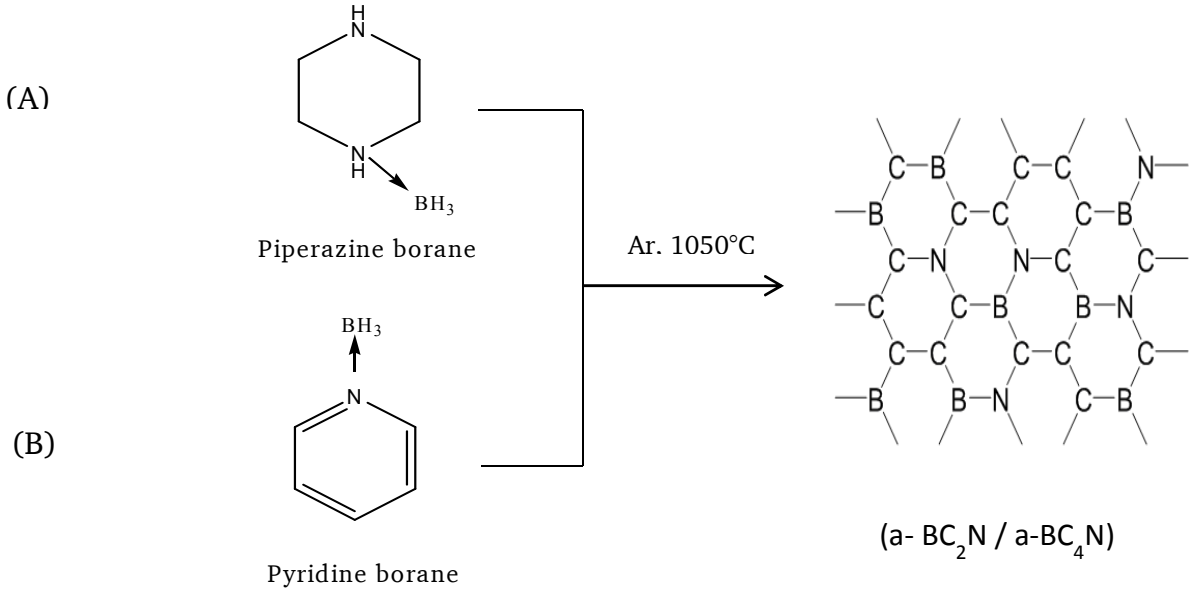

Amorphous B-C-N ceramics were produced by thermal conversion of poly(borosesquicarbodiimide) of an idealized formula $[B_2(NCN)_3]_n$ at 1100 °C in an argon atmosphere [150]. X-ray wide-angle scattering measurements showed that the ceramics consist of an amorphous structure with hexagonal planar near-range ordered atomic arrangements similar to graphite. NMR investigation of the products showed the presence of BN structures with mainly trigonally coordinated boron and nitrogen nuclei and the presence of amorphous (graphite-like) carbon within the B-C-N ceramics at the same time. The authors concluded that the BCN phase tends to undergo a short-range phase separation into BN and C regions.

Another amorphous B-C-N ceramic with the composition of B_4CN_4 was prepared via a non-oxide sol-gel process [151]. In this approach *B*-trichloroborazene, $B_3N_3H_3Cl_3$, reacts with bis-(trimethylsilyl)-carbodiimide $Me_3Si\text{-}NCN\text{-}SiMe_3$ in THF or toluene, or without any solvent, to form non-oxide gels. The BCN_2H_2-xerogels, obtained after aging and drying, are practically free of any chlorine or oxygen and contain only small amounts of silicon. At 1200 °C a novel amorphous B_4CN_4 phase is formed, which is stable up to 1600 °C where it starts to crystallize. This novel nitrogen-rich B_4CN_4 phase may be a promising amorphous precursor for high-pressure synthesis of crystalline BCN phases.

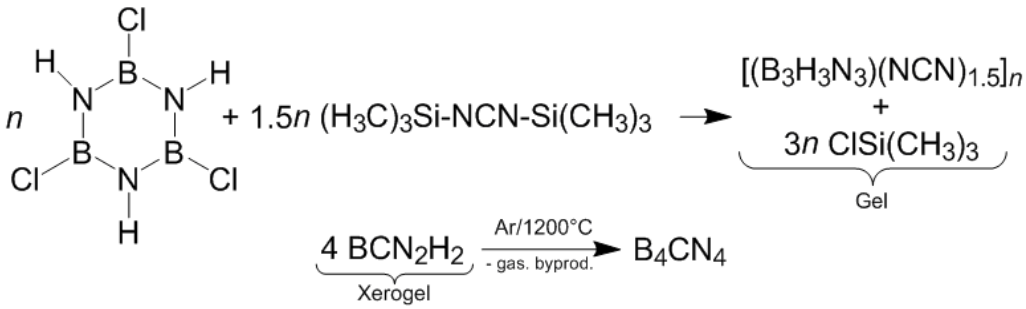

A series of graphitic B-C-N compounds (g-BC_xN) were prepared in good yield by pyrolysis of the polymers between BCl_3 and commercially available nitriles at 1773 K [152]. Acrylonitrile, malononitrile, acetonitrile, tetracyanoethylene (TCNE) and poly-acrylonitrile (PAN) were used as the C-N sources while BCl_3 was used as the B-source. The g-BC_xN samples were prepared in three steps: (1) adduct-formation at ambient temperature, followed by dehydrochlorination/polymerization at temperatures up to 773 K; (2) carbonization of the polymeric materials at 1273 K; (3) graphitization at 1773 K. The products were characterized by combustion elemental analysis, XPS, FT-IR spectroscopy and XRD. The obtained powders of g-BC_xN ($2 \leq x \leq 5$) were subsequently used for the shock-synthesis of B-C-N heterodiamonds, c-BC_xN [152].

Tian et al.[153] synthesized the B-C-N precursor by mixing boric acid H_3BO_3 with melamine $C_3N_6H_6$ (1:2 ratios) in an agate mortar. Mixture was heated to 200°C for 1 hr and then at 300°C for an additional 2 hr, after cooling down the pulverized powder was exposed

to 1600°C in nitrogen atmosphere for 15mins. Li et al. [154], in a similar approach, exposed mixture of Boron oxide and melamine to 770°C in vacuum for 2 h which lead synthesizing the B-C-N precursor. However, as boric acid coverts into boron oxide at 300°C, both reactions would look the same even though the starting material is different. Amorphous BCN was prepared by solid-state reaction between the above mentioned reactants – boric acid and melamine – via heat treatment at 1273 K under 10^{-3} Pa [155, 156]. For the H_3BO_3 to $C_3N_6H_6$ mass ratio of 1:3 the obtained B-C-N material revealed the chemical composition of $B_{0.48}C_{0.29}N_{0.23}$. Annealed for 40 min at 1473 K under 4.0 GPa, the amorphous BCN crystallized into single-phase hexagonal (h-BCN) compound with lattice constants of $a_0 = 0.2506$ nm and $c_0 = 0.6652$ nm.

Hubacek and Sato at el., [72] prepared B-C-N precursor by simultaneous nitridation of boric acid and carbonization of saccharose in molten urea followed by annealing in nitrogen at 1500 °C. Results showed graphite-like BC_2N and BC_4N depending on saccharose content, having broad x-ray diffraction analogues to like turbostratic layered structures. This precursor preparation method was later used by Solozhenko at el., [51] in the synthesis of super-hard c-BC_2N phase. Reaction of low-surface-area amorphous carbon spheres with a mixture of urea and boric acid at 930 °C yields a composition close to BC_4N with a graphitic structure [157]. The obtained product was characterized by electron energy loss spectroscopy (EELS), X-ray photoelectron spectroscopy (XPS), transmission electron microscopy (TEM), Raman spectroscopy, and XRD, revealing a porous ceramic material composed of BCN spheres (Figure 1-5) with a layered structure involving random distribution of boron, carbon, and nitrogen atoms. In turn, reaction of amorphous carbon nanotubes with boric acid and urea was shown to yield nanotubes with the approximate composition of BC_4N [158].

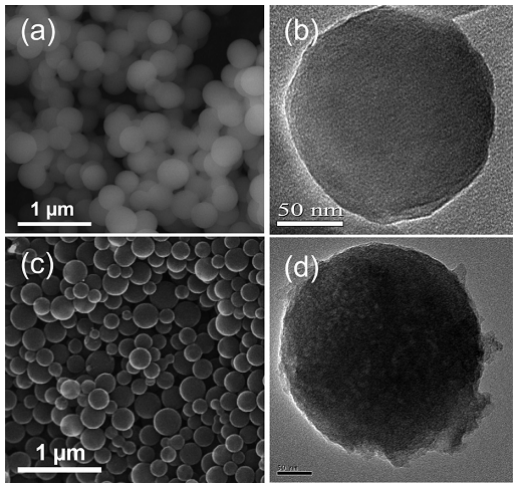

Figure 1-5. High-temperature reaction of amorphous carbon spheres ((a) - SEM and (b) TEM image) with boric acid and urea yields spheres with graphitic structure and composition of BC_4N: (c) SEM and (d) TEM image. Reprinted with permission from [157].

A solvothermal reaction of $CH_3CN{\cdot}BCl_3$ and lithium nitride (Li_3N) using benzene as the solvent has been successfully applied to prepare boron carbonitride at 300 °C and less than

about 7 MPa [159]. X-ray diffraction (XRD) and transmission electron microscopy (TEM) investigation of the obtained powder revealed hexagonal ordering. The product predominately consisted of B, C and N elements (B: 14.4 %, C: 36.6 %, N: 20.8%) with some amount of O and H (O: 8.0 %, H: 4.2 %) determined by combustion elemental analysis. X-ray photoelectron spectroscopy (XPS) and Fourier transform infrared FT-IR spectroscopy confirmed the chemical composition and atomic-level hybrid. Hexagonal graphite-like BCN compound was also prepared by the reaction between carbon tetrachloride (CCl_4), boron tribromide (BBr_3), lithium nitride (Li_3N) and sodium at temperature of 400°C [160]. Further characterization indicated formation of two compounds: hexagonal polycrystalline BC_2N phase was found to coexist with hollow sphere-like amorphous C–N phase with a composition close to C_3N.

Another approach in synthesizing low density ternary B-C-N compounds comprises mechanical mixing and alloying. In this method boron, carbon and nitrogen containing materials are mixed together to form B-C-N complex in easiest possible way, for example boron nitride powder with carbon/graphite powder or boron powder with carbon nitride powder. Homogenous samples with well distributed B, C and N are obtained via prolonged (high-energy) ball milling. Knittle et al., [49] was the first to try mechanical mixtures of graphitic-boron nitride (h-BN) and graphite (g-C) in different compositions. Mixtures were ground together under acetone to get uniformity. The authors compared the results with that of chemically prepared BCN microcrystalline powders and the performed high-pressure high-temperature experiments provided solid solutions of c-BN and diamond. Zhao et al., [53] tried very similar approach like former one, to get BC_2N and BC_4N mixtures. Precursor materials were prepared by stoichiometric 2:1 and 4:1 molar ratio mixture of graphite and hexagonal boron nitride (h-BN) to get BC_2N and BC_4N respectively. Mixture was ball-milled for 34h in tungsten carbide vial to get good homogeneity. The idea was to break sp^2 bonding among hexagonal rings of graphite and h-BN crystal structure and to get amorphous BCN fine powder [53]. Similar approach was applied by Huang et al., [161] to synthesize amorphous B-C-N (a-BC_2N) phase. Electron energy-loss spectroscopy and TEM studies indicated the sp^2-hybridized bonding of the a-BC_2N as well as that the mixing between the BN and the C species was achieved at a nanometer scale, thus the a mechanical mixture rather than a chemical mixture is obtained. Filonenko et al., [162, 163] used starting material as mixtures of boron (B)(35-50%) and carbon nitrides powders. Commercially available boron ranging from 1-10 μm particle size mainly consisted of β-phase was mechanically mixed with graphitic carbon nitride (C_3N_4) nanospheres. The authors reported that, boron content in mixture was varied from 20-80%, low B (less than 35 %) leading to decomposition of C_3N_4 and higher B (more than 50 %) content leading to synthesis of boron carbides at HP-HT conditions; however reaction mechanism is still unclear.

1.3.2.3 HP-HT behavior of BCN compounds

The high pressure synthesis approach in ternary B-C-N systems can be broadly classified into two categories; namely a) aspiring well crystallized ternary B-C-N materials but not intend to obtain super-hard phase or the dense B-C-N materials, b) targeting the dense super-hard B-C-N materials. In the following the beginning part refers to the efforts of HP-HT experiments towards the first approach and which precedes the attempts in the direction of obtaining a super-hard phase.

As mentioned above, techniques employed in synthesize low-density B-C-N phases (in section 1.3.2.2), such as high temperature nitridiation, solid phase pyrolysis, chemical and physical vapor deposition, ball milling, generally result in the poorly crystallized, turbostratic or amorphous products. Well crystallized B-C-N compounds having hexagonal structure (h-BCN) were successfully obtained by applying of high-pressures and high temperatures. Thus amorphous B-C-N precursors were transformed into h-BCN using a belt-type apparatus [149] and Bridgman anvils [155, 156] at pressures of 3-5 GPa and temperatures 1000-1500 °C. Yamada produced a graphite-like phase by shock-synthesis of a mechanical mixture of graphite and h-BN [164]. The hexagonal lattice parameters of a_0= 0.2475 nm and c_0= 0.676 nm were determined by transmission electron microscopy (TEM) from a cluster of sheet-like particles, whose composition corresponded to BC_2N. Electron energy-loss spectroscopy (EELS) confirmed the presence of boron, carbon, and nitrogen – all sp^2-hybridized – in a single graphite-like crystal. A highly crystalline hexagonal BC_2N compound was prepared by the compression of a turbostratic B-C-N precursor (synthesized via a high-temperature reaction between melamine and boric acid) using an iron catalyst at temperature and pressure as high as 1500 °C and 5.5 GPa, respectively [165]. Yang et al. obtained h-BCN from a mixture of boron powder and CNH compound prepared by pyrolysis of melamine ($C_3H_6N_6$) under high temperature (1400–1500°C) and high pressure (5.0–5.5 GPa) [166]. X-ray photoelectron spectroscopy, FT-IR and Raman spectroscopy showed the presence of B-N, C-B-N, C-N and B-C bonds in the final product with the overall composition of $B_{0.18}C_{0.64}N_{0.16}$ (near BC_4N). X-ray diffraction analysis confirmed a hexagonal structure. Scanning and transmission electron microscopy revealed the flaky h-BC_4N particles of about 1 μm with thickness of 200 nm.

The conditions normally employed to synthesize super-hard materials require extreme pressures and temperatures. Badzian [48] prepared cubic BN-C mixed crystals by the HP-HT technique (14 GPa, 3600 °C , Bridgman apparatus), using starting material hexagonal BN-C prepared from CVD. He obtained solid solution of diamond and c-BN along with mixed crystal of graphite and h-BN. Sasaki et al., [167] made some attempt targeted at the transforming graphitic BC_2N [118] into a cubic phase under relatively mild HP-HT conditions (5.5 GPa, 1400-1600 °C, Belt Press) using a Co catalyst, but they obtained the phase-separated mixture of cubic phases, i.e. the well crystallized diamond and c-BN crystals up to 3 μm in size. Expecting the catalytic promotion of the phase separation in the B-C-N system,

Nakano et al.,[168] tried the direct transformation of g-BC_2N into cubic phase, without additives under higher HP-HT conditions (7.7 GPa, 2000-2400°C, Belt Press). Presence of several cubic phases with a diamond-like structure, namely c-BN, diamond containing minor amount of B and N, and a cubic B-C-N substance, were confirmed in the products above 2150 °C by the powder X-ray diffraction patterns. At 2400 °C, however, the cubic B-C-N product tended to segregate into c-BN and diamond. Authors concluded that c-BC_2N is not stable, and a mixture of c-BN and diamond is thermodynamically favorable in the B-C-N system under the conditions employed [168]. Similar result were reported recently by Huang et al.[161], where the HP-HT treatment at 7.7 GPa and 2300 °C of the amorphous a-BC_2N phase resulted in complete segregation of the carbon and BN species, namely c-BN, amorphous carbon, and turbostratic graphite. No mutual solubilities between c-BN and carbon were found at these P-T conditions.

Knittle et al., [49] prepared a cubic $C_x(BN)_{(1-x)}$ (x = 0.3-0.6) solid solution under high pressures (30-50 GPa) and high temperatures (2000-2500 K) from mechanical mixtures of graphitic-boron nitride and graphite using a laser-heated diamond anvil cell (LH-DAC). Measurements of the lattice parameters of samples quenched to ambient pressure showed that the solid solution series was non-ideal, with molar volumes up to 1% larger than expected (Vegard's Law) based on ideal mixing between C (diamond) and cubic-BN. Bulk modulus of $C_{0.3}(BN)_{0.7}$ was found to be 355±19 GPa, which was lower than the ideal solid solution of diamond and cubic BN. Ionic bonding nature in these solid solutions were confirmed by Raman spectra of $C_{0.3}(BN)_{0.7}$ which exhibited LO-TO splitting of the phonon modes.

Komatsu et al., [50, 54, 152, 169, 170] converted the graphitic $BC_{2.5}N$ (g-$BC_{2.5}N$) obtained by CVD technique to heterodiamond c-$BC_{2.5}N$ using cylindrical shock compression technique. The shock pressure and temperature on the sample was estimated to be 35-50 GPa and 3000-10000 °C respectively. They also studied bulk synthesis from different starting materials, g-BC_xN ($2 \leq x \leq 5$) obtained by both CVD or solid phase pyrolysis, using shock compression method and explored the properties like thermal oxidation resistance, thermal expansion coefficient and bulk modulus of the high-pressure products[54, 152]. Heterodiamond c-$BC_{2.5}N$ crystals were 5-20 nm in size, showed polycrystalline behavior. Lattice constant was measured to be 3.605 Å, which is between those of diamond (3.5667 Å) and cubic BN (3.6158 Å). The material revealed a thermal oxidation resistance (stable up to 700°C) higher than that of diamond, a low thermal expansion coefficient ($\sim 10^{-6}$ K^{-1}), and a bulk modulus (401 GPa) higher than that of cubic BN.

Solozhenko et al., [51] prepared cubic BC_2N from graphitic BC_2N synthesized according to the method of Hubacek & Sato [72] using the HP-HT conditions (18-25 GPa, 2000-2200 °C in a LH-DAC and multi-anvil-press, MAP). The lattice parameter of the c- BC_2N determined at ambient conditions was 3.642±0.002 Å, much larger than those of diamond and c-BN (Figure 1-6). For the large volume sample, the hardness (Hv) was measured to be 76 GPa, which is higher than that of c-BN. Surprisingly, the determined bulk modulus of the

c-BC_2N was 282 GPa which is significantly lower than the values for c-BN or c-BC_2N reported by other authors [49, 54]. Zhao et al., [53] pointed out a possible reaction of the sample with MgO capsule material in that work as well as large deviation of the lattice constant of c-BC_2N from Vegard's law. Solozhenko and co-workers in their further research, came up with detailed characterization of the synthesized c-BC_2N sample [112, 171, 172] Raman spectroscopy studies attributed the Raman band 1326 cm^{-1} to LO mode of c- BC_2N, whereas TO mode was missing [171]. AFM images revealed the c-BC_2N grains of 200 nm in size in contrast to initially reported 10-30 nm from TEM images [172]. The authors also reported Knoop hardness (H_K) of 55 GPa, Young's modulus (E) of 980 GPa, sheer modulus (G) of 447 GPa and fracture toughness (K_{Ic}) of 4.5 $MPa \cdot m^{1/2}$ for their c-BC_2N and proclaim it the hardest known solid after diamond [112]. Subsequent Brillouin scattering measurements on the same cubic BC_2N phase provided even lower bulk modulus and shear modulus values of 259 GPa and 238 GPa, respectively [173]. Nevertheless, it should be emphasized that the B, E and G values of c-BC_2N reported by Solozhenko and co-workers significantly deviate from the elastic moduli relationship for homogeneous isotropic materials. Theoretical attempts to explain lower bulk modulus, large lattice constant and missing TO modes in Raman spectra of the synthesized c-BC_2N and to correlate these issues with possible B-C-N structure [87, 93, 94] could not give an unambiguous answer so far.

Zhao et al., [53] synthesized super-hard phase of BC_2N and BC_4N in nanostructured bulks under HP-HT conditions (20 GPa, 2000 °C, Multi anvil press) from mixture the of graphite and h-BN powders in 2:1 and 4:1 molar ratio, respectively. The mixture was ball-milled in a tungsten carbide vial for 34 hr which allowed to obtain homogeneous starting materials with randomly bonded B, C and N atoms. The authors expected to break the sp^2 bonding among the hexagonal rings of the graphite and h-BN crystal structures and to introduce some initial amount of hybrid sp^3 bonding., X-ray diffraction (XRD), scanning electron microscopy and Raman spectroscopy studies of the ball milled mixture showed that the BC_2N and BC_4N starting material was completely amorphized with a median particles size of about 2–3 nm. Comparative studies of synchrotron XRD, HR-TEM, EELS, and Vegard's law of the unit-cell volume versus chemical compositions all indicated that the high-pressure BC_2N and BC_4N products were single B-C-N ternary phases with crystallites of about 5 nm in size. Assuming a face-centered cubic zinc-blende structure the authors derived a unit-cell parameter of a_0 = 3.595(7) Å and a_0 = 3.586(9) Å for the synthesized BC_2N and BC_4N material, respectively. The hardness measurements showed the nominal hardness of 62 GPa for c-BC_2N and 68 GPa for c-BC_4N, which is between the hardness values of diamond and cubic boron nitride. A plot of unit-cell parameters as a function of chemical composition showed a good agreement with Vegard's law (Figure 1-6), with the exception of Solozhenko et al.'s data,[51] which deviates significantly from the line. The authors suggested that the composition of Solozhenko et al.'s [51] sample was not the solid solution of BC_2N and clearly had a different chemistry [53]. Taking in to account the XRD and Raman spectroscopy

measurements of Solozhenko et al., [51] and Zhao et al., [53] theoreticians suggested two tetragonal (z*-BC_2N and t-BC_2N) [94] and one rhombohedral (rh-BC_2N) [97] as the most likely structures describing experimentally obtained c-BC_2N. In turn, 3C-BC_4N structure with trigonal symmetry [98] was found to give the best agreement with experimental XRD pattern of c-BC_4N [53].

Boron rich B-C-N compositions, "$B(C_xN_{1-x})$", were chosen by Guo et al., [174] for their HP-HT experiments. B_2CN precursor was prepared by mechanical vibration-milling process from amorphous boron, graphite and h-BN powders with mole ratio of 1:1:1 and mixed with $Ca_3B_2N_4$ catalyst. The authors claimed that a boron rich cubic phase is formed at 5.5 GPa and 1500 °C. The carbon content (detected by EDX) was found to vary from 0 to 16 at.% depending on the investigated crystal. The average composition is reported to be $B_{0.58}C_{0.16}N_{0.26}$. Despite the evident oxygen peak in the EDX spectra, the authors gave no comment on the oxygen presence in the product [174]. Moreover, the cubic lattice parameter of $a_0 = 3.618$ Å of the claimed BCN phase is similar to that of c-BN.

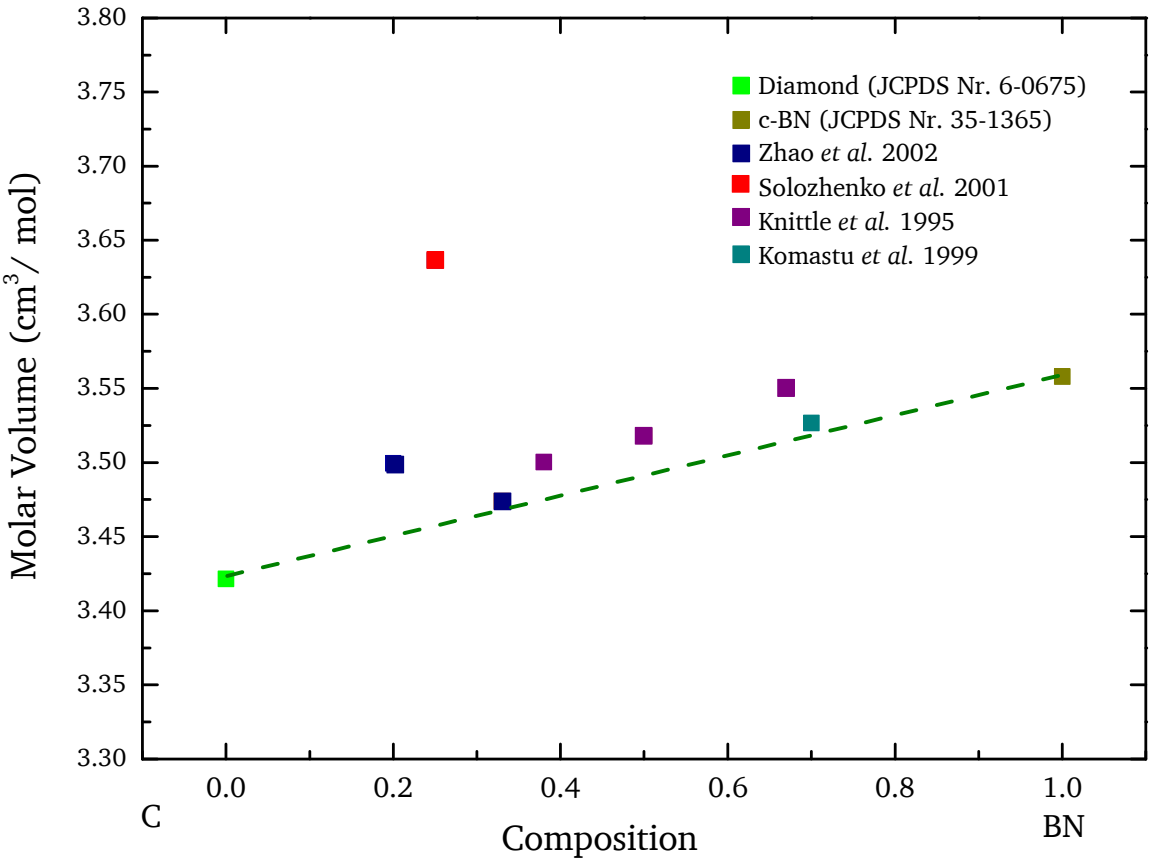

Figure 1-6. Plot of all observed unit-cell volumes in the B–C–N system of cubic zinc-blende structure.[53] The relationship of unit-cell volume vs chemical composition shows a clear trend closely obeying Vegard's law for ideal solid solutions, except for data of Solozhenko et al. Reproduced with permission from [51]

Nicolich et al., [175], attempted to form cubic ternary crystals from turbostratic BCN starting materials [146] at HP-HT conditions (3-5 GPa, 1200-1500 °C, Belt-type apparatus) obtained from ternary graphitic crystals. In earlier attempts Solozhenko et al., [176] tried to

compress g-BC_4N up to 7GPa at 1900°C in a multi-anvil press and succeeded only in densifying the starting material. Tian et al.[153] , Li et al.[154], and Da-Peng et al., [166] studied the HP-HT behavior (5-6 GPa, 1400-1700 °C, Multi anvil press) of BCN precursor prepared by reaction between melamine and boric acid derivatives (method is explained in Section 1.3.2.2), which led to the formation of hexagonal-BCN (h-BCN). The lattice constants a_0 = 2.506 Å and c_0 = 6.657 Å, [153] and a_0 = 2.510 Å and c_0 = 6.690 Å [154] were reported. A completely new $BC_{3.3}N$ crystalline compound with low-density orthorhombic structure has been synthesized using an amorphous B-C-N precursor at 6 GPa and 1773 K [177]. Results of energy-dispersive spectroscopy (EDS) and electron energy loss spectroscopy (EELS) showed that the compound has a 1.04:3.27:1 B:C:N chemical stoichiometry. The lattice parameters of $BC_{3.3}N$ crystal were obtained to be a_0 = 6.610 Å, b_0= 4.977 Å, and c_0 = 8.509 Å by XRD and select area electron diffraction (SAED). On the basis of XRD refinement and EELS results, one possible $BC_{3.3}N$ ($B_3C_{10}N_3$) model with a space group *Pmma* (No. 51) is proposed.

Li et al., [178] studied high pressure phase transition of h-BCN[153] having the composition of $B_{0.47}C_{0.23}N_{0.30}$ up to 30 GPa in a DAC. Transformation from h-BCN to the wurzite BCN (w-BCN) structure was observed for pressures above 15 GPa and bulk modulus of 275 GPa was derived from the equation of state for w-BCN. The bulk modulus value is very close to that reported earlier by Solozhenko et al., [51] for c-BC_2N, and is significantly smaller than those of c-BN and w-BN. The authors however neither verify the composition of the new high-pressure phase nor provide any data about its stability at ambient pressure.

Filonenko et al. [162, 163] reported high-pressure synthesis of heterodiamond phase using the powder mixtures of graphite-like carbon nitride g-C_3N_4 and crystalline boron (35-50 wt.%) as the starting materials (cf. page no 22) . A “toroid” type apparatus was employed to apply high pressure (6-15 GPa) and high temperature (1000-1600 °C). Treatment at pressures above 8 GPa and temperatures in the range of 1450–1600 ºC resulted in the formation of a cubic phase with the unit cell parameter a_0 = 3.6551 Å. It is noteworthy that the employed HP-HT conditions are very mild when compared to the other reports of the diamond-like B-C-N syntheses. The highest yield of the cubic BCN phase has been obtained from mixtures with ~50 wt.% of boron. EDX analysis of the synthesized c-BCN crystals revealed an average atomic composition of 45.3% B, 36.5% N, 11.6% C (roughly ~ B_4CN_4), and considerable amount of oxygen (6.6 at.%). On the basis of the Rietveld structure refinement of the c-BCN the authors propose that carbon atoms partially replace boron and nitrogen in their positions in the structure of c-BN, while oxygen takes only nitrogen positions [162, 163]. This statement, however, requires further experimental verification. Moreover, the reported unit cell parameter of 3.6551 Å exceeds that of c-BN, thus ruling out the possibility of matching with Vegard’s law for diamond/c-BN alloys. A detailed characterization of the synthesized c-BCN phase with respect to the chemical bonding and properties as well as unambiguous conclusion on the oxygen presence were not provided.

Recently, a single-phase cubic BC_4N solid solution was claimed to be formed at high pressure and temperature (18-20 GPa, 2000-2200 K, MAP) starting with either a mixture of diamond and c-BN or graphite and h-BN [179]. The authors reported high Vickers hardness (85 ± 4 GPa) of the HP-products, reaching that of single crystal diamond. However authors did not provide sufficient evidence to prove ternary BCN compound. Properties and XRD of the synthesized compounds can also be explained by mixture of c-BN and diamond.

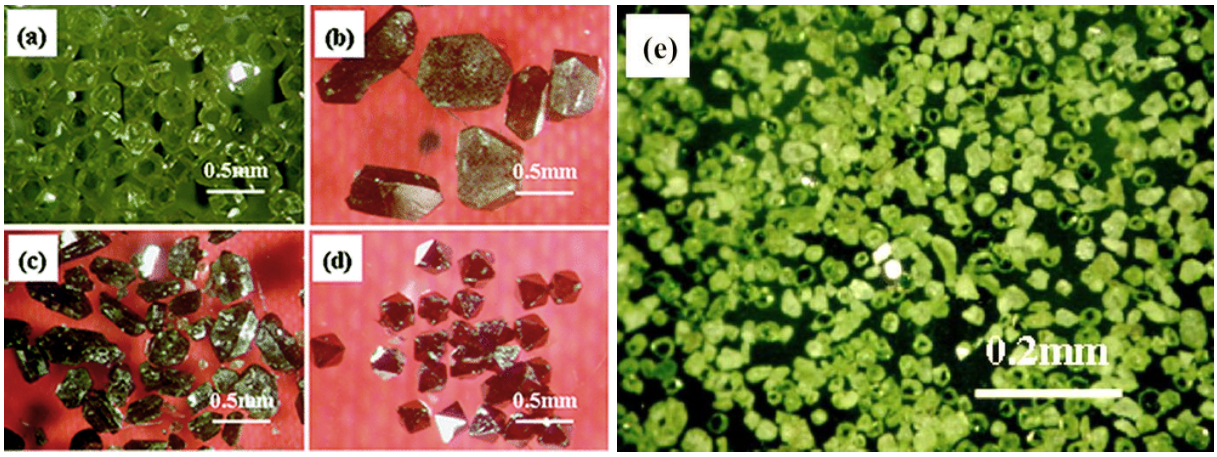

Figure 1-7. Optical images of diamond crystals obtained at HP-HT using Fe-Ni alloy as catalyst starting from graphite (a) or mixtures of graphite and h-BN with stoichiometries of (b) $C_{0.98}(BN)_{0.02}$; (c) $C_{0.9}(BN)_{0.1}$; (d) $C_{0.9}(BN)_{0.1}$ with 1 wt.% Al additive; (e) $C_{0.5}(BN)_{0.5}$. Reprinted with permission from [180].

Based on the measured and calculated XRD patterns the authors concluded that the synthesized products are solid solutions of diamond and c-BN with a zinc-blende structure (*F*-43*m*) [179]. It should be, however, emphasized that the presented XRD data alone does not provide unambiguous evidence of the presence of single B-C-N phase. In particular, formation of c-BN/diamond nano-composite cannot be excluded.

Very intriguing results were reported lately by Liu et al.,[180] who succeeded in preparation of diamond crystals doped with B and N atoms, starting from graphitic mixtures of C and BN with compositions of $C_{1-x}(BN)_x$ where x = 0.02, 0.1 or 0.5. The BN-doped diamond crystals were grown in a large volume cubic multi-anvil press (MAP) using iron-nickel alloy as catalysts at pressures of 5.0-7.2 GPa and temperatures of 1500-2300 K. Variation in morphology and color of the obtained crystals (Figure 1-7) was attributed to the different amounts of B and N atoms incorporated into the crystal structure. XRD, XPS, Raman- and FT-IR spectroscopy were used to verify the structure, chemical composition and bonding of the crystals, in particular the presence of all three elements as well as of the C-C, B-N, B-C and C-N bonds. The authors have noted that the $C_{0.9}(BN)_{0.1}$ tends to separate into several cubic phases having different B/N ratios, while in the $C_{0.5}(BN)_{0.5}$ system no phase separation was found and the obtained single-phase “BCN”-diamond exhibited cuboctahedral shape, light yellow in color, and nearly transparent [180]. The derived cubic lattice parameter of the “BCN”-diamond of 3.575 Å is in a good agreement with Vegard’s law for a diamond/c-BN

alloy. The exact chemical composition of the BN-doped diamond crystals phases was not determined.

1.3.2.4 Electrochemical studies of BCN compounds

Concerning B-C-N systems, only handful number of materials has been investigated with respect to the lithium storage properties. Ishikawa et al., [181] was the first to explore BCxN, systems (x= ~ 3,7, 19) as anode materials, and found that storage capacity increases with an increase in the carbon content. BCN compounds for anode materials were prepared by Huback and Sato [72] method (cf. section 1.3.2.2). The observed capacities were in the range of 180 mAh g^{-1} for the studied materials. Later, Kawaguchi et al., [182] studied graphitic BC_6N materials synthesized by CVD method [183] as an anode materials. BC_6N had an improved capacity of 303 mAh g^{-1} during first discharge. Authors claimed crystalline BC_6N, similar to graphitic structure however, did not provide details on unambiguous evidence for composition and crystal structure. These studies showed that Li-intercalation into bulk BCNs occurred with a smaller interlayer expansion ratio than that of graphite, thus suggesting better cyclability. However, these bulk materials exhibited low capacity. Recently Lei et al., [22] reported nanostructured B-C-N layers (nanosheets) with improved capacities of 390 mAh g^{-1} and cycling stabilities at higher current rates.

2. Experimental Techniques

The present section covers the experimental techniques and devices employed in this work. In the beginning (Chapter 2.1) precursor [2] synthesis procedure and techniques are explained. The following chapter (Chapter 2.2) gives concise overview about modern high-pressure techniques; multi-anvil (MA) apparatus and diamond anvil cell (DAC) techniques used in studying the high-pressure high-temperature behavior of polymer derived B-C-N ceramics. Analytical methods applied for characterization of precursors and recovered materials are briefly presented in Chapter 2.3. It includes powder X-ray diffraction, elemental analysis, Raman spectroscopy, X-ray Photoelectron Spectroscopy, scanning electron microscopy (SEM), transmission electron microscopy (TEM) and electrochemical characterization. As the major findings in the present thesis are based on TEM, more elaborated explanations of principles and sample preparation procedures are given.

2.1. Synthesis of BCN and BON compounds

BC_2N and BC_4N precursors are prepared according to the Riedel [21, 146] and Bill [71] method. BC_2N is synthesized by a solid phase pyrolysis of a piperazine borane complex ($C_4H_{10}N_2.BH_3$) via a polymer derived ceramics (PDCs) route. As the piperazine borane complex is not readily available on the market, in house synthesis is carried out using a reaction of peperazine with boron dimethyl sulfide complex. BC_4N is synthesized from the solid phase pyrolysis of the cross-linked pyridine borane. In the following sections the step by step procedures to obtain the BC_2N and BC_4N precursors are given in detail.

2.1.1. Synthesis of BC_2N

Step 1 - synthesis of piperazine borane : A Schlenk technique [184] is used in the synthesis of piperazine borane. Set up consists of a Schlenk line, having two lines or tubes inter connected with several ports to allow either vacuum or inert gas to be selected without the need of a separate line. (Schematic is given in Figure 2-1). Thus one of the end is connected to a source of ultra-pure inert gas which is vented through an oil bubbler to prevent air contamination. A high vacuum pump equipped with a digital meter reading is connected on the other end with a liquid nitrogen trap (cold trap) to prevent solvent vapors and gaseous products from contaminating the pump. The reaction vessels are connected to the ends through the ports by high pressure nylon tubing. In this apparatus, several reactions can be carried out simultaneously.

[2] The material used as starting materials in high-pressure synthesis experiments

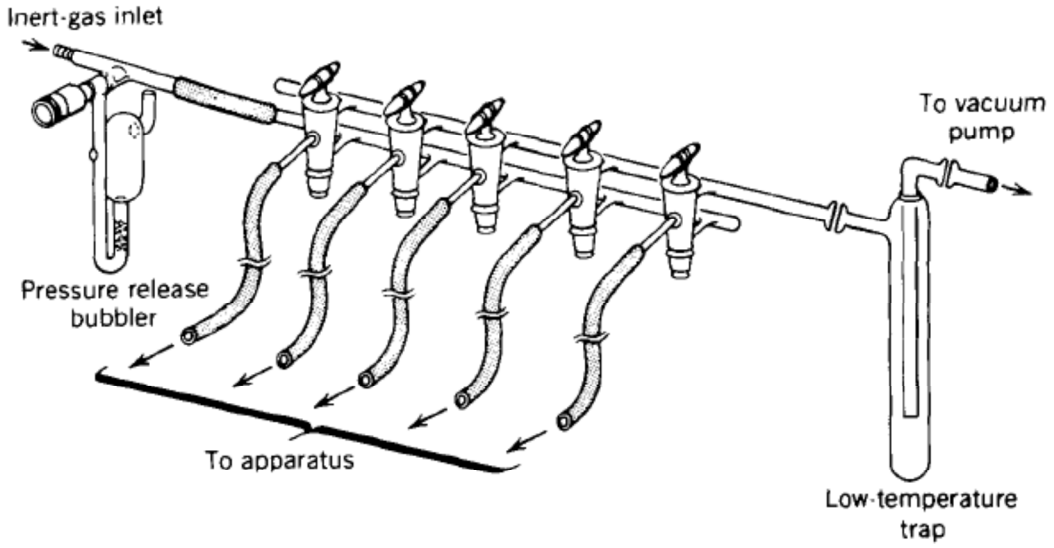

Figure 2-1. Schematic diagram of the Schlenk line [184] used during the precursor synthesis to control argon atmosphere.

Piperazine borane ($C_4H_{10}N_2{\cdot}BH_3$) complex was obtained through the reaction of piperazine ($C_4H_{10}N_2$)(Sigma Aldrich, 99% purity), with a borane dimethyl-sulfide (Sigma Aldrich) (CH_3-S-CH_3:BH_3) (BMDS) complex. Typically 0.23 mol of piperazine were dissolved in 500 ml of dry toluene and continuously stirred under Ar flow in a round bottom flask at room temperature until complete dissolution. The solution was placed in an ice bath to maintain a reaction condition at 0 °C. Addition of 0.28 mol of borane dimethyl-sulfide complex by a drop-wise injection method is followed to start the reaction. A cloudy white solid was formed immediately. Stirring is continued up to 2 h after completing the addition of BMDS complex (at 0°C and Ar flow). The reaction products (white color solid) were separated by applying vacuum of 5 Pa under mild heating of 50-80 °C. The reaction was repeated several times to obtain the desired amounts of the piperazine borane complex. After recovery white color chunks were crushed into fine powder using an agate mortar in glove box in Argon atmosphere (< 1-5 ppm of O_2 and H_2O). This product was used in the next step of the synthesis. The first step synthesis reaction can be written as follows.

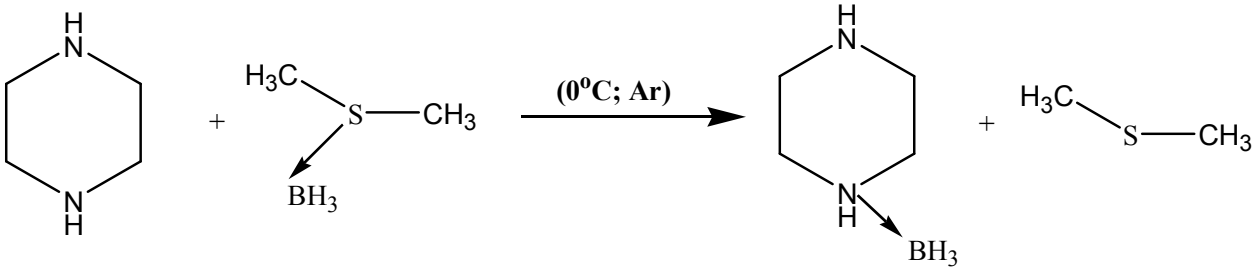

Piperazine Borane dimethyl sulfide Piperazine borane

Step 2 - Cross linking and Pyrolysis: A horizontal tube furnace was used for the cross-linking and pyrolysis reactions. A Schlenk tube of 500 mm in length and 40 mm internal

diameter was used. The inert gas (Argon) was allowed to flow through nylon tubes connected to the reaction chamber through glass connections. The outlet was vented through an oil bubbler. The heating/cooling cycles were programmed by a temperature controller. The furnace was equipped with a platinum-rhodium thermocouple. Schematic of the setup is given in Figure 2-2.

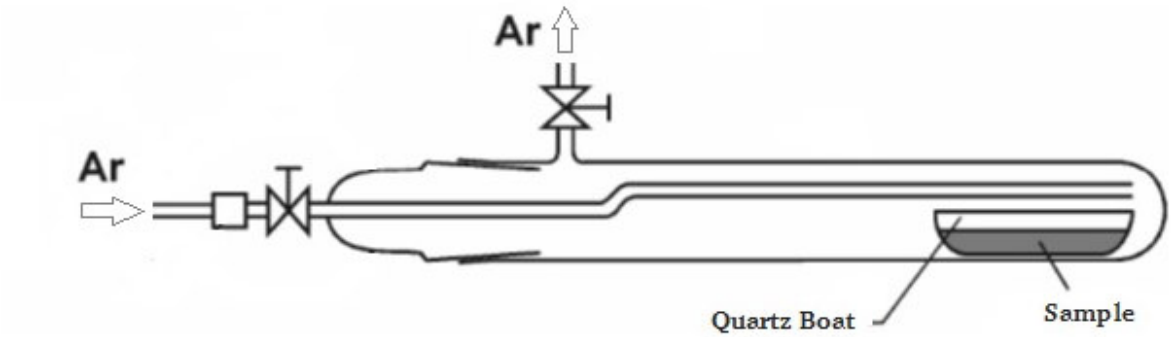

Figure 2-2. Schematic diagram of the Schlenk (quartz) tube used during the precursor synthesis to control argon atmosphere

The piperazine borane (white) powder was heat-treated at 400°C for 10 h in a quartz boat placed inside the Schlenk tube. Heating rate of 50°C/h was maintained. After heat treatment the white powder turns to yellow in color, which is indicative of a polymerization stage. This polymer derivative was subsequently pyrolysed at 1050°C for 2 h under Argon flow; a heating rate of 50°C/h was used. Compared to Riedel method [21, 71, 146] a lower heating rate was used to minimize the effect of sudden release of gaseous mixtures. A controlled cooling rate of 200°C/h was maintained upto 600 °C. The second step synthesis reaction can be written as follows. Black chunks were recovered in glove box and crushed in to fine powder using an agate mortar. The above synthesis steps can be described as single-source precursor method via polymer derived ceramics route [185].

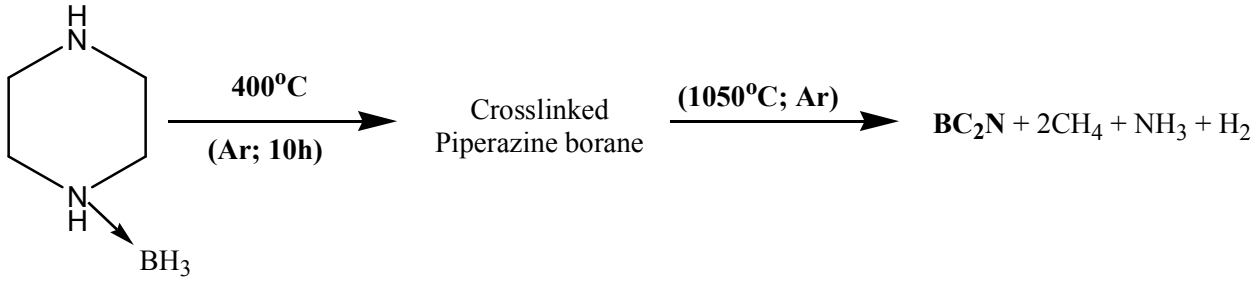

Piperazine borane

2.1.2. Synthesis of BC_4N

BC_4N can be synthesized in a single step compared to BC_2N. It is similar to step 2 of the BC_2N preparation, involving cross-linking and pyrolysis. The pyridine borane (Sigma Aldrich) (colorless liquid) was heat-treated at 120°C around for 1 h in a Schlenk tube directly. Heating rate of approx. 50 °C / hr was maintained. The synthesis reaction can be written as follows.

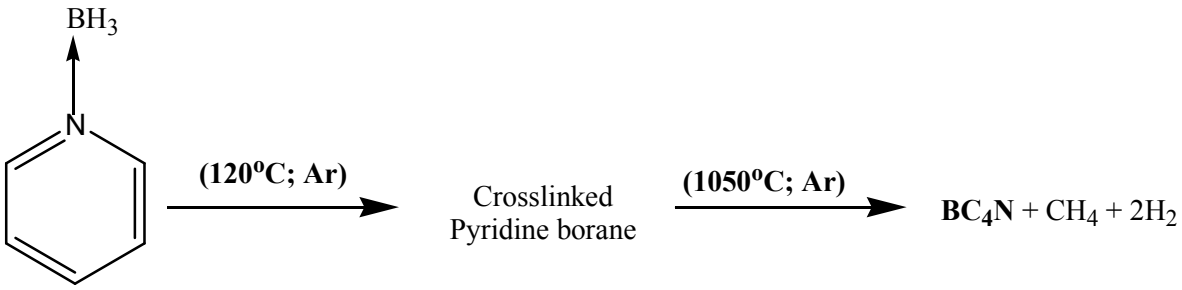

Pyridine borane

The crosslinking step was performed in a setup similar to Figure 2-2 (without quartz boat) but held in vertical position. Vertical setup is essential to contain and handle liquid reactant and gaseous byproducts during crosslinking. Temperature control below 150 °C in a tube furnace is not that precise, so heating was performed using an oil bath facility inside the fume hood equipped with Schlenk lines (Argon atmosphere). After reaching 120 °C, there was sudden exothermic reaction, releasing considerable amount of gaseous mixtures and solidification of the liquid reactant was occurred. Figure 2-3 shows the photograph of the cross-linked solid. This product was subsequently pyrolysed at 1050°C for 2 h under argon flow. Heating rate was maintained at 60 °C/ h. The above synthesis steps can also be described as a single-source precursor method via the polymer derived ceramic (PDC) route [185].

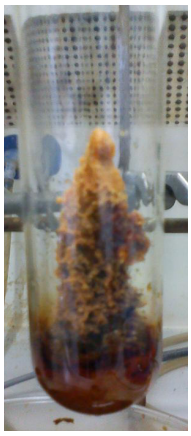

Figure 2-3. Photograph of the cross-linked pyridine borane inside the Schlenk tube

Sample Handling: During the synthesis, an important point to consider is maintaining inert atmosphere throughout the reaction. Even tiny mistakes in handling like short time exposure to air or water traces in the glassware can lead to oxygen contamination in the resultant material. In the present work synthesis conditions and reactant ratios were maintained as in the case of Riedel and Bill method [71, 146]. However process optimization and efficient handling of inert atmosphere during reaction rendered products with considerably low oxygen contamination. After pyrolysis, both precursors had turned into black ceramics chunks (solids with full of voids). These chunks were recovered in a glove box and crushed into fine power using an agate mortar. These precursors (in powder form) are stored in a glove box in argon atmosphere where oxygen and moisture (H_2O) levels are controlled below 2-3 ppm.

2.1.3. Synthesis of B-O-N (BN / B_2O_3 mixtures)

The starting materials for our synthesis were prepared by ball-milling of different molar mixtures of hexagonal BN (99.5% purity, Alfa Aesar) and B_2O_3 (99.98% purity, Alfa Aesar) in the ratio from 1:1 to 4:1 (wt. %). Ball milling experiments were carried out at 300 rpm for 4 h, with zirconia vessel and balls and tungsten carbide vessels and balls. Results of these experiments are given in section 3.1.6.

2.2. High-Pressure High-Temperature experiments

High-pressure techniques used in the present work, cover three different pressure ranges. Firstly, 5-7 GPa using single stage cubic multi anvil apparatus; secondly around 12GPa using toroid press; thirdly 15-39 GPa using diamond anvil cells and two-stage multi anvil press (16 GPa).

In this chapter brief overview of and introduction to the most important static high-pressure techniques able to generate pressures above 2 GPa are considered. The moderate-pressure equipment (up to 1.5 GPa), such as cold-seal vessels and auto-claves [186, 187], is not considered here because it operates below the pressures related to this work. Description of dynamic methods of pressure generation is also omitted. These methods allow achievement of ultra-high pressures ≈ 100 GPa and higher and simultaneous ultra-high temperatures via generation of shock waves by hypervelocity impact or explosion[188]. As in the present work multi-anvil apparatus and a diamond anvil cell are used, little more attention is given in the details of these techniques. Introduction to high pressure techniques is discussed in section 2.2.1, toroid press experiments are discussed in section 2.2.2. The multi anvil experiments are discussed in section 2.2.3. The later contains two sub sections namely; section 2.2.3.1 single-stage multi anvil experiments and section 2.2.3.2 two-stage multi anvil experiments. Finally diamond anvil cell experiments are discussed in section 2.2.4.

2.2.1. Introduction to high pressure techniques

Static pressures exceeding 2 GPa can be generated by only a few high-pressure apparatuses. Namely i) piston-cylinder systems, ii) belt-type apparatuses, iii) toroid-type cells, iv) multi-anvil apparatuses and v) diamond anvil cells (DAC). These apparatuses are differing considerably in design, maximal achievable pressure, temperature and sample volume. This also results in huge variation in production/operation costs. However design of the above listed devices can be broadly classified based on two main principles of static pressure generation: piston-cylinder and opposed anvils.

In a piston-cylinder system [189, 190] pressure is generated by forcing a piston into a sample chamber within a cylinder. Figure 2-4a shows the schematic diagram of the piston cylinder assembly. The volume of a high-pressure chamber can vary from 1 to 100 cm^3. In these systems, both the piston and the cylinder should be supported, if pressures of the order of 5 GPa to be reached. The maximum achievable pressure with this apparatus is limited by the tensile yield strength of the cylinder. As a rule, the higher the sample volume the lower is the resulting pressure. Samples can be heated by a resistance furnace assembly located within the pressure chamber up to 2000 K.

In 1952 P. W. Bridgman [191] (Bridgman 1952) designed the opposed anvils apparatus. Schematic diagram of the device is shown in Figure 2-4b. In this method thin disc

of sample material is compressed between two opposed anvils made of hard and strong material like tungsten carbide (WC). The sample disc is contained by a gasket ring (either pyrophyllite or metallic materials) which seals the pressure chamber by friction. The maximum pressure achievable by this method is determined by the ratio between the force applied to anvils and the anvil-face (culet) area and is limited by the compressive yield strength of the anvil material. The geometry and massive support mechanism helps to achieve pressures even higher than the compressive strength of the anvil material. For example for cone angle $\alpha = 5°$ pressures up to $\sim$ 20 GPa can be reached in sintered WC anvils (having compressive strength of 5 GPa). Even though the original Bridgman's anvils are rarely used today, in design of the most modern high-pressure devices like diamond anvil cells (see more details in section 2.2.4), the principle of opposed anvils is applied to a considerable extent.

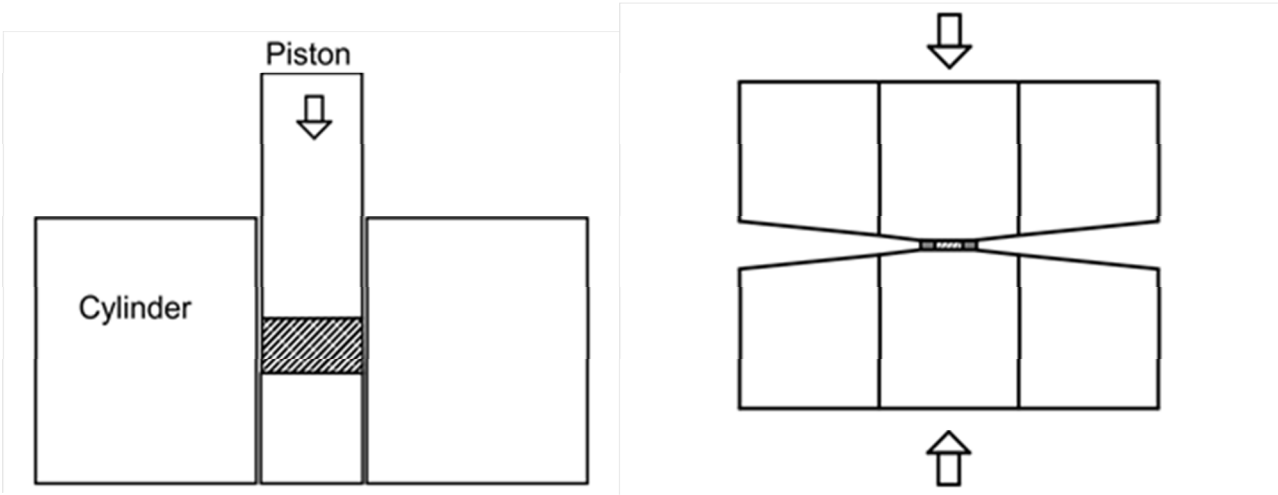

Figure 2-4. Schematic diagram of the (a) Piston cylinder apparatus, and (b) Bridgman opposed anvil apparatus

However, for larger sample volume (>1 mm^3), pressures higher than 5 GPa is not possible to reach with the above mentioned techniques. The efforts in this direction resulted in the development of new high-pressure techniques, such as belt, toroid and multi-anvil apparatuses. In Belt-type apparatus routine experiments up to 8 GPa and temperatures of 2300 K can be performed with the sample volume of about 100 mm^3. Different versions of this high-pressure device are used today for industrial production of diamond and cubic boron nitride. Detailed principles, schematics related to belt apparatus are excluded here as the present work does not describe any experiment using a belt type apparatus. In the next sections detailed explanations for multi anvil press (cubic and two-stage octahedral), toroid press and diamond anvil cells are discussed.

2.2.2. Toroid Experiments

For the HP-HT experiments of BC_2N and BC_4N at ~ 12 GPa, presented in this thesis, toroid press was used. The experiments were performed at the Institut für Anorganische Chemie, TU-Bergakademie Freiberg, Freiberg, Germany. Description of this device, its working principle and sample environment is given in the following.

Toroid press basically works on Bridgman opposed anvil principle. Here sample space is hallowed out to provide large sample volume. The lateral support is provided by a suitable gasket assembly [192, 193]. Figure 2-5a shows the schematic diagram of the toroid anvils. This geometry allows pressure generation of 15 GPa for sample volume up to ~ 100 mm^3. Anvils having lens-shaped pressure chamber encircled by a toroidal support are press-fitted into the steel supporting rings used in this device. Gasket is a circular disk, repeating the shape of the anvils, having a hole in the middle which also serves as sample chamber. Normally anvils are made of hard tungsten carbide and gaskets are made up of soft material like pyrophyllite and lithographic stone. When the pressure required is less than 10 GPa, samples volume can be considerably increased to ~ 300 mm^3. The advantages of the apparatus also include handling liquid or fluid samples and possibilities of electrical contact during experiment. It makes measurements of electric, thermal, magnetic and volume properties of matter in a hydrostatic environment at room and elevated temperatures as well as during material synthesis experiments possible.

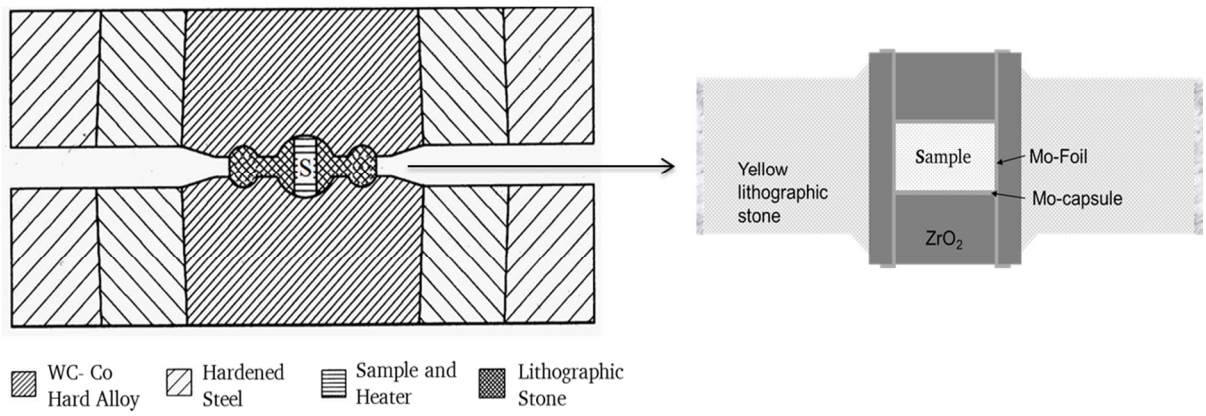

Figure 2-5. Schematic diagram of the (a) toroid press (Reprinted with permission from [194]) (b) sample assembly used in toroid experiments

Experimental set up and procedure: Experiment in the toroid-type press was carried out using a 8.5 mm sample assembly with a lithographic limestone gasket. The starting amorphous BC_2N and BC_4N powders were pre-compressed in a metal die and loaded into molybdenum (Mo) capsules (2.8 mm outside diameter, 0.05 mm wall thickness, and 2.5 mm length). The capsule was inserted into the middle of the Mo cylinder of 7.5 mm in height and 0.0025 mm in thickness, serving as heating chamber. The rest of the volume in the cylinder was filled by zirconium oxide plungers. The schematic diagram of the sample assembly is

given in figure above (Figure 2-5b). The pressure was monitored by pre-calibrated curve (pressure vs. hydraulic pressure gauge), where the device had been calibrated using phase transformations of standard elements (e.g., Bi at 2.55 and 7.7 GPa) [192]. The temperature was estimated from the applied electric power using the spontaneous nucleation of diamond from Ni-Mn-Graphite (~ 1500 °C) [195] and sintering of α-Si_3N_4 powder as reference points. After compression to ~ 12.0 GPa at room temperature, the samples were heated up to the target power level (corresponding to T = 1000-1100 °C) and kept at that temperature for 5 min. Then, the samples were quenched to room temperature before the pressure was released.

2.2.3. Multi Anvil Experiments

Two different types of multi anvil device were used for the HP-HT experiments at 5-7 GPa and 16 GPa. Namely; i) Single stage cubic-anvil device- MAX80 installed at the F2.1 beam-line of storage ring DORIS III with *in-situ* energy-dispersive X-ray powder-diffraction (EDXRD) possibilities, ii) Two stage 6 / 8 Walker type device – offline large volume press (LVP). Both the apparatus are located at Deutsche Elektronen-Synchrotron (DESY) Hamburg Germany. Description of these devices, its working principle and sample environment are given below.

2.2.3.1 Single-stage cubic anvil device (MAX80)

In cubic anvil devices, six pistons are made to advance simultaneously towards the barycenter of the experimental volume or pressure chamber [189]. Moving mechanism and geometry can vary based on the press and module. Each anvil has flat face assembled to move towards centroid forms cubic pressure chamber. This experimental space is filled with the sample, which is enclosed in an adequate pressure transmitter, which also acts as the gasket material and as an insulator for high temperature operation. Pyrophyllite is classically used for this. For *in-situ* X-ray diffraction measurements pyrophyllite is replaced by boron epoxy mixtures, which are transparent to photons with energies greater than 2 keV [189]. The schematic of in-situ measurement and anvil assembly of the MAX80 press is given below (Figure 2-6a). With the tungsten carbide anvils, this type of devices can be used up to 10 GPa. This geometry also allows access of the incident and scattered X-ray beams between the anvils and so enables using it for synchrotron sources.

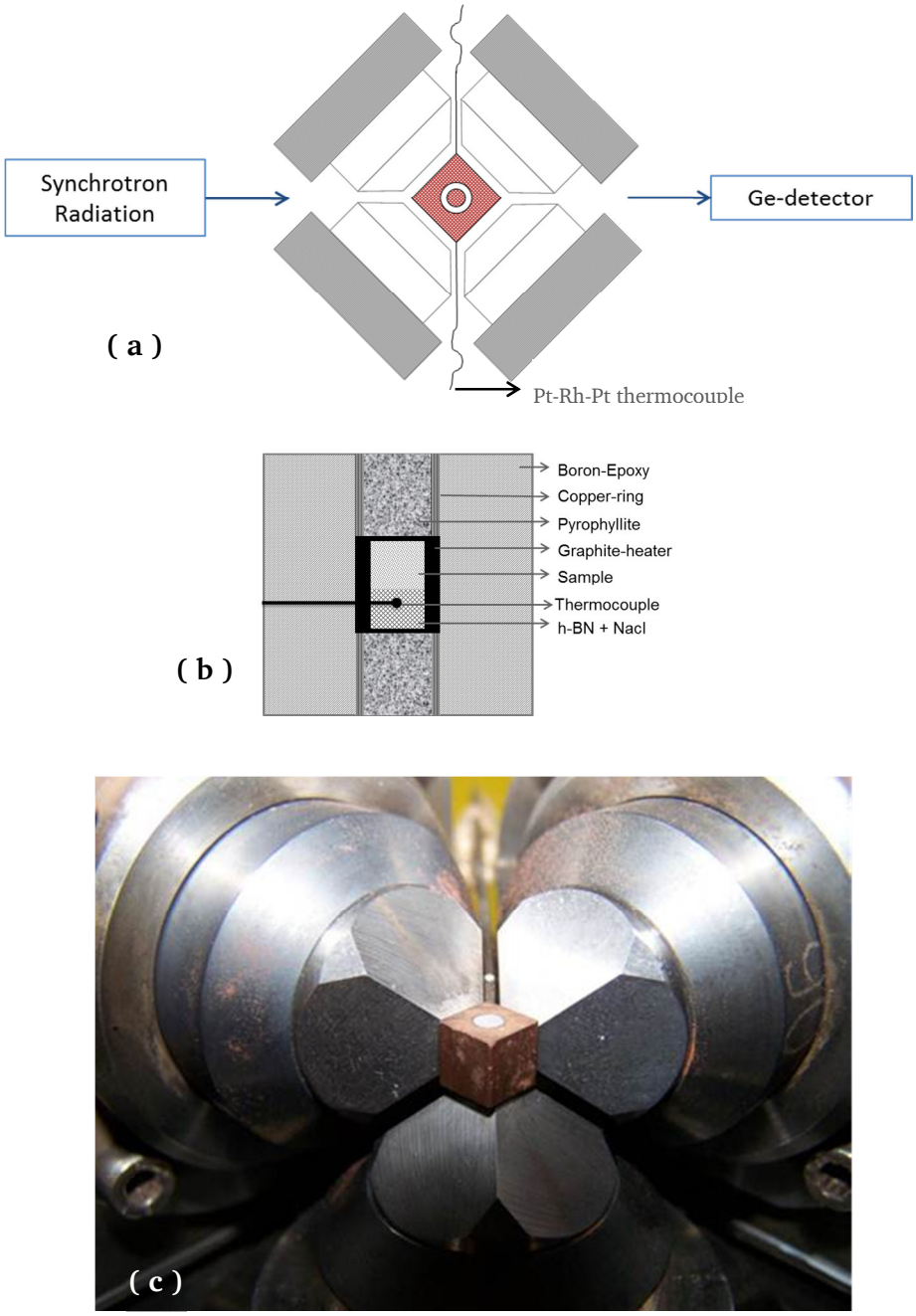

Figure 2-6. (a) Schematic diagram of the of in-situ measurement and anvil assembly of the MAX80 press, (b) schematic diagram of the boron-epoxy cubic cell, and (c) photograph showing three of the MAX80 anvils with the boron epoxy cell [196].

Experimental set up and procedure: A few milligrams of samples were loaded into a graphite cylinder, serving as sample chamber as well as resistance heater in the middle of a boron-epoxy cube. A mixture of NaCl/h-BN for pressure calibration was placed above and below the sample in the cylinder. The sample was separated from the pressure standard with a thin layer of h-BN. The cubic cell was located between six tungsten carbide anvils driven by

the large hydraulic press. Electric current was sent through the graphite heater via two opposite anvils. The temperature was measured with a Pt10%Rh-Pt thermocouple, inserted perpendicularly relative to the axis of the furnace in the h-BN layer above the sample. Actual pressure applied to the samples was calculated from the equation of state of NaCl [197]. The 8 mm and 6 mm cubes were used for experiments up to 5 GPa and 7 GPa, respectively. The schematic diagram of the cube is given above (Figure 2-6b). Samples were heated up to 1700 °C in steps of 100 °C/min and ED-XRD patterns were collected at every step. After the desired temperature was reached, samples were quenched by turning off the electric current and the sample cube was recovered after slow decompression. ED-XRD was collected by using a white beam with a spot size of 0.7 mm in the energy range 2-80 keV and a high purity Ge solid state detector fixed at the angle of $2\theta = 9.03°$. The detector angle was calculated from the NaCl reflection measurement at ambient pressure. In the figures, the ED-XRD data were plotted as intensity vs. 2θ (by fixing $\lambda = 0.70931$ Å) for the sake of comparison with other XRD data.

2.2.3.2 Two-stage multi anvil (6 / 8 Walker type) device

In the two-stage multi anvil device uniaxial load of hydraulic press is uniformly distributed over both the stages. The name 6/8 indicates six outer anvils in the first stage and followed by eight inner cubic anvils in the second stage. A Walker-type module [198] represents a load redistribution mechanism, which consists of six anvils or wedges cut as segments from a cylinder and shaped to compress the cubic second stage. This cylindrical assembly (with cubic second stage inside) fits into a massively supported containment ring and is loaded with an uniaxial hydraulic press via pressure distribution plates. The schematic of the Walker-type module including two stage system and pressure distribution mechanism are given below (Figure 2-7 (a) to (d)).

In the second stage, eight tungsten carbide (WC5-6%Co composite) anvils having triangular corner truncation are used for compression. When all the eight anvils are assembled in cubic form, the corner truncations form an octahedral pressure chamber in the middle (Figure 2-8). A ceramic pressure-transmitting medium containing encapsulated sample, furnace and thermocouple (optional) is placed in this chamber (Figure 2-8). In order to allow volume reduction, to support the anvils on loading and to seal the high-pressure chamber, pyrophyllite gaskets are placed between the WC-Co cubes as shown in Figure 2-8. Anvils also insulated with Teflon tape in such a way that, current can only passed via sample heater.

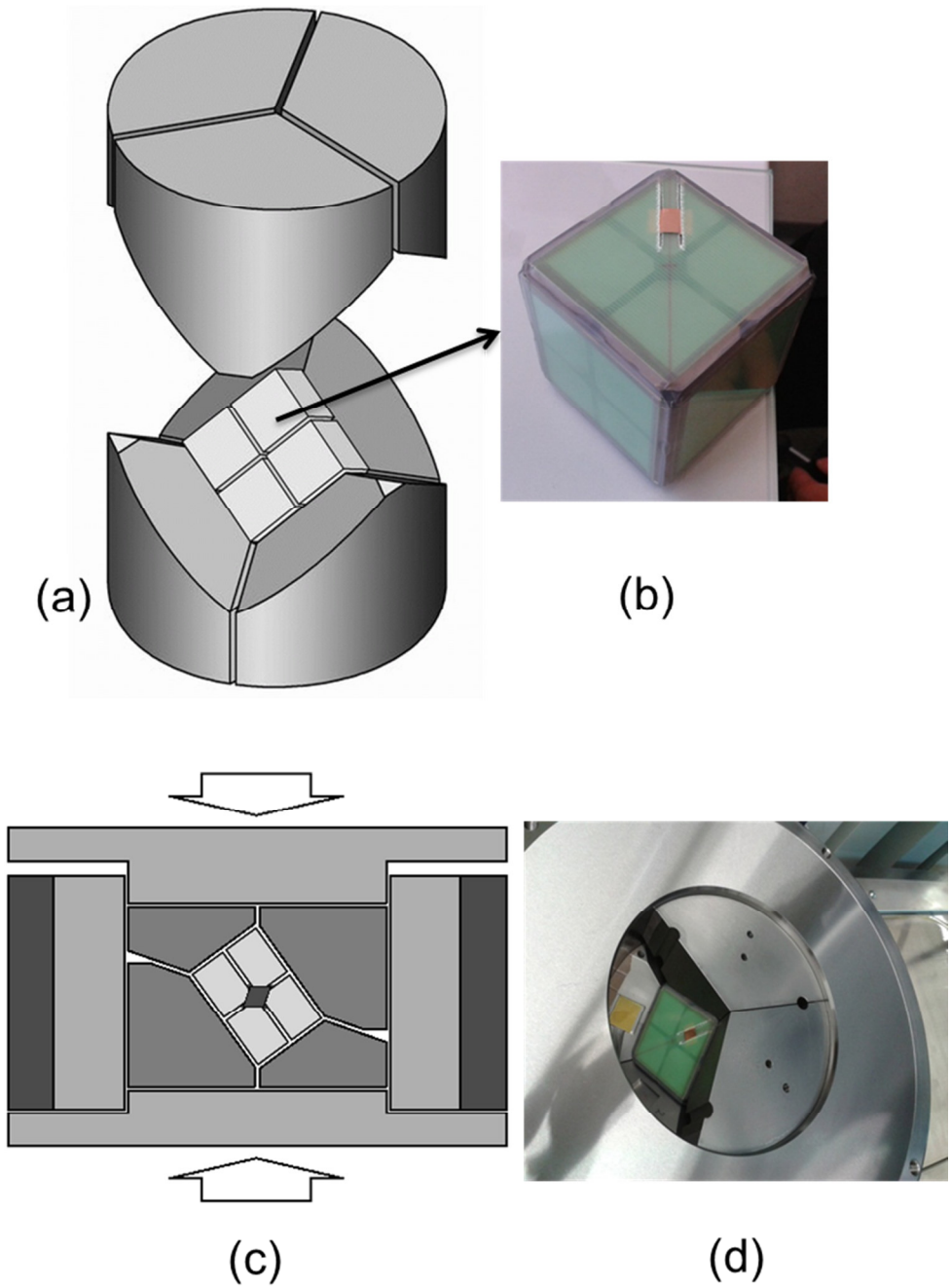

Figure 2-7 . Working principle of the Walker-type module: a) the cubic second compression stage is nested within split-cylinder six-wedge cluster [199]; b) photo of the assembled 2^{nd} stage anvil, copper electrode used to pass current to sample heater via anvil ; c) the module is loaded uniaxially via pressure distribution plates [199]; d) top view photo of the pressure distribution plate

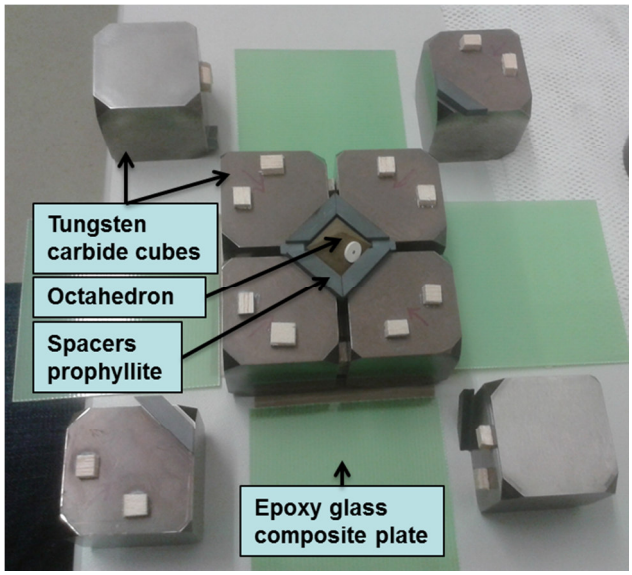

Figure 2-8. Prepared tungsten carbide anvils/cubes for second compression stage of a 6/8 type Walker module. Photograph also shows the octahedron placed between the truncation of anvils, surrounded by prophyllite gaskets.

In the Walker-type module, the maximum pressure which can be achieved is determined by the maximal applied uniaxial load and effective area of anvils-to-pressure medium contact. The capability of a hydraulic press limits the maximum attainable pressure [199]. On the other hand, attainable pressure can be increased (up to the compressive strength of the anvils) by decreasing of truncation area of the anvils (i.e. truncation edge length, TEL) and, correspondingly, of volume of the octahedral pressure medium (characterized by octahedral edge length, OEL) [199-201]. There are several particular sizes of assemblies, described by the OEL/TEL notations (for e.g., 18/11, 14/7, 10/4). For the present high-pressure experiments the 14/7 assembly was chosen. It employs 32 mm edge length WC-Co cubes with TEL of 7 mm and ceramic (MgO) octahedral pressure medium with OEL of 14 mm. In order to heat the sample at high pressures, a resistance furnace was used. An external power supply (DC power) allows to apply a voltage / current to the opposite tungsten carbide cubes which are in contact with the furnace. The resulting electric current sent through the furnace leads to heat emission. In order to prevent short circuit between the anvils, WC-Co cubes faces were additionally insulated from each other by an adhesive Teflon tape and from the Walker module by fiber-glass plastic plates.

The octahedral pressure assembly: As stated above a 6/8 –type multi anvil compresses an octahedral pressure medium, which not only acts as sample chamber, but also includes resistance furnace, a thermal insulation. With little more effort it would be even possible to include thermocouple for temperature control. We have not used the thermocouple during our experiments. Temperature was controlled via the applied DC power according to

calibrated power vs. temperature curve. In following paragraph octahedral assembly details are described. The schematic of the octahedral assembly is given in the **Figure 2-9**.

MgO-octahedron: The octahedron made up of porous MgO ceramic doped with Cr_2O_3 (5 wt.%) having OEL of 14mm was used in multi-anvil experiments. The MgO-based ceramics are usually used as a pressure transmitting medium in multi-anvil apparatuses because magnesium oxide has high melting point and is soft at high-temperatures, thus providing nearly hydrostatic pressure conditions. Cr_2O_3 doping helps to lower the thermal conductivity of octahedron (MgO) which is useful in high temperature experiments (e.g., 1500-2000 °C) and longer holding time (e.g, for 30-60 min) [202].

Furnace: The cylindrical furnace made up of lanthanum chromate ($LaCrO_3$) was used in experiments. It was mounted in the middle of hole drilled in the MgO-octahedron as shown in **Figure 2-9**. Outer and inner diameter of the furnace was 6.0 mm and 4.0 mm respectively. In order to achieve electrical contact, molybdenum disks (diameter 5.9 mm, thickness 0.1 mm) were placed in both ends of the furnace. Then these disk were connected to the molybdenum rod(1.0mm) surrounded by zirconia (ZrO_2) cylinder (outer diameter 6.0 mm, inner diameter 1.0 mm) till the surface of the octahedron. This rod or pin will have direct contact with the WC-Co cubes. Zirconia top cover(s) for the furnace also act as thermal insulator which help to reduce heat loss while in contact with the WC-Co cubes.

Sample encapsulation: Usually the sample is loaded in a noble metal capsule in order to prevent reaction of sample material with the surrounding pressure medium. In the present work pre-compressed pellet (height 1.4 mm and diameter 2.4 mm) made up samples were used in experiments. These pellets were introduced in cylinder made up of platinum foil (thickness 0.05 mm). Two circular disks of same foils were placed in top and bottom of the pellet to avoid direct contact with the surrounding MgO. It is better to load the sample in glove box and seal the capsule in both ends, in order to avoid moisture or to perform experiment with less oxygen contamination. However, at the time of experiment these facilities were not available in DESY (Hamburg Germany) off-line LVP press, we stick to the best possible way of protecting the sample like double layered Pt-foil. Finally the sample capsule of about 1.4 mm in height was placed in the center of the octahedron and was insulated from the $LaCrO_3$ furnace by MgO sleeve. MgO tube (for covering the Pt. foil cylinder) and MgO-rod filled the space at the top and bottom of the sample capsule, respectively.

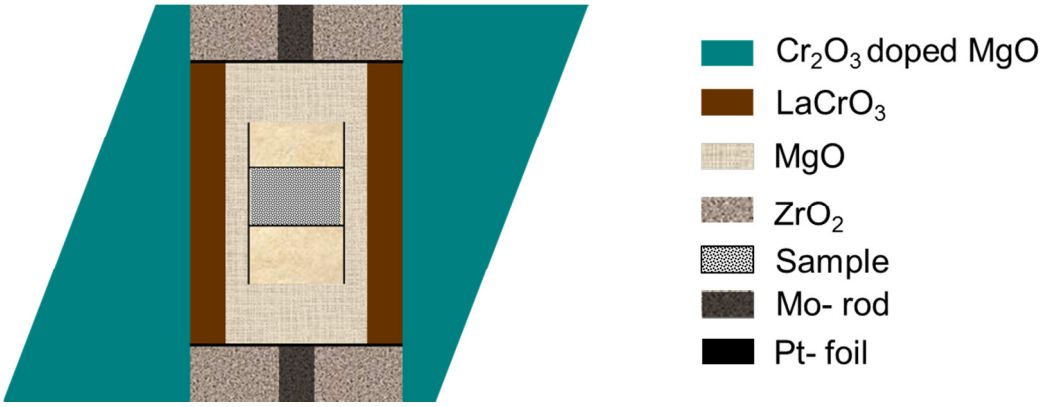

Figure 2-9. Schematic diagram of the octahedron cell used in LVP experiments

Pressure and temperature measurement: The actual pressure applied on the sample in the multi-anvil experiments was determined from the pre-calibrated curve (pressure vs. hydraulic pressure gauge). For 14/7 (OEL/TEL) assembly the sample pressure as a function of the press load was calibrated using known high-pressure phase transitions. The room temperature (RT) calibration is based on the HP phase transitions of Bi and ZnTe. The high-temperature calibration is performed on the known HP-HT phase equilibrium in minerals, for example $CaGeO_3$ (garnet to perovskite), SiO_2 (coesite to stishovite) and Mg_2SiO_4 (forsterite to wadsleyite). Further experimental details on the low- and high-temperature pressure calibration can be found elsewhere in the literature [15, 200, 203]. If sample octahedron is built with thermocouple, it is possible to get actual sample temperature from the thermocouple signal. However in the experiments reported here, our octahedron did not have thermocouple. So the temperature during the experiments have been monitored with the input power (in watt) applied to $LaCrO_3$. Calibration of input power verses the temperature was carried out using the same 14/7 assembly size and octahedral (design) geometry at the corresponding pressure.

HP-HT experimental procedure: The assembled octahedron inside the Walker module was compressed with the uniaxial hydraulic press to the required sample pressure in accordance with a HT pressure-calibration curve. Before that wedge calibration or alignment of the first stage anvils (six) was carried out at the around 50 bar pressure. The required pressure was reached in ~ 2 h. Typical loading parameter are analogous to e Step 1 : 30min- 30 bar , Step 2: 30 min – 100 bar, Step 3: 60 min- 465 bar (according to the calibration curve this was the required oil pressure in bar to reach 15.6 GPa in 14 / 7 mm assembly in that particular press). After reaching the required pressure, the sample was heated at the rate of 50 °C/min to 500 °C, and then raised to 1900 °C in two minutes time. Then the sample was kept at the maximum temperature for about 20 minutes and quenched by switching off the heating electric power. This rapid heating was only possible in DESY offline LVP which is specially equipped with DC heater. After quenching, the load was reduced slowly to zero (in the press)

in order to release the large residual stresses in WC-Co cubes. Normally program is set in such a way that in 8-10 h. oil pressure in press approaches to zero.

Sample recovery: After complete decompression, the WC-Co cubes assembly was removed from the Walker module and opened. The compressed MgO-octahedron was crushed in order to recover the encapsulated sample. Then the MgO- and Pt- capsules were cut by using a diamond wire saw and a hard metal tool, respectively.

2.2.4. Diamond Anvil Cell Experiments

The principle of pressure generation in a diamond anvil cell (DAC) is similar to the Bridgman's opposed anvils. It consists of two opposed diamond anvils with flat-polished tips (culets) between which a sample is quasi-hydrostatically compressed in a pressure transmitting medium (solid, liquid or gaseous) within a gasket hole to get the desired pressure. DAC combined with laser-heating technique, is apparently, the most powerful high-pressure device with respect to generation of high pressures and high temperatures and to employment for in situ studies [189, 204-206]. The schematic diagram of the DAC is given in the Figure 2-10. Due to the exceptional strength of diamond (more than 20 times as much as that of tungsten carbide [207]), a DAC can generate much higher pressures than can be achieved, for example, with WC-Co anvils. Tungsten carbide seats are used to mount the diamonds. The typical diamond culet diameter is between 0.1 and 0.5 mm. However the diameter of the diamond is usually around 3 mm (either surface opposite to the culet or diameter of the conical seat). The conical shape of diamond anvils allows pressure multiplication: the maximum pressure achievable in a DAC increases with reduction in culet area of diamonds. DAC experiments with pressure above 600 GPa (6 Mbar) are being reported [208]. A sample in a DAC is loaded inside a hole drilled in the center of pre-indented thin metal gasket which is then compressed between the anvils. Gasket seals the pressure chamber by friction and provides lateral support to diamond anvils at high pressures. Liquids or gases can also be used as a nearly hydrostatic pressure transmitting medium even if they transform to solid state on compression.

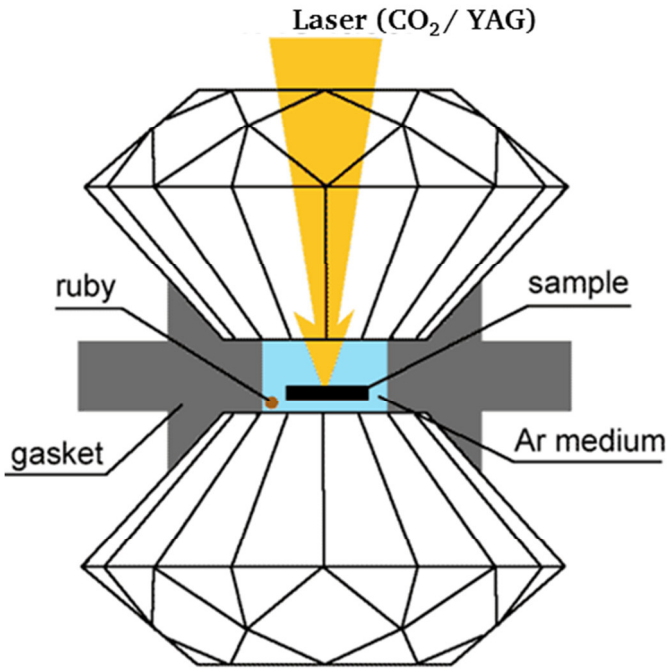

Figure 2-10. The schematic diagram of the diamond anvil cell (DAC) [209].

For heating of samples in a DAC several techniques can be used. The external heating with a resistance heater located around the diamonds is limited to about 1000 K in air and up to 1800 K in vacuum. Beyond this temperature diamond transforms to graphite even in inert atmosphere [190]. The most popular way of heating samples (internally) in a DAC is by optical absorption of infrared laser radiation. In this method intense Nd-YAG or CO_2 laser spot is focused on a sample through the IR-transparent diamond anvil [204-206]. High temperatures up to 7300 K have been reported using this technique [210].

Apart from the extreme high pressure another abundant advantage of a DAC technique is due to the diamond transparency to X-ray radiation, IR and visible light. This allows application of a variety of *in situ* spectroscopic and diffraction methods for examination of samples in a DAC even under extreme pressure. For example the compressibility of the synthesized materials and phase transformation during the laser heating at desired pressure can be measured and monitored in a DAC. Also in the present work some of the *in situ* measurements in DAC in the synchrotron beam-lines were performed. The only significant drawback of a laser-heated DAC (LH-DAC) technique is the extremely small sample size. The typical culet diameter of 0.1-0.5 mm implies that only very small samples ($\sim 10^{-5}$ mm^3) can be loaded in a DAC. Such sample amounts can be characterized only using micro scale techniques. In the following sections actual design of the employed DAC and experimental setups like sample loading, pressure measurement, laser heating and temperature measurement procedures are stated.

Cell design: Boehler-Almax (BOA) DACs [211] supplied by Almax easyLab were used in the underlying experiments. This cell designed by Prof. Reinhard Boehler at the Max Planck

Institute in Mainz, Germany, employs conical diamond anvils and offers easy operation (pressurizing and diamond alignment) and very large conical apertures. Another major advantage of the BOA DAC is the possibility of using gases (like argon, neon) as the pressure medium providing the quasi-hydrostatic environment to the sample.

Gasket preparation: The gasket together with the anvils builds up the pressure chamber for the sample. Different types of material are known to be used as gasket materials. Stainless steel or different alloys have the advantages of being inexpensive and easy to drill. For pressures in Mbar ranges, tungsten and rhenium are used, and they show strong X-ray absorption. Except pre-indentation difficulties (may cause damage to diamond culet edge) rhenium is more stable for high-temperature experiments under high pressure compared to tungsten. For all the DAC experiments performed and reported in this work, rhenium gaskets have been used with a thickness between 350-400 μm. They were polished both sides to get flat and smother surface (mirror like) before fixing into gasket holder by quick fix glue. By closing up the cell, a pre-indentation into the gasket with a thickness of around 30-50 μm was done. The thickness of the gasket indentation has been measured mechanically by using a micrometer. A hole was then drilled with a laser drilling (Nd: YAG laser) machine setup in Institut für Geowissenschaften, Goethe-Universität Frankfurt, Frankfurt am Main, Germany. Normally hole diameter was around 150 μm for the diamond culet size of 400 μm. The quality of the centering is important to ensure the stability of the experimental volume under pressure.

Sample loading: Depending of the sample, mainly two types of loadings were done in the experiments. Firstly, gas loading, the sample having the around 100 μm diameter was introduced in to the middle of the gasket hole with careful observation under optical microscope. The sample was separated from the highly thermal conducting diamond anvil (bottom) either by placing a thin disk ($<$10 μm in thickness) of alkali halide (NaCl or KCl) or using flaky curved sample touching only in one or two points of the anvil. Then the cell was filled with argon or neon gas using the gas loading device setup in Institut für Geowissenschaften, Goethe-Universität Frankfurt, Frankfurt am Main, Germany. Prior to gas loading and closing the cell, a micron sized ruby (used as pressure marker) ball was introduced sample chamber at some distance to the sample. Schematic of sample chamber is given in the Figure 2-11a.

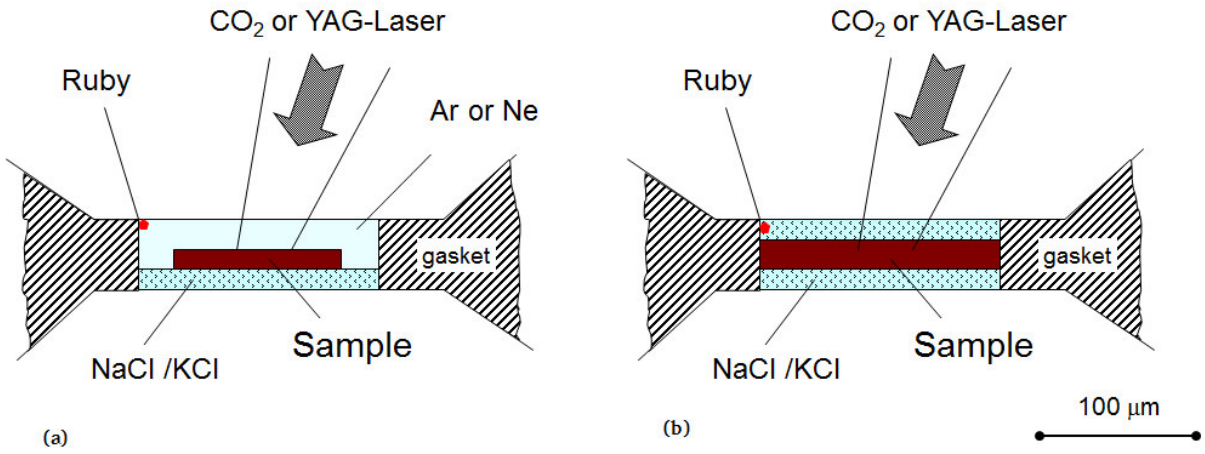

Figure 2-11. The schematic diagram of the sample chamber inside DAC in case of a) gas loading, b) solid loading.

In the case of solid loading the sample is covered with thin disk (<10 μm in thickness) of alkali halide (NaCl or KCl) on both sides. The rest of the volume is filled by the sample. The pellets (of desired thickness) either of the sample or alkali halides were formed by pressing the respective material in-between diamond or hard anvils. Apart from being a solid quasi hydrostatic pressure medium, these alkali halides are also transparent to laser and provide thermal insulation by avoiding the direct contact of the sample with the diamond. The schematic is given in the Figure 2-11b. Advantage of this loading is the higher amount of the sample compared to gas loading; however it also has some disadvantages like being more prone to moisture surrounding by alkali halides. Prior to closing the cell, vacuum drying at 100 °C is followed to avoid possible moisture contamination.

Pressure measurement: The ruby fluorescence scale is the most commonly used pressure gauge for DAC experiments. The R_1 lines of the Cr^{3+} -ions in Al_2O_3 shift linearly by 0.365 nm GPa^{-1} up to 20 GPa with negligible deviations. Above this pressure correction needs to be applied. General equation for the pressure determination from shift of the R_1 lines of fluorescence spectrum is well established [203, 212] and written as below.

$$P = \frac{A}{B}\left[\left(1 + \frac{\Delta\lambda}{\lambda_o}\right)^B - 1\right]$$

Where $\boldsymbol{P}$ is pressure in GPa and $\boldsymbol{\lambda_o}$ (= 694.24) is the wavelength of ruby R_1 line at 1 bar in nm, $\boldsymbol{\Delta\lambda}$ is the change in wavelength of ruby R_1 line in nm (which is measured). Parameter $\boldsymbol{B}$ = 7.665 for quasi-hydrostatic conditions, and $\boldsymbol{B}$ = 5 for non-hydrostatic conditions and **A** = 1904 is a constant. During *in-situ* experiments like in synchrotron beam-line facilities the pressure medium and / or thermal insulation layer like NaCl can be used in pressure measurement. Real pressure can be obtained by knowing the shift or lattice contraction from the i*n-situ* XRD and then fitting into well-established high pressure equation of state[197]. In

those cases ruby loading is not necessary in DAC sample chamber. Ruby pressure scale is reliable up to 1 Mbar (100 GPa), experiments above this pressure range are measured with the Raman shift associated with the diamond edge [208, 213]. However for the lower pressure experiments shift associated to diamond edge cannot be measured precisely.

Sample heating and temperature measurement: Heating of the sample was performed with a CO_2 laser (10.6 μm, 10-250 W, pulsed) at the Institut für Geowissenschaften, Goethe-Universität Frankfurt, Frankfurt am Main, Germany. The spot size of the laser beam could be varied via optical system and the laser power was controlled with pulse width and pulse period. Temperature was estimated by fitting the emission spectrum of the sample to the Plank formula under the assumption for the grey body emission behavior. The Plank formula for ideal black body contains the temperature and the wavelength dependence of the thermal radiation intensity I_{BB} (T, λ) is written as follows [206].

$$I_{BB}(T,\lambda) = \frac{8\pi hc}{\lambda^5(e^{hc/\lambda kT} - 1)}$$

Where h is the Plank constant, k the Boltzmann constant, c the velocity of light in vacuum, T temperature of the black body and λ the wavelength. To get the real body thermal radiation spectrum I_{RB}(T, λ) the factor emissivity is introduced. Emissivity (ε) is simply the ratio of intensities of the real body to the ideal black body at the same λ and T. written as follows.

$$I_{RB}(T,\lambda) = \varepsilon(T,\lambda) I_{BB}(T,\lambda)$$

For the ideal black body emissivity is one. However in real case we assumed gray body then it is less than unity. Wavelength dependence of the emissivity is known for few materials in vacuum or at atmospheric pressure. If we assume that emissivity of investigated material has same wavelength dependence as tungsten the temperature estimation will have accuracy of ±100 K at 3000 K[206].

Sample recovery: After all in situ measurements samples are recovered. Special care is needed not lose the sample while recovery due to their extremely small size. Sample is recovered in ultra-clean glass plate for easy identification. Most of the cases sample is picked up along with the solid pressure medium or thermal insulation like NaCl. It is hard to distinguish between sample and pressure medium or thermal insulation, while picking up in the needle tip. Then the sample was washed in high purity water to remove NaCl or KCl using the micro syringe and the needle tip.

2.3. Characterization Methods

This chapter introduces analytical techniques used in the present work for examination of structure, composition and morphology of the synthesized high-pressure nitrides: powder X-ray diffraction, transmission (TEM) and scanning electron microscopy (SEM), and Raman spectroscopy. TEM section also includes a little more focus on the techniques used in present work like high resolution transmission electron microscopy (HRTEM), scanning transmission electron microscopy (STEM), Advanced diffraction tomography (ADT), Electron energy loss spectroscopy (EELS) and Energy-dispersive X-ray spectroscopy (EDS / EDX) .

2.3.1. Powder X-ray diffraction

X-ray diffraction (XRD) is a powerful non-destructive characterization method for determining a range of physical and chemical characteristics of materials, especially for shedding a light on the crystal structure. This technique is widely used in all fields of science and technology. XRD is based on the constructive interference of X-rays elastically scattered by a regular periodic system of atoms (more precisely, electrons) in a crystalline solid. The Bragg's law describes the basic condition for the constructive interference for wavelength *'λ'* diffracted by atomic planes with spacing *'d'*.

$$n\lambda = 2d\ sin\theta$$

Where n is an integer and θ is the angle between the incident beam and the diffracting atomic planes. In other words, when the path difference between two diffracted rays differs by an integral number of wavelengths, Bragg- conditions or constructive interference occurs. The diffractogram or diffraction pattern is represented by intensity I as a function of diffraction angle 2θ, where diffraction peaks or reflections correspond to the particular d-spacings of the crystal lattice. Here, 2θ is the angle between the incident and the diffracted beam for given monochromatic X-ray (λ=*const.*) beam. This technique is referred to as the angle dispersive X-ray diffraction (AD-XRD). Alternatively, powder X-ray diffraction measurement can be accomplished using polychromatic X-ray radiation at a fixed diffraction angle (2θ = const.). This technique provides the diffracted intensity I as a function of the radiation energy E = hc/λ, (where h is Planck's constant and c is the light speed in vacuum) and is referred to as energy dispersive X-ray diffraction (ED-XRD). In this case condition for the constructive interference of diffracted radiation at the angle 2θ is given by Bragg's law with $\lambda = hc/E$.

In the present work AD-XRD technique was used in most cases for instance employing either in-house diffractometer or synchrotron radiation facility (details are given in following section). However, ED-XRD technique is also uses a synchrotron beam line for *in-situ* cubic multi anvil experiments. For the samples exceeding 1 mm^3 volume, the standard in-house diffractometer at the FG Strukturforschung, FB Material- und Geowissenschaften, TU

Darmstadt, was utilized. For *in-situ* experiments and for small size sample (like in DAC), measurements were performed at different beam-lines at the synchrotron radiation facilities like DESY Hamburg, Germany and ALS Berkeley, USA.

2.3.2. In-house X-ray diffractometer

The precursor materials and some of the HP-HT synthesized materials were measured in transmission mode. All the samples are measured in the Debye-Scherrer geometry using a STOE STADI P diffractometer (Stoe & Cie GmbH) with Mo-Kα_1 radiation (λ = 0.70932 Å). The diffractometer is equipped with a position sensitive detector with 6° aperture and a germanium monochromator in Debye-Scherrer geometry. A NIST-NBS640b Si standard was used for preliminary calibration of sample-to-detector distance. The powdered sample was filled in a glass capillary of 0.3 mm in diameter which was the rotated in order to obtain texture-free powder XRD pattern. The sample height was about 2-2.5 mm. Intensity, I, versus diffraction angle 2θ from 5° to 50° was collected. In the case of very compact HP-HT synthesized samples, a slice of the sample was cut with a diamond wire saw and crushed into powder using a tungsten carbide tool before filling into capillary.

2.3.3. Synchrotron radiation

As mentioned earlier, the main limitation of the HP-HT synthesis experiments in DAC is the small sample volume. In addition to that, the present work deals with low Z- materials like boron, carbon, nitrogen and oxygen. It is highly unlikely to get any reasonable XRD data from our in-house diffractometer. Therefore a high-brilliance X-radiation source was necessary for the XRD study of materials reported in this thesis. The XRD experiments (both *in-situ* and *ex-situ*) were performed at the beam-line P02.2 of the PETRA III storage ring in Deutsches Elektronen-Synchrotron (DESY) Hamburg, Germany and the beam-line 12.2.2 of the Advanced Light Source Berkeley, USA. Both beam-lines are especially dedicated to high pressure experiments particularly for LH-DAC experiments, have special capabilities like on and off axis laser heating (Nd-YAG) in side DAC and *in-situ* and *ex-situ* high pressure XRD measurements.

At the beam-line P02.2 XRD data were collected with PE XRD1621 (PerkinElmer, Inc.) image plate detector using monochromatic synchrotron radiation (wavelength λ = 0.28962 Å, 42.8 keV). The sample-to-detector distance was calibrated using a NIST-SRM674b Cerium oxide (CeO_2). In the beam-line 12.2.2 XRD data were collected with MAR3450 (Rayonix, L.L.C., USA) image plate detector using monochromatic synchrotron radiation (wavelength λ = 0.4959 Å, 25 keV). The detector distortion and sample-to-detector distance was calibrated using a NIST-SRM660a Lanthanum hexa-borate (LaB_6). In order to get texture free diffraction pattern or to avoid preferred orientation, the sample was rotated during the measurement time. The two-dimensional XRD patterns were integrated using Fit2D software [214] in order

to obtain conventional diffractograms, where the diffraction intensity I(2θ) is a function of the diffraction angle 2θ.

Apart from above two synchrotron facilities, XRD measurements were also performed at the beam-line F2.1 at DORIS III, HASYLAB/DESY Hamburg, Germany dedicated to *in-situ* multi anvil experiments (where the MAX80 multi anvil device has been installed). Here ED-XRD was collected using a white beam with a spot size of 0.7 mm in the energy range 2-80 keV and a high purity germanium (Ge) solid state detector fixed at the diffraction angle 2θ = 9.03°. The diffraction angle was calculated from NaCl reflections taken at ambient pressure. In some of the figures, the ED-XRD data were plotted as intensity vs. 2θ (by fixing λ= 0.70931 Å) for the sake of comparison with other XRD data. For all the acquired XRD, phase identification was done with the help of the ICSD database (Inorganic Crystal Structure Database by Fachinformationszentrum (FIZ) Karlsruhe).

2.3.4. Transmission electron microscopy (TEM)

Transmission electron microscopy (TEM) was used to examine the structure and phase content of the synthesized materials. In a transmission electron microscope the electrons are accelerated to high energies (normally 60-400 keV) and focused on a material. Using electron radiation, with a wavelength several magnitudes shorter than those of X-rays (due to very high energies), the theoretical resolution limit drops to a few pico-meter. In modern TEM equipped with C_s correction (spherical aberration), the practical resolution limit is reported to be 0.7-1Å [215]. The basic components of TEM are; a) source, b) condenser lenses (to focus the electron beam on the sample), c) sample (to be investigated), d) objective lenses (to form image or diffraction pattern (DP)), e) intermediate and projector lenses (magnification system) and detectors, e.g. CCD camera, EDX, EELS, etc.

The two basic TEM modes are imaging and diffraction mode. In imaging mode the intermediate lens is focused onto the back image plane of the objective lens. Then the image is projected onto viewing screen or CCD. In diffraction mode the intermediate lens is focused onto the back focal plane of the objective lens. Then the diffraction pattern is projected onto viewing screen or CCD. A diffraction pattern can either be acquired by taking the selected area-aperture using a parallel beam (this is called selected area electron diffraction (SAED)) or by converging the beam at the specimen (this is called convergent beam electron diffraction (CBED). SAED and CBED are formed due to crystals satisfying the Bragg condition (elastic scattering). Both the techniques are widely used in TEM, for example assigning the d-values, deriving the lattice parameter, to find out crystal symmetry etc. One can easily distinguish nano-crystalline, polycrystalline and single crystal sample just by looking at the electron diffraction pattern.

Typically SAED pattern comprise a bright central spot containing transmitted un-scattered electrons and scattered electron (spots or rings), the distribution of which depend

on the nature of the sample (for example single crystals have spots, polycrystalline samples have rings of spot and amorphous samples have diffuse circles). Thus, SAED is a useful technique, which allows selection of a specific area of the sample (e.g., single grain / crystal). If the selected area is chosen aptly, a SAED pattern can even be obtained from a nano-crystal (c.f. BON electron diffraction).

Image formation in TEM can be explained by different contrast mechanisms and its combinations. Bright-field (BF), Dark-field (DF) and centered dark-field (CDF) are the basic imaging modes used in TEM. The schematic or ray diagram of BF, DF and CDF imaging are shown in Figure 2-12 [215]. A BF image is formed by selecting the transmitted beam, where the crystalline samples in the Bragg condition appear as dark. Amorphous and crystalline samples not in Bragg condition appear as bright in a BF image. A DF is formed by selecting the diffracted beam, where the crystalline parts in the Bragg condition appear bright. Image formation mechanism in TEM could also be explained by an amplitude contrast, mass-thickness contrast, Z-contrast and their combinations. Explanation of each mechanism and its application is excluded here.

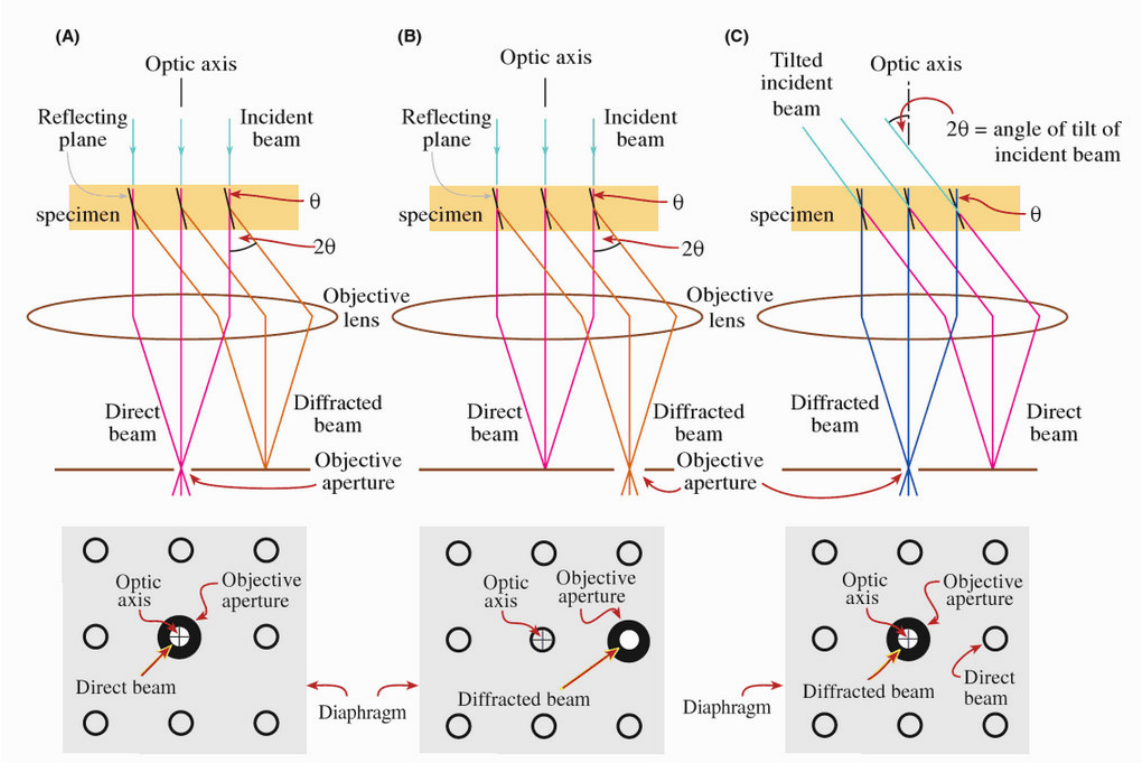

Figure 2-12. The ray diagram or schematic of (A) a BF formed form the transmitted beam (B) a DF formed with specific off axis scattered beam and (C) a CDF image where incident beam is titled so that scattered beam emerges on the optic axis. Reprinted with permission from [215].

2.3.4.1 TEM specimen preparation

In TEM, specimen preparation plays a major role in determining the yield and sample quality. TEM samples need to be electron transparent (less than 150 nm) for performing a TEM analysis. Especially in cases like HRTEM and EELS specimen thicknesses < 50 nm are essential. There are many different techniques available for specimen preparation that can be found e.g. in reference [215]. Below, details about the specimen preparation methods applied in the present work are discussed. HP-HT synthesis techniques produce a very small amount of materials. It is great challenge to prepare these specimens for TEM analysis. TEM sample preparation (less than 100 nm thickness) and final transfer to the TEM grid (sample holder) which happens to be a tedious procedure and needs a special expertise. In addition to this, the materials studied in the present work are belong to a family of super-hard materials like c-BN or diamond.

The DAC synthesized samples are typically of size 70 μm x 70 μm x 30 μm and therefore an optical light microscope is needed to handle them. The recovered sample mounted on a glass plate is carefully crushed by using a hard needle (tungsten carbide) under optical microscope. Much attention should be paid not to lose the sample during crushing. Very fine particles are picked by a special needle and are spread over the TEM grid. In this process there are a lot of uncertainties in size and distribution of the single particles on the TEM grid. However, this can only be realized if the sample is put into the TEM for measurement.

In case of the multi anvil experiment, the sample size is quite large (diameter 2 mm, height 1.2 mm) compared to DAC. Difficulties arise due to the super-hardness of the synthesized materials. Micron size flakes are grinded in an agate mortar with an ultra-pure solvent like methanol until they are invisible in a light microscope. Afterwards this mixture is transferred to a beaker placed in an ultrasonic bath to disperse the particles for 20-30 min. Soon afterwards a few drops of this mixture are put onto a TEM grid by using a pipette. This method is much better than hand picking by needle and placing on a TEM grid. However, the main problem was SiO_2 contamination, coming from agate mortar. As the synthesized materials are super hard in nature, they chip away softer materials during grinding. We have also tried to prepare samples using Utramicrotomy [215] method by embedding in epoxy. However, the epoxy resin slice came along with sample while transferring it to the TEM grid. This was getting damaged under the electron beam and ruined the image quality. Out of these different methods, specimen preparation by crushing and grinding the samples between tungsten anvils seemed to have worked better. Crushing was performed in the presence of little drops liquid on top of the anvil to prevent the sample spill. Then it was transferred to a beaker, containing methanol placed in a ultrasonic bath, for 20-30 min. As in the case of mortar crushing method, here also right after sonification few drops of this mixture were put on the TEM grid using a pipette. However, uncertainties in size and distribution of the single

particles on TEM grid still remains, this can only be realized if the sample is put into the TEM for measurement.

2.3.4.2 High Resolution TEM and Energy-dispersive X-ray spectroscopy

High resolution TEM (HRTEM) is one of the imaging modes of the TEM, where it allows direct imaging of the atomic structure like atomic columns or lattice planes of the sample. This technique uses both scattered as well as transmitted beam for image formation. HRTEM is often referred as phase contrast imaging in TEM, where contrast arises due to the differences in the phase of electron waves propagating through a thin specimen. This contrast mechanism is difficult to interpret, as it is sensitive to several factors. The appearance of the image contrast varies with small changes in the sample thickness, the sample orientation, the atomic scattering factors of the specimen, the defocus and further aberrations. With a very thin sample resolution on the sub atomic scale is possible in aberration corrected TEMs. In the present work, HRTEM images were used to study the possible atomic structure of the samples.

During the TEM measurements, the electron beam interacts with the sample and produces secondary signals (X-rays, secondary electrons and visible light etc.) and inelastically scatters electrons in addition to elastically scattered electrons [215]. The most important secondary signal generated in the sample are X-rays (both characteristic and Bremsstrahlung). These signals are collected, based on the energy of the generated X-rays local elemental composition can be identified. This technique is called energy-dispersive X-ray (EDX) spectroscopy. Most of the TEM setups are equipped an EDX detector consisting of a Si or a Ge crystal. Precise quantification of the elemental composition is possible in EDX for higher Z-elements (Z >11). However, it is challenging to perform reliable qualitative measurements for lower Z- elements like B, C, N and O. In this thesis EDX has been widely used to identify the right sample area while acquiring TEM images and diffraction pattern.

In the present work, high-resolution phase contrast imaging and energy-dispersive X-ray spectroscopy (EDX) were carried out using a Jeol JEM 2100F field emission transmission electron microscope equipped with an Oxford X-max EDX detector. High-resolution phase contrast image simulation was carried out using a multislice implementation in the Java version 4.2231U2014 of the EMS code [216]. The microscope parameters listed in Table 2-1 were used for the simulation. Higher order aberrations as well as drift, vibrations, and the influence of the CCD camera modulation transfer function (MTF) were neglected. For the simulation it was assumed that the experimental images were acquired close to a Scherzer condition.

Table 2-1. The microscope parameters used for the HRTEM simulation

Parameter	**Value**
Acceleration voltage	200 kV
3rd order spherical aberration constant	1.0 mm
Chromatic aberration constant	1.4 mm
Scherzer focus	61.33 nm
Energy-spread	0.8 eV
High voltage stability	2 ppm
Objective lens current stability	1 ppm

2.3.4.3 Scanning transmission electron microscopy (STEM)

STEM is distinguished from conventional TEM by focusing the electron beam into a small spot which is scanned over the sample in a raster. In this sense, a STEM is very similar to a scanning electron microscope (SEM). Being in a STEM mode if we stop the beam from scanning, then one can have CEBD pattern on the viewing screen. In STEM having both BF and DF imaging techniques are possible using annular detector. STEM BF imaging is helpful in thicker sample compared to TEM mode because of using the direct transmitted beam. However resolution is limited as it includes diffracted electrons. The great advantage of STEM comes with the high angle annular dark-field (HAADF) imaging. With this technique, high resolution is possible without the undesirable diffraction contrast, which can mask important structural information. The probe diameter is the primary factor that determines the resolution of the dark-field. Because of the convergent beam STEM provides more reliable signals in EELS and EDX. These techniques are explained in following. In the present work the STEM mode is used to image thick sample areas and EDX data because of the better signal.to noise ratio.

2.3.4.4 Electron energy-loss spectroscopy (EELS)

As stated in EDX section, out of the many different interactions of the electron beam with the sample, inelastic scattering is also a very important one. This would cause electron to lose their energy and deflect from the normal path. The amount of energy-loss can be measured in an electron spectrometer and be interpreted. This technique is called electron energy-loss spectroscopy (EELS). These inelastic scattering events may be due to phonon excitations, inter and intra band transitions, plasmon excitations, inner shell ionizations etc. So this spectrum provides very useful information about the chemistry and electronic structure (valance state, band gap etc.) of the sample in addition to the elemental composition. Compared to EDX,

EELS has advantage that detection and quantification of low Z elements and better spatial resolution are possible. The EELS spectrum can be split into the low-loss region (0-50 eV) and the high-loss (>50 eV). Normally, the low-loss region contains electronic information from weakly bound conduction and valance bond electrons, while the high-loss region contains primarily elemental information from the tight bound or core shell electrons and details of bonding and atomic arrangement in the crystal [215]. In the present work we acquired the EELS spectra of samples mostly in the high-loss region for quantifying the elemental composition and for confirming the EDX findings as well as to study the possible bonding status e.g., B, C, N, and O.

In the present work, an aberration-corrected JEOL JEM ARM-200 (scanning) transmission electron microscope was used for EELS experiments. The microscope was operated at 200 kV. It is equipped with a "Schottky" field-emission gun (FEG) and a Gatan Enfina EELS spectrometer. The energy-resolution in EELS was < 1 eV, as measured from the full-width half maximum of the zero-loss peak. The electron probe size was ~1 nm. EELS spectra were recorded with a dispersion of 0.1 eV/channel, which allowed to simultaneously acquire the B-K, N-K and O-K ionization edges. A power law function and the Hartree-Slater model were used to subtract the background and to quantify the composition. The integration widths for the quantification were 187.1-247.9 eV for the B-K edge, 400-455.6 eV for the N-K edge and 531.6-592.3 eV for the O-K edge.

2.3.4.5 Automated Diffraction Tomography (ADT)

Automated diffraction tomography (ADT) is a TEM diffraction method, where series of diffraction pattern are acquired to determine the crystal structure of the sample. The ADT technique is developed by Ute Kolb's group and extensively used for structure determination [217, 218]. This technique provides the best solution for the classical problems concerned with electron diffraction like the dynamical effect and the data incompleteness. ADT uses the precession electron diffraction (PED) method to collect diffraction patterns. In PED, the electron beam is deflected before it interacts with sample and precessed around the optical axis at high speed. This guarantees less dynamical effects and more complete data which can be directly used for structural refinement by assuming the kinematic approximation. The ADT strategy is based on evaluation of electron diffraction patterns acquired around an arbitrary tilt axis (not correspond to a specific crystallographic orientation).The DP's are and collected in sequential steps of 1 ° within the full tilt range of the microscope (Figure 2-13). All collected diffraction pattern need to be transformed into the three-dimensional reciprocal volume by using a dedicated software package called ADT3D. Then SIR 2011 a 'direct method' program is used for 'solving' the crystal structure (it can be used with X-ray data as well).

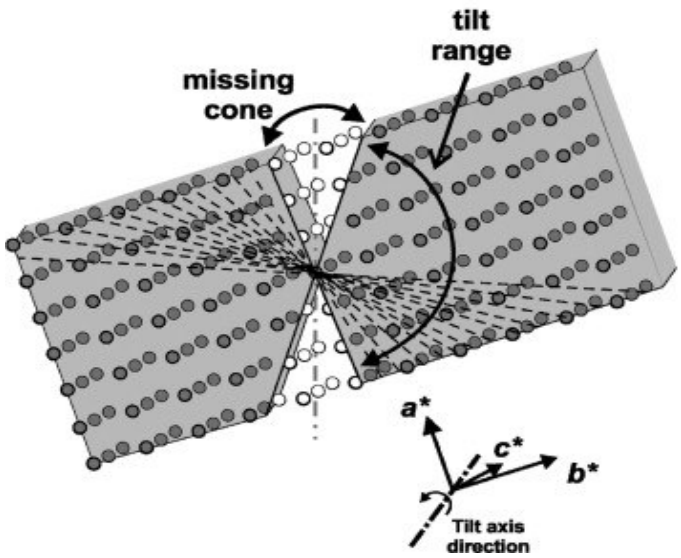

Figure 2-13. Schematic of ADT tomographic acquisition. Reprinted with permission from [219]

In the present work, ADT measurements were carried out with the semi-automatic routine described in [218], using a FEI TECNAI F30 S-TWIN transmission electron microscope equipped with a field emission gun and operated at 300 kV. A condenser aperture of 10 μm and mild illumination setting were used in order to produce a semi-parallel beam of 50 nm in diameter on the sample. Sequential nano electron diffraction (NED) patterns were acquired in steps of 1° with two GATAN CCD cameras: a 794MSC 1024×1024 pixels and a ULTRASCAN 4096x4096 pixels. Scanning transmission electron microscopy (STEM) images for crystal position tracking were collected by a FISCHIONE high angular annular dark field (HAADF) detector. High tilt acquisitions up to ±60° were performed with a FISCHIONE tomography holder. ADT data were collected with a precessing beam in order to improve reflection intensity quality [220, 221]. Beam precession was performed using the Spinning-Star unit of the Nano-MEGAS Company. The precession angle was kept at 1.2°. The ADT3D software package was used for three-dimensional electron diffraction data processing [217, 218, 221, 222], including three-dimensional diffraction volume reconstruction and visualization, cell vector determination and reflection intensity integration

2.3.5. Scanning Electron Microscopy (SEM)

The SEM produces images by detecting low-energy secondary electrons which are emitted from the surface (10- 100 nm) of the sample due to excitation by the primary high-energy electron beam. Investigation of the morphology of the sample surface was performed using a high resolution scanning electron microscope (XL30 FEG, PHILIPS) with the acceleration voltage of 10 to 25 kV. Semi-quantitative elemental analysis is also possible using energy dispersive X-ray (EDX) module (CDU, EDAX Inc.) via detection of the characteristic X-rays excited by the incident electron beam. In the present work, EDX is used only for qualitative

identification of crystals or to identify impurities. As this thesis deals with low- Z elements like B, C, N and O, it is hard to quantify these elements in SEM-EDX. For SEM examination, in some cases the sample surface was sputtered with carbon or gold layer in order to avoid charging effects on the sample surface due to non-conducting nature of sample.

2.3.6. Raman Spectroscopy

Raman spectroscopy is one of the extremely powerful techniques for material characterization. Apart from being capable of measuring both solids and liquid sample, Raman spectroscopy is bereft of the need for arduous sample preparation and vacuuming, over the other spectroscopic techniques. This spectroscopy technique is based on the Raman Effect [223], named after Sir C. V. Raman who discovered the inelastic scattering of light by material based on its characteristic property. When light interacts with the matter, most of the photons are scattered elastically (Rayleigh's scattering), however the incident photon can create or destroy phonon and gain or lose energy, respectively. The light scattered with lower energy (longer wavelength) is called Stokes scattering, while that with higher energy (shorter wavelength) – anti-Stokes scattering. The change in energy of the scattered light is equal to the energy of the phonon and is referred to as Raman shift. The Raman shift depends on the energy spacing of the molecules' modes. However not all modes are "Raman active" i.e. not all appear in Raman spectra. For a mode to be Raman active it must involve a change in the polarisability. Intensities of Raman peaks depend on the wavelength of the incident light and/or on its polarization. For a particular lattice vibration Raman shift is independent of the wavelength of the exciting radiation. Hence, Raman spectrum is a characteristic property of the material which can be used for identification of known phases as well as can provide information about certain bonding states (e.g., sp^2 / sp^3 in carbon) in the investigated material. The Raman spectra contain measured intensity of the scattered light versus Raman shift given in wavenumbers [cm^{-1}] (relative to the laser wavelength). In the present work Raman spectra were collected with a continuous wave Ar-ion laser (wavelength λ = 514.5 nm, Stabilite 2017, Spectra Physics) using a micro-Raman spectrometer (HORIBA HR800).

2.3.7. Elemental Analysis

The carbon (C), nitrogen and oxygen (N & O) content in BC_2N and BC_4N precursors were determined by combustion analysis using LECO C-200 and LECO TC-436 (LECO Corporation), respectively. For the carbon analysis, a weighed sample is melted in a ceramic crucible in a stream of oxygen. Carbon released from the melted sample combines with the oxygen to form CO_2 and CO. The CO is converted by a catalyst to CO_2. From the amount of CO_2 carbon in the sample is quantitatively analyzed by infrared absorption technique. Similarly, for N and O

analysis, powdered samples are burnt in a graphite crucible under helium atmosphere. Oxygen in the samples reacted with carbon forming carbon monoxide which was oxidized to CO_2 using CuO catalyst. The CO_2 is then quantitatively analyzed by infrared absorption technique. Thermally released molecular nitrogen was measured by thermal conductivity method. These methods are in line with ASTM E 1019 and ASTM E 1941 standards. NIST specified standard materials with known C, N and O contents are used as the reference during calibration.

2.3.8. Electrochemical Characterization

Lithium-ion (Li-ion) batteries are one of the most important energy storage devices in the market. A typical Li-ion battery is usually composed of one or more cells. Each cell contains a negative electrode (anode), a positive electrode (cathode) and an electrolyte. Each electrode contains an active material; which is the host material for lithium ions. On the negative electrode, the active material is usually graphite. On the positive electrode (cathode), the active material is normally a transition metal oxide, such as $LiCoO_2$ or $LiMn_2O_4$, together with carbon black, to enhance the electronic conduction. The electrolyte is usually a lithium salt dissolved in organic, water-free liquid solvents absorbed in a porous plastic separator. The working principle of a lithium-ion battery [224] is shown below (Figure 2-14). In the present work B-C-N materials (BC_2N and BC_4N) are studied as anode materials.

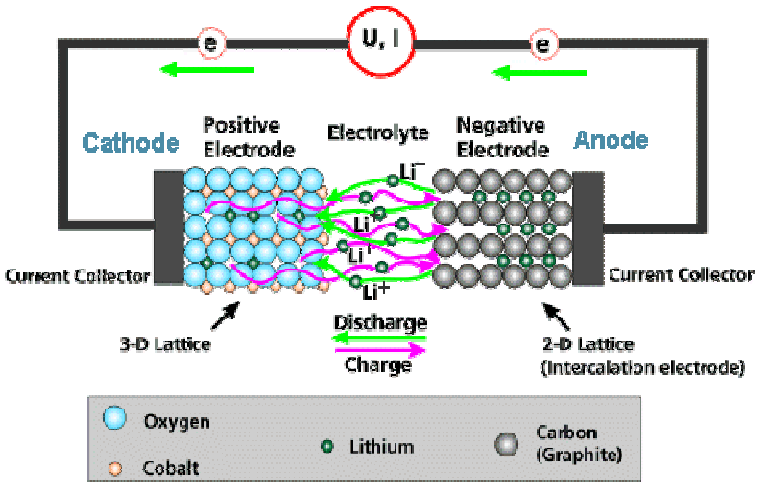

Figure 2-14. The working principle of a Li ion battery. Reprinted with permission from [224].

Electrochemical characterization is carried out using a Swagelok® type cell assembly with lithium metal as the counter/reference electrode (99.9% purity, 0.75 mm thick, Alfa Aesar, Germany) and 1M $LiPF_6$ in ethylene carbonate and diethyl carbonate mixture of volume ratio 1:1 (LP 30, Merck KGaA, Germany) as the electrolyte. A Whatman™ quartz

microfiber filter (QMA, UK) separator is used between the electrodes. The schematic diagram of the cell assembly is shown below (Figure 2-15). BCN samples (precursors) are air sensitive and the electrode coating is made inside an argon filled glove box (MBraun) to prevent oxygen attack. The working electrode is made of 85wt% of BCN +10wt% polyvinylidenefluoride (PVDF, SOLEF, Germany) + 5wt% Carbon Black Super P® (Timcal Ltd., Switzerland) black. N-methyl pyrolidone (NMP, BASF, Germany) is used as the solvent and the slurry is then used to coat on an ultrathin copper foil (10 μm, Copper SE-Cu58, Schlenk Metall-folien Gmbh & Co KG) using a hand blade. The coating is allowed to dry overnight inside the glovebox and electrodes of size 6 mm are cut from the coating. The obtained electrodes are weighed to find out the active mass of the BCN material and then dried under vacuum at 80 °C for 24 hrs using a Buchi oven prior to cell assembly. The electrodes are then transformed again into the argon filled glovebox (MBraun) for cell assembly.

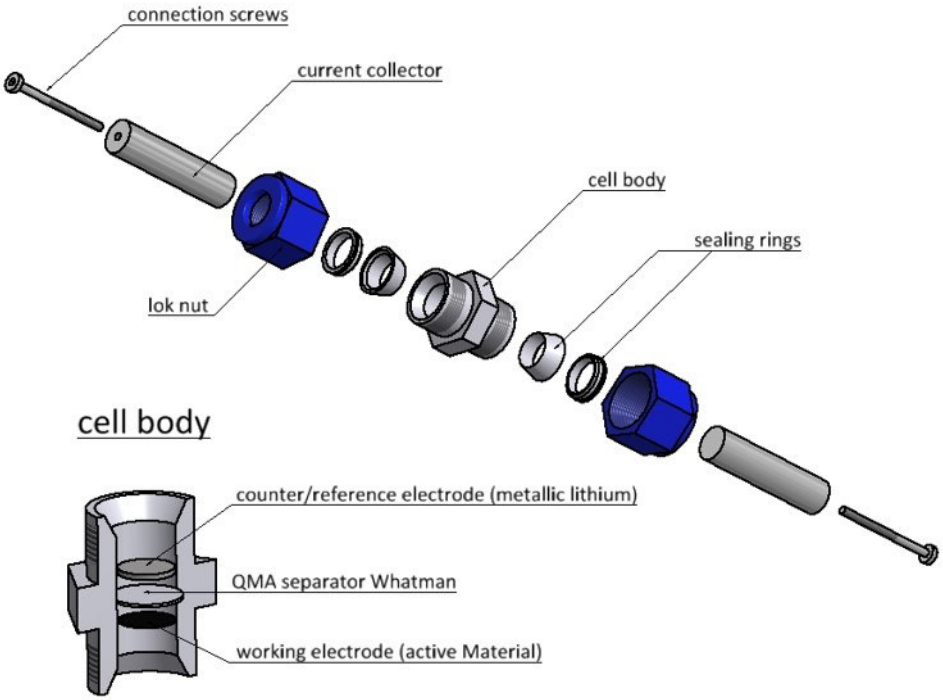

Figure 2-15. The schematic diagram of the Swagelok® type cell assembly [225].

The assembled cells are subjected to galvanostatic charging/discharging studies within a potential window of 0.005-3 V with different current densities using a VMP multipotentiostat (BioLogic Science instruments). The current densities are increased step by step after specified number of cycles and from a faster charging rate of C-rate to 10 C rate. The GCPL (Galvanostatic Cycling with Potential Limitation) cycling rates used are C/20*2 +

C/10*5 + C/5*5 + C/2*20 + C*50 + 2C*50 +C/20*2. Each discharging (D) is performed using the corresponding charging (C) rate (C=D=18 mA g^{-1}). The cells are subjected to initial charging rate after whole cycling to check the reproducibility of the system.

3. Results and discussion

The present section provides results and discussions for all the performed experiments. Chapter 3.1 describes the characterization of the synthesized BCN and BON compounds; chapter 3.2 explains the results of the high-pressure, high-temperature experiments performed on both the BCN and BON systems. Electrochemical performances of the BCN compounds are given in the chapter 3.3. Finally chapter 4 summarizes all the findings in the current thesis with an outlook.

3.1. Analysis of the synthesized BCN and BON compounds

3.1.1. Elemental Analysis of BCN

Elemental analysis measurements were performed by hot gas extraction method as explained in chapter 2.3 (section 2.3.7). Bulk elemental analyses results of C, N and O contents of precursors are given in Table 1-1. Each sample is analyzed by taking five random specimens. All the samples are prepared in glove box for the elemental analysis. So, oxygen pickup during the elemental analysis can be considered as negligible. The results show low standard deviation indicating the homogeneity of the samples. The C to N ratio of precursors (1.85 and 3.97), confirm the empirical formulas of BC_2N and BC_4N. The minor amount of oxygen of 2.4 and 1 wt% observed in BC_2N and BC_4N, respectively, is due to the surface absorption. These precursors are used in the HP-HT experiments. It is worth to mentioning that earlier attempts made by Wallace et. al. [226, 227] to reproduce Riedel and Bill method especially in BC_2N synthesis yielded around 5% oxygen content in the final product. In order to reduce the oxygen content and get the desirable C to N ratio, additional nitridation of pyrolyzed precursor at 1800 °C for 2 h prior to the HP-HT experiments is conducted.

Table 3-1. Bulk elemental analyses results of the BCN precursors.

C [wt %]	**N** [wt %]	**O** [wt %]	Empirical Formula
45.7±0.9	29.17±1.8	2.41±0.2	$BC_{1.85}N_{1.01}O_{0.08}$ ~ **BC_2N**
65.5±1.3	18.32±1.7	0.95±0.25	$BC_{3.97}N_{0.95}O_{0.04}$ ~ **BC_4N**

Even though these precursors are stored in the glove box, during preparation (for example, loading into diamond anvil cell) of samples for HT- HT experiments, samples are exposed to air. In order to check the oxygen contamination due to air exposure during handling, we have also measured the C, N and O content after 1 h and many days of exposure. When these

precursors were exposed to ambient atmosphere, considerable increase in oxygen contamination was observed. As per measured data, 1hr exposure in air leads to 16±2 wt. % oxygen in the BC_2N precursor without major changes in the C and N contents. The same samples, after long term (many days) exposure to air were found to have 26±2 wt. % of oxygen with considerable changes in the C to N contents.

3.1.2. X-ray diffraction analysis of BCN

XRD analyses were carried using an in-house diffractometer in reflection geometry. XRD patterns of the precursors are shown in Figure 3-1. Both the BC_2N and BC_4N precursors indicate an amorphous nature. However 3 broad reflections can be seen in the pattern. These perceived reflections (marked with *) can be due to the turbostratic nature of the BCN coming from the (002) and (10) reflections similar to h-BN and graphite [71, 72, 227]. These observations are consistent with the Riedel and Bill method [71, 146] and the other attempts. XRD measurements were performed in air as well as in a sealed capillary, however there was no change in the XRD reflections while measuring in air. This implies that even though we observe oxygen uptake during the air exposure, this is not leading to any changes in the diffraction pattern.

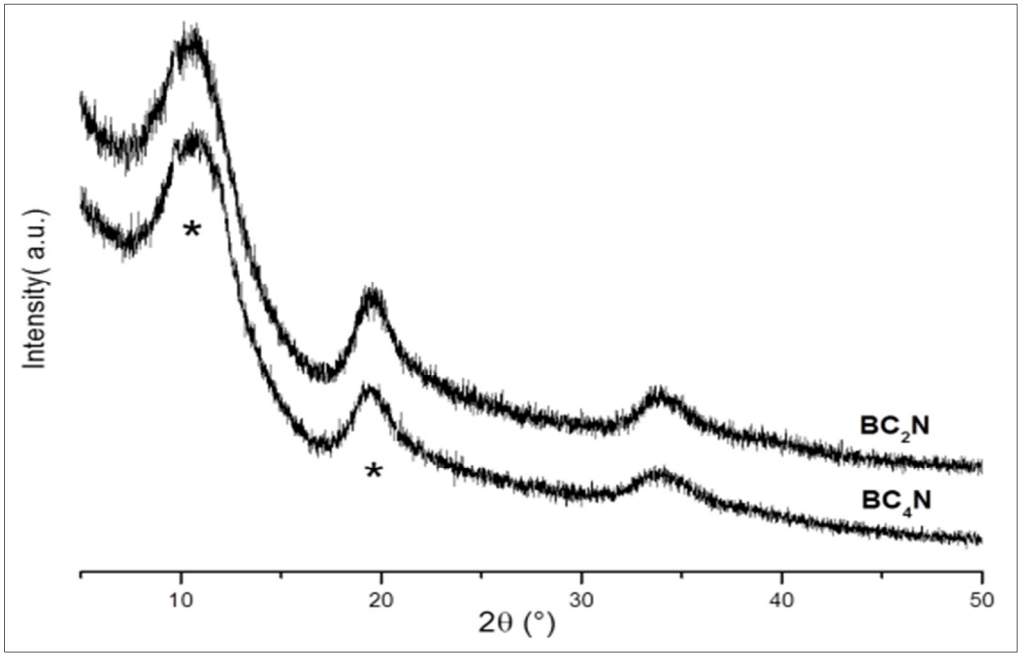

Figure 3-1. XRD patterns of precursors (Mo $K\alpha_1$ λ = 0.70319 Å).

3.1.3. X-ray photoelectron spectroscopy analysis of BCN

X-ray photoelectron spectroscopy (XPS) investigations were carried out in PHI-VersaProbe-II using monochromatic Al-K (1486.6 eV) radiation as a photoelectron excitation source. Here measured photoelectron energies of precursors are listed in Table 3-2 with B1s, C1s and N1s energies (in eV) assigned to particular type of bonding. XPS results confirm the presence of C-C, C-N, N-C, N-B, B-N and B-N-C [124, 228] bonds as well as indicating the presence of C-O or C=O bonds in BC_2N due to surface absorbed oxygen (2.4%), which was also revealed by elemental analysis. Estimation of the intensity ratios of different bonding energies indicates high amount of C-C and B-N type bonding; however, the presence of noticeable amount of N-C, C-N [229] and B-N-C [124] bonds is also clear. In contrast, the B-C bonds were not observed in either precursor.

Table 3-2. XPS peak analysis results of precursors

	BC_2N	BC_4N
C 1s	Position (eV)	Position (eV)
C-C	284.6	284.7
C-N	285.9	286.1
C-O/C=O	287.1	-
N 1s		
N-B	398.4	398.3
N-C	399.6	399.7
B 1s		
B-N-C	192.2	191.9
B-N	190.9	190.5

3.1.4. Raman spectroscopy analysis of BCN

Micro-Raman spectra were recorded using an in-house confocal micro-Raman spectrometer Horiba HR 800 with an Ar laser at a wavelength of 488 nm. Raman studies were performed to find the nature of carbon clusters in BCN compounds. The Raman spectrum of crystalline graphite has only one Raman peak at 1580 cm^{-1}, which is called the *G* band [230, 231]. However samples with some structural disorders (like impurities, edges, finite size effects etc.) an additional feature can be observed at 1350 cm^{-1}, which is usually called the *D* band [230, 232]. Hence the *D* and *G* band reveals the disorder and graphitic nature of the materials respectively. It is well known that, the ratio of the *D* and *G* band intensities (I_D/I_G) is inversely proportional to the in-plane crystallite sizes (L_a), one can calculate L_a using different proposed equations[231, 233]. These *D* and *G* bands along with the L_a values are often used in the

literature to describe the nature of carbon in polymer derived ceramics [185, 234-237]. However it is important to mention that, L_a values calculated for the amorphous compounds cannot be correlated to the crystallite size calculated by XRD or TEM analysis. Therefore L_a values deduced from amorphous compounds are described as lateral cluster size [237] (not to be misinterpreted as crystallite size).

Raman spectra for both amorphous BC_2N and BC_4N compounds are given in Figure 3-2 and Figure 3-3 respectively. The presence of D and G band in the Raman spectra of amorphous BCNs reveals that, these compounds have both graphitic as well as disordered nature. These findings are also consistent with the earlier report on amorphous BC_2N [227]. One can easily notice that, G band contribution is more prominent in amorphous BC_4N compounds. To clarify, integral (area) intensity analysis of the D-band, I_D and G-band, I_G were carried out by fitting Breit-Wigner-Fano (BWF) function. The lateral cluster size (L_a) values were calculated by using the following equation proposed by Cancado et al. with laser wavelength $\lambda = 488$ nm

$$L_a(nm) = (2.4 \times 10^{-10}) \times \lambda^4 \times \left(\frac{I_D}{I_G}\right)^{-1} \text{..... (1)}$$

The L_a values for amorphous BC_2N and BC_4N compounds are found to be around 7.43 and 10.3 nm respectively. These results also confirm that amorphous BC_4N compounds are more graphitic (ordered) in nature compared to amorphous BC_2N compounds.

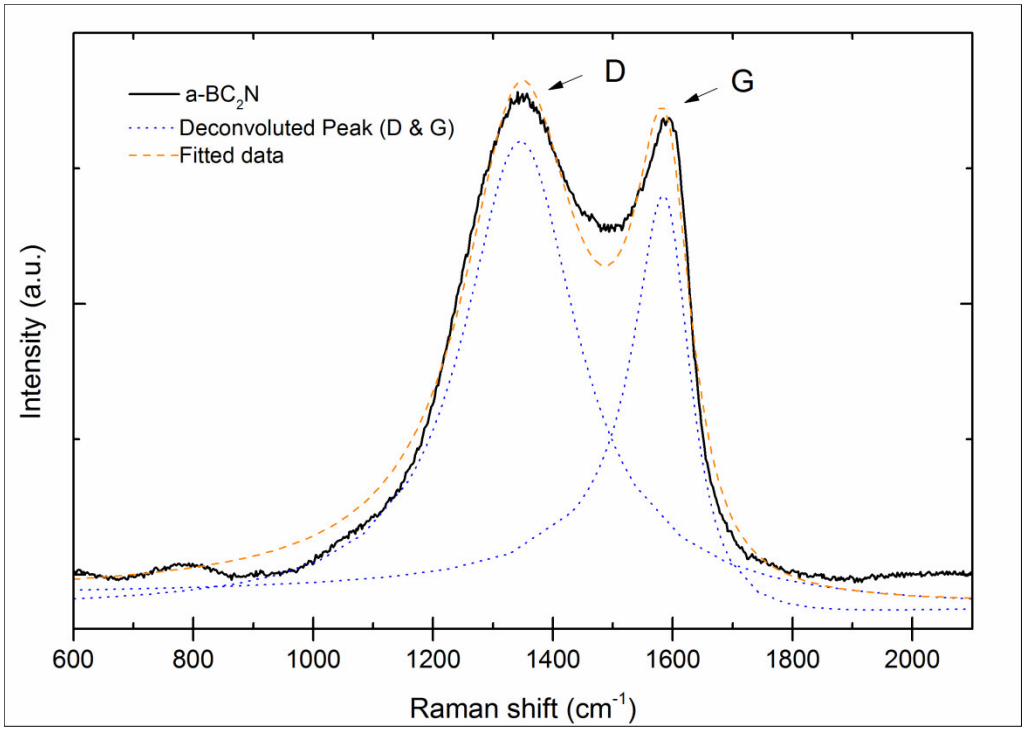

Figure 3-2. Raman spectra of amorphous BC_2N acquired using Ar laser (blue) 488 nm. Black line- acquired spectrum, blue dotted line – deconvoluted peak (D & G band), orange dashed line- fitted curve using Breit-Wigner-Fano(BWF) function.

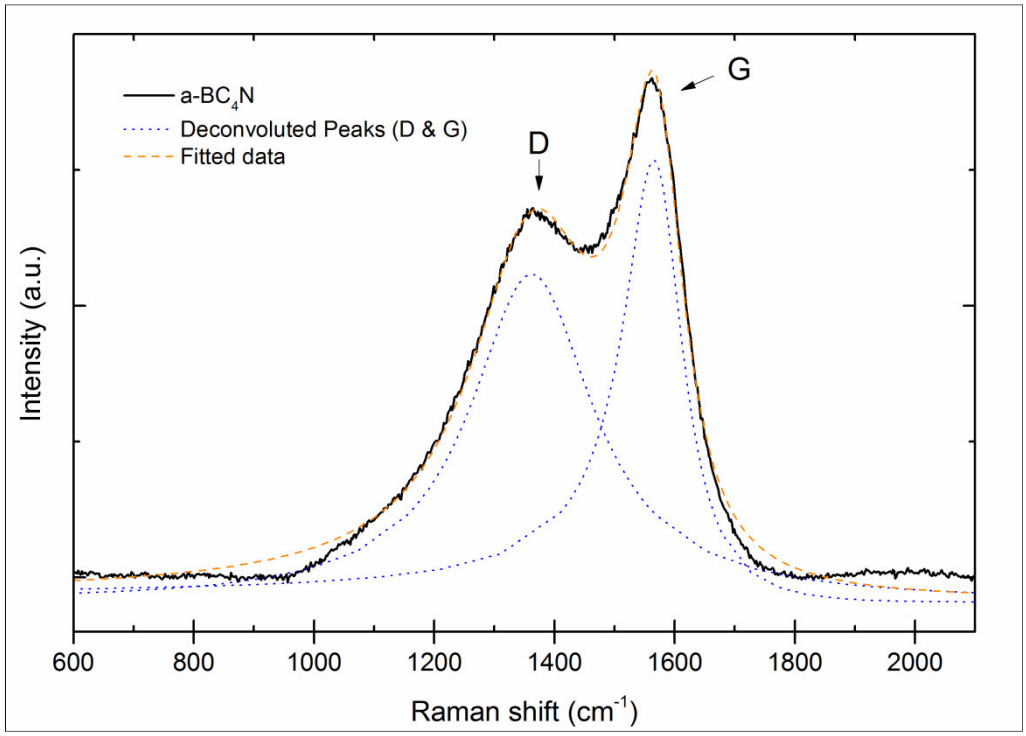

Figure 3-3. Raman spectra of amorphous BC_4N acquired using Ar laser (blue) 488 nm. Black line- acquired spectrum, blue dotted line – deconvoluted peak (D & G band), orange dashed line- fitted curve using Breit-Wigner-Fano(BWF) function

3.1.5. Microscopy analysis of BCN

The morphology and the microstructure of the BCN precursors were analyzed using in-house scanning electron microscope and transmission electron microscope, respectively. The SEM image of both the BC_2N and BC_4N precursors (as synthesized powders) are given in Figure 3-4. These SEM images reveal the flaky morphology of these precursors. The EDX analysis also showed both samples to be homogeneous in their composition and free of any other impurities. These flakes (of approx. size 80 x 80 x 30 μm) were directly used in diamond anvil cell experiments, but for the large volume press and toroid experiments they were further grinded before loading in the pressure cell.

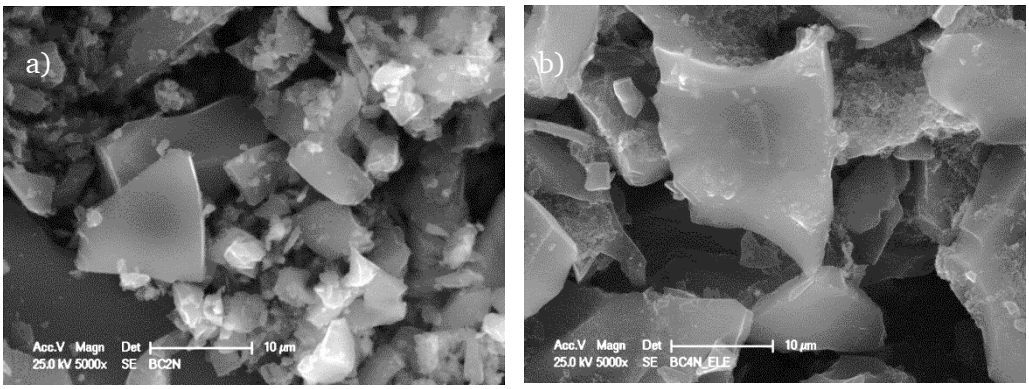

Figure 3-4. SEM image of synthesized BCN powders a) BC_2N , b) BC_4N

TEM micrographs for the BCN precursors are given in Figure 3-5. The corresponding selected area electron diffraction (SAED) image and EDX spectrum are shown in the inset. The SAED and TEM images clearly show that, both precursors are amorphous in nature. The TEM EDX analysis in different regions of the sample indicates the homogeneity (well dispersed B, C and N) in the precursors. The intensity ratios analysis of the B, C N peaks in the EDX spectrum consistently showed the BC_2N and BC_4N composition for the respective sample. Furthermore the oxygen contamination was proved in both the precursors. These results are in agreement with the elemental analysis performed by the hot-gas extraction method (see Table 3-1).

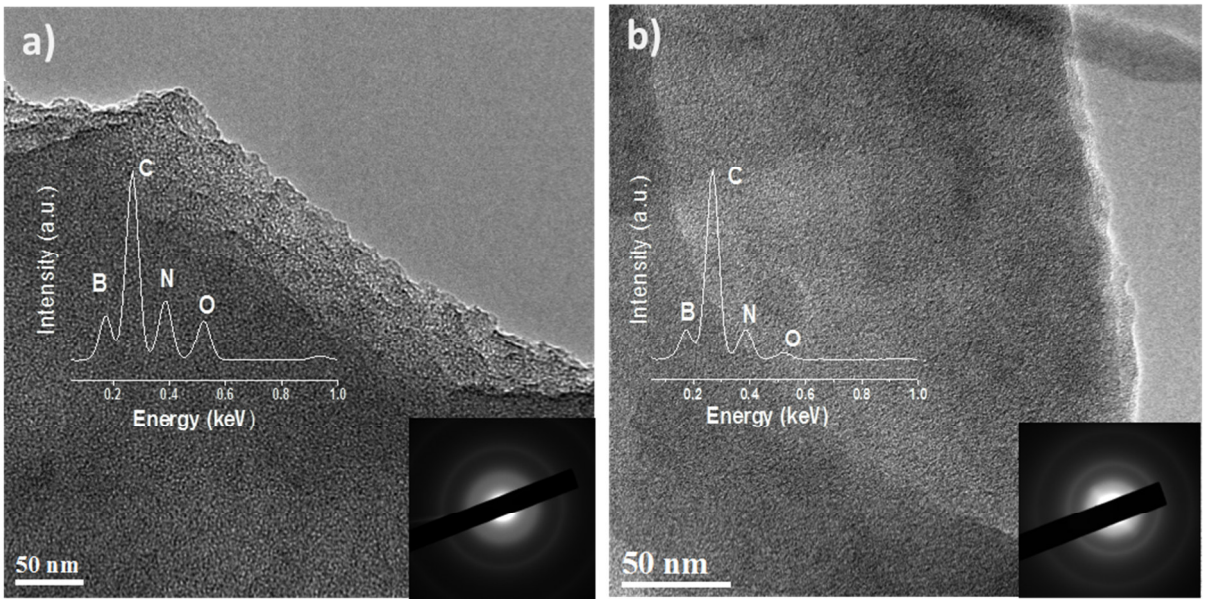

Figure 3-5. TEM images of the a-BC_2N (a) and a-BC_4N (b). The corresponding selected area electron diffraction (SAED) image and EDX spectrum are shown in the inset

3.1.6. X-ray diffraction analysis of BON (BN / B_2O_3 Mixtures)

The starting materials for our synthesis were prepared by ball-milling of different molar mixtures of hexagonal BN and B_2O_3 in the ratios from 1:1 to 4:1 (wt. %). X-ray diffraction patterns for the ball milled mixture along with the starting materials are given below (in Figure 3-6). XRD reflections indicate that, after balling for 2 h, the mixture still remains crystalline, however after ball milling for 4 h, the mixture became completely amorphous. These amorphous mixtures were used as precursor for BON LVP experiments [238].

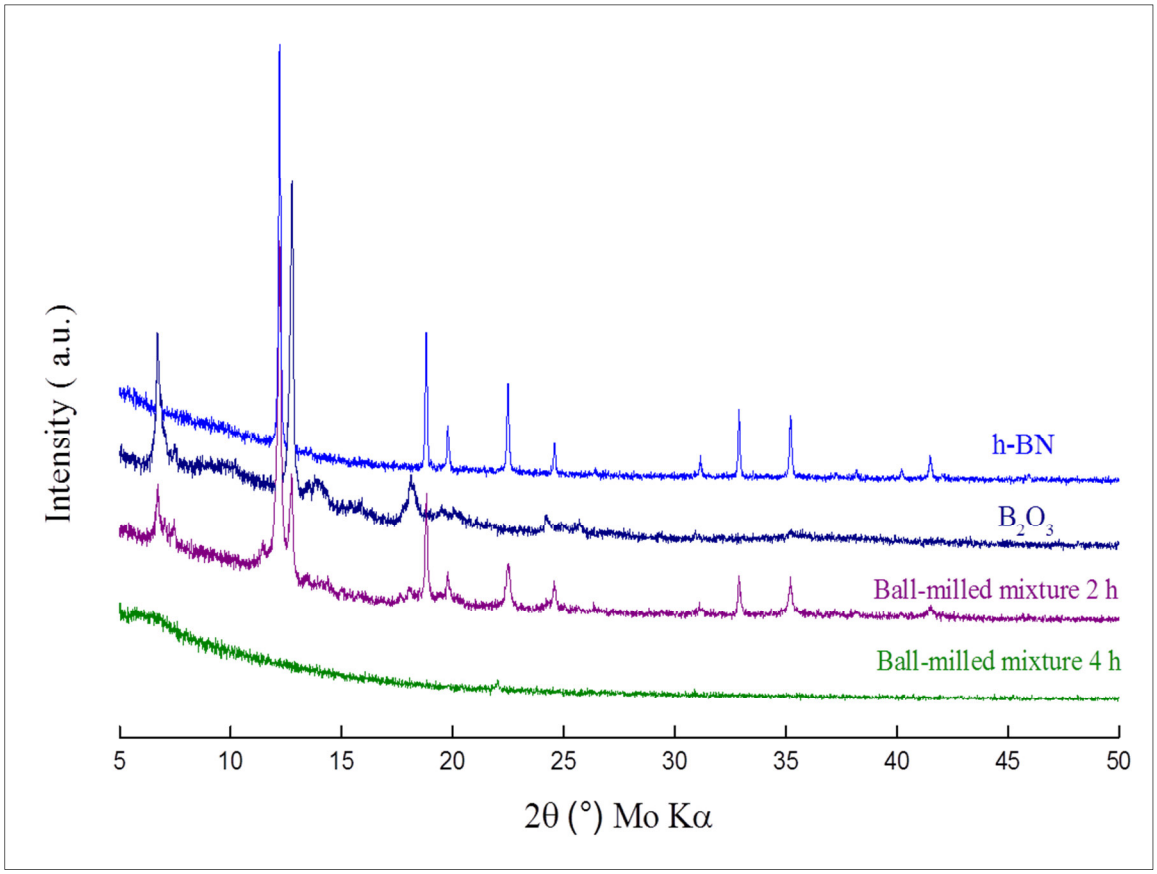

Figure 3-6. X-ray diffraction pattens for the h-BN, B_2O_3 and their mixtures after 2 h (purple) and 4 h (green) ball milling.

3.2. High pressure high temperature experiments

In this chapter results related to high pressure, high temperature (HP-HT) experiments are given. Segment 3.2.1 contains the results of multi anvil experiments under 7 GPa pressure, segment 3.2.2 comprises the outcome of the Toroid experiments up to 12 GPa pressure and segment 3.2.3 includes the results of the large volume press experiments up to 16 GPa pressure. Diamond anvil cell results up to 20- 39 GPa are given in segment 3.2.4. All the results in the above mentioned segments are in connection with the B-C-N compounds. The final segment 3.2.5 contains all the results of B-O-N HP-HT synthesis including the DFT modeling.

3.2.1. Multi anvil (MAX80) experiments – (5 to 7 GPa)

One of the main objectives of this work was to study the behavior of synthesized B-C-N precursors under different high pressure and high temperature conditions. Many earlier attempts regarding HP-HT synthesis of ternary B-C-Ns reported ambiguous results (summarized in section 1.3.2.3). To clarify these claims, more detailed study of these materials including low pressure is essential. In this regard, *in* and *ex-situ* MAX80 experiments are planned. These experiments help to understand the BCNs behavior in a pressure range below 8 GPa. As explained in experimental part (2.2.3.1), in single stage multi anvil device (MAX80) it is possible to reach up to 8 GPa. However, we have compressed amorphous BCN compounds up to 5 GPa (in case of BC_2N) and up to 7 GPa (in case of BC_4N). MAX80 is installed in beam line F2.1 beamline at DORIS III DESY, Hamburg, where it was possible to perform *in-situ* HP-HT energy-dispersive X-ray powder-diffraction (EDXRD) experiments. In the figures here the EDXRD data were plotted as intensity vs. 2θ (by fixing λ= 0.70931 Å) for the sake of comparison with other XRD data.

In-situ XRD patterns for BC_2N at 5 GPa are shown in Figure 3-7. The main intense peak (marked) is related to the graphite heater surrounding the sample. The samples exhibit the broad reflections (*) which are similar to those measured ex-situ on the starting material (see Figure 3-1). As one of the broad reflections (at 2θ ~10°) is over lapping the (002) graphite reflection from heater, the other broad regions give a hint about the nature of the samples under HP-HT conditions. From the graph it can be seen that BC_2N remain amorphous up to 1500 °C. During further heating at a given pressure, a new peak (around 2θ ~ 20°) started to appear at 1600 °C. The corresponding inset in Figure 3-7 give a closer look on the 2θ-region from 15 ° to 35 °, where the new sharp reflection can be clearly seen.

Similarly*, in-situ* XRD patterns for BC_4N at 7 GPa are shown in Figure 3-8. The main intense peak (marked) is related to the graphite heater surrounding the sample. The samples exhibit the broad reflections (*) which are similar to those measured ex-situ on the starting material (see Figure 3-1). As one of the broad reflections (at 2θ ~10°) is over lapping the (002) graphite reflection from heater, the other broad regions give a hint about the nature of

the samples under HP-HT conditions. From the graph it can be seen that BC_4N remain amorphous up to 500 °C. During further heating at a given pressure, a new peak (around 2θ ~ 20°) started to appear at 600 °C. The corresponding inset in Figure 3-8 gives a closer look on the 2θ-region from 15 ° to 35 °, where the new sharp reflection can be clearly seen.

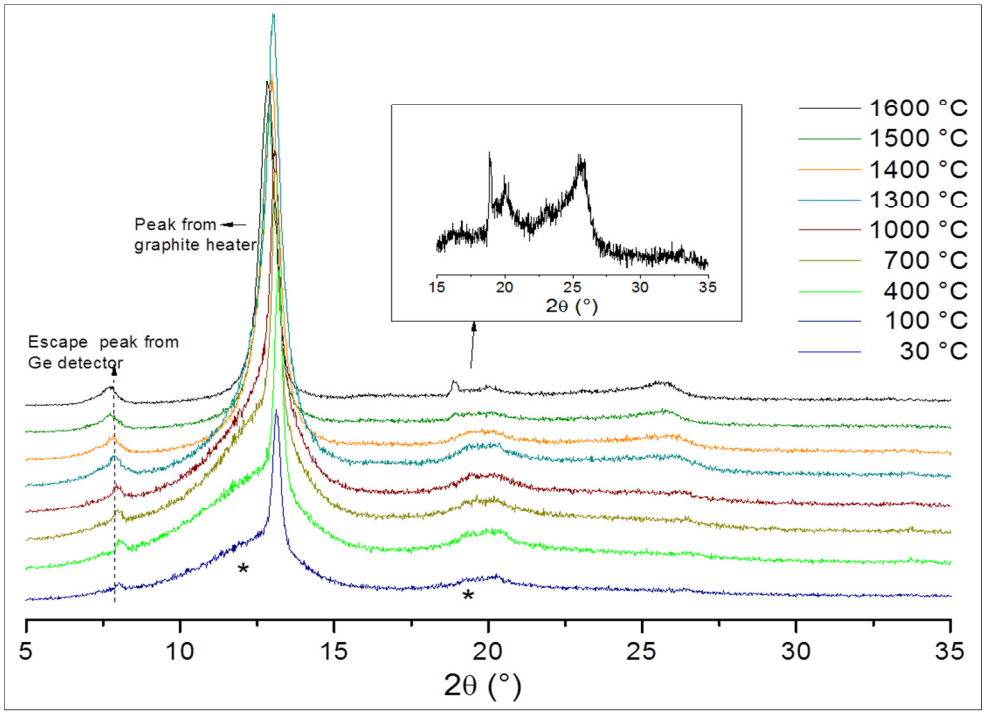

Figure 3-7. *In-situ* XRD patterns for BC_2N taken at 5 GPa in MAX80; inset graph shows a magnification of the 2θ region from 15 to 35 ° for the pattern taken at 1600 °C.

The BC_2N and BC_4N samples were recovered after the HP-HT experiments. Judging by the appearance, recovered sample appeared analogues to starting material (no change in color) from the visual observation. Fine ground powders are transferred to 0.5 mm capillary tube for XRD measurements. XRD patterns of the recovered BC_2N and BC_4N samples are shown in Figure 3-9. Both samples show a crystalline nature with reflections that indicate a mixture of h-BN and graphite. It is apparent that both BC_2N and BC_4N tend to decompose into a mixture of h-BN and graphite under the chosen HP-HT conditions.

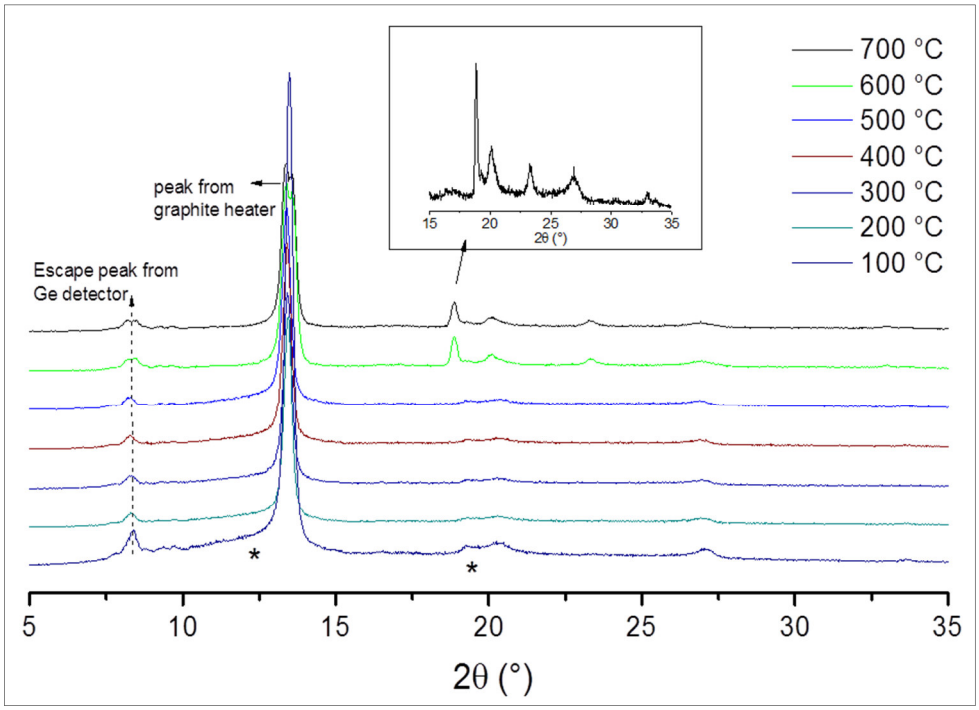

Figure 3-8 . In-situ XRD patterns for BC_4N taken at 7 GPa in MAX80; inset graph shows a magnification of the 2θ region from 15 to 35 ° for the pattern taken at 700 °C

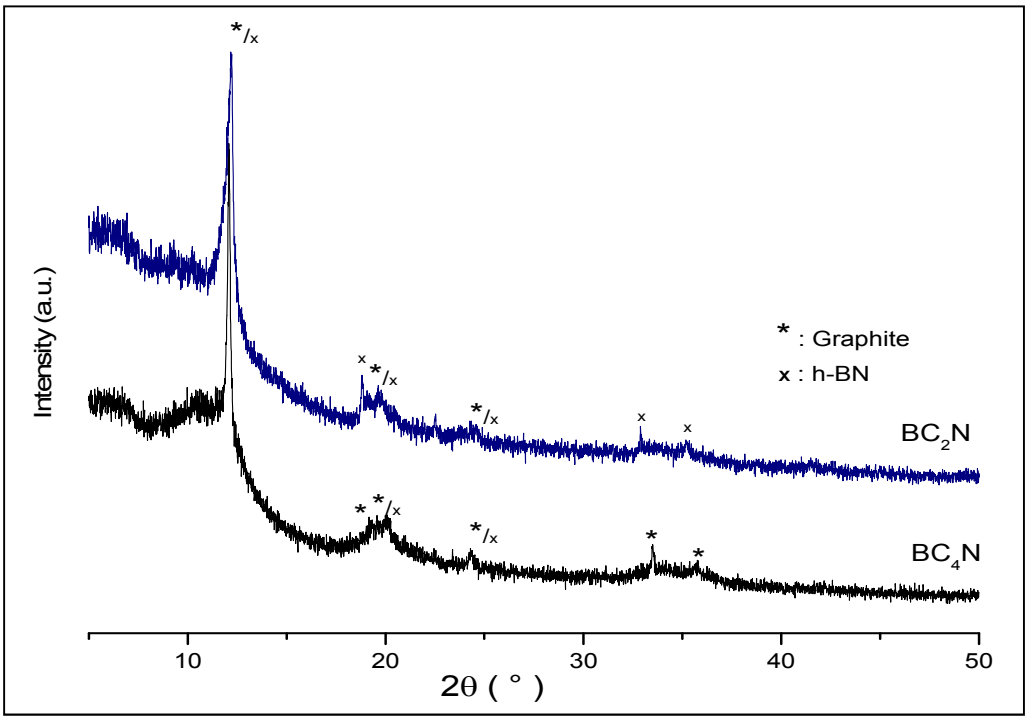

Figure 3-9 . Ex-situ XRD patterns of the samples recovered after MAX80 experiments (Mo Kα λ = 0.70319 Å)

3.2.2. Toroid experiments (12 GPa)

For experiments of medium pressure range (~ 12 GPa) Toroid press was the most suitable choice, providing the larger sample volume. These experiments were carried out at the Institut für Anorganische Chemie, TU Bergakademie Freiberg, Germany. Both BC_2N and BC_4N precursors were compressed up to 12 GPa. Samples were loaded in the glove box to avoid moisture contamination. In experiments double molybdenum (Mo) capsules were used to reduce possible contamination of the products with oxygen due to its diffusion from the surrounding oxide pressure medium. The detailed description of the experiment can be found in section 2.2.2.

XRD patterns of the recovered samples from the toroid experiments at 12 GPa and ~ 1000°C are shown in Figure 3-10. They show that BC_2N remains amorphous even after exposing to HP-HT conditions, whereas BC_4N decomposes into h-BN and graphite. The additional reflections were assigned to molybdenum carbides (Mo_2C and MoC), thus indicating that the molybdenum capsule reacted with the part of the sample. The results of ex-situ toroid experiments are in agreement with the above described in-situ multi-anvil studies, where BC_4N decomposed into h-BN and graphite at temperature exceeding 500 °C. Similarly, BC_2N has been found to maintain its amorphous nature up to 1600 °C at 5 GPa in multi-anvil and up to ~ 1100 °C at 12 GPa in the toroid experiment.

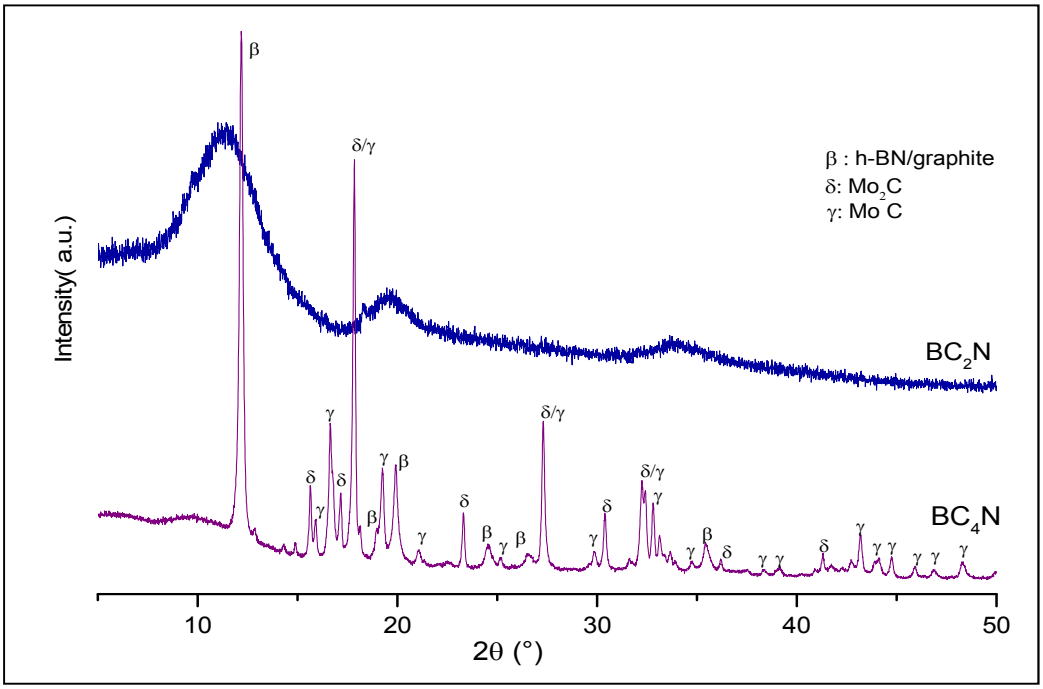

Figure 3-10. Ex-situ XRD patterns of the samples recovered after toroid experiments. (Mo Kα λ = 0.70319 Å)

3.2.3. Large volume press experiments (15.6 GPa)

Large volume press (LVP) HP-HT experiments were performed in a Walker type multi-anvil apparatus (6/8 –type), installed at DESY, Hamburg (offline). All the experiments were performed at a pre-calibrated pressure of 15.6 GPa. The pressure cell, consisting of a 14 mm magnesium oxide (MgO doped with 5% Cr_2O_3) octahedron and cylindrical $LaCrO_3$ (lanthanum chromate) heater, was compressed using WC cubes with 7 mm truncations. More details on the experimental setup and conditions can be found in section 2.2.3.2. In the following, results are divided into 2 sub sections based on the precursor BC_4N and BC_2N.

3.2.3.1 LVP experiments with BC_4N (15.6 GPa)

LVP experiments were conducted at a pressure of 15.6 GPa and heated to 1900°C for 20 min. *The ex-situ* angle dispersive X-ray diffraction pattern of the recovered LVP sample, acquired at ALS Berkeley beamline 12.2.2 is shown in the Figure 3-11. XRD reflections clearly show that a-BC_4N converts into a mixture of c-BN and diamond. Intensities of XRD reflections also indicate that, diamond phase is more dominant in the composition. The Raman spectrum of the recovered LVP sample is shown in Figure 3-12. The intense peak at 1333 cm^{-1} corresponds to the first-order optic mode of diamond [239]. However, no peak corresponding to the c-BN phase (neither LO at 1304 cm^{-1} nor TO at 1056 cm^{-1}) is observed. This can rely on the Raman scattering efficiency of c-BN, which (depending on the excitation laser), is 60-180 times lower than that of diamond [240]. Interestingly, the recovered sample was well sintered and exhibited a dense microstructure. The SEM micrograph of the brittle-fractured surface is shown in Figure 3-13. It would very interesting to study the grain boundary between diamond and c-BN to examine the sintering behavior of this composite. Excessive carbon in the precursor might be forming interface between diamond and c-BN, however detailed TEM analysis is needed to confirm this hypothesis.

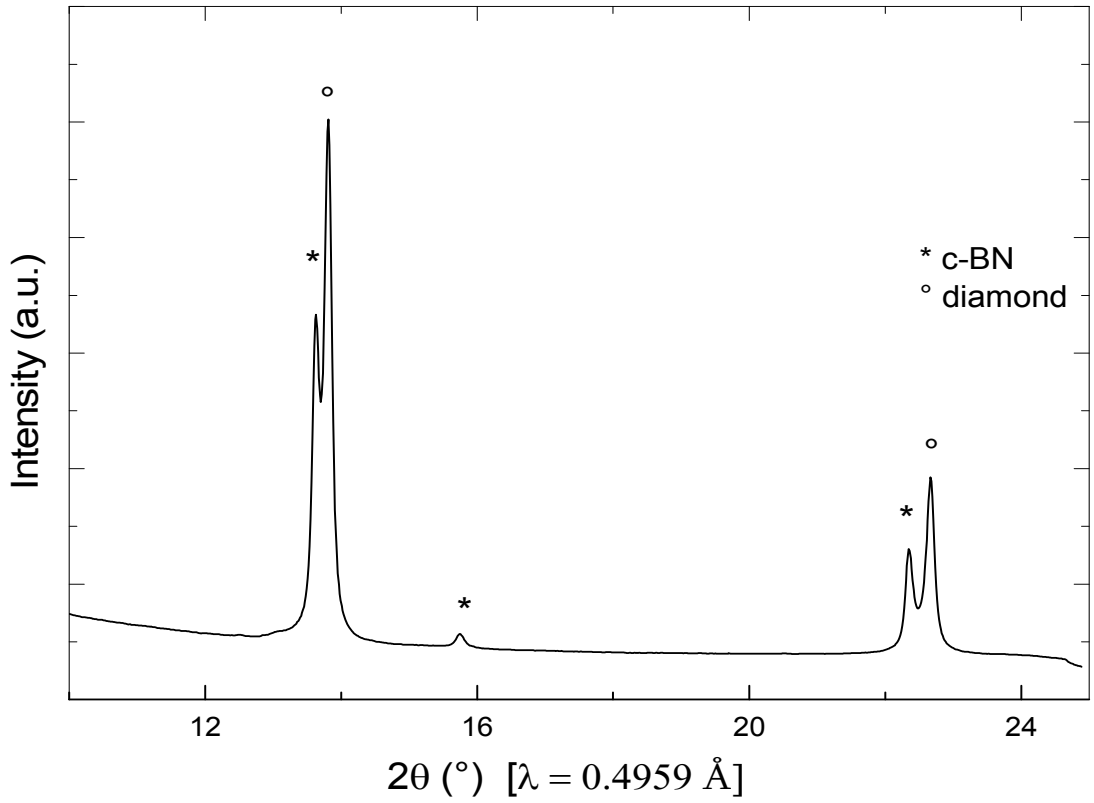

Figure 3-11. Diffraction pattern of the recovered BC_4N after LVP experiments at 15.6 GPa, 1900° C

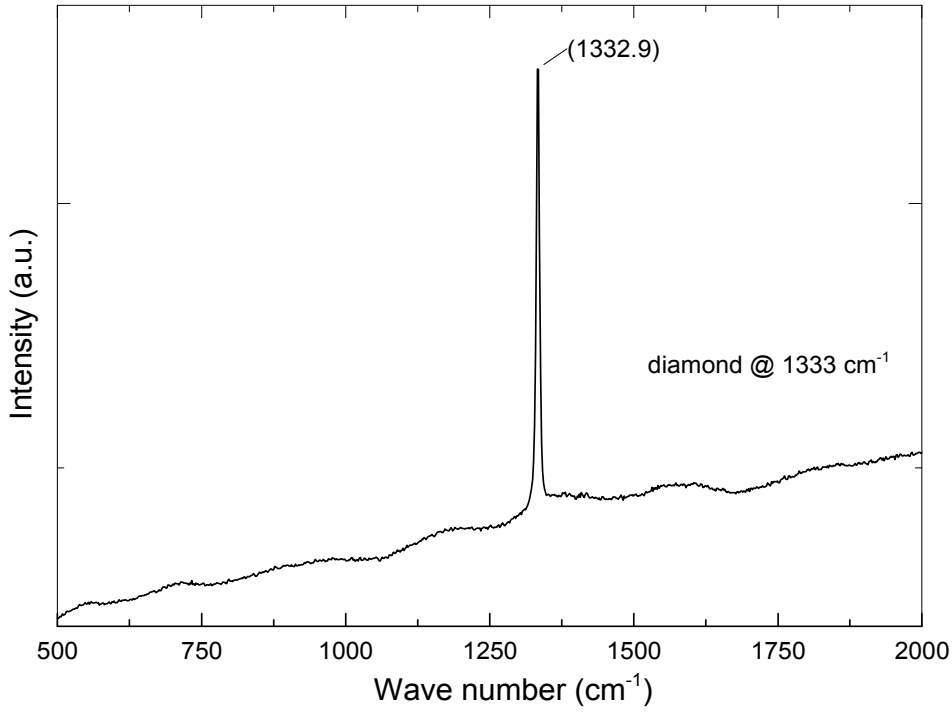

Figure 3-12. Raman spectra of the recovered sample after LVP experiments at 15.6 GPa, 1900° C

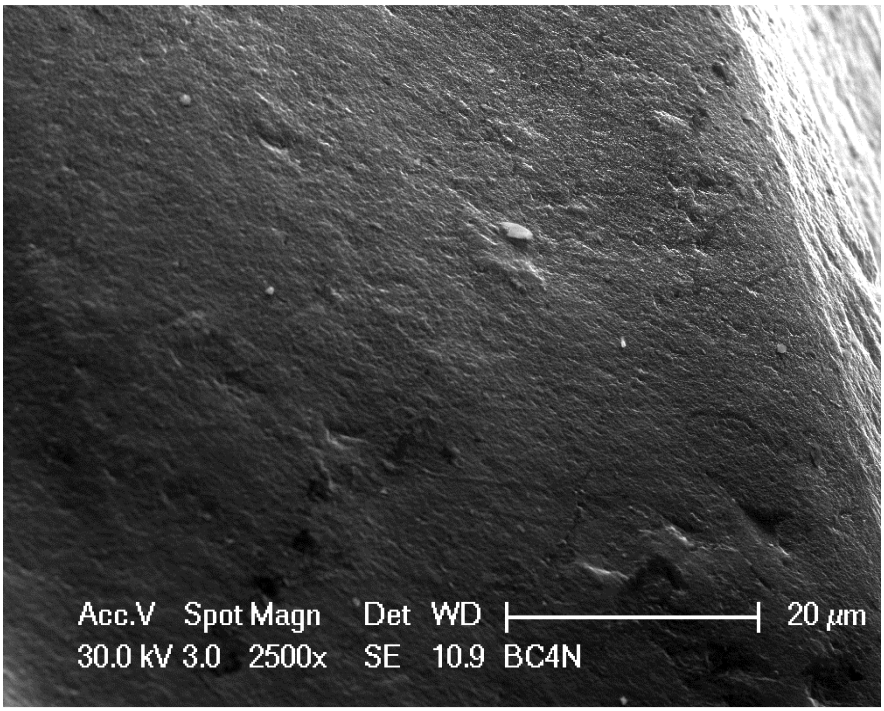

Figure 3-13. The SEM micrograph, brittle-fractured surface of the recovered LVP sample

3.2.3.2 LVP experiments with BC_2N (15.6 GPa)

LVP experiments were conducted at a pressure of 15.6 GPa and heated to 1900°C for 20 min. *The ex-situ* angle dispersive X-ray diffraction pattern of the recovered LVP sample, acquired at ALS Berkeley beamline 12.2.2 is shown in the **Figure 3-14**. XRD reflections clearly show that a-BC_2N converts into a mixture of c-BN and diamond. Intensities of XRD reflections also indicate that, c-BN phase is more dominant in the composition. Results are consistent with BC_4N, where the mixture of c-BN and diamond (major phase) after HP-HT treatment. Other reflections in the diffractogram can be assigned to magnesium borate ($Mg_3B_2O_6$, PDF- 00-038-1475), which indicates that, MgO used as pressure transmitting medium reacted with the starting materials. The platinum capsule used in sealing the sample was found melted during HP-HT treatment (maybe due to forming PtB_2 eutectic mixture after reacting with boron in precursor material). This lead the pressure medium (MgO) in the cell to come in direct contact with the starting material.

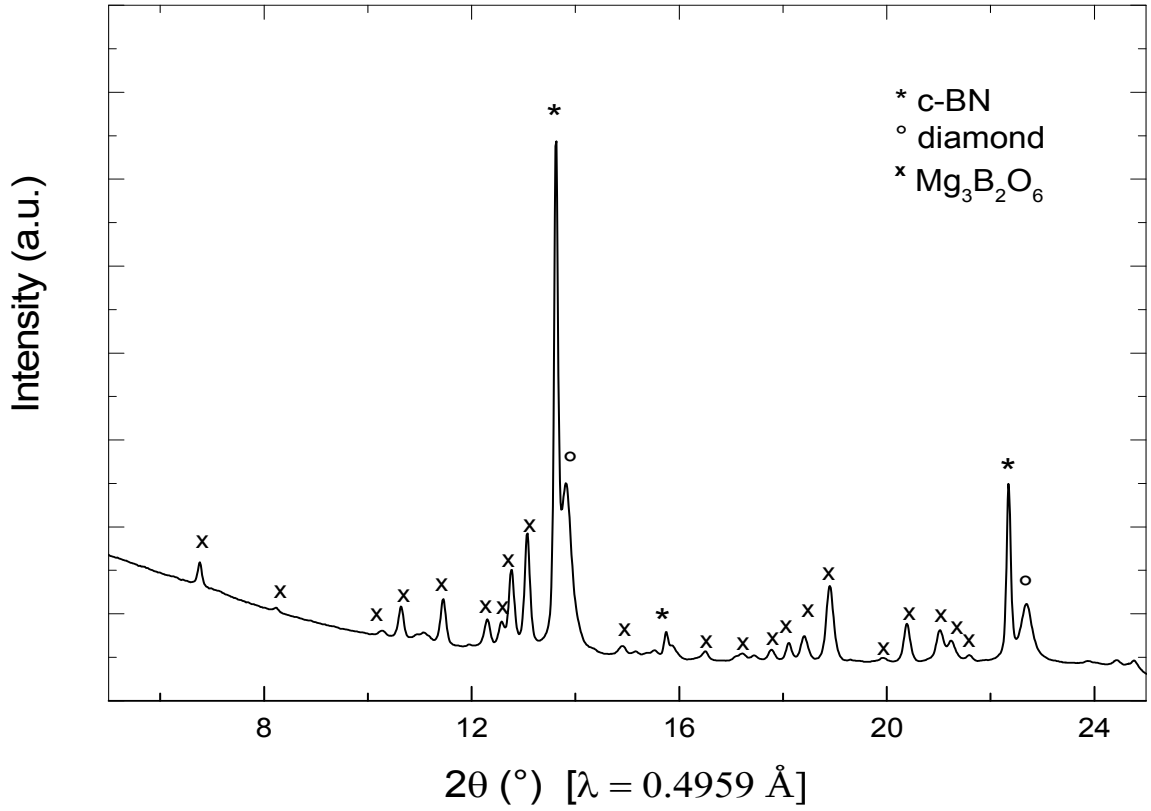

Figure 3-14. Diffraction pattern of the recovered BC_2N after LVP experiments at 15.6 GPa, 1900° C

3.2.4. Diamond anvil cell experiments (20 -39 GPa)

The diamond anvil cell (DAC) experiments were performed in a Boehler Almax [211] type cell with 400 μm diamond culets. The sample chamber was formed upon drilling a 140-160 μm diameter hole in a pre-indented rhenium gasket. The sample was compressed to the required pressure (20- 39 GPa) and heated to 1900 - 2200 °C for 5-10 min with a CO_2 pulsed laser (wavelength 10.6 μm, 250 W). Gas (argon or neon) loading and laser heating was performed in Goethe-Universität Frankfurt. More description of the experimental setup and can be found in the section 2.2.4. In the following, results are divided into 2 sub-sections based on choice of the precursor; BC_4N and BC_2N

3.2.4.1 DAC experiments with BC_4N

Several DAC experiments were conducted in the pressure range from 20 to 35 GPa and at high temperatures (1900 - 2200 °C, for 5-10 min, CO_2 laser heating). The black a-BC_4N precursors were converted into translucent or nearly transparent materials after laser heating at all the applied pressures. Photographs of a sample before and after heating are given in Figure 3-15. *An ex-situ* angle dispersive diffraction pattern of the corresponding sample collected (at PETRA III, P02.2 beamline) after releasing the pressure in the DAC is shown in Figure 3-16. Major reflections in diffractogram belong to NaCl, which was used as thermal insulating medium in DAC experiments. However, in 2 theta region 8° peak corresponding to the sample can be seen (inset graph is given Figure 3-16 shows more clearly). Results clearly indicate the formation of the mixture of c-BN and diamond. We have observed the same behavior for the BC_4N compounds in the used pressure range. Accordingly, under these HP-HT conditions amorphous BC_4N converts into a mixture of c-BN and diamond. These results are in agreement with the LVP experiments discussed above. The results are also consistent with our low-pressure experiments [241], where amorphous BC_4N was found to decompose into a mixture of h-BN and graphite at temperatures above 600 °C and pressures up to 12 GPa.

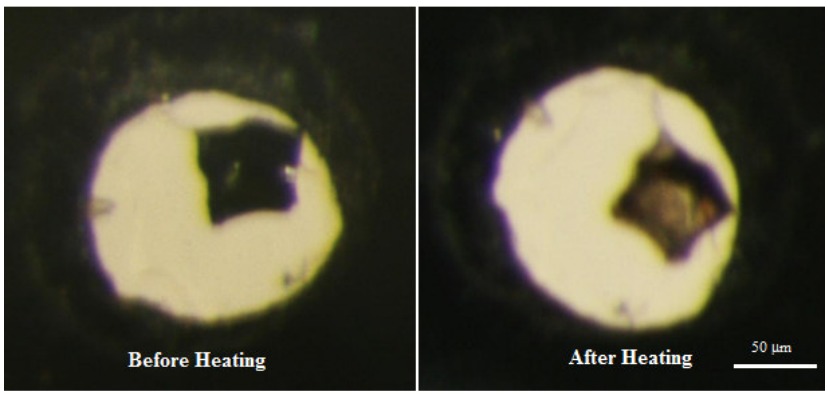

Figure 3-15. BC_4N Sample in inside DAC before and after laser heating

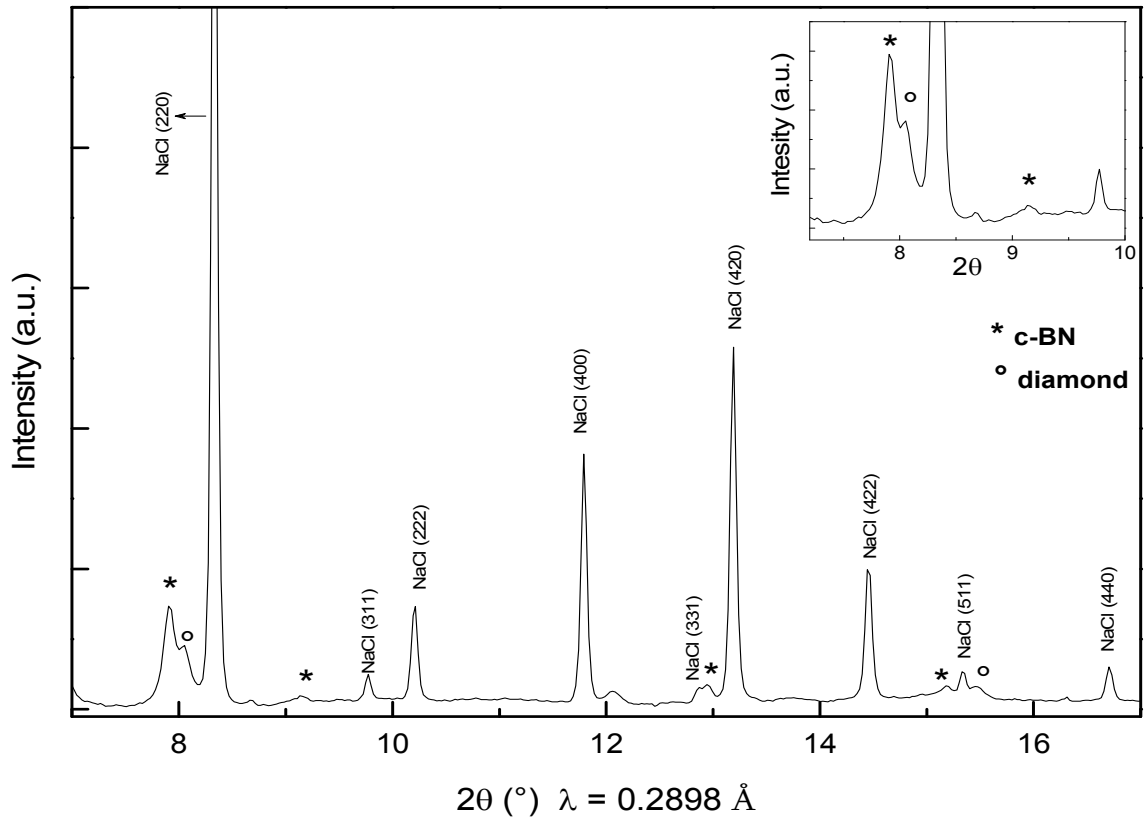

Figure 3-16. Ex-situ angle dispersive X-ray diffraction patterns collected after releasing the pressure in DAC (34 GPa, 1900-2500 °), inset graph shows the 2 theta region from 7-10°

3.2.4.2 DAC experiments with BC_2N

Numerous DAC experiments were conducted in the pressure range from 20 to 39 GPa and at high temperatures (1900 - 2200 °C, for 5-10 min, CO_2 laser heating). After the HP-HT treatment, the black a-BC_2N precursors were converted into translucent or nearly transparent. Photographs of a sample before and after heating are given the Figure 3-17. Other researchers [51, 53] also observed the similar behavior with their BCN compounds. It may be one of the indications of carbon converting from sp^2 to sp^3 configuration, however may not be sufficient to prove the phase transformation. All the DAC experiments samples were recovered (all the pressure ranges 20-39 GPa), to perform the TEM analysis. For the TEM analysis, samples were prepared according to the methods explained in section 2.3.4.1. Bright field TEM image and corresponding dark field TEM image of the BC_2N samples is given in Figure 3-18 (a) and (b) respectively. The bright field TEM image shows that the crystals are agglomerated and their size varies from 15- 150 nm. Interestingly some of these crystals have triangular morphology. The dark field image also confirms the triangular morphology of the crystals.

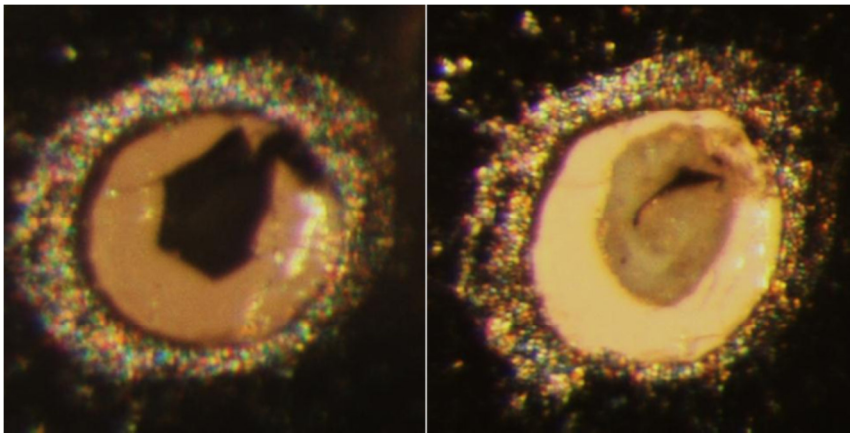

Figure 3-17. BC_2N Sample in inside DAC before and after laser heating

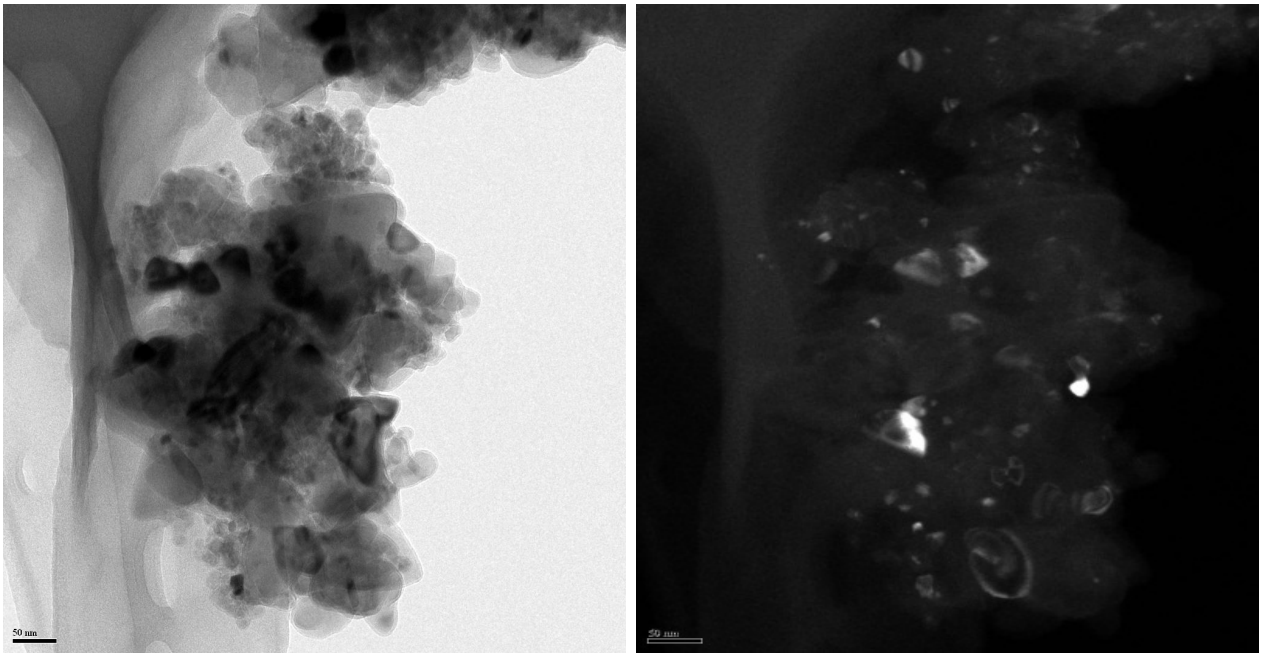

Figure 3-18. (a) Bright field TEM image of recovered BC_2N sample, (b) inset image is respective dark field image

The selected area electron diffraction (SAED) pattern taken in one of the agglomerated region of the crystals is shown in Figure 3-19. The SAED containing reflections in ring patterns confirms the polycrystalline nature of the sample. In order to study the crystal structure of these crystals, *d*-values corresponding to the each ring pattern have been calculated. The respective d- values were marked in the pattern with different color. These reflections could be indexed with respect to a cubic lattice and correspond to (111) with d = 2.1 Å, (200) with d = 1.8 Å, (220) with d = 1.3 Å, (311) with d =1.1 Å. These reflections can be attributed to c-BN and mixtures of c-BN and diamond by considering the experimental error while measuring and analyzing the d-values (± 10%). And also these d-values can be indexed using the some of the claimed c-BC_2N [51, 53]. However, more detailed analysis like precise EDX, EELS are performed to confirm the composition of the synthesized compound.

Energy dispersive X-ray spectroscopy (EDX) was performed in the TEM to identify the local composition. Figure 3-20 shows a new TEM image of single crystal, recovered BC_2N sample after DAC experiment. The figure also includes white circled area, representing the approximate beam diameter used for EDX analysis. The EDX spectrum of the respective single crystal is given in Figure 3-21. The EDX spectrum clearly shows the presence of boron and nitrogen and absence of carbon in the single crystal indicates the phase separation of the starting materials into boron nitride and carbon. In the Figure 3-22 TEM image of one of the fine grain area of recovered BC_2N sample after DAC experiment is shown. The white circled area (marked), represents the approximate beam diameter used for the EDX analysis. The EDX spectrum of the corresponding TEM image is given in the Figure 3-23. It clearly shows the presence of carbon as major phase and existence of negligible amount of boron and nitrogen. It also suggests that, the starting materials have phase separated into carbon and boron nitride. By comparing EDX results with the inference of the above SAED pattern, it seems that, the a-BC_2N precursor phase separates into c-BN and diamond after DAC experiments. These findings are in agreement with that of different research groups, who reported very similar observations [167, 168] of B-C-N compounds after HP-HT treatment. It also noteworthy, c-BN has been synthesized under HP-HT conditions [44, 242-244]; our experimental conditions are suitable to form c-BN. In the EDX spectrum (both in Figure 3-21 and Figure 3-23), there is also minute peak corresponding to the oxygen. This oxygen contamination may be due to precursor (adsorbed moisture while loading into DAC) or surroundings (NaCl or KCl used as thermal insulating medium in DAC experiments), during HP-HT synthesis.

Electron energy-loss spectroscopy (EELS) was performed in the TEM to confirm the presence of the boron, carbon, nitrogen and oxygen (low-Z elements), which were identified in EDX analysis. It is also possibly to identify the local bonding states of these elements by examining the respective near edge fine structure in EELS (ELNES). Figure 3-24 shows the ELNES ionization edges of the B-*K* at 191 eV, N-*K* at 397 eV, O-*K* at 532 eV, and C-*K* at

279 eV after background subtraction. B-*K* , N-*K*, O-*K* ionization edges were acquired on single crystal shown in the Figure 3-20 and C-K was taken in fine grained area of the Figure 3-22. The corresponding fine structure observed strongly suggests a sp^3 type bonding in boron, nitrogen oxygen [245-247] and mixed sp^2 / sp^3 (π^* / σ^*) type bonding in carbon [245]. It is evident that single crystals are boron nitride in sp^3 type bonding i.e., cubic boron nitride with oxygen contamination, and the fine grain area contains carbon in mixed sp^2 / sp^3 bonding sate, meaning carbon in graphitic and diamond state, respectively. Hence a-BC_2N precursor decomposes into diamond / graphite and c-BN (with oxygen contamination) after DAC experiments (20-38 GPa and up to 2200 °C). Mixed bonding states in carbon arise due to partial conversion of graphitic carbon into diamond at HP-HT conditions. More detailed EELS quantification and ELNES are needed to analyze the oxygen containing c-BN. In the next section, hint towards the novel boron oxy-nitrides are explained.

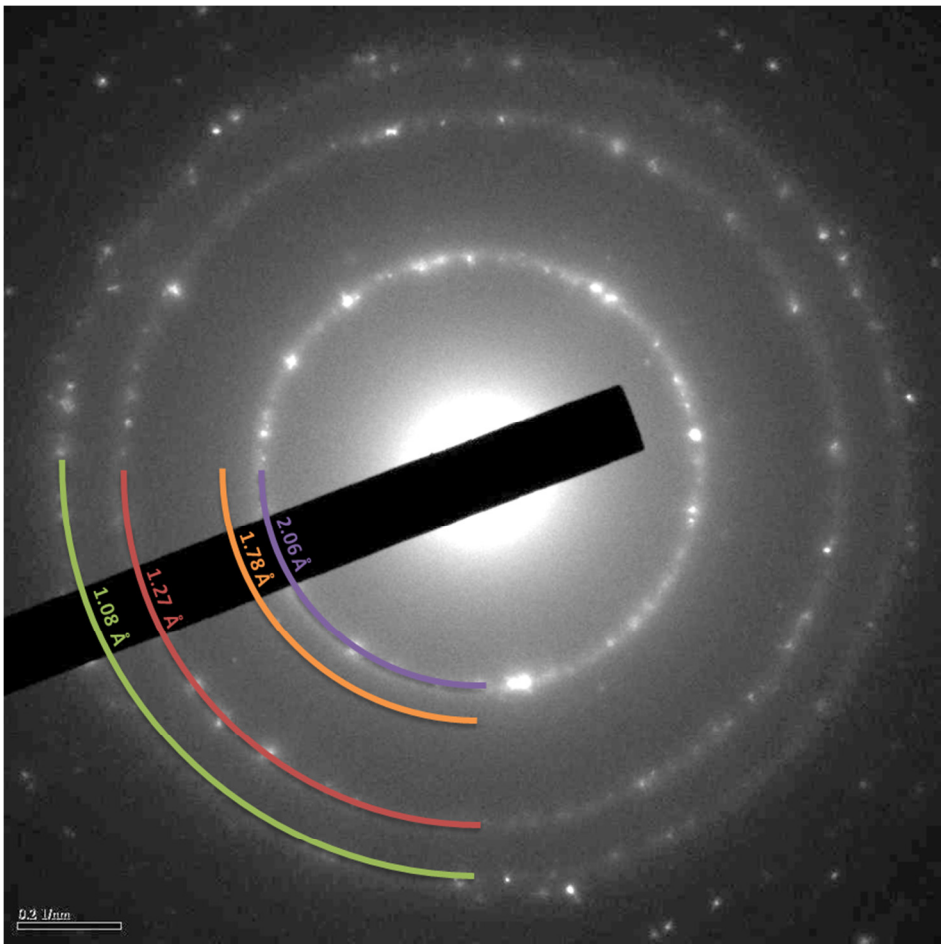

Figure 3-19. SAED pattern of the recovered BC_2N sample, different arcs (violet, orange, red and green) marked in the SAED pattern shows the corresponding *d*-values.

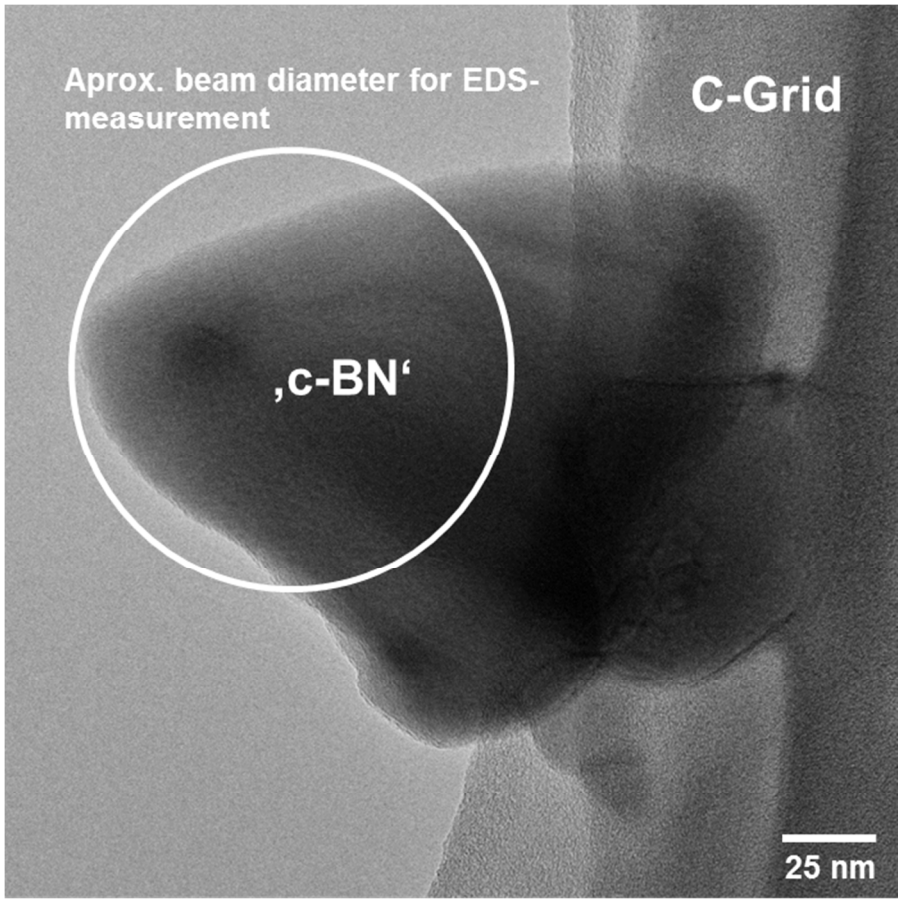

Figure 3-20. TEM image of single crystal of recovered BC_2N sample after DAC experiment, circled area shows approximate beam diameter usedfor EDX measurement.

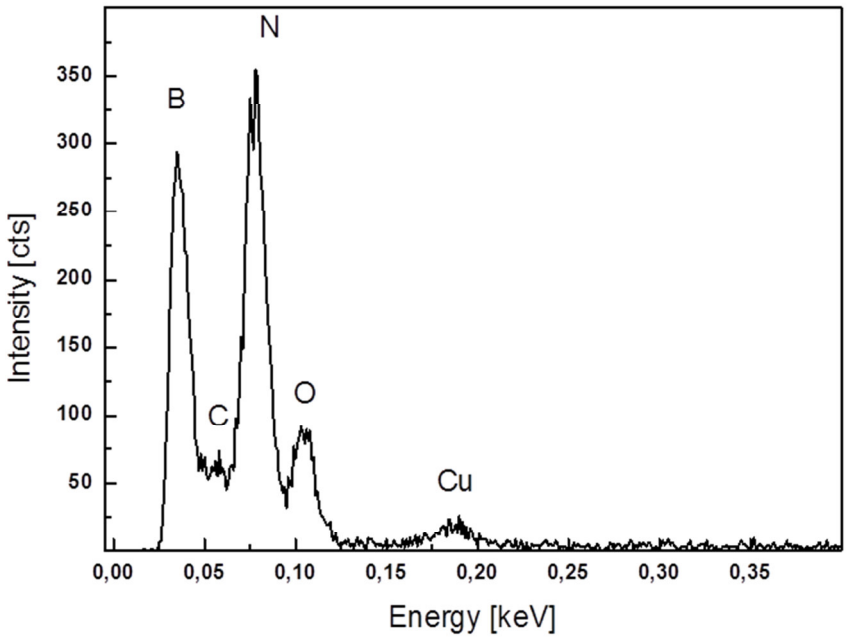

Figure 3-21. EDX spectrum recorded of the single crystal from the recovered BC_2N sample after DAC experiment, recorded in the area highlighted in Figure 3-20.

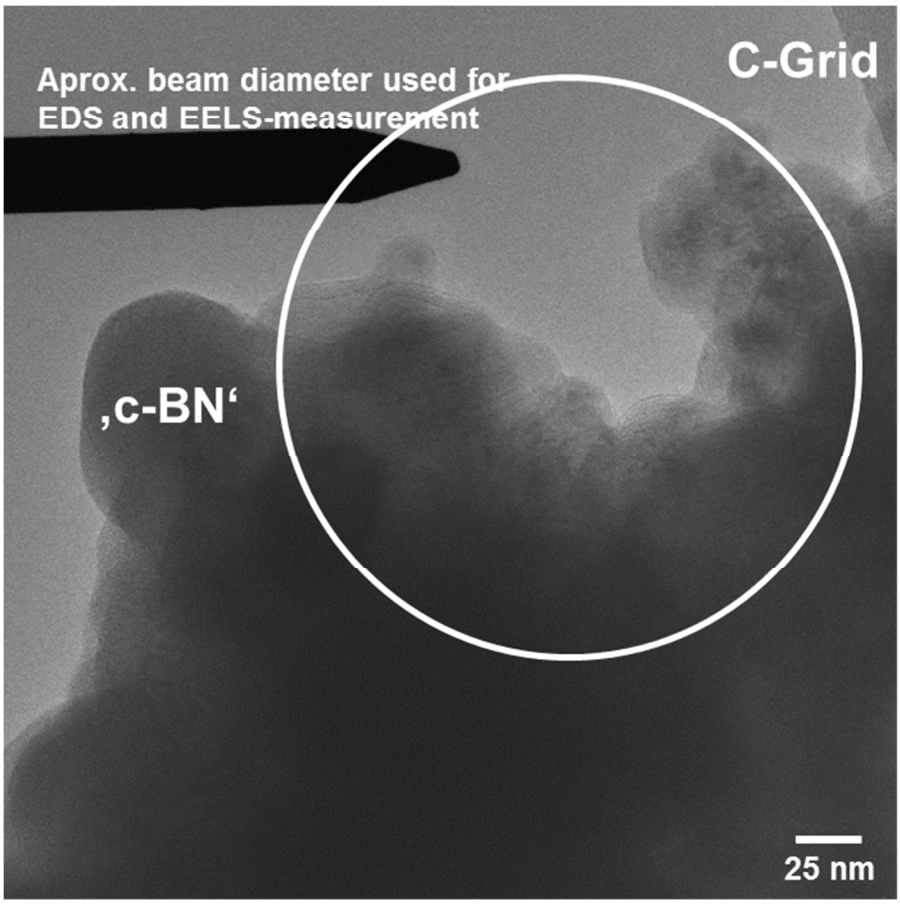

Figure 3-22. TEM image of fine grain area of recovered BC_2N sample after DAC experiment, circled area shows approximate beam diameter used for EDX measurement.

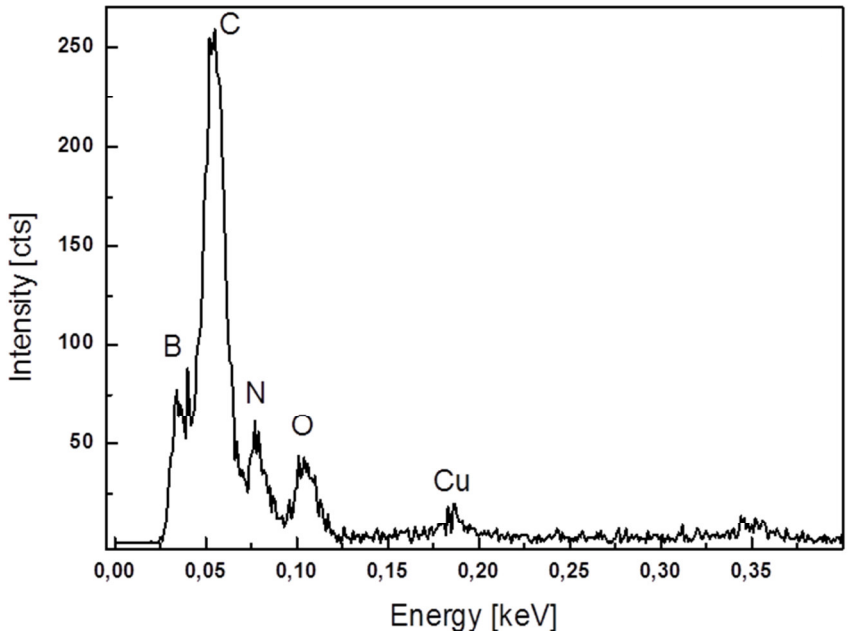

Figure 3-23. EDX spectrum of recovered BC_2N sample after DAC experiment, recorded in fine grain area highlighted in Figure 3-22

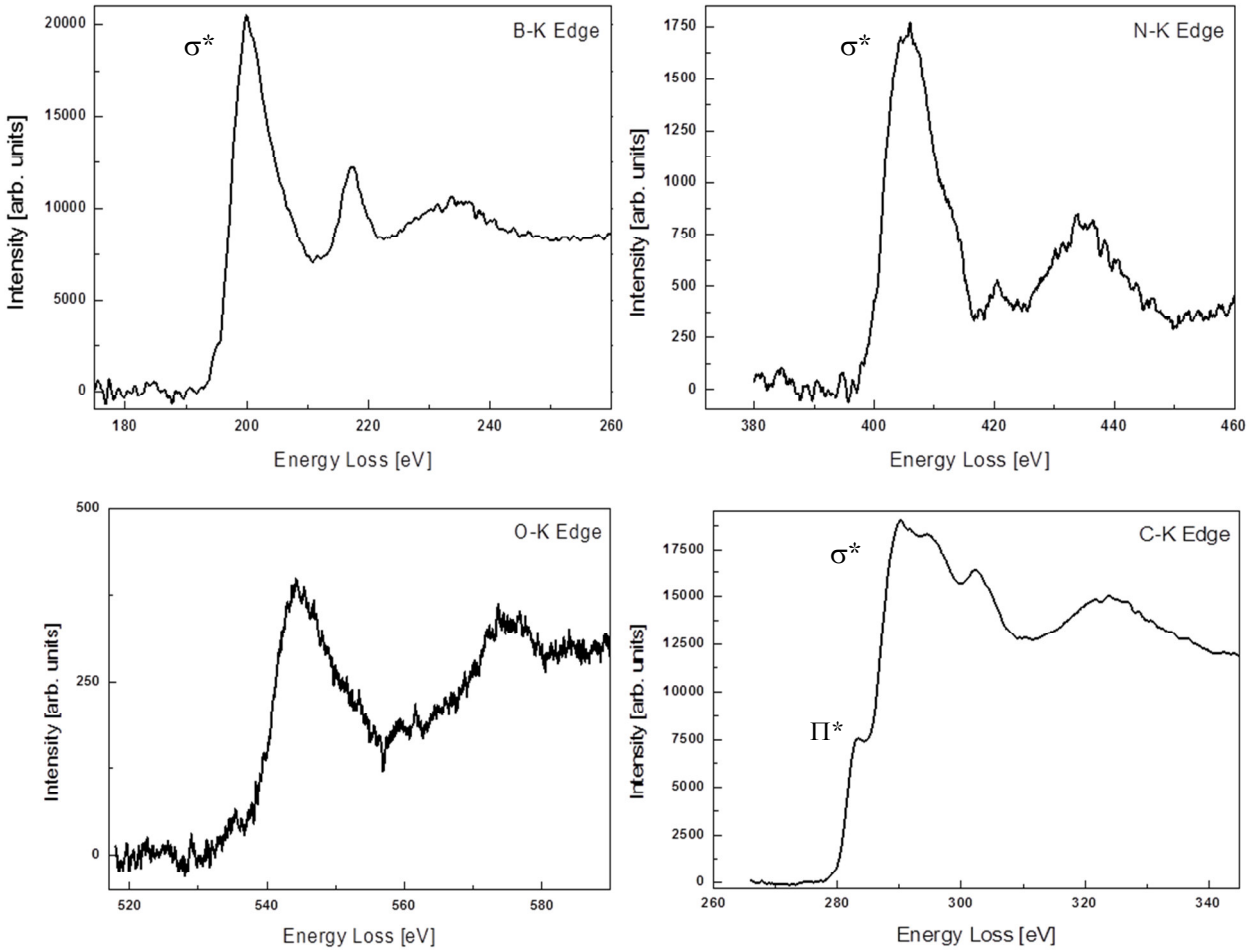

Figure 3-24. Energy-loss near edge fine structure (ELNES) ionization edges of the B-*K*, N-*K*, O-*K*, and C-*K* after background subtraction. B-*K*, N-*K*, O-*K* ionization edges were acquired on single crystal shown in the Figure 3-20 and C-*K* was taken on fine grain area of the Figure 3-22

3.2.4.3 Formation of Boron Oxynitride (BON) Phase

After observing the oxygen contamination in DAC experiments, all sources of oxygen were carefully monitored. As explained earlier, it appears that thermal insulation used in DAC experiments is one of the main causes; however oxygen uptake of the sample while loading into DAC in outside atmosphere cannot be ignored (may be due to adsorption or surface absorption). In order to estimate the oxygen contamination in the precursors during loading into DAC, elemental analysis was repeated on samples which are exposed to air for a specified duration (see section 3.1.1). Results revealed that the precursors contained 16±2% oxygen after 1 h exposure. DAC experiments were repeated (20- 30 GPa, 1900 – 2200 °C, CO_2 laser heating) with BC_2N precursors having 16% oxygen. After HP-HT treatment samples were recovered for TEM analysis. TEM images of two different regions of the recovered BC_2N sample after DAC experiment are given in Figure 3-25 (a) and (b). The corresponding EDX spectrum is given in respective inset.

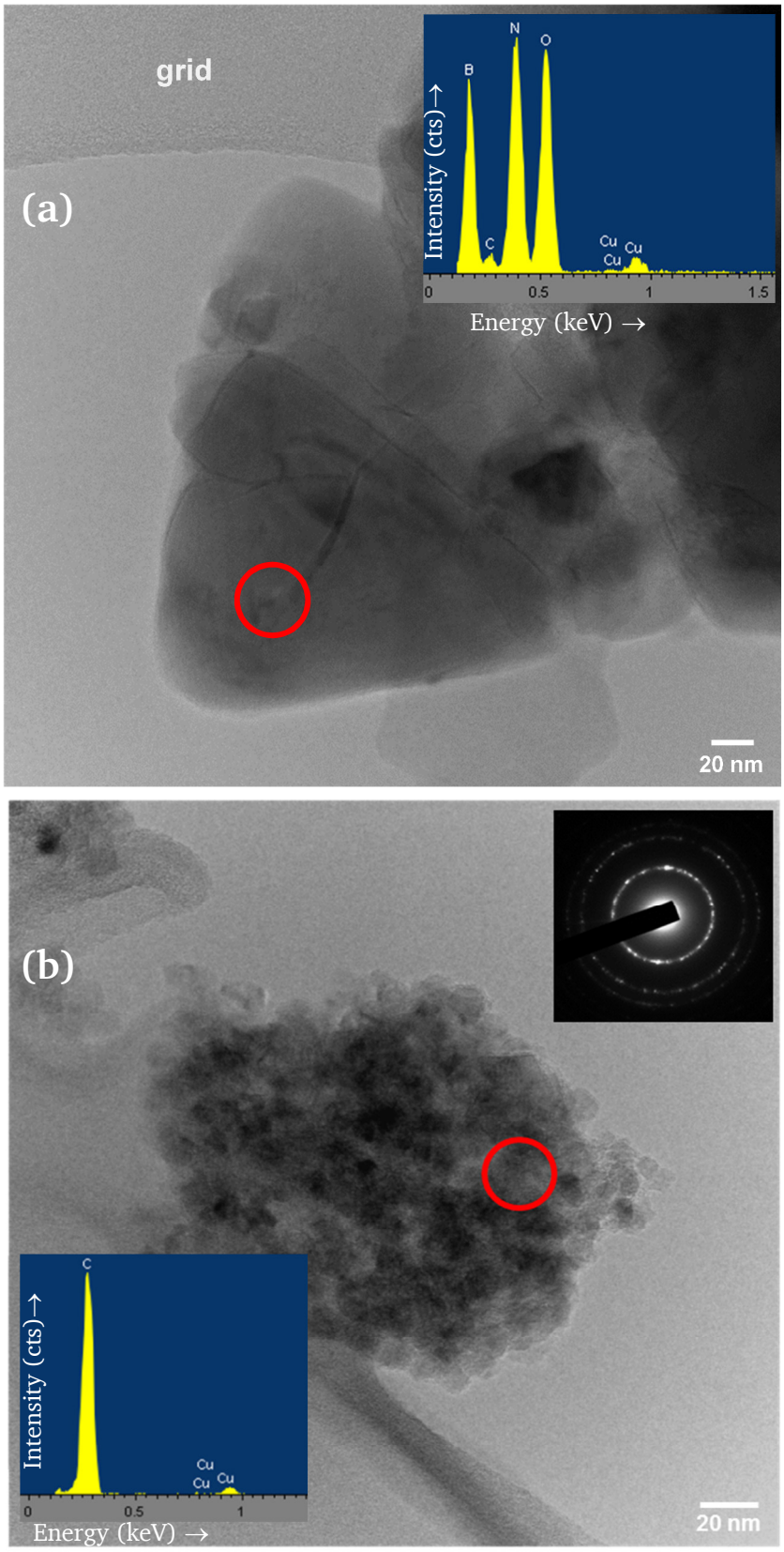

Figure 3-25. TEM images of recovered BC_2N sample after DAC experiment in two different regions (a) and (b). The corresponding EDX spectrum is given in respective inset. Region (b) also includes corresponding SAED inset. Circled (in red) area shows approximate beam diameter used for EDX and SAED.

Crystals in Figure 3-25 (a) appear approx. 100 to 200 nm in size and clearly show triangular morphology and opposite to the region Figure 3-25 (b) where crystals are only few nm. The corresponding EDX spectrum (acquired in the circled area) confirms the presence of B, N and O and absence of carbon in triangular shaped crystals in region (a). Furthermore carbon seems to be agglomerated and crystalized distinctly in region (b). By examining *d*-values in the SAED acquired in fine grained area (inset (b)) and EDX measurement, it appears that, region (b) is graphite. It is apparent that the amorphous BC_2N precursor along with known amount of oxygen, after HP-HT treatment, has crystalized into BN having considerable amount of oxygen and graphite. This observation is also in line with the earlier DAC experimental results, where BN crystals had oxygen along with them.

To reconfirm our finding, the DAC experiment is repeated again, with the air exposed BC_2N precursor with known ammout of oxygen. After HP-HT treatment (25 GPa, ~2000 °C) samples were recovred for TEM analysis. TEM image of BC_2N after DAC experiment is shown in Figure 3-26 along with the EDX spectrum aquired in the highlighted circled area of the sample. From the TEM image and EDX measurement, it is evident that the traingular crystals are BN crystals with considerable amout of oxygen and the carbon is agglomerated discretely. Repeated HP-HT experiments on BC_2N , provides sufficient evidence to belive presence of oxygen along with BN cyrstals. Carbon in the precusor always tends to separate to form graphite or diamond insetad of forming ternary B-C-N compound. However, there was no reference to ternary B-O-N compounds in the literature. This curiosity lead to focusing efforts on the synthesis of B-O-N compounds. In the next section (see section 3.2.5) approaches towards the novel ternary B-O-N compounds are presented.

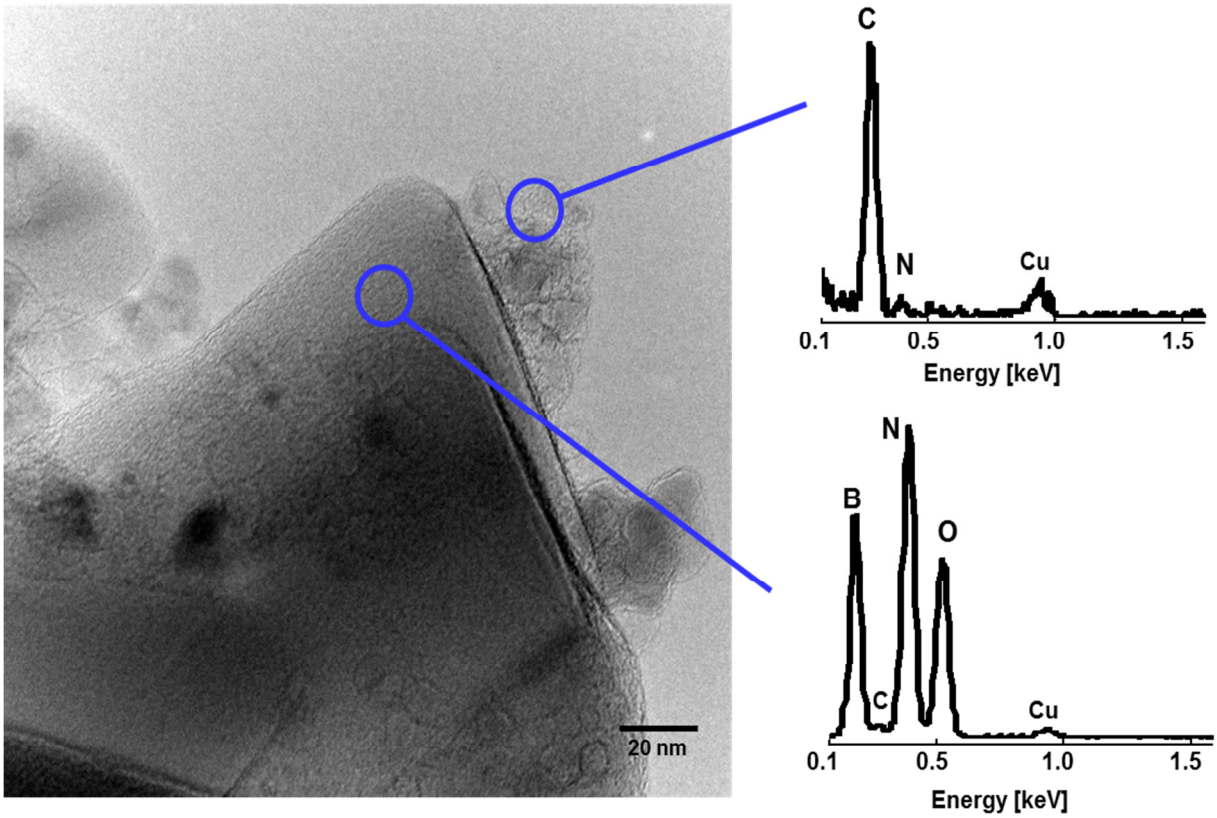

Figure 3-26. TEM image of BC_2N after DAC experiment, along with the EDX spectrum acquired in the highlighted circular area of the sample.

3.2.5. Novel Boron Oxynitride (BON)

The starting material for the B-O-N synthesis was prepared by ball-milling of a mixture of hexagonal BN (99.5% purity, Alfa Aesar) and B_2O_3 (99.98% purity, Alfa Aesar) in the ratio of 3:1 (wt. %), using zirconia anvils and balls. X-ray diffraction patterns (see section 3.1.6) of the starting materials show that the mixture turned completely amorphous after 4 h of ball milling [238]. HP-HT experiments (15.6 GPa and 1900°C for 20 min) were performed in a Walker type multi-anvil apparatus (6/8 type), installed (offline) at DESY, Hamburg (more details in section 2.2.3.2). After HP-HT treatment, the recovered sample contained, besides c-BN, a new phase (BON), which is described in the following sections.

3.2.5.1 Chemical Composition by EELS

Nano-sized crystals of BON with triangular shape were identified in TEM images. The typical morphology of triangular-shaped BON crystals is shown below (Figure 3-27). EELS was performed to quantify the composition of BON. The EELS spectrum clearly shows the presence of boron, nitrogen and oxygen, but no carbon (see Figure 3-28) with the onset of K-ionization edges at 187.5 eV (B), 399.7 eV (N) and 531.5 eV (O). The sp^2 signature (pre-peaks) were not observed in the fine structure of the B, N and O ionization edges of the recorded electron energy-loss spectra, thus strongly indicating a sp^3 type of bonding [245-247]. After careful background subtraction, the ionization edges were treated using the Hartree-Slater cross-section model. The corresponding chemical quantification yielded 42 at.% B , 35 at.% N and 23 at.% O (=5.3 : 4.4 : 3). Because of the need for balanced charges of the B^{3+}, N^{3-}, and O^{2-} ions, the composition should be a mixture of x BN and y B_2O_3, which constrains the difference of the number of boron and nitrogen ions to be two third of the number of oxygen ions. Recalculation of the EELS results accordingly gives 46.1 at.% B, 30.8 at.% N and 23.1 at.% O, or B:N:O = 6:4:3 which is within the experimental error of ±10% [53, 248].

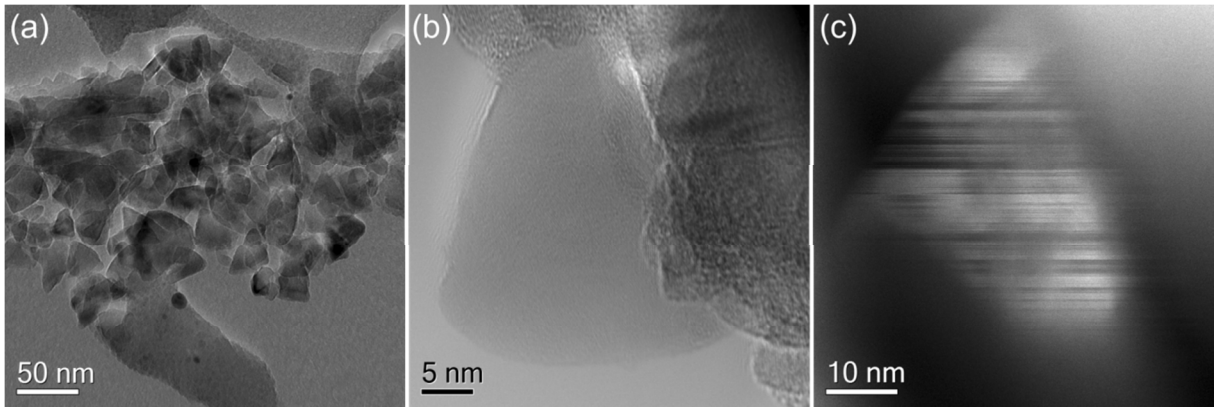

Figure 3-27. Typical triangular-shaped BON crystals (a) Overview bright-field TEM image, (b) large magnification TEM image of a BON crystal. (c) STEM Z-contrast image of a BON crystal [238].

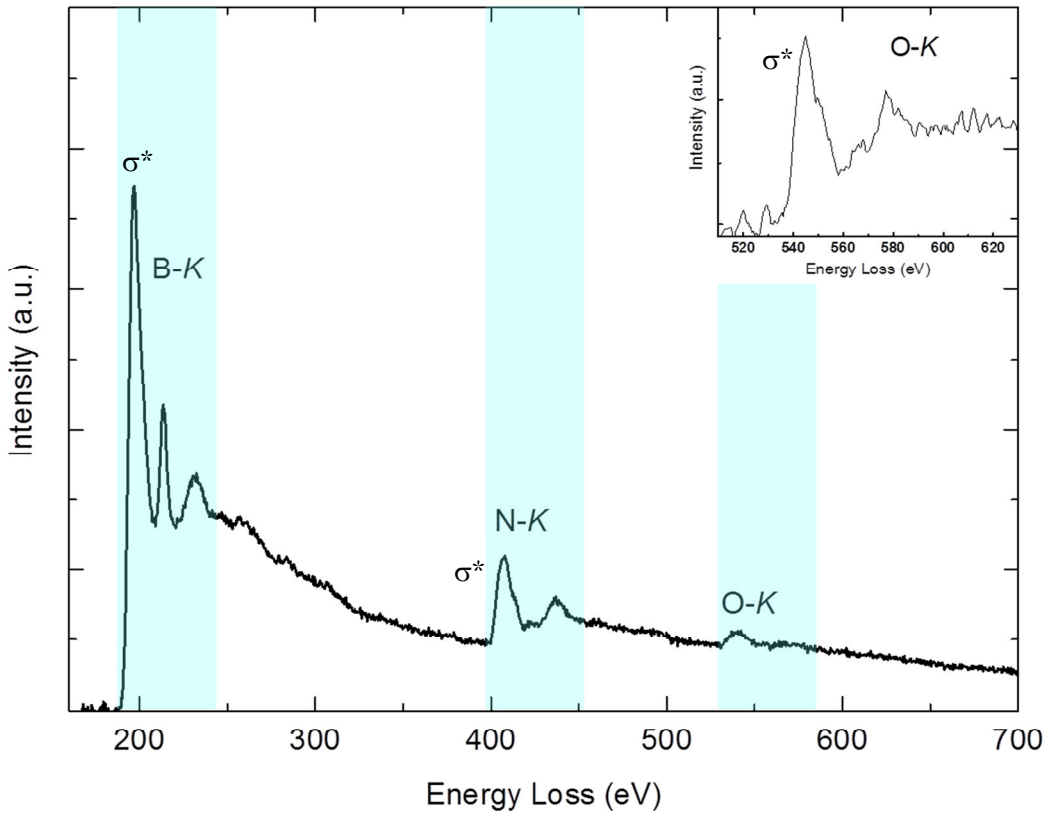

Figure 3-28. Electron energy-loss spectrum (EELS) showing the B-K, N-K and O-K ionization edges after background subtraction. The highlighted light blue areas indicate the integration width used for quantification. The inset figure shows the electron energy-loss near edge fine structure (ELNES) of the O-K edge (in order to reduce the noise, the data were smoothened by the Savitzky-Golay method) [238].

3.2.5.2 Crystal Structure

Electron diffraction experiments were performed on triangular single crystals of BON less than 50 nm in size. 3D diffraction intensity data were collected coupling ADT and precession electron diffraction (PED)[238]. The reflections could be indexed using a hexagonal unit cell with a = 2.55 (5) Å, c = 6.37(13) Å and Z=3. The symmetry is pseudo cubic with a_{cub} = 3.63 Å, Z=4. The experimental $(c/a)^2$= 6.24, while the ideal $(c/a)^2$= 6 for cubic crystals, which corresponds to the experimental values within the limits of error. BON structure was initially solved with respect to a hexagonal lattice in space group $P3_1$ (because of the presence of reflections, which cannot be indexed by a single cubic or rhombohedral cell). The solution showed essentially an arrangement of atoms similar to that of the sphalerite structure of cubic boron nitride with space group $F\bar{4}3m$. Therefore, a high-symmetry subgroup of $F\bar{4}3m$, namely $R3m$ (No. 160) was chosen for further structure refinement (Figure 3-29a) [238]. Relation between rhombohedral, hexagonal and cubic unit cells is shown in Figure 3-30. From this we can clearly see that, the face-centered cubic cell

corresponds to an R-centered hexagonal cell where the rhombohedral cell is the common primitive cell of both the hexagonal and the cubic lattice (see Figure 3-30).

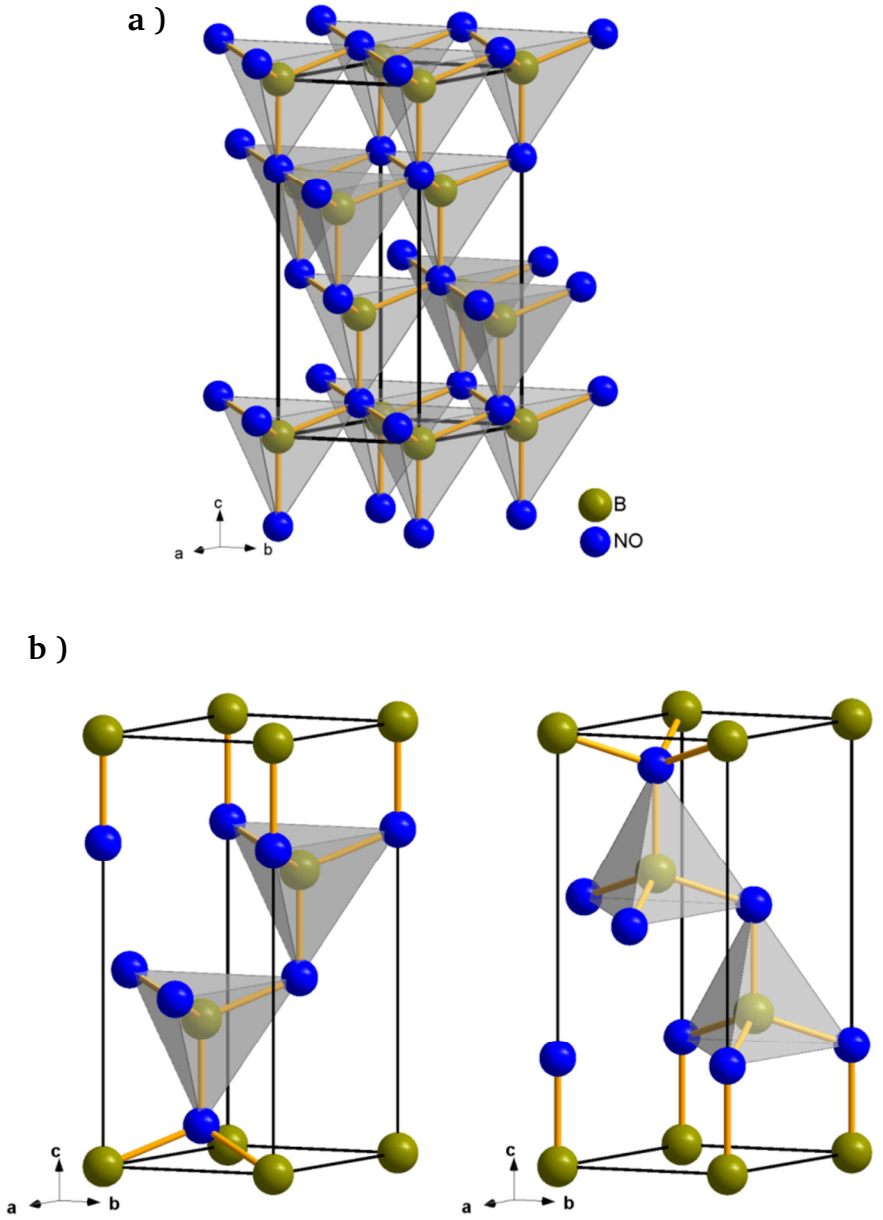

Figure 3-29. (a) Unit cell of BON, (b) Left: Obverse main domain, Right: Reverse twin domain due to spinel law [238].

The majority of reflections (on the whole 99), including all strong reflections, can be indexed by a rhombohedral unit cell in either the obverse or the reverse setting. The strongest reflections (58 out of 164) were assigned to the obverse setting and another set of 60 less strong reflections (with an overlap of 19) to the reverse setting. This also implies that the

crystal was twinned. The HRTEM image (Figure 3-31), which shows a (111) twin plane, also supports this observation according to the well-known spinel law as illustrated in Figure 3-29b. Structure refinements were performed in space group R3m, using the hexagonal unit cell and a twin law relating the obverse and reverse settings of the rhombohedral cell. From the EELS results, the chemical composition is fixed to B:N:O = 6:4:3 (after charge balance B^{3+}, N^{3-} and O^{2-}). Due to the similarity of the B, N and O scattering factors (no superstructure reflections found), we observe an average structure with cations and anions distributed statistically over their respective lattice sites.

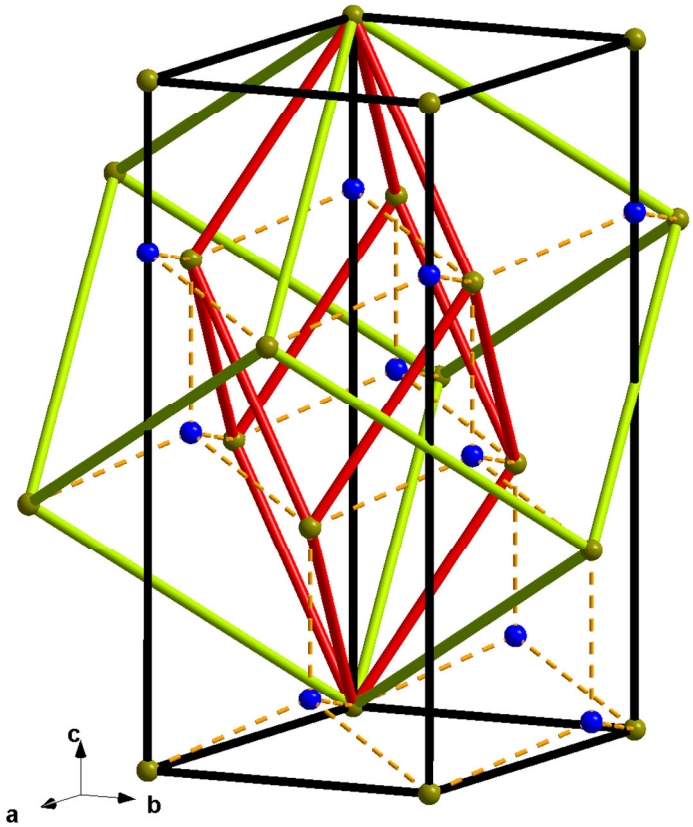

Figure 3-30. Relation between unit cells: rhombohedral (red), hexagonal (black) and cubic (green) [238].

It is reasonable to assume that oxygen atoms together with nitrogen atoms occupy anion positions. Since the number of N+O atoms (anions) is larger than the number of boron atoms (cations), cation sites are only partially occupied to achieve charge balance [238]. These requirements lead to occupancies of 4/7 (57%) for nitrogen, 3/7 (43%) for oxygen and 6/7 (86%) for boron, i.e. 14% of the cation sites are empty. These are structural vacancies, such

as known e.g. in the spinel-type aluminium oxynitrides (γ-ALON) [249, 250], not to be misinterpreted as point defects.

This structure model was refined successfully and resulted in a residual of R1= 0.189 (R1 = Σ_{hkl} | $|F_{obs}| - |F_{calc}|$ | / Σ_{hkl} $|F_{obs}|$) and a refined twin fraction of 11%. A test refinement without oxygen atoms and cation vacancies, i.e. with an ideal c-BN structure, however worsened the fit. On the contrary, it was even possible to refine (R1= 0.190) the chemical composition under the constraint of balanced charges which resulted in 46 at.% B, 32 at.% N and 22 at.% O, being in good agreement with the EELS results [238].

The hexagonal BON structure (*R3m,* Z=3) may be compared with the structure of cubic boron nitride (*F$\bar{4}$3m*, Z=*4*) via their common primitive rhombohedral lattice (see Figure 3-30). The unit cell volume of BON (V_{cub}= 47.83 Å^3) is slightly larger than that reported for cubic boron nitride with values [243, 251, 252] of 47.28 Å^3, 47.40 Å^3 or 47.63 Å^3. Nitrogen and oxygen atoms are assumed to be distributed statistically over the anion sites while boron and structural vacancies are distributed statistically over the cation sites (Figure 3-29). All atoms, N/O as well as B, are situated on three-fold axes and mirror planes and show a slightly distorted tetrahedral coordination with three B-O/N distances of 1.57(3) Å and one B-O/N distances of 1.58(10) Å, which are equal within the limits of error. The reported B-N distances in c-BN [243, 251, 252] of 1.566 Å, 1.567 Å or 1.570 Å are similar [238].

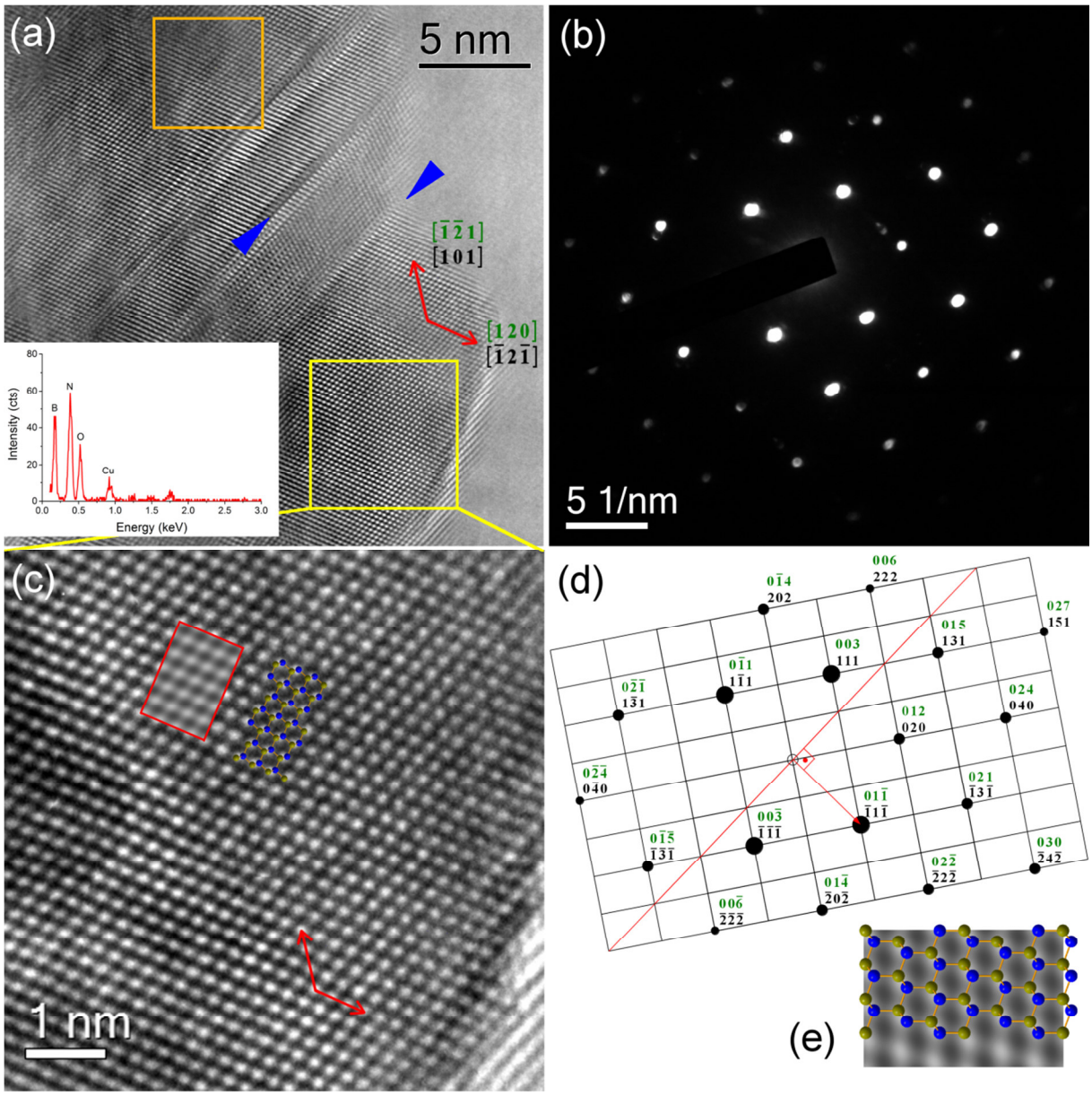

Figure 3-31. (a) High-resolution phase contrast image. The orange square denotes the area at which the EDX spectrum shown in the inset was acquired. The blue triangles denote twin boundaries. (b) Electron diffraction pattern of BON in $[100]_{hex}$ ($[10\text{-}1]_{cubic}$) zone axis orientation. The spots can be indexed with respect to a hexagonal (green) or cubic lattice (black), as shown in (d). The red line indicates a [111] type twin plane, which can be seen in the HRTEM image. (c) Magnified view of the area marked by the yellow box in part (a). The red bordered inset is a simulated image of BON in $[100]_{hex}$ ($[10\text{-}1]_{cubic}$) zone axis orientation and contains 2x4 unit cells. (e) View of the crystal structure (B: green, N/O: blue) projected along the hexagonal a-axis, overlaid on the simulated HRTEM image [238].

3.2.5.3 High Resolution Transmission Electron Microscopy

A HRTEM image in $[100]_{hex}$ zone axis orientation of the synthesized BON sample is given in Figure 3-31. The corresponding electron diffraction pattern, is shown in Figure 3-31b. The reflections could be indexed with respect to a cubic lattice and correspond to *d* values (in Å) of 2.1 {111}, 1.8 (020), 1.3 {202}, 1.1 {131} and 0.9 (040). A full indexation with respect to the cubic (black) and the hexagonal (green) lattice is given in Figure 3-31d. EDX measurements (see the inset in Figure 3-31a) confirmed that the crystals with triangular morphology consistently contain considerable amounts of oxygen along with boron and nitrogen. These findings are also consistent with our earlier experimental results of the ternary BCN compounds where the triangular shaped crystals showed the same composition [27]. Figure 3-31c shows an enlarged section of the HRTEM image that is compared with a simulated image overlaid within the red frame. We used the JEMS [216] software to carry out multislice calculations (see Figure 3-32**)** by using the atomic model from the crystal structure refinement of BON in $[100]_{hex}$ zone axis orientation. In this thickness and defocus range the bright dots correspond to two atomic columns, i.e. B and N/O, being so close that they cannot be separated using the employed imaging conditions, as can be seen in the overlaid structure picture in Figure 3-31e [238].

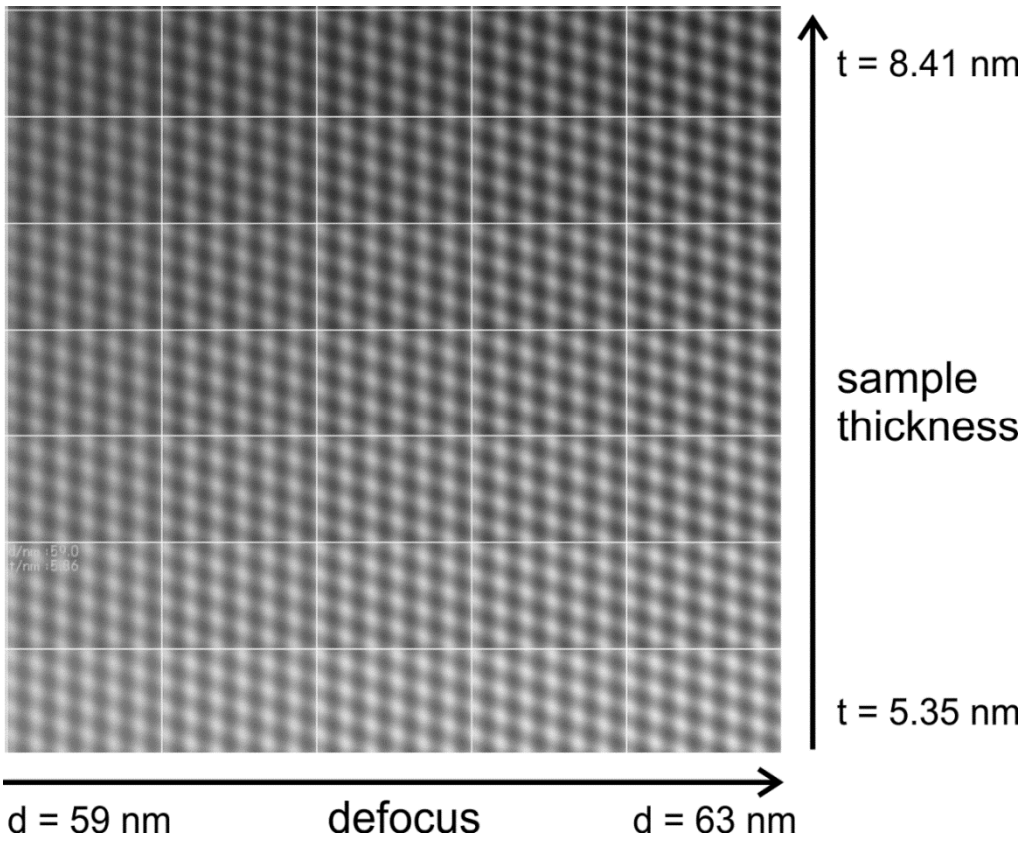

Figure 3-32. Simulated thickness-defocus map of BON in $[100]_{hex}$ ($[10\text{-}1]_{cubic}$) zone axis orientation. The unit cell duplication was 2x in horizontal direction and 4x in vertical direction [238].

3.2.5.4 Density Functional Theory (DFT) Calculations

Calculations in the framework of Density Functional Theory (DFT) have been performed in collaborations with the group of Prof. Peter Kroll (UT Arlington, USA) and Prof. Karsten Albe (TU Darmstadt, Germany). The structural, electronic, mechanical and thermodynamic properties of proposed models with the composition $B_6N_4O_3$ were studied. The discussion of algorithms, methods and functionalisms can be found in elsewhere [238]. In the present thesis, details are limited to predicted models and its properties.

DFT calculations were performed to identify structures with the composition $B_6N_4O_3$ suggested by the EELS results and to analyze possible structural motifs. The candidates with lowest enthalpy at 20 GPa are two isoenergetic (within 0.01 eV per formula unit) monoclinic structures (*Cm*). They are best described as ordered sphalerite type structures, with structural vacancies (1/7 of all cation sites) tetrahedrally surrounded by oxygen atoms. With only oxygen located adjacent to vacancies, these $B_6N_4O_3$ structures exhibit all B and N atoms as four-fold coordinated, but O atoms as three- and two-fold coordinated. The lattice parameters (a, b, c, β, V) are 10.972 Å, 2.502 Å, 6.134 Å, 67.614°, 155.71 Å^3 ("Cm-1") and 8.229 Å, 2.477 Å, 7.454 Å, 96.008°, 151.11 Å^3 ("Cm-2") [238]. From the models (Figure 3-33 a, b) we can also see that, the coordination tetrahedra of the cation-vacancies share an oxygen atom and are arranged in channels along the b-axis. The structures differ only by the arrangement of the channels on the (010) plane.

Results [238] revealed that, monoclinic structure models contain chains of cation vacancies have lowest enthalpy of formation of 0.9 eV, compared to different models with disorder on cation and anion positions. The most favorable disordered model (shown in Figure 3-33c) had a formation enthalpy of +1.5 eV per formula unit at 20 GPa. Theoretical studies [238] infer that, the presence of boron vacancies arranged in channels is a crucial prerequisite for the stabilization of BON, although the coordination environment of boron vacancies has an even more dramatic effect on stability than the disruption of the vacancy ordering.

To compare the predicted properties of our BON models with the calculated properties of cubic BN, the electronic density of states of c-BN and our BON models (see Figure 3-34) were calculated [238]. With Local Density Approximation (LDA), the calculated band-gap for c-BN is 4.44 eV. As expected, this value severely underestimates the experimental band-gap of 6.36 eV [253], but still allows for a qualitative comparison with the newly found oxynitride compound. The calculated bandgaps for Cm-1, Cm-2 and disordered structure models are 3.88 eV, 3.24 eV and 3.46 eV, respectively.

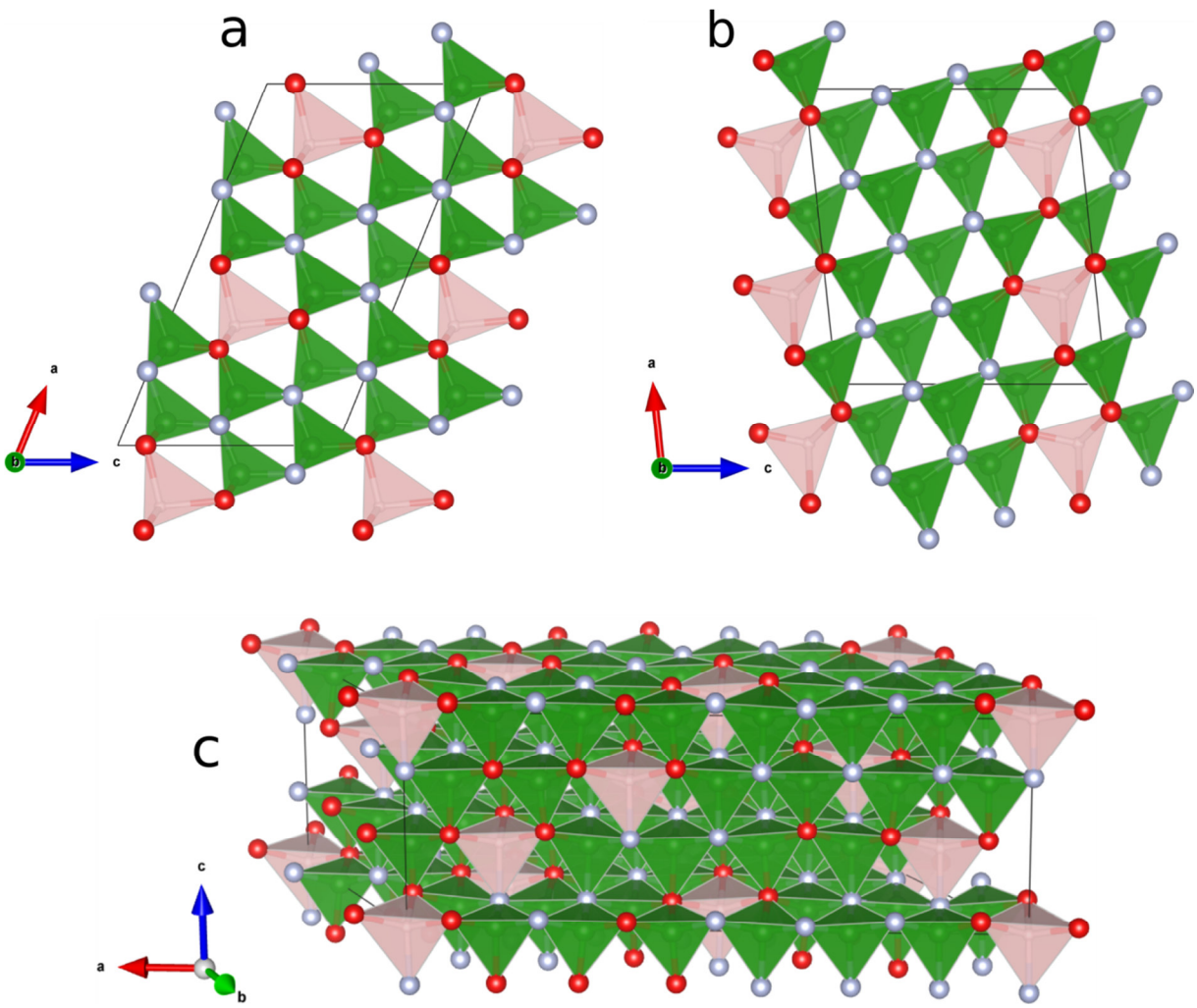

Figure 3-33. Relaxed structures of the Cm-1 (a), Cm-2 (b), and disordered (c) BON models. Boron atoms are depicted in green, nitrogen in light blue and oxygen in red. Green polyhedra represent B-centered tetrahedra; vacancy-centered tetrahedra are depicted in pink [238].

The bulk moduli of the three materials have been calculated by fitting their energy-volume dependence to the third-order Birch-Murnaghan equation of state [254] (see Table 3-3). This procedure yields a bulk modulus of 398(4) GPa for c-BN, being in good agreement with the experimental value of 396(2) GPa [255]. With the same procedure, we find bulk moduli of 306(3) and 298(4) GPa, for the *Cm* models respectively, and a value of 314(1) GPa for the disordered model [238]. These values are higher than any other known oxynitride.

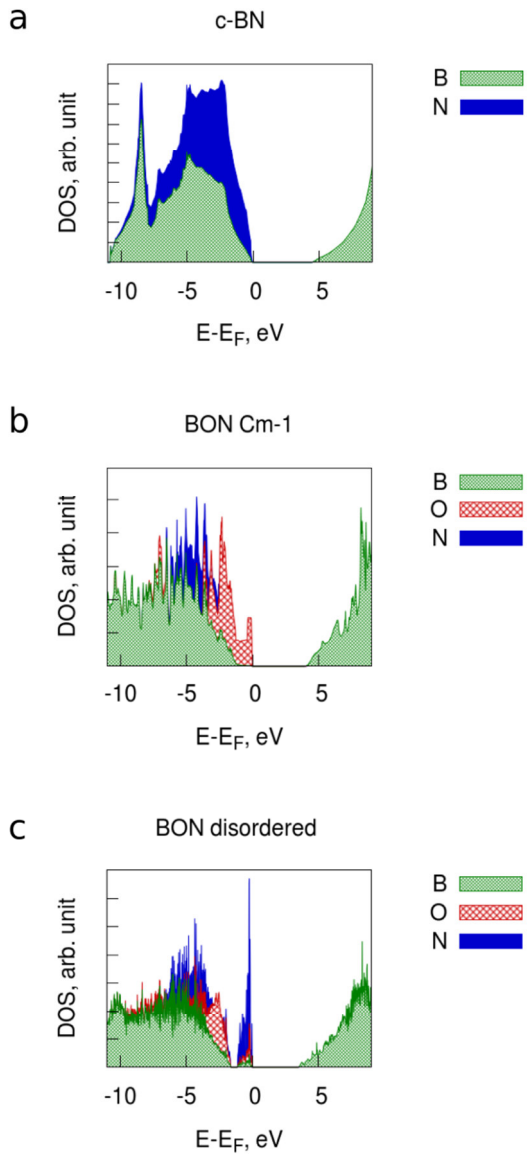

Figure 3-34. Calculated electronic density of states of c-BN (a), BON Cm-1 (b) and BON disordered (c). As the features of the two Cm models are very similar, only Cm-1 is displayed.

Table 3-3. Fitted bulk moduli and their derivatives of c-BN and BON (Cm-1, Cm-2, disordered)

	c-BN	Cm-1	Cm-2	disordered
$B = -V(\partial P/\partial V)_{P=0}$, GPa	398 ± 4	306 ± 3	298 ± 4	314 ± 1
$D = (\partial B/\partial P)_{P=0}$	4.0 ± 0.6	3.5 ± 0.5	3.9 ± 1.4	4.8 ± 0.1
V_0, Å^3	11.501± 0.002	80.03 ± 0.06	80.44 ± 0.12	79.83 ± 0.09

3.3. Electrochemical studies on B-C-N

First cycle charge/discharge profiles of both a-BC_2N and a-BC_4N electrodes are presented in **Figure 3-35**. The charging/discharging rate is the same for both lithium insertion and extraction, equal to 18 mA g^{-1}, the data are summarized in Table 3-4. Electrochemical capacity data for BC2N and BC4N. The charging and discharging capacities of the BC_2N amount 667 and 235 mAh g^{-1}, respectively. The BC_2N material reveals a large irreversible capacity loss during first cycle, with columbic efficiency of around 30%. The first cycle charging capacity of BC_4N is much higher and amounts 1030 mAh g^{-1}. The discharge capacity of 737 mAh g^{-1} leads to a much higher first cycle efficiency of 72%. It should also be noticed that most of the capacity is recovered below 1.5 V, the investigated materials present reduced hysteresis in comparison to other polymer-derived electrode material [234, 236].

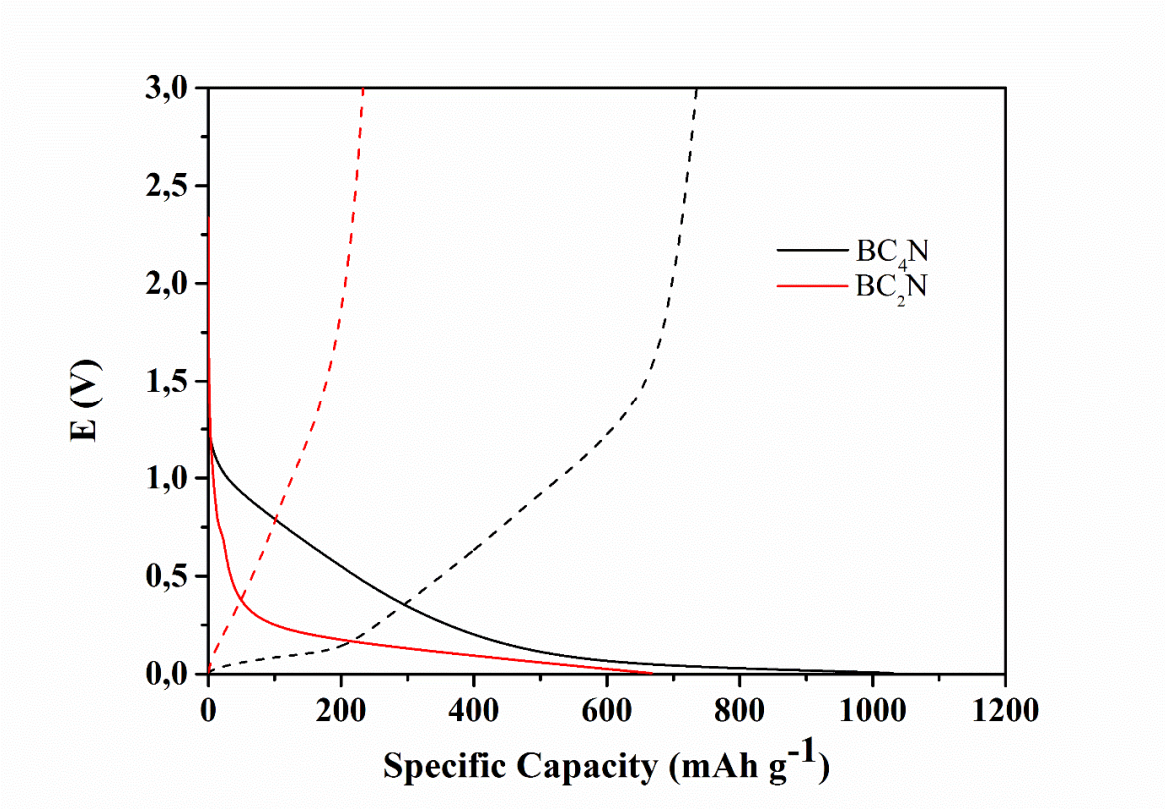

Figure 3-35. First cycle lithiation/delithiation profiles of the studied BCN samples at a rate of C/20 (18 mA g-1). Solid line represents lithiation and dotted line represents delithiation [256].

Table 3-4. Electrochemical capacity data for BC_2N and BC_4N.

Sample	Li $_{insertion}$ (mAh g^{-1})	Li $_{extraction}$ (mAh g^{-1})	Efficiency (%)	Capacity Recovery (mAh g^{-1})
BC_2N	667	235	35	265
BC_4N	1030	737	72	600

The enhanced electrochemical lithium storage properties registered for BC_4N with respect to BC_2N (=BNx2C) are attributed to the increased amount of carbon content in the BC_4N (=BNx4C) material, which is 65 wt% with respect to 45 wt% present within the BC_2N structure. It has been already reported in previous studies that increasing the carbon content in BCN based anodes increases the electrochemical lithium storage capacities [181]. This report is in agreement with the reduced performance of comparatively less carbon content BC_2N ceramics, and for BC_4N the increased carbon content of 65 wt% of the total carbon in bulk ceramics explains the high storage capacities. The capacities of the BC_2N and BC_4N recovered during extended cycling with increasing rate are presented in

Figure 3-36. Initially at slow rates, the fading of capacity is registered. The values stabilize after 10-15 cycles and remain stable during extended cycling. BC_2N cells show good cycling stability but low capacities of 125 mAh g^{-1} at C/2 rate, ~ 100 mAh g^{-1} at C rate and ~80 mAh g^{-1} at 2C rate. BC_4N gains the stability after 15 cycles and recovers capacities of ~400 mAh g^{-1} at C/2 (180 mA g^{-1}), ~300 mAh g^{-1} at C (360 mA g^{-1}) and ~200 mAh g^{-1} is maintained at a rate of 2C (720 mA g^{-1}).

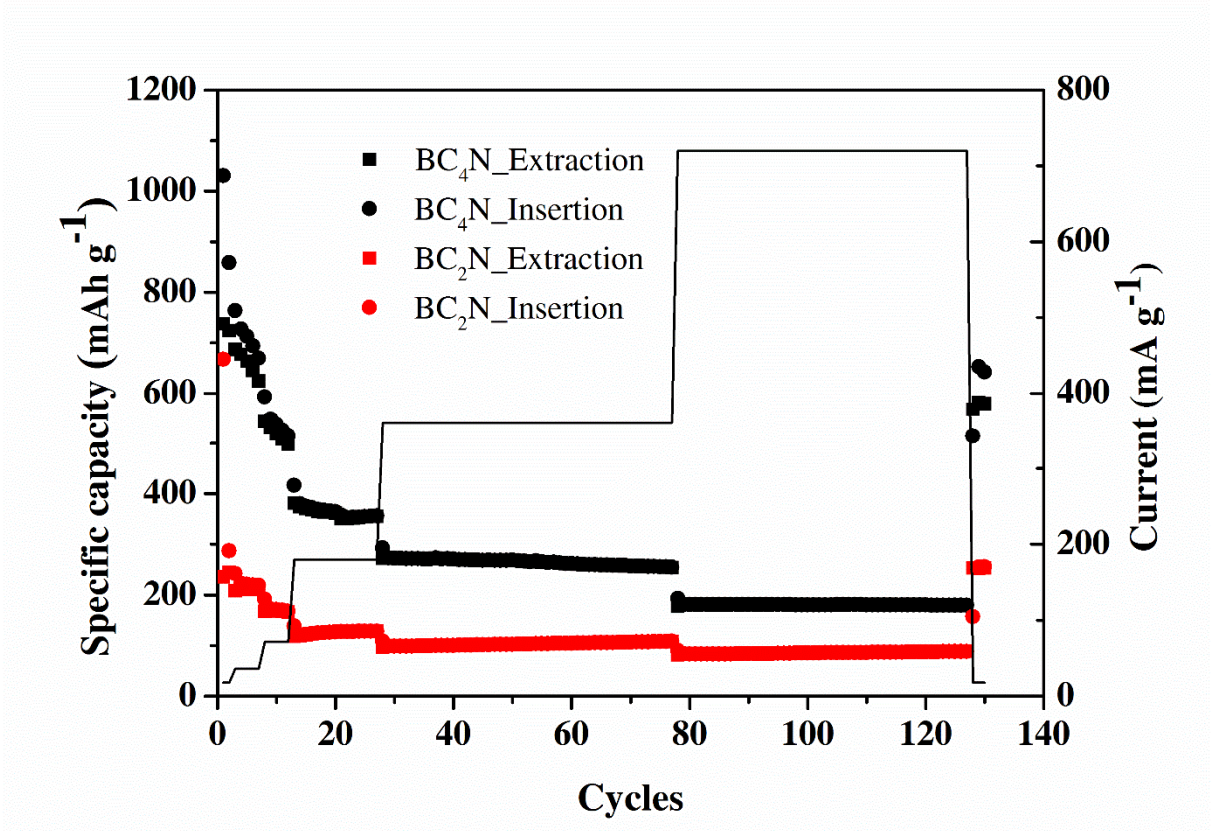

Figure 3-36. Electrochemical cycling of BCN samples at different current rates, from C/20 to 2C (18 mA g^{-1} – 720 mA g^{-1}) [256].

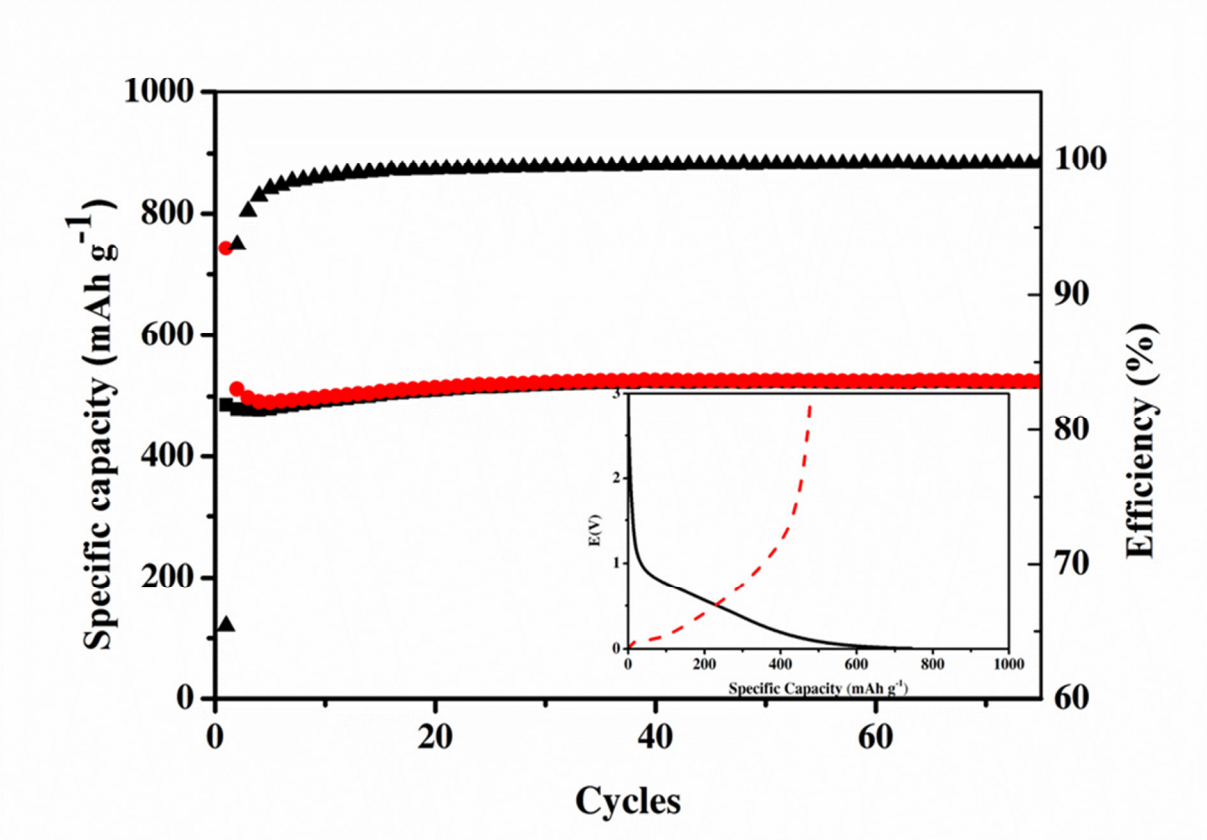

Figure 3-37. Cycling of BC_4N electrode for 75 cycles at 100 mA g^{-1}. Inset shows the first cycle charging/discharging profile [256].

Both BCN compounds demonstrate good capacity recovery when the initial rate was imposed after high currents. A reversible capacity of 600 mAh g^{-1} is recovered for BC_4N cell and a capacity of ~265 mAh g^{-1} is recovered in case of the BC_2N electrode, respectively. The BC_4N cells with high specific capacity has been subjected to cycling at a constant rate for 75 cycles at 100 mA g^{-1} to check the long term cycling stability. The cycling data is presented in Figure 3-37. The cells cycled at this rate have an initial charging capacity of 730 mAh g^{-1} and a discharge capacity of 500 mAh g^{-1} with first cycle columbic efficiency of 65 %. BC_4N shows excellent cycling stability with an almost constant specific capacity higher than 500 mAh g^{-1}. The charging/discharging efficiency of the cells reached ~99% from the 10^{th} cycle.

With respect to carbon-poor BCN, carbon rich BCN electrodes show significantly larger reversible capacity. The coulombic efficiency of 73% for the initial slow rate lithiation/delithiation cycle is registered for BC_4N composition. From the structural investigations there is no significant difference between the bonding pattern in both BC_2N and BC_4N ceramics: The two compounds extensively differ in the amount of free carbon phase in the final ceramics which in turn seems to influence their final electrochemical performance.

By analogy, we assume that a decreased carbon content, which serves as the major active phase for reversible Li insertion in polymer derived SiCN and SiOC ceramics [257-260] is considered to be the main reason for a diminished electrochemical performance.

The complex nanostructure of BCN materials makes it difficult to identify the Li storage mechanism inside this ceramic matrix. The presence of boron and nitrogen atoms having different electronic configuration in a largely distributed free carbon network may help in attracting excess electrons, and making way for more lithium storage. Boron can also act as an electron acceptor, facilitating fast lithium ion diffusion through the doped carbon matrix. A clear mechanism for lithium insertion in case of BCN based anodes has not been reported in literature, yet. Kawaguchi et al. [182] stated that the amorphous nature is the main reason of poor cycling stability and high irreversible capacity reported for BCN ceramics [181]. Authors claim that, higher crystallinity of BC_6N made the potentials of lithium insertion/extraction to this material lower and insertion/extraction E (V) vs. time transients flatter than those of lower crystallinity, which is in good analogy to the relation between graphite and non-graphitic carbon [261]. It is stated that rapid intercalation of lithium ions into BC_6N ceramic results in the formation of the 1st stage intercalation compound Li_XBC_6N. It in turn suggests the strong interaction between the intercalate Li and the host material BC_6N. The 1st stage compound of Li_XBC_6N prepared by the electrochemical method had the d-spacing of 0.355 nm which is smaller than that of 1st stage GIC LiC_6 (0.370 nm). Nevertheless, the capacities of the first extraction do not exceed 300 mAh g^{-1}, and fading is found for subsequent cycles. Lei et al [22] synthesized BCN nanosheets and registered a very good rate capability and reasonable stability, however the low rate capacity does not exceed 400 mAh g^{-1}.

Within this study we investigated the BCN ceramics of amorphous nature which recover a stable capacity of 500 mAh g^{-1}. Although BC_4N contains less carbon than that of BC_6N [182], it demonstrates significantly enhanced electrochemical performance. The capacity stabilizes after several cycles when cycled with increasing currents, while with constant current of C/5 extremely stable behavior over 70 cycles and high capacity of ~500 mAh g^{-1} is registered. We explain these excellent electrochemical properties with respect to BC_6N using the analogy to graphite and disordered carbon. Whereas graphite with its common staging intercalation behavior presents low voltage plateaus, but low capacity, disordered carbons demonstrate often hysteresis in their potential vs. capacity curves, but much higher capacity and rate capability [262]. In similar way, the capacity of claimed crystalline BCN ceramics is limited by the ordered graphite-like structure. The amorphous compound investigated within this study can store much more lithium due to their disordered carbon phase.

4. Conclusions and Outlook

Studies of B-C-N under HP-HT conditions:

In the present work amorphous BC_2N and BC_4N are synthesized via thermal conversion of piperazine borane and pyridine borane, respectively. Synthesis process optimization of these compounds assisted preparing the starting materials with very less or negligible oxygen contamination compared to some of the earlier reports. These B-C-N compounds prepared according to the Riedel and Bill method [71, 146] are amorphous in nature and show the presence of mixed C-C, C-N and B-N bonds. Elemental analysis of the precursors by hot gas extraction methods confirmed the C/N ratios of 2:1 and 4:1 in BC_2N and BC_4N, respectively. The Riedel and Bill method which can also be described as single-source precursor route via the polymer derived ceramics method, offers the flexibility of controlling the final composition based on the starting materials. Compared to earlier studied B-C-N precursors [51, 72] prepared via solid phase pyrolysis, our precursors are free from impurities (like Cl, Si etc.) and have predefined bonds in an amorphous matrix. Hence BCN compounds were studied under HP-HT conditions, as potential starting materials for the formation of crystalline ternary B-C-N compounds.

In the present study amorphous BC_2N and BC_4N are studied under a wide range of HP-HT conditions (5- 39 GPa and 200 – 2000 °C) using different high-pressure techniques. One of the uniqueness of the current thesis is the pressure-range employed in studying the B-C-N compounds. HP-HT conditions are realized using a single-stage multi anvil (MA) press (5-7 GPa, 100- 1700 °C), toroid press (12 GPa, ~ 1000 °C), a double stage large volume press (15.6 GPa, 1900 °C) and also diamond anvil cell (DAC) (20-39 GPa, 1900 - 2000 °C). *In-situ* and *ex-situ* X-ray diffraction revealed that BC_2N remains amorphous up to 1500 °C, below 12 GPa and it starts to decompose into mixtures of graphite and h-BN above 1600 °C. In contrast, BC_4N starts to decompose into mixtures of graphite and h-BN between 7 and 12 GPa above 500 °C. HP-HT experiments performed in large volume presses and DACs showed that amorphous BC_2N and BC_4N transform into mixtures of c-BN and diamond at pressures above 15 GPa. These results were also supported by HRTEM, EDX, EELS and Raman spectroscopy.

HP-HT behavior of the BC_2N and BC_4N compounds are summarized in the pressure vs. temperature (P-T) diagram shown in Figure 4-1 and Figure 4-2, respectively. Based on the HP-HT experiment results, the P-T diagram has been marked with different regions (in different colors) indicating the different phases of the BCN compounds. Amorphous phase, mixture of h-BN and graphite and mixture of c-BN and diamond regions are highlighted using light blue, light gray, and light pink color, respectively. It is also clear from Figure 4-1 and Figure 4-2, that amorphous BC_2N compounds are more stable (remains amorphous up to 1500 °C) as compared to amorphous BC_4N compounds (up to 500 °C). The shaded gray and orange regions drawn, point towards a probable mixture of h-BN and graphite and mixture of c-BN and diamond (based on the phase-diagram of carbon [263] and boron nitride [264]),

respectively. The approximate P-T range for h-BN to c-BN and graphite to diamond (without catalyst HP-HT synthesis) transition is drawn in the both figures.

Solozhenko et al., [51] and Zhao et al., [53]claimed the successful synthesis of cubic BCN compounds over a decade ago (details cf. Chapter 1.3.2.3) using the multi anvil technique. However they failed to provide unambiguous evidence for ternary BCN compounds. For example, the results obtained by Solozhenko et al.,[51] did not obey Vegards law and the results reported by Zhao et al.,[53] can also be explained by a mixture of c-BN and diamond. It is important to mention that, in the X-ray diffractogram the predicted [87, 92] diamond-like ternary BCN compound reflections are hard to distinguish from those of c-BN and diamond even when using synchrotron radiation. The lattice parameter of c-BN (a= 3.6158 Å) and diamond (a= 3.5667 Å) are quite close, so the strong intense (111) reflections are inseparable ($d_{(111)}$ diamond = 2.059 Å and $d_{(111)}$ c-BN = 2.087 Å). According to the Vegard's law and theoretical predictetions [87, 92] diamond-like ternary BCN compounds are expected to have lattice parameter in between c-BN and diamond. That means that differentiating of the (111) reflection is more difficult even in ambient pressure and temperature conditions. In addtion to that, under HP-HT conditions peak broadening (may be due to nano-sized crystals, pressure induced strain in in-situ measurements) creates further ambiguity.

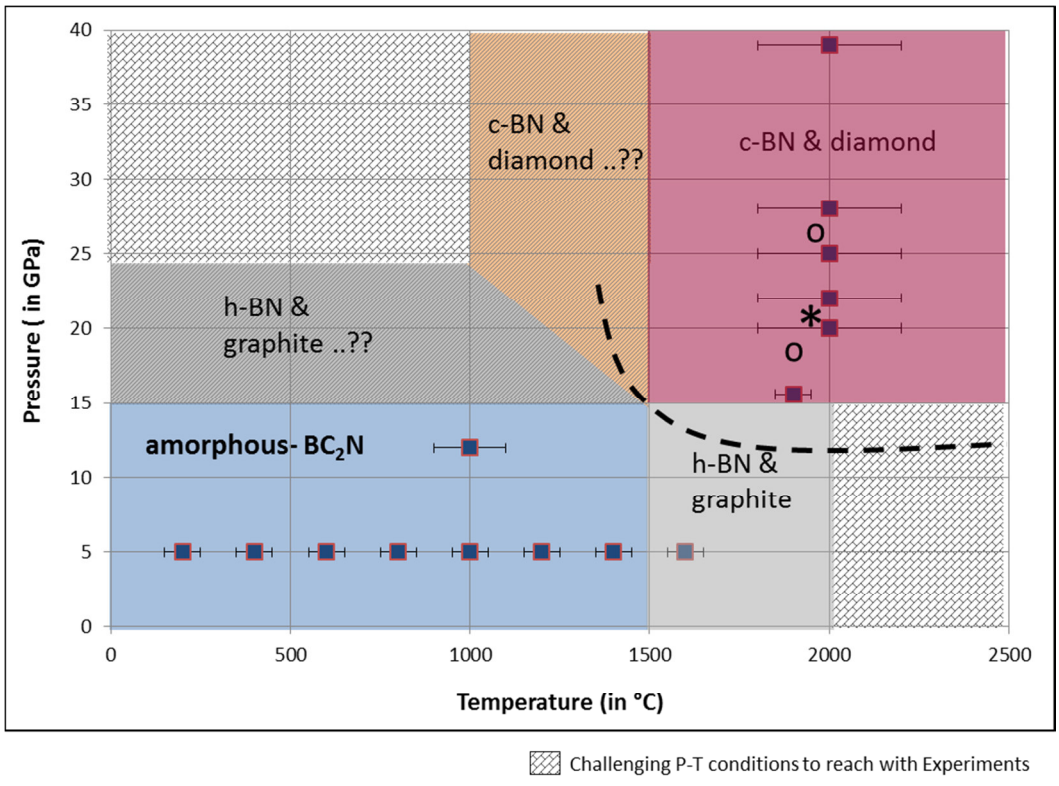

Figure 4-1. Pressure Vs Temperature (P-T) diagram for amorphous BC_2N compounds. The dotted line indicates approximate P-T range for h-BN to c-BN and graphite to diamond transition. Mark (*) and (o) shows the P-T conditions for claimed c-BC_2N by Zhao et al. and Solozhenko et al. respectively.

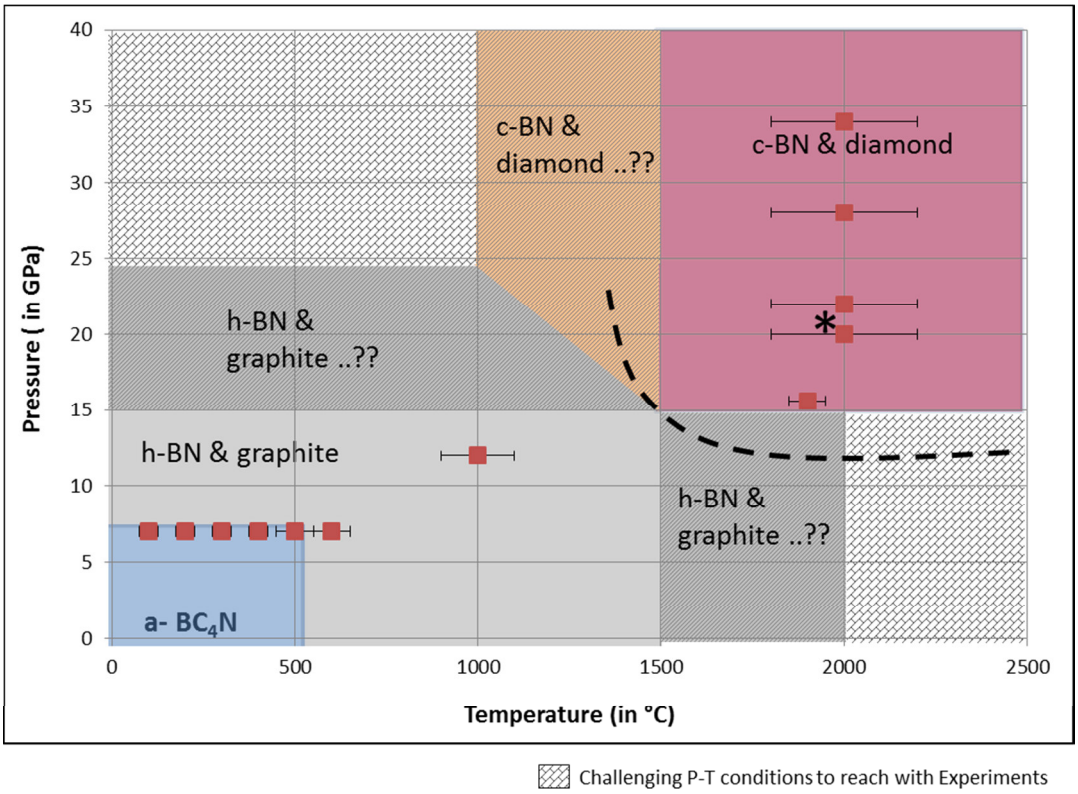

Figure 4-2. Pressure Vs Temperature (P-T) diagram for amorphous BC_4N compounds. The dotted line indicates approximate P-T range for h-BN to c-BN and graphite to diamond transition. Mark (*) shows the P-T conditions for claimed c-BC_4N by Zhao et al.

Zhao et al. emphasized on the presence of (200) reflection (at d ≈ 1.8 Å) in ternary cubic BCNs, which is absent in diamond (space group $Fd\bar{3}m$). However when the synthesized compound is a mixture of c-BN and diamond, we could have (200) reflection coming from c-BN alone. In the literature, it has been custom to support XRD findings with TEM analysis (e.g., SAED, EDX, EELS). However in case of BCN compounds, it would enhance uncertainty as *d*-values (are quite close as stated above) reported using SAED likely to have ± 10% error. It is also very important to perform TEM analysis (EDX, EELS) with precise probing beam-diameter. As our findings (cf. e.g., Figure 3-20, Figure 3-26) with the appropriate beam-diameter suggest, one should avoid probing the surrounding crystals (or agglomerated crystals) and carbon film (holy or lacy form of carbon film is used as support layer in the copper grid). We believe, to claim a reliable and an unambiguous ternary BCN phase, one should probe the sample lying outside (projected out in holes or vacuum) of the carbon film (inside the copper grid) using the beam diameter smaller than that of the probing sample (preferably a single crystal). Unfortunately all the successfully claimed reports [50-54, 152, 162] on ternary BCN compounds are lacking the aforementioned clarity in TEM analysis.

In summary, the present studies on amorphous BCN derived from piparazine borane and pyridine borane compounds reveal that upon HP-HT treatment, the amorphous BCN phase decomposes into either a mixture of h-BN and graphite or into a mixture of c-BN and diamond. We have also noticed that the decomposition temperature depends on the precursor composition. The amorphous BC_4N compounds found to decompose at lower temperature compared to that of the amorphous BC_2N compound. Our findings are also in line with some of the earlier studies [48, 49, 168] which reported simultaneous crystallization of c-BN and diamond upon HP-HT treatment. It is also important to mention that one of the recent theoretical studies, by examining the pressure effects on the phase stability [85] revealed the possibility of decomposition of c-BNC into c-BN and diamond increase with applied pressure (cf. see section 1.3.2.1.a). As ternary BCN compounds are likely metastable, it is reasonable to assume under HP-HT conditions that they form a thermodynamically stable mechanical mixture of h-BN and graphite or c-BN and diamond. From the boron nitride [264] and the carbon [263] phase diagram, we also learn that c-BN and diamond are stable above 15 GPa.

Future studies on ternary B-C-N compounds should involve the time factor along with HP-HT conditions. Systematic kinetic studies at high pressure (e.g., upon variation of the heating time and temperature) are necessary in order to evaluate the formability of ternary B-C-N phases in future HP-HT experiments. It would be very interesting to study the HP-HT behavior of these BCN compounds (derived from amine-boranes) using the dynamic high-pressure techniques like Shock-wave synthesis. One should also explore the possibilities of catalyst (like Fe-Ni, Li, Li-Mg-B) assisting the HP-HT synthesis of ternary B-C-N compounds.

Studies of B-C-N as an anode material for lithium ion batteries:

Amorphous BC_2N and BC_4N compounds are synthesized and investigated towards lithium storage properties. The BC_4N composition delivers reversible Li storage capacity as high as 735 mAh g^{-1} at a slow rate of C/20 and has a stable capacity of ~500 mAh g^{-1} at a charging/discharging rate of 100 mA g^{-1} during extended cycling. Low carbon BC_2N composition has lower specific capacities, but presents stable behavior over extended cycling. Both the B-C-N compounds are able to recover their initial capacities after cycling the cells for 135 cycles indicating the stability of the BCN-microstructure towards multiple lithiation/delithiation. Interesting electrochemical properties of these materials are generally explained in connection with their amorphous nature and with the presence of high amount of disordered and *in situ* formed carbon along with boron and nitrogen hetero atoms distributed in the structural network.

Discovery of boron oxynitrides

Our newly discovered BON reported here is the first example of the existence of a crystalline ternary oxynitride phase of boron and complements and extends the well-known group 13

element oxynitrides of aluminum and gallium. The BON phase was synthesized in single-crystalline form by HP-HT technique [238]. With the help of advanced methods related to electron diffraction (ADT and PED) the crystal structure was solved. The refined structure of BON shows a hexagonal cell (*R3m*, Z=3) with lattice parameters a = 2.55(5) Å and c = 6.37(13) Å. This structure is closely related to the cubic sphalerite type, similar to c-BN. The EELS quantification (of individual nanocrystals) yielded 42 at.% B , 35 at.% N and 23 at.% O (B:N:O ≈ 6:4:3 or $B_6N_4O_3$). In the refined model, nitrogen and oxygen share the anion position, while boron and structural vacancies occupy the cation position.

Supporting DFT calculations identify structures with the composition $B_6N_4O_3$ and low enthalpy of formation at 20 GPa that agree with our experimental results, i.e. are compatible with the intensities from electron diffraction. DFT results revealed that monoclinic structure models containing chains of cation vacancies have lowest enthalpy of formation, compared to different models with disorder on cation and anion positions. Further studies on vacancy ordering infer that, the presence of boron vacancies arranged in channels is a crucial prerequisite for the stabilization of BON along with the coordination environment.

The calculated band gap of BON models varies from 3.24 eV to 3.88 eV depending on the model. As LDA severely underestimates the band gap values, the real band gap of the BON compounds may be well above 4 eV, suggesting an insulating nature. The calculated bulk moduli values are around 300 GPa, higher than any other known oxynitride.

For future studies, one should focus on synthesizing phase pure $B_6N_4O_3$ compounds as it would help to study the properties of novel material. Since these are one of the first examples of the BON family, it would be very interesting analogy to the AlON family to study the formability of different BON compositions and their properties.

References

[1] Supplementary Report of the Committee on the Survey of Materials Science and Engineering, N. A. o. S., *Materials and Man's Needs: Materials Science and Engineering*. Vol. 1. 1975, USA: National Academy of Sciences.

[2] *Oxygen*. Available from: https://web.archive.org/web/20071026034224/http://periodic.lanl.gov/elements/8.html.

[3] Croswell, K., *Alchemy of the Heavens*. 1996: Random House Publishers.

[4] *Encyclopedia of Materials*. Vol. 7, p. 6161. 2001, Amsterdam: Elsevier.

[5] Fuertes, A., *Synthesis and properties of functional oxynitrides - from photocatalysts to CMR materials.* Dalton Trans., 2010. 39(26): p. 5942-5948.

[6] Ettmayer, P. and Lengauer, W., *Nitrides*, in *Ullmann's Encyclopedia of Industrial Chemistry*. 2000, Wiley-VCH Verlag GmbH & Co. KGaA.

[7] Roberts, K. L. and Covington, L., *Nitrides*, in *Kirk-Othmer Encyclopedia of Chemical Technology*. 2000, John Wiley & Sons, Inc.

[8] Xie, R.-J. and Hintzen, H. T., *Optical Properties of (Oxy)Nitride Materials: A Review*. J. Am. Ceram. Soc., 2013. 96(3): p. 665-687.

[9] Zerr, A., Riedel, R., Sekine, T., Lowther, J. E., Ching, W. Y., and Tanaka, I., *Recent Advances in New Hard High-Pressure Nitrides.* Adv. Mater., 2006. 18(22): p. 2933-2948.

[10] Horvath-Bordon, E., Riedel, R., Zerr, A., McMillan, P. F., Auffermann, G., Prots, Y., Bronger, W., Kniep, R., and Kroll, P., *High-pressure chemistry of nitride-based materials.* Chem. Soc. Rev., 2006. 35(10): p. 987-1014.

[11] Schnick, W., *Solid-State Chemistry with Nonmetal Nitrides.* Angewandte Chemie International Edition in English, 1993. 32(6): p. 806-818.

[12] Zeuner, M., Pagano, S., and Schnick, W., *Nitridosilicates and Oxonitridosilicates: From Ceramic Materials to Structural and Functional Diversity.* Angew. Chem. Int. Ed., 2011. 50(34): p. 7754-7775.

[13] Xie, R.-J. and Hirosaki, N., *Silicon-based oxynitride and nitride phosphors for white LEDs—A review.* Science and Technology of Advanced Materials, 2007. 8(7-8): p. 588.

[14] *The Nobel Prize in Physics 1946*. Available from: http://www.nobelprize.org/nobel_prizes/physics/laureates/1946/bridgman-bio.html.

[15] Keppler, H. and Frost, D. J., *Introduction to minerals under extreme conditions*, in *EMU Notes in Mineralogy, Vol. 7: Mineral Behaviour at Extreme Conditions*, R., M., Editor. 2005, Eötvös University Press: Budapest. p. 1-30.

[16] Chandra Shekar, N. V. and Rajan, K. G., *Kinetics of pressure induced structural phase transitions—A review.* Bull. Mater. Sci., 2001. 24(1): p. 1-21.

[17] Zerr, A., Miehe, G., Serghiou, G., Schwarz, M., Kroke, E., Riedel, R., Fuesz, H., Kroll, P., and Boehler, R., *Synthesis of cubic silicon nitride.* Nature, 1999. 400(6742): p. 340-342.

[18] Zerr, A., Miehe, G., and Riedel, R., *Synthesis of cubic zirconium and hafnium nitride having Th_3P_4 structure.* Nat. Mater., 2003. 2(3): p. 185-189.

[19] Wentorf, R. H., *Cubic Form of Boron Nitride.* J. Chem. Phys., 1957. 26(4): p. 956-956.

[20] Bailey, M. W., *Superabrasive tools: A Brief Introduction*, in *Handbook of Ceramic Hard Materials*, Riedel, R., Editor. 2000, WILEY-VCH: Weinheim. p. 479-485.

[21] Riedel, R., *Materials harder than diamond?* Adv. Mater., 1992. 4(11): p. 759-761.

[22] Lei, W. W., Qin, S., Liu, D., Portehault, D., Liu, Z. W., and Chen, Y., *Large scale boron carbon nitride nanosheets with enhanced lithium storage capabilities.* Chem. Commun., 2013. 49(4): p. 352-354.

[23] Ci, L., Song, L., Jin, C., Jariwala, D., Wu, D., Li, Y., Srivastava, A., Wang, Z. F., Storr, K., Balicas, L., Liu, F., and Ajayan, P. M., *Atomic layers of hybridized boron nitride and graphene domains.* Nat. Mater., 2010. 9(5): p. 430-435.

[24] Lei, W., Portehault, D., Dimova, R., and Antonietti, M., *Boron Carbon Nitride Nanostructures From Salt Melts: Tunable Water-Soluble Phosphors.* J. Am. Chem. Soc., 2011. 133(18): p. 7121-7.
[25] Bhattacharya, S., Majumder, C., and Das, G. P., *Hydrogen Storage in Ti-Decorated BC_4N Nanotube.* J. Phys. Chem. C, 2008. 112(45): p. 17487-17491.
[26] Portehault, D., Giordano, C., Gervais, C., Senkovska, I., Kaskel, S., Sanchez, C., and Antonietti, M., *High-Surface-Area Nanoporous Boron Carbon Nitrides for Hydrogen Storage.* Adv. Funct. Mater., 2010. 20(11): p. 1827-1833.
[27] Bhat, S., Molina-Luna, L., Mugnaioli, E., Lauterbach, S., Bayarjargal, L., Kolb, U., Winkler, B., and Riedel, R. *Hint towards novel Boron Oxy-Nitrides (BON)?* in *52nd EHPRG Meeting*. 2014. Lyon, France.
[28] McCauley, J. W., *A Simple Model for Aluminum Oxynitride Spinels.* J. Am. Ceram. Soc., 1978. 61(7-8): p. 372-373.
[29] Fuertes, A., *Chemistry and applications of oxynitride perovskites.* J. Mater. Chem., 2012. 22(8): p. 3293-3299.
[30] McCauley, J. W., Patel, P., Chen, M., Gilde, G., Strassburger, E., Paliwal, B., Ramesh, K. T., and Dandekar, D. P., *AlON: A brief history of its emergence and evolution.* J. Eur. Ceram. Soc., 2009. 29(2): p. 223-236.
[31] Maeda, K. and Domen, K., *Oxynitride materials for solar water splitting.* MRS Bull., 2011. 36(01): p. 25-31.
[32] Jack, K. H., *Sialons and related nitrogen ceramics.* J Mater Sci, 1976. 11(6): p. 1135-1158.
[33] K. H. JACK, W. I. W., *Ceramics based on the Si-Al-O-N and Related Systems.* Nature physical science, 1972. 238: p. 2.
[34] Ekström, T. and Nygren, M., *SiAlON Ceramics.* J. Am. Ceram. Soc., 1992. 75(2): p. 259-276.
[35] *ALON® Optical Ceramic*. Available from: http://www.surmet.com/technology/alon-optical-ceramics/index.php.
[36] Maeda, K., Teramura, K., Takata, T., Hara, M., Saito, N., Toda, K., Inoue, Y., Kobayashi, H., and Domen, K., *Overall Water Splitting on $(Ga_{1-x}Zn_x)(N_{1-x}O_x)$ Solid Solution Photocatalyst: Relationship between Physical Properties and Photocatalytic Activity.* J. Phys. Chem. B, 2005. 109(43): p. 20504-20510.
[37] Maeda, K., Teramura, K., Lu, D., Takata, T., Saito, N., Inoue, Y., and Domen, K., *Photocatalyst releasing hydrogen from water.* Nature, 2006. 440(7082): p. 295-295.
[38] Hubáček, M., Sato, T., and Ishii, T., *A Coexistence of Boron Nitride and Boric Oxide.* J. Solid State Chem., 1994. 109(2): p. 384-390.
[39] Gouin, X., Grange, P., Bois, L., L'Haridon, P., and Laurent, Y., *Characterization of the nitridation process of boric acid.* J. Alloys Compd., 1995. 224(1): p. 22-28.
[40] Xie, Y. P., Liu, G., Lu, G. Q., and Cheng, H.-M., *Boron oxynitride nanoclusters on tungsten trioxide as a metal-free cocatalyst for photocatalytic oxygen evolution from water splitting.* Nanoscale, 2012. 4(4): p. 1267-1270.
[41] Chen, G. C., Lim, D.-C., Lee, S.-B., Boo, J.-H., Kim, Y. J., and Hong, B. Y., *Synthesis of a material for semiconductor applications: Boron oxynitride prepared by low frequency rf plasma-assisted metalorganic chemical vapor deposition.* J. Vac. Sci. Technol., B, 2003. 21(4): p. 1886-1890.
[42] Badi, N., Vijayaraghavan, S., Benqaoula, A., Tempez, A., Tauziède, C., and Chapon, P., *P^2IMS depth profile analysis of high temperature boron oxynitride dielectric films.* Appl. Surf. Sci., 2014. 292: p. 1-4.
[43] Sawamura, A., *Superhard boron oxynitride and method for Producing the same*, USPTO, Editor. 2014, Sumitomo Electric Indusstries, Ltd., Osaka JP: USA.
[44] Wentorf, R. H., *Cubic Form of Boron Nitride.* The Journal of Chemical Physics, 1957. 26(4): p. 956-956.

[45] Dubrovinskaia, N., Solozhenko, V. L., Miyajima, N., Dmitriev, V., Kurakevych, O. O., and Dubrovinsky, L., *Superhard nanocomposite of dense polymorphs of boron nitride: Noncarbon material has reached diamond hardness.* Appl. Phys. Lett., 2007. 90(10): p. 101912-3.

[46] Tian, Y., Xu, B., Yu, D., Ma, Y., Wang, Y., Jiang, Y., Hu, W., Tang, C., Gao, Y., Luo, K., Zhao, Z., Wang, L.-M., Wen, B., He, J., and Liu, Z., *Ultrahard nanotwinned cubic boron nitride.* Nature, 2013. 493(7432): p. 385-388.

[47] Huppertz, H., Hering, S. A., Zvoriste, C. E., Lauterbach, S., Oeckler, O., Riedel, R., and Kinski, I., *High-Pressure Synthesis, Electron Energy-Loss Spectroscopy Investigations, and Single Crystal Structure Determination of a Spinel-Type Gallium Oxonitride* $Ga_{2.79}\square_{0.21}(O_{3.05}N_{0.76}\square_{0.19})$. Chem. Mater., 2009. 21(10): p. 2101-2107.

[48] Badzian, A. R., *Cubic boron nitride - diamond mixed crystals.* Mater. Res. Bull., 1981. 16(11): p. 1385-1393.

[49] Knittle, E., Kaner, R. B., Jeanloz, R., and Cohen, M. L., *High-pressure synthesis, characterization, and equation of state of cubic C-BN solid solutions.* Phys. Rev. B, 1995. 51(18): p. 12149-12156.

[50] Komatsu, T., Nomura, M., Kakudate, Y., and Fujiwara, S., *Synthesis and characterization of a shock-synthesized cubic B-C-N solid solution of composition* $BC_{2.5}N$. J. Mater. Chem., 1996. 6(11): p. 1799.

[51] Solozhenko, V. L., Andrault, D., Fiquet, G., Mezouar, M., and Rubie, D. C., *Synthesis of superhard cubic* BC_2N. Appl. Phys. Lett., 2001. 78(10): p. 1385.

[52] Zhao, Y. and He, D., *Preparation of bulk superhard B-C-N nanocomposite compact* in *US Patent No: US7938997 B2*.

[53] Zhao, Y., He, D. W., Daemen, L. L., Shen, T. D., Schwarz, R. B., Zhu, Y., Bish, D. L., Huang, J., Zhang, J., Shen, G., Qian, J., and Zerda, T. W., *Superhard B–C–N materials synthesized in nano-structured bulks.* J. Mater. Res.,, 2002. 17(12): p. 3139-3145.

[54] Komatsu, T., Samedima, M., Awano, T., Kakadate, Y., and Fujiwara, S., *Creation of superhard B–C–N heterodiamond using an advanced shock wave compression technology.* J. Mater. Process. Technol., 1999. 85(1-3): p. 69-73.

[55] Tian, Y., He, J., and Yu, D., *BCN crystal with orthogonal structure and its preparing process*, in *Chinise Patent CN1382622-A; CN1159213-C*. Univ Yanshan (Uyan).

[56] Komatsu, T. and Tomokuni, K., *Active boron carbonitride material used for exhaust gas purification has predetermined oxygen content, specific surface area and mean pore diameter*. Asahi Kasei Kk (Asah) Zh Noguchi Kenkyusho (Nogk). p. 16.

[57] Yu, J., Wang, E. G., Ahn, J., Yoon, S. F., Zhang, Q., Cui, J., and Yu, M. B., *Turbostratic boron carbonitride films produced by bias-assisted hot filament chemical vapor deposition.* J. Appl. Phys., 2000. 87(8): p. 4022-4025.

[58] Gago, R., Jimenez, I., Agullo-Rueda, F., Albella, J. M., Czigany, Z., and Hultman, L., *Transition from amorphous boron carbide to hexagonal boron carbon nitride thin films induced by nitrogen ion assistance.* J. Appl. Phys., 2002. 92(9): p. 5177-5182.

[59] Kurapov, D. and Schneider, J. M., *Structure, composition, mechanical, and tribological properties of BCN films deposited by plasma enhanced chemical vapor deposition.* Plasma Chem. Plasma Process., 2005. 25(6): p. 613-623.

[60] Tsai, P. C., *The deposition and characterization of BCN films by cathodic arc plasma evaporation.* Surface & Coatings Technology, 2007. 201(9-11): p. 5108-5113.

[61] Ying, Z. F., Yu, D., Ling, H., Xu, N., Lu, Y. E., Sun, J., and Wu, J. D., *Synthesis of BCN thin films by nitrogen ion beam assisted pulsed laser deposition from a* B_4C *target.* Diamond Relat. Mater., 2007. 16(8): p. 1579-1585.

[62] Krause, M., Bedel, L., Taupeau, A., Kreissig, U., Munnik, F., Abrasonis, G., Kolitsch, A., Radnoczi, G., Czigany, Z., and Vanhulsel, A., *Structural and mechanical characterization of* BC_xN_y *thin films deposited by pulsed reactive magnetron sputtering.* Thin Solid Films, 2009. 518(1): p. 77-83.

[63] Mannan, M. A., Kida, T., Noguchi, H., Nagano, M., Shimoyama, I., Hirao, N., and Baba, Y., *Atomic arrangement, composition and orientation of hexagonal BCN films synthesized by radiofrequency plasma enhanced CVD.* J. Ceram. Soc. Jpn., 2009. 117(1364): p. 503-507.
[64] Castillo, H. A., Arango, P. J., Velez, J. M., Restrepo-Parra, E., Soto, G., and De la Cruz, W., *Synthesis and characterization of cubic BC_2N grown by reactive laser ablation.* Surface & Coatings Technology, 2010. 204(24): p. 4051-4056.
[65] Chen, X. Y., Wang, Z. H., Ma, S. L., Ji, V., and Chu, P. K., *Microstructure and tribological properties of ternary BCN thin films with different carbon contents.* Diamond Relat. Mater., 2010. 19(10): p. 1225-1229.
[66] Essafti, A. and Ech-chamikh, E., *Optical and electrical characteristics of amorphous boron carbonitride thin films deposited by radiofrequency sputtering.* J Mater Sci, 2011. 46(17): p. 5847-5850.
[67] Liu, A. Y., Wentzcovitch, R. M., and Cohen, M. L., *Atomic arrangement and electronic structure of BC_2N.* Phys. Rev. B, 1989. 39(3): p. 1760-1765.
[68] Nozaki, H. and Itoh, S., *Lattice dynamics of BC_2N.* Phys. Rev. B, 1996. 53(21): p. 14161-14170.
[69] Nozaki, H. and Itoh, S., *Lattice dynamics of a layered material BC_2N.* Physica B-Condensed Matter, 1996. 219-20: p. 487-489.
[70] Nozaki, H. and Itoh, S., *Structural stability of BC_2N.* J. Phys. Chem. Solids, 1996. 57(1): p. 41-49.
[71] Bill, J., Riedel, R., and Passing, G., *Amin-Borane als Precursoren für Borcarbidnitrid.* Z. Anorg. Allg. Chem., 1992. 610(4): p. 83-90.
[72] Sato, M. H. a. T., *Preparation and Properties of a compound in the BCN system.* J. Solid State Chem., 1995. 114: p. 258.
[73] Azevedo, S. and Paiva, R. d., *Structural stability and electronic properties of carbon-boron nitride compounds.* EPL (Europhysics Letters), 2006. 75(1): p. 126.
[74] Tapas Kar, M. C. u., and Steve Scheiner, *Structure, Stability, and Bonding of BC_2N: An ab Initio Study.* J. Phys. Chem. A, 1998. 102.
[75] Tateyama, Y., Ogitsu, T., Kusakabe, K., Tsuneyuki, S., and Itoh, S., *Proposed synthesis path for heterodiamond BC_2N.* Phys. Rev. B, 1997. 55(16): p. R10161-R10164.
[76] Lambrecht, W. R. L. and Segall, B., *Electronic structure of (diamond C)/(sphalerite BN) (110) interfaces and superlattices.* Phys. Rev. B, 1989. 40(14): p. 9909-9919.
[77] Lambrecht, W. R. L. and Segall, B., *Anomalous band-gap behavior and phase stability of c-BN–diamond alloys.* Phys. Rev. B, 1993. 47(15): p. 9289-9296.
[78] Mattesini, M. and Matar, S. F., *Search for ultra-hard materials: theoretical characterisation of novel orthorhombic BC_2N crystals.* Int. J. Inorg. Mater., 2001. 3(7): p. 943-957.
[79] Sun, J., Zhou, X.-F., Qian, G.-R., Chen, J., Fan, Y.-X., Wang, H.-T., Guo, X., He, J., Liu, Z., and Tian, Y., *Chalcopyrite polymorph for superhard BC_2N.* Appl. Phys. Lett., 2006. 89(15): p. 151911-3.
[80] Chang, J., Chen, X.-R., Wei, D.-Q., and Yuan, X.-L., *Elastic constants and anisotropy of β-BC2N under pressure.* Physica B: Condensed Matter, 2010. 405(17): p. 3751-3755.
[81] Sun, J., Zhou, X.-F., Fan, Y.-X., Chen, J., Wang, H.-T., Guo, X., He, J., and Tian, Y., *First-principles study of electronic structure and optical properties of heterodiamond BC_2N.* Phys. Rev. B, 2006. 73(4): p. 045108.
[82] Yuge, K., Seko, A., Koyama, Y., Oba, F., and Tanaka, I., *First-principles-based phase diagram of the cubic BNC ternary system.* Phys. Rev. B, 2008. 77(9).
[83] Zheng, J. C., Wang, H. Q., Wee, A. T. S., and Huan, C. H. A., *Possible complete miscibility of $(BN)_x(C_2)_{1-x}$ alloys.* Phys. Rev. B, 2002. 66(9).
[84] Yuge, K., *Trends in solubility between boron nitride and carbon.* Phys. Rev. B, 2011. 84(13).

[85] Yuge, K., *Pressure effects on the phase stability of cubic BNC ternary alloys.* J. Phys.: Condens. Matter, 2009. 21(5): p. 055403.
[86] Zhuang, C., Zhao, J., Jiang, X., and Jiang, X., *Structural stability, mechanical and electronic properties of cubic BC_xN crystals within a random solid solution model.* J. Phys.: Condens. Matter, 2009. 21(40): p. 405401.
[87] Sun, H., Jhi, S.-H., Roundy, D., Cohen, M., and Louie, S., *Structural forms of cubic BC_2N.* Phys. Rev. B, 2001. 64(9).
[88] Pan, Z., Sun, H., and Chen, C., *Diverging synthesis routes and distinct properties of cubic BC_2N at high pressure.* Phys. Rev. B, 2004. 70(17): p. 174115.
[89] Pan, Z., Sun, H., and Chen, C., *Ab initio pseudopotential studies of cubic BC_2N under high pressure.* J. Phys.: Condens. Matter, 2005. 17(21): p. 3211.
[90] Pan, Z., Sun, H., and Chen, C., *Ab initio structural identification of high density cubic BC_2N.* Phys. Rev. B, 2006. 73(21): p. 214111.
[91] Chen, S., Gong, X., and Wei, S.-H., *Superhard Pseudocubic BC_2N Superlattices.* Phys. Rev. Lett., 2007. 98(1).
[92] Kim, E., Pang, T., Utsumi, W., Solozhenko, V., and Zhao, Y., *Cubic phases of BC_2N: A first-principles study.* Phys. Rev. B, 2007. 75(18).
[93] Zhou, X.-F., Sun, J., Fan, Y.-X., Chen, J., Wang, H.-T., Guo, X., He, J., and Tian, Y., *Most likely phase of superhard BC_2N by ab initio calculations.* Phys. Rev. B, 2007. 76(10): p. 100101.
[94] Xiang-Feng, Z., Jian, S., Quang-Rui, Q., Xiaoju, G., Zhongyuan, L., Yongjun, T., and Hui-Tian, W., *A tetragonal phase of superhard BC_2N.* J. Appl. Phys., 2009. 105(9): p. 093521 -093525.
[95] Luo, X., Guo, X., Liu, Z., He, J., Yu, D., Xu, B., Tian, Y., and Wang, H.-T., *First-principles study of wurtzite BC_2N.* Phys. Rev. B, 2007. 76(9): p. 092107.
[96] Luo, X., Guo, X., Xu, B., Wu, Q., Hu, Q., Liu, Z., He, J., Yu, D., Tian, Y., and Wang, H.-T., *Body-centered superhard BC_2N phases from first principles.* Phys. Rev. B, 2007. 76(9): p. 094103.
[97] Li, Q., Wang, M., Oganov, A. R., Cui, T., Ma, Y., and Zou, G., *Rhombohedral superhard structure of BC_2N.* J. Appl. Phys., 2009. 105(5): p. 053514-4.
[98] Luo, X., Zhou, X.-F., Liu, Z., He, J., Xu, B., Yu, D., Wang, H.-T., and Tian, Y., *Refined Crystal Structure and Mechanical Properties of Superhard BC_4N Crystal:First-Principles Calculations.* J. Phys. Chem. C, 2008. 112: p. 9516–9519.
[99] Tang, M. J., He, D. W., and He, L., *First-principle study of electronic structure and optical properties of 3C-BC_4N.* Physica B: Condensed Matter, 2011. 406(17): p. 3154-3159.
[100] Luo, X. G., Li, L. Y., Wang, W. H., and Tian, Y. J., *Superhard $B_2C_2N_2$ compounds from first-principles calculations.* J. Appl. Phys., 2011. 109(2).
[101] Luo, X., Guo, X., Liu, Z., He, J., Yu, D., Tian, Y., and Wang, H.-T., *Ground-state properties and hardness of high density BC_6N phases originating from diamond structure.* J. Appl. Phys., 2007. 101(8): p. 083505-4.
[102] Weihrich, R., Matar, S. F., and Betranhandy, E., *In search of new candidates for ultra-hard materials: the ternary BC_3N_3 stoichiometry.* J. Phys. Chem. Solids, 2003. 64(9–10): p. 1539-1545.
[103] Jiang, X., Zhuang, C., Li, X., Sai, L., Zhao, J., and Jiang, X., *Mapping distributions of mechanical properties and formation ability on the ternary B—C—N phase diagram.* Diamond Relat. Mater., 2011. 20(7): p. 891-895.
[104] Martinez, E., Andújar, J. L., Polo, M. C., Esteve, J., Robertson, J., and Milne, W. I., *Study of the mechanical properties of tetrahedral amorphous carbon films by nanoindentation and nanowear measurements.* Diamond Relat. Mater., 2001. 10(2): p. 145-152.

[105] Brazhkin, V. V., Lyapin, A. G., and Hemley, R. J., *Harder than diamond: dreams and reality*. Philosophical Magazine A: Physics of Condensed Matter: Defects and Mechanical Properties, 2002. 82(2): p. 231-253.
[106] Teter, D. M., *Computational Alchemy: The search for new superhard materials.* Materials Research Society Bulletin, 1998. 23(1): p. 22-27.
[107] Zhang, Y., Sun, H., and Chen, C., *Superhard Cubic BC_2N Compared to Diamond.* Phys. Rev. Lett., 2004. 93(19): p. 195504.
[108] Zhuang, C., Li, X., Zhao, J., Samra, H. A., and Jiang, X., *Fluctuations of tensile strength and hardness of c-BC_2N crystals induced by difference in atomic configuration.* J. Phys.: Condens. Matter, 2011. 23(46): p. 465401.
[109] Zang, C.-P. and Sun, H., *Chemical anisotropy in diamondlike BC_2N: First-principles calculations.* Phys. Rev. B, 2010. 81(1): p. 012106.
[110] Miyamoto, Y., Rubio, A., Cohen, M. L., and Louie, S. G., *Chiral tubules of hexagonal BC_2N.* Phys. Rev. B, 1994. 50(7): p. 4976-4979.
[111] Watanabe, M. O., Itoh, S., Sasaki, T., and Mizushima, K., *Visible-Light-Emitting Layered BC_2N Semiconductor.* Phys. Rev. Lett., 1996. 77(1): p. 187-189.
[112] Solozhenko, V. L., Dub, S. N., and Novikov, N. V., *Mechanical properties of cubic BC_2N, a new superhard phase.* Diamond Relat. Mater., 2001. 10(12): p. 2228-2231.
[113] Zhang, R. Q., Chan, K. S., Cheung, H. F., and Lee, S. T., *Energetics of segregation in β-C_2BN.* Appl. Phys. Lett., 1999. 75(15): p. 2259-2261.
[114] Mattesini, M. and Matar, S. F., *First-principles characterisation of new ternary heterodiamond BC_2N phases.* J. Comput. Mater. Sci., 2001. 20(1): p. 107-119.
[115] Chen, S., Gong, X. G., and Wei, S.-H., *Crystal structures and mechanical properties of superhard BC_2N and BC_4N alloys: First-principles calculations.* Phys. Rev. B, 2008. 77(1): p. 014113.
[116] Kosolapova, T. Y., Makarenko, G. N., Serebryakova, T. I., E.V. Prilutskii, Khorphyakov, O. T., and Chernysheva, O. I., Poroshk. Metall., 1971. 1: p. 27.
[117] Zhuge, F. and Yamanaka, S., *Ternary compound B_4CN_4 prepared by direct nitridation of B_4C.* J. Alloys Compd., 2008. 466(1-2): p. 299-303.
[118] Kouvetakis, J., Sasaki, T., Shen, C., Hagiwara, R., Lerner, M., Krishnan, K. M., and Bartlett, N., *Novel aspects of graphite intercalation by fluorine and fluorides and new B/C, C/N and B/C/N materials based on the graphite network.* Synth. Met., 1989. 34(1-3): p. 1-7.
[119] Krishnan, K. M., Kouvetakis, J., Sasaki, T., and Bartlett, N., *Characterization of Newly Synthesized Novel Graphite Films.* MRS Online Proceedings Library, 1988. 121: p. null-null.
[120] Kaner, R. B., Kouvetakis, J., Warble, C. E., Sattler, M. L., and Bartlett, N., *Boron-carbon-nitrogen materials of graphite-like structure.* Mater. Res. Bull., 1987. 22(3): p. 399-404.
[121] Moore, A. W., Strong, S. L., Doll, G. L., Dresselhaus, M. S., Spain, I. L., Bowers, C. W., Issi, J. P., and Piraux, L., *Properties and characterization of codeposited boron nitride and carbon materials.* J. Appl. Phys., 1989. 65(12): p. 5109-5118.
[122] Besmann, T. M., *Chemical Vapor Deposition in the Boron-Carbon-Nitrogen System.* J. Am. Ceram. Soc., 1990. 73(8): p. 2498-2501.
[123] Watanabe, M. O., Itoh, S., Mizushima, K., and Sasaki, T., *Electrical properties of BC_2N thin films prepared by chemical vapor deposition.* J. Appl. Phys., 1995. 78(4): p. 2880-2882.
[124] Watanabe, M. O., Itoh, S., Mizushima, K., and Sasaki, T., *Bonding characterization of BC_2N thin films.* Appl. Phys. Lett., 1996. 68(21): p. 2962-2964.
[125] Kawaguchi, M., Kawashima, T., and Nakajima, T., *Syntheses and Structures of New Graphite-like Materials of Composition BCN(H) and $BC_3N(H)$.* Chem. Mater., 1996. 8(6): p. 1197-1201.

[126] Hegemann, D., Riedel, R., Dressler, W., Oehr, C., Schindler, B., and Brunner, H., *Boron carbonitride thin films by PACVD of single-source precursors.* Chem. Vap. Deposition, 1997. 3(5): p. 257-262.
[127] Kim, H. S., Choi, I. H., and Baik, Y. J., *Characteristics of carbon incorporated BN films deposited by radio frequency PACVD.* Surf. Coat. Technol., 2000. 133–134(0): p. 473-477.
[128] Yuki, T., Umeda, S., and Sugino, T., *Electrical and optical characteristics of boron carbon nitride films synthesized by plasma-assisted chemical vapor deposition.* Diamond Relat. Mater., 2004. 13(4–8): p. 1130-1134.
[129] Stöckel, S., Weise, K., Dietrich, D., Thamm, T., Braun, M., Cremer, R., Neuschütz, D., and Marx, G., *Influence of composition and structure on the mechanical properties of BCN coatings deposited by thermal CVD.* Thin Solid Films, 2002. 420–421(0): p. 465-471.
[130] Zhou, F., Adachi, K., and Kato, K., *Friction and wear behavior of BCN coatings sliding against ceramic and steel balls in various environments.* Wear, 2006. 261(3–4): p. 301-310.
[131] Caretti, I., Jiménez, I., Gago, R., Cáceres, D., Abendroth, B., and Albella, J. M., *Tribological properties of ternary BCN films with controlled composition and bonding structure.* Diamond Relat. Mater., 2004. 13(4–8): p. 1532-1537.
[132] Wada, Y., Yap, Y. K., Yoshimura, M., Mori, Y., and Sasaki, T., *The control of B N and B C bonds in BCN films synthesized using pulsed laser deposition.* Diamond Relat. Mater., 2000. 9(3–6): p. 620-624.
[133] Ling, H., Wu, J. D., Sun, J., Shi, W., Ying, Z. F., and Li, F. M., *Electron cyclotron resonance plasma-assisted pulsed laser deposition of boron carbon nitride films.* Diamond Relat. Mater., 2002. 11(9): p. 1623-1628.
[134] Ying, Z. F., Yu, D., Ling, H., Xu, N., Lu, Y. F., Sun, J., and Wu, J. D., *Synthesis of BCN thin films by nitrogen ion beam assisted pulsed laser deposition from a B_4C target.* Diamond Relat. Mater., 2007. 16(8): p. 1579-1585.
[135] Guan, C., Zhao, J., Jia, F., Zhuang, C., Bai, Y., and Jiang, X., *Relationship between chemical compositions of magnetron sputtered B–C–N films and various experimental parameters.* Vacuum, 2012. 86(10): p. 1499-1504.
[136] Ulrich, S., Kratzsch, A., Leiste, H., Stüber, M., Schloßmacher, P., Holleck, H., Binder, J., Schild, D., Westermeyer, S., Becker, P., and Oechsner, H., *Variation of carbon concentration, ion energy, and ion current density of magnetron-sputtered boron carbonitride films.* Surf. Coat. Technol., 1999. 116–119(0): p. 742-750.
[137] Zhou, Z. F., Bello, I., Lei, M. K., Li, K. Y., Lee, C. S., and Lee, S. T., *Synthesis and characterization of boron carbon nitride films by radio frequency magnetron sputtering.* Surf. Coat. Technol., 2000. 128–129(0): p. 334-340.
[138] Linss, V., Hermann, I., Schwarzer, N., Kreissig, U., and Richter, F., *Mechanical properties of thin films in the ternary triangle B–C–N.* Surf. Coat. Technol., 2003. 163–164(0): p. 220-226.
[139] Kim, D. H., Byon, E., Lee, S., Kim, J.-K., and Ruh, H., *Characterization of ternary boron carbon nitride films synthesized by RF magnetron sputtering.* Thin Solid Films, 2004. 447–448(0): p. 192-196.
[140] Zhuang, C., Zhao, J., Jia, F., Guan, C., Wu, Z., Bai, Y., and Jiang, X., *Tuning bond contents in B–C–N films via temperature and bias voltage within RF magnetron sputtering.* Surf. Coat. Technol., 2009. 204(5): p. 713-717.
[141] Lechner, M., *Darstellung und Untersuchung parakristalliner Borcarbonitride*, in *Fakultät für Chemie und Pharmazie*. 1981, Ludwig-Maximilians-Universität München: München, Germany.

[142] Seyferth, D. and Rees, W. S., *Preparation, characterization, and pyrolysis of [-$B_{10}H_{12}$.diamine]-n polymers: a new route to boron nitride.* Chem. Mater., 1991. 3(6): p. 1106-1116.
[143] Rees, W. S. and Seyferth, D., *Preparation, Characterization, and Pyrolysis of Decaborane (14) -Based Polymers: B_4C/BN and BN Procedures*, in *A Collection of Papers Presented at the 13th Annual Conference on Composites and Advanced Ceramic Materials: Ceramic Engineering and Science Proceedings*. 2008, John Wiley & Sons, Inc. p. 837-845.
[144] Maya, L., *Aminoborane Polymers as Precursors of C-N-B Ceramic Materials.* J. Am. Ceram. Soc., 1988. 71(12): p. 1104-1107.
[145] Maya, L., *Derivatization of Preformed Polymers to Produce Ceramic Precursors.* J. Am. Ceram. Soc., 1990. 73(9): p. 2714-2719.
[146] Riedel, R., Bill, J., and Passing, G., *A Novel Carbon Material Derived from Pyridine-Borane.* Adv. Mater., 1991. 3(11): p. 551-552.
[147] Bill, J., Friess, M., and Riedel, R., *Conversion of amine-boranes to boron-carbide nitride.* Eur. J. Solid State Inorg. Chem., 1992. 29: p. 195-212.
[148] Riedel, R., *Novel Ultrahard Materials.* Adv. Mater., 1994. 6(7-8): p. 549-560.
[149] Nicolich, J. P., Hofer, F., Brey, G., and Riedel, R., *Synthesis and Structure of Three-Dimensionally Ordered Graphitelike BC_2N Ternary Crystals.* J. Am. Ceram. Soc., 2001. 84(2): p. 279-82.
[150] Sauter, D., Weinmann, M., Berger, F., Lamparter, P., Müller, K., and Aldinger, F., *X-ray and Neutron Scattering and Solid State NMR Investigations on Precursor-Derived B−C−N Ceramics Using Isotopic Substitution.* Chem. Mater., 2002. 14(7): p. 2859-2870.
[151] Volger, K. W., Kroke, E., Gervais, C., Saito, T., Babonneau, F., Riedel, R., Iwamoto, Y., and Hirayama, T., *B/C/N materials and B_4C synthesized by a non-oxide sol-gel process.* Chem. Mater., 2003. 15(3): p. 755-764.
[152] Komatsu, T., *Bulk synthesis and characterization of graphite-like B-C-N and B-C-N heterodiamond compounds.* J. Mater. Chem., 2004. 14(2): p. 221-227.
[153] Tian, Y. J., He J. L., Yu D. L., Li D. C., Zou G. T., Jia, X. P., Chen L. X., Yanagisawa O., *B-C-N Compound Synthesized Under High Temperature and High Pressure.* Radiat Eff. Defects Solids, 2002. 157(1-2): p. 245-251.
[154] Li, X. F., Zhang, J., Shen, L. H., Lei, W. W., Yang, D. P., Cui, Q. L., and Zou, G. T., *Synthesis and characterization of nanocrystalline hexagonal boron carbo-nitride under high temperature and high pressure.* J. Phys.: Condens. Matter, 2007. 19(42): p. 425235.
[155] Bai, S. Z., Yao, B., Xing, G. Z., Zhang, K., and Su, W.-H., *Synthesis, conductivity and high-pressure phase transition of amorphous boron carbon nitride.* Physica B: Condensed Matter, 2007. 396(1–2): p. 214-219.
[156] Bai, S. Z., Bin, Y., and Su, W. H., *Synthesis, characterization and properties of $B_{0.44}C_{0.27}N_{0.29}$ compounds.* Acta Physica Sinica, 2005. 54(10): p. 4627-4632.
[157] Raidongia, K., Hembram, K. P. S. S., Waghmare, U. V., Eswaramoorthy, M., and Rao, C. N. R., *Synthesis, Structure, and Properties of Mesoporous B/C/N Microspheres* Z. Anorg. Allg. Chem., 2010. 636(1): p. 30-35.
[158] Raidongia, K., Jagadeesan, D., Upadhyay-Kahaly, M., Waghmare, U. V., Pati, S. K., Eswaramoorthy, M., and Rao, C. N. R., *Synthesis, structure and properties of homogeneous BC4N nanotubes.* J. Mater. Chem., 2008. 18(1): p. 83-90.
[159] Huang, F. L., Cao, C. B., Xiang, X., Lv, R. T., and Zhu, H. S., *Synthesis of hexagonal boron carbonitride phase by solvothermal method.* Diamond Relat. Mater., 2004. 13(10): p. 1757-1760.
[160] Sun, G., Liu, Z.-Y., He, J.-L., Yu, D.-L., and Tian, Y.-J., *Chemical Synthesis of C_3N and BC_2N Compounds.* Chinese Physics Letters, 2007. 24(4): p. 1092.

[161] Huang, J., Zhu, Y. T., and Mori, H., *Structure and phase characteristics of amorphous boron–carbon–nitrogen under high pressure and high temperature.* J. Mater. Res., 2001. 16(04): p. 1178-1184.
[162] Filonenko, V. P., Khabashesku, V. N., Davydov, V. A., Zibrov, I. P., and Agafonov, V. N., *Synthesis of a new cubic phase in the B-C-N system.* Inorg. Mater., 2008. 44(4): p. 395-400.
[163] Filonenko, V. P., Davydov, V. A., Zibrov, I. P., Agafonov, V. N., and Khabashesku, V. N., *High pressure synthesis of new heterodiamond phase.* Diamond Relat. Mater., 2010. 19(5-6): p. 541-544.
[164] Yamada, K., *Shock Synthesis of a Graphitic Boron-Carbon-Nitrogen System.* J. Am. Ceram. Soc., 1998. 81(7): p. 1941-1944.
[165] Wu, Q., Liu, Z., Hu, Q., Li, H., He, J., Yu, D., Li, D., and Tian, Y., *The thermal expansion of a highly crystalline hexagonal BC_2N compound synthesized under high temperature and pressure.* J. Phys.: Condens. Matter, 2006. 18(41): p. 9519-9524.
[166] Yang, D. P., Li, Y. A., Yang, X. X., Du, Y. H., Ji, X. R., Gong, X. L., Su, Z. P., and Zhang, T. C., *Chemical synthesis and characterization of flaky h-BCN at high pressure and high temperature.* Chinese Physics Letters, 2007. 24(4): p. 1088-1091.
[167] Sasaki, T., Akaishi, M., Yamaoka, S., Fujiki, Y., and Oikawa, T., *Simultaneous crystallization of diamond and cubic boron nitride from the graphite relative boron carbide nitride (BC_2N) under high pressure/high temperature conditions.* Chem. Mater., 1993. 5(5): p. 695-699.
[168] Nakano, S., Akaishi, M., Sasaki, T., and Yamaoka, S., *Segregative Crystallization of Several Diamond-like Phases from the Graphitic BC_2N without an Additive at 7.7 GPa.* Chem. Mater., 1994. 6(12): p. 2246-2251.
[169] Komatsu, T., Hosomi, S., and Fujiwara, S., *Use of a Ti/C/N ceramic to promote sintering of nanoparticles of shock-synthesized superhard B/C/N with a diamond-like structure.* J. Mater. Chem., 2001. 11(7): p. 1781-1782.
[170] Komatsu, T., Kakudate, Y., and Fujiwara, S., *Heat resistance of a shock-synthesized B-C-N heterodiamond.* J. Chem. Soc., Faraday Trans., 1996. 92(24): p. 5067-5071.
[171] Hubble, H. W., Kudryashov, I., Solozhenko, V. L., Zinin, P. V., Sharma, S. K., and Ming, L. C., *Raman studies of cubic BC_2N, a new superhard phase.* Journal of Raman Spectroscopy, 2004. 35(10): p. 822-825.
[172] Zinin, P. V., Solozhenko, V. L., Malkin, A. J., and Ming, L. C., *Atomic force microscopy studies of cubic BC_2N, a new superhard phase.* J Mater Sci, 2005. 40(11): p. 3009-3011.
[173] Tkachev, S. N., Solozhenko, V. L., Zinin, P. V., Manghnani, M. H., and Ming, L. C., *Elastic moduli of the superhard cubic BC_2N phase by Brillouin scattering.* Phys. Rev. B, 2003. 68(5): p. 052104.
[174] Guo, L.-C., Hu, W.-T., He, J.-L., Yu, D.-L., Liu, S.-M., Li, D.-C., and Tian, Y.-J., *Synthesis of Boron-Rich Cubic $B(C_xN_{1-x})$ Compounds.* Chinese Physics Letters, 2005. 22(12): p. 3141.
[175] Nicolich, J. P., Hofer, F., Brey, G., and Riedel, R., *Synthesis and Structure of Three-Dimensionally Ordered Graphitelike BC_2N Ternary Crystals.* J. Am. Ceram. Soc., 2001. 84(2): p. 279-282.
[176] Solozhenko, V. L. and Turkevich, V. Z., *Phase Stability of Graphitelike BC_4N up to 2100 K and 7 GPa.* J. Am. Ceram. Soc., 1997. 80(12): p. 3229–3232.
[177] Li, D., Yu, D., Xu, B., He, J., Liu, Z., Wang, P., and Tian, Y., *Synthesis of Semimetallic $BC_{3.3}N$ with Orthorhombic Structure at High Pressure and Temperature.* Crystal Growth & Design, 2008. 8(7): p. 2096-2100.
[178] Li, M., Lin, P., Gao, Y., and Gao, C., *High pressure phase transition study of B–C–N compound.* J. Appl. Phys., 2010. 107(7): p. 073508.
[179] Tang, M., He, D., Wang, W., Wang, H., Xu, C., Li, F., and Guan, J., *Superhard solid solutions of diamond and cubic boron nitride.* Scripta Mater., 2012. 66(10): p. 781-784.

[180] Liu, X., Jia, X., Zhang, Z., Zhao, M., Guo, W., Huang, G., and Ma, H.-a., *Synthesis and Characterization of New "BCN" Diamond under High Pressure and High Temperature Conditions.* Crystal Growth & Design, 2011. 11(4): p. 1006-1014.
[181] Ishikawa, M., Nakamura, T., Morita, M., Matsuda, Y., Tsujioka, S.-i., and Kawashima, T., *Boron-carbon-nitrogen compounds as negative electrode matrices for rechargeable lithium battery systems.* J. Power Sources, 1995. 55(1): p. 127-130.
[182] Kawaguchi, M., Imai, Y., and Kadowaki, N., *Intercalation chemistry of graphite-like layered material BC_6N for anode of Li ion battery.* J. Phys. Chem. Solids, 2006. 67(5–6): p. 1084-1090.
[183] Kawaguchi, M. and Wakukawa, Y., *Synthesis of graphite-like material of composition BC_6N by CVD at high temperature.* Carbon, 1999. 37(1): p. 147-149.
[184] Shriver, D. F. and Drezdzon, M. A., *The Manipulation of Air-Sensitive Compounds, 2nd Edition*. 1986: Wiley: New York.
[185] Colombo, P., Mera, G., Riedel, R., and Sorarù, G. D., *Polymer-Derived Ceramics: 40 Years of Research and Innovation in Advanced Ceramics.* J. Am. Ceram. Soc., 2010. 93(7): p. 1805-1837.
[186] Spain, I. L. and Paauwe, J., eds. *High Pressure Technology*. Vol. Vol. I and II. 1977, M. Dekker (New York).
[187] J., H. J. R. a. W. B., *Simulating the Earth*. 1988, London: Harper Collins Academic.
[188] Davison, L., Hori, Y., and Sekine, T., *Shock Compression of Solids* 2002, New York: Springer-Verlag.
[189] Holzapfel, W. B. and Isaacs, N. S., eds. *High-Pressure Techniques in Chemistry and Physics*. 1997, Oxford University Press. 385.
[190] Eremets, M. I., ed. *High Pressure Experimental Methods*. 1996, Oxford University Press. 383.
[191] Bridgman, P. W., *The Resistance of 72 Elements, Alloys and Compounds to 100,000 Kg/Cm²*. Proceedings of the American Academy of Arts and Sciences, 1952. 81(4).
[192] Khvostantsev, L. G. S., V. A.; Tsiok, O., *High pressure toroid cell: Applications in planetary and material sciences*, in *Properties of Earth and Planetary Materials at High Pressure and Temperature*, Manghnani, M.H.Y., T., Editor. 1998, Geophys. Monogr. Ser.: Washington, D. C. p. 562 (89-96).
[193] Khvostantsev, L. G., Slesarev, V. N., and Brazhkin, V. V., *Toroid type high-pressure device: history and prospects.* High Pressure Research, 2004. 24(3): p. 371-383.
[194] *Toroid Press - Schematic diagram*. Available from: http://www.hppi.troitsk.ru/products/Toroid2/Toroid1.htm.
[195] Giardini, A. and Tydings, J., *Diamond Synthesis - Observations On Mechanism Of Formation.* Am. Mineral., 1962. 47(11-1).
[196] Wehber, M., *Thermische Eigenschaften von Spinellen als Funktion des Druckes*, in *FB Geowissenschaften*. 2010, Freien Universität Berlin: Berlin. p. 121.
[197] Decker, D. L., *High-Pressure Equation of State for NaCl, KCl, and CsCl.* J. Appl. Phys., 1971. 42(8): p. 3239-3244.
[198] Walker, D., Carpenter, M. A., and Hitch, C. M., *Some simplifications to multianvil devices for high pressure experiments.* Am. Mineral., 1990. 75: p. 8.
[199] Dzivenko, D. A., *High-pressure synthesis, structure and properties of cubic zirconium(IV)- and hafnium(IV) nitrides*, in *Fachbereich Material- und Geowissenschaften*. 2008, Technische Universität Darmstadt: Darmstadt.
[200] Walter, M. J., Thibault, Y., Wei, K., and Luth, R. W., *Characterizing experimental pressure and temperature conditions in multi-anvil apparatus.* Can. J. Phys., 1995. 73(5-6): p. 273-286.
[201] Huppertz, H., *Multianvil high-pressure / high-temperature synthesis in solid state chemistry*, in *Zeitschrift für Kristallographie/International journal for structural, physical, and chemical aspects of crystalline materials*. 2004. p. 330.

[202] Leinenweber, K. D., Tyburczy, J. A., Sharp, T. G., Soignard, E., Diedrich, T., Petuskey, W. B., Wang, Y., and Mosenfelder, J. L., *Cell assemblies for reproducible multi-anvil experiments (the COMPRES assemblies)*. Am. Mineral., 2012. 97(2-3): p. 353-368.
[203] Rubie, D. C., *Characterising the sample environment in multianvil high-pressure experiments.* Phase Transitions, 1999. 68(3): p. 431-451.
[204] Boehler, R., *High-pressure experiments and the phase diagram of lower mantle and core materials.* Rev. Geophys., 2000. 38(2): p. 221-245.
[205] Boehler, R. and Chopelas, A., *A new approach to laser heating in high pressure mineral physics.* Geophys. Res. Lett., 1991. 18(6): p. 1147-1150.
[206] Zerr A., S. G., Boehler R. , *Phase Transitions and Material Synthesis using the CO_2-Laser Heating Technique in a Diamond Cell*, in *Handbook of Ceramic Hard Materials*, Riedel, R., Editor. 2000, WILEY-VCH: Weinheim. p. 41-65.
[207] Eremets, M. I., Trojan, I. A., Gwaze, P., Huth, J., Boehler, R., and Blank, V. D., *The strength of diamond.* Appl. Phys. Lett., 2005. 87(14): p. -.
[208] Dubrovinsky, L., Dubrovinskaia, N., Prakapenka, V. B., and Abakumov, A. M., *Implementation of micro-ball nanodiamond anvils for high-pressure studies above 6 Mbar.* Nature Communications, 2012. 3: p. 1163.
[209] Horvath-Bordon, E., *Laser Heated Diamond Anvil Cell (LH-DAC)*, (PPT), H.P.L., Editor. 2008.
[210] Zerr, A., Serghiou, G., Boehler, R., and Ross, M., *Decomposition of alkanes at high pressures and temperatures.* High Pressure Research, 2006. 26(1): p. 23-32.
[211] Boehler, R. and De Hantsetters, K., *New anvil designs in diamond-cells.* High Pressure Research, 2004. 24(3): p. 391-396.
[212] Mao, H. K., Xu, J., and Bell, P. M., *Calibration of the ruby pressure gauge to 800 kbar under quasi-hydrostatic conditions.* Journal of Geophysical Research: Solid Earth, 1986. 91(B5): p. 4673-4676.
[213] Eremets, M. I., Hemley, R. J., Mao, H.-k., and Gregoryanz, E., *Semiconducting non-molecular nitrogen up to 240 GPa and its low-pressure stability.* Nature, 2001. 411(6834): p. 170-174.
[214] Hammersley, A. P., Svensson, S. O., Hanfland, M., Fitch, A. N., and Hausermann, D., *Two-dimensional detector software: From real detector to idealised image or two-theta scan.* High Pressure Research, 1996. 14(4-6): p. 235-248.
[215] Williams, D. B. and Carter, C. B., *Transmission Electron Microscopy*. 2nd Edition ed. 2009, New York, USA: Springer. 760.
[216] Stadelmann, P. A., *EMS - a software package for electron diffraction analysis and HREM image simulation in materials science.* Ultramicroscopy, 1987. 21(2): p. 131-145.
[217] Kolb, U., Gorelik, T., and Otten, M. T., *Towards automated diffraction tomography. Part II—Cell parameter determination.* Ultramicroscopy, 2008. 108(8): p. 763-772.
[218] Kolb, U., Gorelik, T., Kübel, C., Otten, M. T., and Hubert, D., *Towards automated diffraction tomography: Part I—Data acquisition.* Ultramicroscopy, 2007. 107(6–7): p. 507-513.
[219] Mugnaioli, E. and Kolb, U., *Applications of automated diffraction tomography (ADT) on nanocrystalline porous materials.* Microporous Mesoporous Mater., 2013. 166(0): p. 93-101.
[220] Vincent, R. and Midgley, P. A., *Double conical beam-rocking system for measurement of integrated electron diffraction intensities.* Ultramicroscopy, 1994. 53(3): p. 271-282.
[221] Mugnaioli, E., Gorelik, T., and Kolb, U., *"Ab initio" structure solution from electron diffraction data obtained by a combination of automated diffraction tomography and precession technique.* Ultramicroscopy, 2009. 109(6): p. 758-765.
[222] Schlitt, S., Gorelik, T. E., Stewart, A. A., Schömer, E., Raasch, T., and Kolb, U., *Application of clustering techniques to electron-diffraction data: determination of unit-cell parameters.* Acta Crystallogr. Sect. A, 2012. 68(5): p. 536-546.

[223] Raman, C. V. and Krishnan, K. S., *New Type of Secondary Radiation.* Nature, 1928. 121(3048).
[224] Föll , H., *The Li Ion Battery*. p. Electronic Materials - Script. Available from: http://www.tf.uni-kiel.de/matwis/amat/elmat_en/kap_2/advanced/t2_1_3.html
[225] Reinold, L. M., *SiCN based Anode Materials for Lithium-Ion Batteries*, in *FB Material- und Geowissenschaften*. 2015, Technische Universität Darmstadt: Darmstadt.
[226] Wallace, R. M., *A Study on the Synthesis of ultrahard cubic BC_2N heterodiamond.* , in *Faculty of Engineering and the Built Environment*. 2010, University of the Witwatersrand: Johannesburg, South Africa. p. 156.
[227] Matizamhuka, W. R., Sigalas, I., Herrmann, M., Dubronvinsky, L., Dubrovinskaia, N., Miyajima, N., Mera, G., and Riedel, R., *Characterization of the Materials Synthesized by High Pressure-High Temperature Treatment of a Polymer Derived t-BC_2N Ceramic.* Materials, 2011. 4(12): p. 2061-2072.
[228] Watanabe, M. O., Sasaki, T., Itoh, S., and Mizushima, K., *Structural and electrical characterization of BC_2N thin films.* Thin Solid Films, 1996. 281–282(0): p. 334-336.
[229] Marton, D., Boyd, K. J., Al-Bayati, A. H., Todorov, S. S., and Rabalais, J. W., *Carbon Nitride Deposited Using Energetic Species: A Two-Phase System.* Phys. Rev. Lett., 1994. 73(1): p. 118-121.
[230] Tuinstra, F. and Koenig, J. L., *Raman Spectrum of Graphite.* J. Chem. Phys., 1970. 53(3): p. 1126-1130.
[231] Cançado, L. G., Takai, K., Enoki, T., Endo, M., Kim, Y. A., Mizusaki, H., Jorio, A., Coelho, L. N., Magalhães-Paniago, R., and Pimenta, M. A., *General equation for the determination of the crystallite size La of nanographite by Raman spectroscopy.* Appl. Phys. Lett., 2006. 88(16): p. 163106.
[232] Knight, D. S. and White, W. B., *Characterization of diamond films by Raman spectroscopy.* J. Mater. Res., 1989. 4(02): p. 385-393.
[233] Ferrari, A. C. and Robertson, J., *Interpretation of Raman spectra of disordered and amorphous carbon.* Phys. Rev. B, 2000. 61(20): p. 14095-14107.
[234] Graczyk-Zajac, M., Reinold, L., Kaspar, J., Sasikumar, P., Soraru, G.-D., and Riedel, R., *New Insights into Understanding Irreversible and Reversible Lithium Storage within SiOC and SiCN Ceramics.* Nanomaterials, 2015. 5(1): p. 233-245.
[235] Kaspar, J., Graczyk-Zajac, M., and Riedel, R., *Lithium insertion into carbon-rich SiOC ceramics: Influence of pyrolysis temperature on electrochemical properties.* J. Power Sources, 2013. 244: p. 450-455.
[236] Pradeep, V. S., Graczyk-Zajac, M., Riedel, R., and Soraru, G. D., *New Insights in to the Lithium Storage Mechanism in Polymer Derived SiOC Anode Materials.* Electrochim. Acta, 2014. 119: p. 78-85.
[237] Graczyk-Zajac, M., Mera, G., Kaspar, J., and Riedel, R., *Electrochemical studies of carbon-rich polymer-derived SiCN ceramics as anode materials for lithium-ion batteries.* J. Eur. Ceram. Soc., 2010. 30(15): p. 3235-3243.
[238] Bhat, S., Wiehl, L., Molina-Luna, L., Mugnaioli, E., Lauterbach, S., Sicolo, S., Kroll, P., Duerrschnabel, M., Nishiyama, N., Kolb, U., Albe, K., Kleebe, H.-J., and Riedel, R., *High-Pressure Synthesis of Novel Boron Oxynitride $B_6N_4O_3$ with Sphalerite Type Structure.* Chem. Mater., 2015. 27(17): p. 5907-5914.
[239] Solin, S. A. and Ramdas, A. K., *Raman Spectrum of Diamond.* Phys. Rev. B, 1970. 1(4): p. 1687-1698.
[240] Reich, S., Ferrari, A., Arenal, R., Loiseau, A., Bello, I., and Robertson, J., *Resonant Raman scattering in cubic and hexagonal boron nitride.* Phys. Rev. B, 2005. 71(20).
[241] Bhat, S., Lauterbach, S., Dzivenko, D., Lathe, C., Bayarjargal, L., Schwarz, M., Kleebe, H.-J., Kroke, E., Winkler, B., and Riedel, R., *High-pressure high-temperature behavior of polymer derived amorphous B-C-N.* Journal of Physics: Conference Series, 2014. 500(18): p. 182004.

[242] Bundy, F. P. and Wentorf, R. H., *Direct Transformation of Hexagonal Boron Nitride to Denser Forms.* J. Chem. Phys., 1963. 38(5): p. 1144-1149.
[243] Solozhenko, V. L., Chernyshev, V. V., Fetisov, G. V., Rybakov, V. B., and Petrusha, I. A., *Structure analysis of the cubic boron nitride crystals.* J. Phys. Chem. Solids, 1990. 51(8): p. 1011-1012.
[244] Yogo, T., Naka, S., and Iwahara, H., *Synthesis of cubic boron nitride with boron nitride powder formed from triammoniadecaborane.* J Mater Sci, 1991. 26(14): p. 3758-3762.
[245] Langenhorst, F. and Solozhenko, V. L., *ATEM-EELS study of new diamond-like phases in the B-C-N system.* Phys. Chem. Chem. Phys., 2002. 4(20): p. 5183-5188.
[246] Schmid, H. K., *Phase Identification in Carbon and BN Systems by EELS.* Microsc. Microanal. Microstruct., 1995. 6(1): p. 99-111.
[247] Gauquelin, N., Benckiser, E., Kinyanjui, M. K., Wu, M., Lu, Y., Christiani, G., Logvenov, G., Habermeier, H. U., Kaiser, U., Keimer, B., and Botton, G. A., *Atomically resolved EELS mapping of the interfacial structure of epitaxially strained $LaNiO_3$ /$LaAlO_3$ superlattices.* Phys. Rev. B, 2014. 90(19): p. 195140.
[248] Garvie, L. A. J., Hubert, H., Rez, P., McMillan, P. F., and Buseck, P. R., *$BN_{0.5}O_{0.4}C_{0.1}$: Carbon- and oxygen-substituted hexagonal BN.* J. Alloys Compd., 1999. 290(1–2): p. 34-40.
[249] Schwarz, M., Zerr, A., Kroke, E., Miehe, G., Chen, I. W., Heck, M., Thybusch, B., Poe, B. T., and Riedel, R., *Spinel Sialons.* Angew. Chem. Int. Ed., 2002. 41(5): p. 789-793.
[250] Tu, B., Wang, H., Liu, X., Wang, W., and Fu, Z., *First-Principles Insight into the Composition-Dependent Structure and Properties of γ-Alon.* J. Am. Ceram. Soc., 2014. 97(9): p. 2996-3003.
[251] Christensen, N. E. and Gorczyca, I., *Optical and structural properties of III-V nitrides under pressure.* Phys. Rev. B, 1994. 50(7): p. 4397-4415.
[252] Kupcik, V., Grochowski, J., and Serda, P., *Twinning model for a new pseudo-hexagonal BN.* Z. Kristallogr., 1994. 209(3): p. 236.
[253] Evans, D. A., McGlynn, A. G., Towlson, B. M., Gunn, M., Jones, D., Jenkins, T. E., Winter, R., and Poolton, N. R. J., *Determination of the optical band-gap energy of cubic and hexagonal boron nitride using luminescence excitation spectroscopy.* J. Phys.: Condens. Matter, 2008. 20(7): p. 075233.
[254] Birch, F., *Finite Elastic Strain of Cubic Crystals.* Phys. Rev., 1947. 71(11): p. 809-824.
[255] Datchi, F., Dewaele, A., Le Godec, Y., and Loubeyre, P., *Equation of state of cubic boron nitride at high pressures and temperatures.* Phys. Rev. B, 2007. 75(21): p. 214104.
[256] Bhat, S., Sasikumar, P., Molina-Luna, L., Graczyk-Zajac, M., Kleebe, H.-J., and Riedel, R., *Electrochemical Li Storage Properties of Carbon-Rich B–C–N Ceramics.* C, 2016. 2(2): p. 9.
[257] Fukui, H., Ohsuka, H., Hino, T., and Kanamura, K., *Preparation of Microporous Si–O–C Composite Material and Its Lithium Storage Capability.* Chem. Lett., 2009. 38(1): p. 86-87.
[258] Fukui, H., Ohsuka, H., Hino, T., and Kanamura, K., *A Si-O-C composite anode: high capability and proposed mechanism of lithium storage associated with microstructural characteristics.* ACS applied materials & interfaces, 2010. 2(4): p. 998-1008.
[259] Baek, S.-H., Reinold, L. M., Graczyk-Zajac, M., Riedel, R., Hammerath, F., BÃ¼chner, B., and Grafe, H.-J., *Lithium dynamics in carbon-rich polymer-derived SiCN ceramics probed by nuclear magnetic resonance.* J. Power Sources, 2014. 253(0): p. 342-348.
[260] Graczyk-Zajac, M., Wimmer, M., Neumann, C., and Riedel, R., *Lithium intercalation into SiCN/disordered carbon composite; Part1: Influence of initial carbon porosity on cycling performance/capacity.* J. Solid State Electrochem., 2015. 19(9): p. 2763-2769.
[261] Kanamura, K., Shiraishi, S., Takezawa, H., and Takehara, Z.-i., *XPS Analysis of the Surface of a Carbon Electrode Intercalated by Lithium Ions.* Chem. Mater., 1997. 9(8): p. 1797-1804.

[262] Winter, M., Besenhard, J. O., Spahr, M. E., and Novak, P., *Insertion electrode materials for rechargeable lithium batteries.* Adv. Mater., 1998. 10(10): p. 725-763.
[263] Bundy, F. P., *The P, T phase and reaction diagram for elemental carbon, 1979.* Journal of Geophysical Research: Solid Earth, 1980. 85(B12): p. 6930-6936.
[264] Solozhenko, V. L., Turkevich, V. Z., and Holzapfel, W. B., *Refined Phase Diagram of Boron Nitride.* J. Phys. Chem. B, 1999. 103(15): p. 2903-2905.

List of Tables

Table 1-1. Calculated lattice parameters, bulk moduli (**B**), shear moduli (**G**) and estimated hardness (**Hv**) (if available) of the predicted super-hard B-C-N phases. The experimental values for dense carbon and BN modifications are given for comparison. 15

Table 2-1. The microscope parameters used for the HRTEM simulation 55

Table 3-1. Bulk elemental analyses results of the BCN precursors. 63

Table 3-2. XPS peak analysis results of precursors..... 65

Table 3-3. Fitted bulk moduli and their derivatives of c-BN and BON (Cm-1, Cm-2, disordered) 99

Table 3-4. Electrochemical capacity data for BC_2N and BC_4N. 101

List of Figures

Figure 1-1. A representative atomic arrangement in the unit cell of cubic β-BC_2N structure. Reprinted with permission from [75]. 8

Figure 1-2. All the possible topologically different c-BC2N structures (after structural relaxation) starting from an eight-atom zinc-blende structured unit cell. Reprinted with permission from [87]. The dotted bonds indicate the broken covalent bonds between N atoms 11

Figure 1-3. Proposed tetragonal crystal structures of diamond-like BC_2N: (a) z*-BC_2N with P-42m symmetry and (b) t-BC_2N with P-421m symmetry. Reprinted with permission from [93, 94] 11

Figure 1-4. (a) Theoretically predicted distribution of formation energy (eV/atom) on the upper rhombus of ternary B−C−N phase diagram using full spectrum. Less formation energy means that the corresponding composition is easier to form. (b) $B_xC_yN_z$ compositions synthesized in previous experiments. Most compositions locate in the area with negative formation energy, in agreement with the theoretical prediction. Reprinted with permission from [103]. 12

Figure 1-5. High-temperature reaction of amorphous carbon spheres ((a) - SEM and (b) TEM image) with boric acid and urea yields spheres with graphitic structure and composition of BC_4N: (c) SEM and (d) TEM image. Reprinted with permission from [157]..... 20

Figure 1-6. Plot of all observed unit-cell volumes in the B–C–N system of cubic zinc-blende structure.[53] The relationship of unit-cell volume vs chemical composition shows a clear trend closely obeying Vegard's law for ideal solid solutions, except for data of Solozhenko et al. Reproduced with permission from [51] 25

Figure 1-7. Optical images of diamond crystals obtained at HP-HT using Fe-Ni alloy as catalyst starting from graphite (a) or mixtures of graphite and h-BN with

stoichiometries of (b) $C_{0.98}(BN)_{0.02}$; (c) $C_{0.9}(BN)_{0.1}$; (d) $C_{0.9}(BN)_{0.1}$ with 1 wt.% Al additive; (e) $C_{0.5}(BN)_{0.5}$. Reprinted with permission from [180]. 27
Figure 2-1. Schematic diagram of the Schlenk line [184] used during the precursor synthesis to control argon atmosphere. 30
Figure 2-2. Schematic diagram of the Schlenk (quartz) tube used during the precursor synthesis to control argon atmosphere 31
Figure 2-3. Photograph of the cross-linked pyridine borane inside the Schlenk tube..... 32
Figure 2-4. Schematic diagram of the (a) Piston cylinder apparatus, and (b) Bridgman opposed anvil apparatus 35
Figure 2-5. Schematic diagram of the (a) toroid press (Reprinted with permission from [194]) (b) sample assembly used in toroid experiments..... 36
Figure 2-6. (a) Schematic diagram of the of in-situ measurement and anvil assembly of the MAX80 press, (b) schematic diagram of the boron-epoxy cubic cell, and (c) photograph showing three of the MAX80 anvils with the boron epoxy cell [196]. 38
Figure 2-7 . Working principle of the Walker-type module: a) the cubic second compression stage is nested within split-cylinder six-wedge cluster [199]; b) photo of the assembled 2^{nd} stage anvil, copper electrode used to pass current to sample heater via anvil ; c) the module is loaded uniaxially via pressure distribution plates [199]; d) top view photo of the pressure distribution plate 40
Figure 2-8. Prepared tungsten carbide anvils/cubes for second compression stage of a 6/8 type Walker module. Photograph also shows the octahedron placed between the truncation of anvils, surrounded by prophyllite gaskets. 41
Figure 2-9. Schematic diagram of the octahedron cell used in LVP experiments..... 43
Figure 2-10. The schematic diagram of the diamond anvil cell (DAC) [209]. 45
Figure 2-11. The schematic diagram of the sample chamber inside DAC in case of a) gas loading, b) solid loading. 47
Figure 2-12. The ray diagram or schematic of (A) a BF formed form the transmitted beam (B) a DF formed with specific off axis scattered beam and (C) a CDF image where incident beam is titled so that scattered beam emerges on the optic axis. Reprinted with permission from [215]. 52
Figure 2-13. Schematic of ADT tomographic acquisition. Reprinted with permission from [219] 57
Figure 2-14. The working principle of a Li ion battery. Reprinted with permission from [224]. 59
Figure 2-15. The schematic diagram of the Swagelok® type cell assembly [225]..... 60
Figure 3-1. XRD patterns of precursors (Mo $K\alpha_1$ λ = 0.70319 Å)..... 64

Figure 3-2. Raman spectra of amorphous BC_2N acquired using Ar laser (blue) 488 nm. Black line- acquired spectrum, blue dotted line – deconvoluted peak (D & G band), orange dashed line- fitted curve using Breit-Wigner-Fano(BWF) function. 67
Figure 3-3. Raman spectra of amorphous BC_4N acquired using Ar laser (blue) 488 nm. Black line- acquired spectrum, blue dotted line – deconvoluted peak (D & G band), orange dashed line- fitted curve using Breit-Wigner-Fano(BWF) function 67
Figure 3-4. SEM image of synthesized BCN powders a) BC_2N , b) BC_4N..... 68
Figure 3-5. TEM images of the a-BC_2N (a) and a-BC_4N (b). The corresponding selected area electron diffraction (SAED) image and EDX spectrum are shown in the inset ... 69
Figure 3-6. X-ray diffraction pattens for the h-BN, B_2O_3 and their mixtures after 2 h (purple) and 4 h (green) ball milling. 70
Figure 3-7. *In-situ* XRD patterns for BC_2N taken at 5 GPa in MAX80; inset graph shows a magnification of the 2θ region from 15 to 35 ° for the pattern taken at 1600 °C. 72
Figure 3-8 . In-situ XRD patterns for BC_4N taken at 7 GPa in MAX80; inset graph shows a magnification of the 2θ region from 15 to 35 ° for the pattern taken at 700 °C. 73
Figure 3-9 . Ex-situ XRD patterns of the samples recovered after MAX80 experiments (Mo Kα λ = 0.70319 Å) 73
Figure 3-10. Ex-situ XRD patterns of the samples recovered after toroid experiments. (Mo Kα λ = 0.70319 Å) 74
Figure 3-11. Diffraction pattern of the recovered BC_4N after LVP experiments at 15.6 GPa, 1900° C 76
Figure 3-12. Raman spectra of the recovered sample after LVP experiments at 15.6 GPa, 1900° C 76
Figure 3-13. The SEM micrograph, brittle-fractured surface of the recovered LVP sample 77
Figure 3-14. Diffraction pattern of the recovered BC_2N after LVP experiments at 15.6 GPa, 1900° C 78
Figure 3-15. BC_4N Sample in inside DAC before and after laser heating..... 79
Figure 3-16. Ex-situ angle dispersive X-ray diffraction patterns collected after releasing the pressure in DAC (34 GPa, 1900-2500 °), inset graph shows the 2 theta region from 7-10°..... 80
Figure 3-17. BC_2N Sample in inside DAC before and after laser heating..... 81
Figure 3-18. (a) Bright field TEM image of recovered BC_2N sample, (b) inset image is respective dark field image 81
Figure 3-19. SAED pattern of the recovered BC_2N sample, different arcs (violet, orange, red and green) marked in the SAED pattern shows the corresponding *d*-values..... 83
Figure 3-20. TEM image of single crystal of recovered BC_2N sample after DAC experiment, circled area shows approximate beam diameter usedfor EDX measurement. 84
Figure 3-21. EDX spectrum recorded of the single crystal from the recovered BC_2N sample after DAC experiment, recorded in the area highlighted in Figure 3-20. 84

Figure 3-22. TEM image of fine grain area of recovered BC_2N sample after DAC experiment, circled area shows approximate beam diameter used for EDX measurement. ... 85
Figure 3-23. EDX spectrum of recovered BC_2N sample after DAC experiment, recorded in fine grain area highlighted in Figure 3-22 85
Figure 3-24. Energy-loss near edge fine structure (ELNES) ionization edges of the B-*K*, N-*K*, O-*K*, and C-*K* after background subtraction. B-*K* , N-*K*, O-*K* ionization edges were acquired on single crystal shown in the Figure 3-20 and C-*K* was taken on fine grain area of the Figure 3-22..... 86
Figure 3-25. TEM images of recovered BC_2N sample after DAC experiment in two different regions (a) and (b). The corresponding EDX spectrum is given in respective inset. Region (b) also includes corresponding SAED inset. Circled (in red) area shows approximate beam diameter used for EDX and SAED..... 87
Figure 3-26. TEM image of BC_2N after DAC experiment, along with the EDX spectrum acquired in the highlighted circular area of the sample. 89
Figure 3-27. Typical triangular-shaped BON crystals (a) Overview bright-field TEM image, (b) large magnification TEM image of a BON crystal. (c) STEM Z-contrast image of a BON crystal [238]. 90
Figure 3-28. Electron energy-loss spectrum (EELS) showing the B-K, N-K and O-K ionization edges after background subtraction. The highlighted light blue areas indicate the integration width used for quantification. The inset figure shows the electron energy-loss near edge fine structure (ELNES) of the O-K edge (in order to reduce the noise, the data were smoothened by the Savitzky-Golay method) [238]..... 91
Figure 3-29. (a) Unit cell of BON, (b) Left: Obverse main domain, Right: Reverse twin domain due to spinel law [238]. 92
Figure 3-30. Relation between unit cells: rhombohedral (red), hexagonal (black) and cubic (green)[238]. 93
Figure 3-31. (a) High-resolution phase contrast image. The orange square denotes the area at which the EDX spectrum shown in the inset was acquired. The blue triangles denote twin boundaries. (b) Electron diffraction pattern of BON in $[100]_{hex}$ ($[10\text{-}1]_{cubic}$) zone axis orientation. The spots can be indexed with respect to a hexagonal (green) or cubic lattice (black), as shown in (d). The red line indicates a [111] type twin plane, which can be seen in the HRTEM image. (c) Magnified view of the area marked by the yellow box in part (a). The red bordered inset is a simulated image of BON in $[100]_{hex}$ ($[10\text{-}1]_{cubic}$) zone axis orientation and contains 2x4 unit cells. (e) View of the crystal structure (B: green, N/O: blue) projected along the hexagonal a-axis, overlaid on the simulated HRTEM image [238]..... 95

Figure 3-32. Simulated thickness-defocus map of BON in $[100]_{hex}$ ($[10\text{-}1]_{cubic}$) zone axis orientation. The unit cell duplication was 2x in horizontal direction and 4x in vertical direction [238]. 96

Figure 3-33. Relaxed structures of the Cm-1 (a), Cm-2 (b), and disordered (c) BON models. Boron atoms are depicted in green, nitrogen in light blue and oxygen in red. Green polyhedra represent B-centered tetrahedra; vacancy-centered tetrahedra are depicted in pink [238]. 98

Figure 3-34. Calculated electronic density of states of c-BN (a), BON Cm-1 (b) and BON disordered (c). As the features of the two Cm models are very similar, only Cm-1 is displayed. 99

Figure 3-35. First cycle lithiation/delithiation profiles of the studied BCN samples at a rate of C/20 (18 mA g-1). Solid line represents lithiation and dotted line represents delithiation [256]. 101

Figure 3-36. Electrochemical cycling of BCN samples at different current rates, from C/20 to 2C (18 mA g^{-1} – 720 mA g^{-1}) [256]. 102

Figure 3-37. Cycling of BC_4N electrode for 75 cycles at 100 mA g^{-1}. Inset shows the first cycle charging/discharging profile [256]. 103

Figure 4-1. Pressure Vs Temperature (P-T) diagram for amorphous BC_2N compounds. The dotted line indicates approximate P-T range for h-BN to c-BN and graphite to diamond transition. Mark (*) and (o) shows the P-T conditions for claimed c-BC_2N by Zhao et al. and Solozhenko et al. respectively. 106

Figure 4-2. Pressure Vs Temperature (P-T) diagram for amorphous BC_4N compounds. The dotted line indicates approximate P-T range for h-BN to c-BN and graphite to diamond transition. Mark (*) shows the P-T conditions for claimed c-BC_4N by Zhao et al. 107

Abrivations

a-BC_2N	Amorphous BC_2N
a-BC_4N	Amorphous BC_4N
ADT	Automated Diffraction Tomography
ALS	Advanced Light Source
BCN	Boron-Carbon-Nitrides
BON	Boron Oxynitride
CVD	Chemical Vapor Deposition
DAC	Diamond Anvil Cell
DESY	Deutsches Elektronen-Synchrotron
DFT	Density Functional Theory
EDS	Energy Dispersive Spectroscopy
EELS	Electron Energy-loss spectroscopy
GGA	Generalized Gradient Approximation
HP-HT	High-Pressure High-Temperature
HRTEM	High Resolution Transmission Electron Microscopy
LDA	Local Density Approximation
LH-DAC	Laser Heated Diamond Anvil Cell
LIB	Lithium Ion Battery
LVP	Large Volume Press
MA	Multi Anvil
MAP	Multi Anvil Press
PDCs	Polymer Derived Ceramics
SAED	Selected Area Electron Diffraction
TEM	Transmission Electron Microscopy
WC	Tungsten Carbide
XPS	X-ray Photoelectron Spectroscopy
XRD	X-ray diffraction

Acknowledgement

I am grateful to Prof. Dr. Ralf Riedel, my doctoral advisor, for giving me the opportunity to perform this research in his group. His supervision, support and belief in my abilities helped me to overcome all my scientific and personal difficulties during my Ph.D. period. I also thank him for special interest in my topic of research (high-pressure science), ongoing encouragement throughout my work, and for giving me responsibilities like, organizing International conference and workshops.

I would like to thank Dr. Dmytro Dzivenko, who introduced me to the world of high-pressure techniques, for guidance and strong motivation, fruitful discussions and constructive criticism.

My special thanks to PD. Dr. Leonore Wiehl, for helping in correcting my thesis, solving the BON structure and for her constant support and guidance.

I would like to thank Prof. Dr. Hans-Joachim Kleebe, Earth Science department, TU Darmstadt for accepting to become co-referee of my thesis as well as supporting this work through excellent TEM analysis. My special thanks to his group members Dr. Leopoldo Molina-Luna, Dr. Stefan Lauterbach, Dr. Michael Duerrschnabel and Mrs. Ulrike Kunz for their TEM / EDS / EELS measurement.

I also would like to thank Prof. Karsten Albe and Dr. Sabrina Sicolo Materials Modeling group, TU Darmstadt for DFT studies on BON compound.

I would like to specially thank our all collaborators listed below. As here in TU Darmstadt, we are limited with experimental facilities related to high pressure and high temperature techniques without their fruitful collaborations, results stated in thesis are challenging to realize.

Dr. Norimasa Nishiyama DESY Hamburg
Dr. Christian Lathe, GFZ Potsdam
Dr. Ute Kolb, University of Mainz
Prof. Dr. Peter Kroll, University of Texas at Arlington, USA
Dr. Enrico Mugnaioli, University of Siena, Italy
Dr. Marcus Schwarz and Prof. Dr. Edwin Kroke, TU-Bergakademie Freiberg
Dr. Lkhamsuren Bayarjargal and Prof. Dr. Björn Winkler, Goethe-Universität Frankfurt

I would like to also thank Dr. Andreas Zerr, CNRS, Paris, France, for his discussions, suggestions regarding BCN compounds and support during ALS Berkeley USA beam-time.

Thanks to Dr. Emanuel Ionescu, Dr. Magdalena Graczyk-Zajac, Dr. Gabriela Mera, Dr. Pradeep Warrier, Claudia Fasel, Lukas Schlicker, Sarabjeet Kaur, Felix Roth and all other Dispersive Solids group members, material science department, TU Darmstadt who supported my work in many different ways.

Last but not the least; I am grateful to my parents Mr. Krishna Bhat and Mrs. Kusuma Bhat, who made me what I am today. I would like to thank my grandmother Mrs. Saraswati T. Hegde for her kind support throughout my studies (from 8th grade to bachelor degree). I would like to acknowledge the support of my better-half Mrs. Shobha Herur during PhD period. I am dedicating present thesis to my son Omkar Bhat.

This work was financially supported by the German research foundation (Deutsche Forschungsgemeinschaft, **DFG**) through special priority program SPP1236 and German federal state of Hessen through its excellence program LOEWE "RESPONSE"

DFG Deutsche Forschungsgemeinschaft

Curriculum Vitae

Shrikant Bhat
Technische Universität Darmstadt, Germany

Parkstrasse, 19
64289, Darmstadt, Germany
Email : bhat@materials.tu-darmstadt.de ; urshrikant@gmail.com

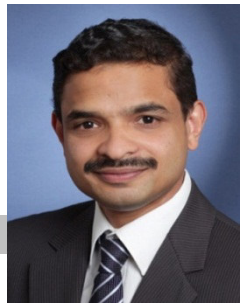

Personal Details

Date of Birth: 22nd July 1982
Nationality: Indian
Family Status: Married to Shobha Herur, and we have a child

Objective

To pursue excellence in engineering & technological skill sets, master the application of emerging technologies for providing solutions and be a continuous learner and a dependable team player. In long run, plan is to climb few steps towards the limitless ladder of excellence in the respective field.

Educational Qualification

- **Double Master Degree (M. Sc.)** 2008-2010: International double masters in *Functional Advanced Materials and Engineering* (FAME) with **European Union '*Erasmus Mundas*' fellowship (42,000.00 €)**.
  - University of Augsburg, Germany- specialized in Materials Interfaces & Composites
  - University of Liege, Belgium- specialized in Nano-Materials

  Overall Note/ Grade: *Grand Distinction*

- **Bachelor Degree (B. E.)** 2000-2004**:** *Bachelor of Engineering* in Polymer Science & Technology, Visveswaraiah Technological University (SJCE Mysore), Karnataka, India
  Note/ Grade: *First Class with Distinction* (83 %)

Professional Experience

Duration	Designation and Organization with Accomplishments
Feb 2011 - Present *~ 5 years*	**Scientific Co-worker Material Science** in **Technische Universität Darmstadt,** Institute of Material Science, Dispersive Solids Group. ▪ *Experience as coordinator* of the International Symposium on Nitrides (ISNT2014), from Aug 31st – Sept 5th , 2014 held in Wildbad Kreuth, Germany ▪ *Collaborative research experience*: PhD thesis project was executed in collaboration with 3 different universities and two Synchrotron facilities ▪ Experience of working in one of the world's finest synchrotron research facilities like Deutsches Elektronen-Synchrotron (DESY) Hamburg, Germany and Advanced Light Source (ALS) Berkeley, USA ▪ Hands on experience in synthesis, processing and characterization of Polymer Derived Ceramics (PDCs) ▪ Teaching practical courses for bachelor and master level students

Feb 2010- Jan 2011 *11 months*	**Research Associate in Fraunhofer Institute for Chemical Technology, Karlsruhe/ Pfinztal, Germany, Polymer Engineering Composites Group.** ▪ Project assistance in polymer engineering composites team ▪ From Feb 2010- August 2010 as master thesis student in Pultrusion Technology ▪ Completed master thesis titled 'Development of commingled natural fiber-reinforced composite profiles based on the pultrusion process' ▪ Hands on experience in Pultrusion of thermoplastic and thermoset polymers with synthetic (glass, carbon etc.) or natural (flax, jute etc.) fibers reinforcements
July 2004 – Sept 2008 *4 years, 3 months*	**Research Associate** in **GE Plastics India (**now **SABIC – Innovative Plastics), GE India Technology Center** / John F. Welch Technology Center Bangalore**,** Polymer Science and Technology Lab ▪ Project assistance to polymer engineering and composites team. ▪ Direct association with the Global Technology team and Planning, Execution and Report out of the assigned task ▪ Hands on experience in Research and Development of engineering thermoplastics (like Polycarbonate, ABS, Nylon, PBT etc) and their composites (talk, glass fibers etc.) for specialty applications based on customer demand ▪ Experience being part of global analytical team and processing team ▪ Familiarity of Six-sigma tools (Green Belt trained), used extensively in project execution ▪ Bronze-Patent Award and 4 internal technical reports

Technical Contributions

❖ Present Thesis Related Publications

- **Bhat, S.,** Wiehl, L., Molina-Luna, L., Mugnaioli, E., Lauterbach, S., Sicolo, S., Kroll, P., Duerrschnabel, M., Nishiyama, N., Kolb, U., Albe, K., Kleebe, H.-J., and Riedel, R., *High-Pressure Synthesis of Novel Boron Oxynitride $B_6N_4O_3$ with Sphalerite Type Structure.* Chemistry of Materials, 2015. 27(17): p. 5907-5914. doi:10.1021/acs.chemmater.5b01706.
- **Bhat, S.**, Sasikumar, P., Molina-Luna, L., Graczyk-Zajac, M., Kleebe, H.-J., and Riedel, R., Electrochemical Li Storage Properties of Carbon-Rich B–C–N Ceramics. Journal of Carbon Research, 2016. 2(2): p. 9. doi:10.3390/c2020009.
- **Bhat, S.**, Lauterbach, S., Dzivenko, D., Lathe, C., Bayarjargal, L., Schwarz, M., Kleebe, H.-J., Kroke, E., Winkler, B., and Riedel, R., *High-pressure high-temperature behavior of polymer derived amorphous B-C-N.* Journal of Physics: Conference Series, 2014. 500(18): p. 182004. doi:10.1088/1742-6596/500/18/182004.

❖ Other Publications

- Linganiso, L. Z., Bezerra, R., **Bhat, S.,** John, M., Braeuning, R., and Anandjiwala, R. D., *Pultrusion of flax/poly(lactic acid) commingled yarns and nonwoven fabrics.* Journal of Thermoplastic Composite Materials, 2014. 27(11): p. 1553-1572.
- Rajulu, A. V., Rao, G. B., Devi, L. G., Ramaiah, S., Prada, D. S., **Bhat, K. S.,** and Shylashree, R., *Mechanical Properties of Short, Natural Fiber Hildegardia populifolia-reinforced Styrenated Polyester Composites.* Journal of Reinforced Plastics and Composites, 2005. 24(4): p. 423-428.
- + 4 Technical Reports confidential (*SABIC – Innovative Plastics)* related to Engineering Thermoplastics and their modification to specific properties and applications.

❖ International Conference Oral /Poster Presentations

- Invited Talk: "Single-Source-Precursor Synthesis of Novel Functional Polymer-Derived Ceramic Nanocomposites (PDC-NCs) for Energy-Related Applications". Intl. Conference organized by Indian Ceramic Society, CAMEE2015, Bangalore Dec 14-17, 2015.
- Oral presentation: "Novel Boron Oxy-Nitrides", International Symposium On Nitrides (ISNT2014), held in Wildbad Kreuth, Germany from 31st Aug. – 5th Sept. 2014
- Oral presentation: "Hints towards novel boron oxy-nitrides?" EHPRG52 Conference held in Lyon France, form 7-12th Sept 2014.
- Poster presentation: "High-pressure high-temperature behavior of polymer derived amorphous B-C-N", AIRAPT- 24 Biennial International conference, Seattle-WA USA, July 7-12th 2013.
- Oral presentation: "Microwave assisted thermoplastic pultrusion of flax fibre reinforced polypropylene (PP) and poly (lactic acid) (PLA)", 3rd Global Pultrusion Conference and 8th COBRAE Composite Bridges Conference, 27 – 29 March 2011, Marnela Vallée, France
- Poster presentation: "Processing and Properties of Sustainable Green Composites" 10th International Conference on Wood and Bio-fiber Plastic Composites held in Madison-WI, USA from May 11-13th 2009.

❖ Patent

- US Patent Application 20090111943. Granted in 2009, talks about modification of filler (SABIC – *Innovative Plastics rights reserved)* Title- Engineering Thermoplastics and their modification to specific properties and applications. Authors: **Shrikant B**., Sriram K., Roopali R., Sandeep T., Andre V.

Declaration

This work described in this thesis was carried out at the Department of Materials Science, Technische Universität Darmstadt, Germany. This thesis represents the author's original work, except where otherwise stated, and no part of it has been submitted for a degree at any other university. Prior to the submission of this thesis, some work has been published as described in the relevant chapters herein.

Eidesstattliche Erklärung

Hiermit erkläre ich an Eides statt, dass ich die vorliegende Dissertation selbstständig und nur mit den angegebenen Hilfsmitteln angefertigt habe. Von mir wurde weder an der Technischen Universität Darmstadt noch einer anderen Hochschule ein Promotionsversuch unternommen

Darmstadt, den

Shrikant Bhat